Exploring the environment of high Rotation Measure Active Galactic Nuclei through wide-band radio spectropolarimetry observations

Dissertation

zur **Erlangung des Doktorgrades (*Dr. rer. nat.*)**

der **Rheinischen Friedrich–Wilhelms–Universität, Bonn**

vorgelegt von

Alice PASETTO

aus Mantova, Italy

Bonn 2016

Angefertigt mit Genehmigung der Mathematisch-Naturwissenschaftlichen
Fakultät der Rheinischen Friedrich–Wilhelms–Universität Bonn

1. Referent: Prof. Dr. Michael Kramer
2. Referent: Prof. Dr. Thomas H. Reiprich
Tag der Promotion: 17-10-2016
Erscheinungsjahr: 2016

RHEINISCHEN
FRIEDRICH–WILHELMS–UNIVERSITÄT BONN

Abstract

by Alice Pasetto

for the degree of

Doctor rerum naturalium

In this Thesis we present an observational study of a sample of radio AGN sources. We study their radio polarization properties in a wide frequency range by observing with the 100-m Effelsberg telescope and the Karl G. Jansky Very Large Array (VLA) interferometer. Our aim was 1) to define a sample of AGN candidates to contain an extreme environment around the SMBH and, 2) to explore the possibility of studying the AGN environment and/or structure by modeling of the polarization properties within a wide frequency range.

We selected an initial sample of 537 sources from the entire northern sky. These are sources that do not show detectable polarized flux at 1.4 GHz in the NVSS radio survey catalogue, a characteristic indicating a strong depolarization probably due to a high value of their Rotation Measure (RM) at low frequencies. This characteristic is suggestive of an extreme (high dense and magnetized) medium in these sources. We performed single dish observations at 10.45 GHz using the 100-m Effelsberg telescope on the initial sample. At this high frequency, we detected polarized flux density on 30 sources, which became our high-RM candidates. We then characterized their radio spectra and determined their RMs through a single dish follow up campaign in the 2 to 15 GHz frequency range.

The Effelsberg campaign allow us to characterize their radio spectra and to estimate their single dish RM as a linear regression fit of the polarization angle versus λ^2. We found that the polarization angle behavior deviates significantly from the λ^2 law. This is a clear

sign of complex medium, suggesting that several Faraday screens are present in the intervening medium.

To characterize the complex Faraday behavior we studied the most interesting high-RM cases through wide-band high sensitive observations performing radio interferometric observations at L C and X bands using the JVLA. We were able to follow the behavior of the fractional polarization and the polarization angle in a well-sampled wide frequency range. This allows us to properly model the polarization properties and thus to obtain important information of the ambient medium characteristics. Our JVLA polarization results confirmed the complexity of the medium surrounding the AGN. Indeed, we found that the complexity of the RM increases towards high frequencies.

We constructed a set of models which are combination of simple internal and the external Faraday screens. This new approach of polarization study allows to spectrally resolve multiple polarized components of unresolved AGN with the result to trace some clumpy and dense region surrounding them. We gave a first interpretation of the environment of the AGN taking into account the JVLA wide-band results (their radio spectra, the polarization information and the depolarization modeling results) together with higher resolution VLBI images from literature and other information when available.

Our study demonstrates that this new spectropolarimetry approach can be adopted as a new way to trace in the radio band some clumpy and dense regions surrounding the AGN but also study the evolution in time of the jet through an inhomogeneous medium.

To Andrea and Carolina.

Acknowledgements

My sincere gratitude goes to my advisor Prof. Dr. Michael Kramer; thank you for the opportunity you gave me to work in an Institute of excellence and to develop my skills. A enormous Thank you to my supervisor Dr. Alex Kraus my guide during this journey, thank you for your teaching, experience and advices. Another special Thank you goes to Dr. Karl-Heinz Mack that told me to persevere in this field. Thank you to my friends and collaborators: Dr. Carlos Carrasco-González, Dr. Gabriele Bruni, Dr. Aritra Basu, Dr. Bia Boccardi, Dr. Alberto Sanna, Dr. Lorenzo Lovisari, Dr. Andrea Giannetti...
Finally, I really want to Thank my family which support me, always and in all the circumstances.
I love you all.

Contents

1 Introduction **1**
- 1.1 The AGN anatomy . . . 3
  - 1.1.1 The supermassive black hole . . . 3
  - 1.1.2 The accretion disk . . . 5
  - 1.1.3 The broad and the narrow line regions . . . 5
  - 1.1.4 The torus . . . 7
  - 1.1.5 The jet . . . 9
- 1.2 AGN and the unified scheme . . . 15
- 1.3 Synchrotron radiation . . . 21
  - 1.3.1 The synchrotron radio spectrum of an AGN . . . 23
  - 1.3.2 The polarization of the synchrotron radiation . . . 25
  - 1.3.3 Depolarization models . . . 28
- 1.4 The environment of an AGN . . . 30
- 1.5 The High-RM project . . . 35

2 Effelsberg campaign **39**
- 2.1 Introduction . . . 39
- 2.2 Sample selection criteria . . . 39
- 2.3 Possible selection biases . . . 41
- 2.4 Observations . . . 41
  - 2.4.1 10.45 GHz observations . . . 41
  - 2.4.2 Follow-up program . . . 42
  - 2.4.3 Time variability . . . 43
  - 2.4.4 Data reduction . . . 43
- 2.5 Comparison samples . . . 44
- 2.6 Results and discussion . . . 44
  - 2.6.1 Spectral index distribution . . . 48
  - 2.6.2 The radio spectral energy distribution . . . 50
  - 2.6.3 Magnetic field estimation . . . 53
  - 2.6.4 Rotation measure . . . 54
  - 2.6.5 Fractional polarization, depolarization, and repolarization . 55
- 2.7 Summary and conclusions . . . 58

3 JVLA campaign **61**
- 3.1 Introduction . . . 61
- 3.2 Observations and data reduction . . . 62
- 3.3 Depolarization models . . . 64

3.3.1 Depolarization models: possible improvements 68
3.4 Results 70
3.5 Discussion 96
3.5.1 Comments on the individual sources 96
3.5.2 Depolarization scenarios 107
3.5.3 The projected linear size and the synchrotron emission . . 109
3.5.4 RM vs frequency dependence 112
3.5.5 Magnetic field order 112
3.5.6 Implications of this JVLA study 113
3.6 Conclusions 114

4 Summary and future work **117**

A Effelsberg Appendix **121**
A.1 Single dish information 121
A.2 Parameters used for the SEDs fit 128
A.3 Plots single dish data 129

B JVLA Appendix **135**

Bibliography **147**

Chapter 1

Introduction

The history of the discovery of Quasars (QSOs) started around the mid '50s and the '60s and was based on determination of accurate positions of radio sources. Carl Seyfert already found evidence in the early '40s for some spiral galaxies with active nuclei (Seyfert, 1943), but this discovery was somehow unnoticed. In the mid of '50s few people (e.g. Baade & Minkowski, 1954; Minkowski & Greenstein, 1954) found some strange and energetic episodes connected with a recently discovered radio loud galaxies. Moreover, with the discovery in the late '50s of the first double-lobed radio sources, it was clear that galaxies were able of showing strong energetic phenomena. These powerful radio events were lately associated to non-thermal phenomena, and the idea that they were powered by relativistic jets, started to hold among astronomical community (Shklovskii, 1969; Scheuer, 1974). People then started to look at the optical counterpart of those radio sources (e.g. Messier 87, Cygnus A, Centaurus A) and people realized that these systems are not quiescent.

The radio surveys (e.g. the 3C and 4C - Cambridge survey in 1959, the PKS - Parkes survey in 1969) started to be essential and, as a consequence, the previously mentioned accuracy of the radio position improved highly. Therefore, people clearly realized that some apparently starlike objects were also strong radio sources. This result led to the discovery of quasars.

The existence of a connection between stellar-like objects and powerful radio sources, motivated spectroscopic observations by Maarten Schmidt and Jesse Greenstein on 3C273 (Schmidt, 1963) and 3C48 (Greenstein & Matthews, 1963) (see spectra in Fig. 1.1).
The principal characteristic, that it is still one of the most important sign of the presence of a QSO, was the detection of redshifted broad emission-lines that implied large cosmological distances, with z=0.16 for 3C273 and z=0.37 for 3C48 (high redshift for that time), and huge energy involved. Shortly thereafter, sources were found at even higher redshift (e.g. QSO 0237–23 with z=2.2 Arp et al., 1967).

Another important discovery at that time was that these sources were variable in intensity and on small timescales (weeks/months). This implied a very small emitting volumes (Greenstein & Schmidt, 1964). Things got more and more complicated by the mid '60s, when Sandage (1965) revealed that many sources, identical to quasars, were radio quiet instead (today ≈90% of known broad-line

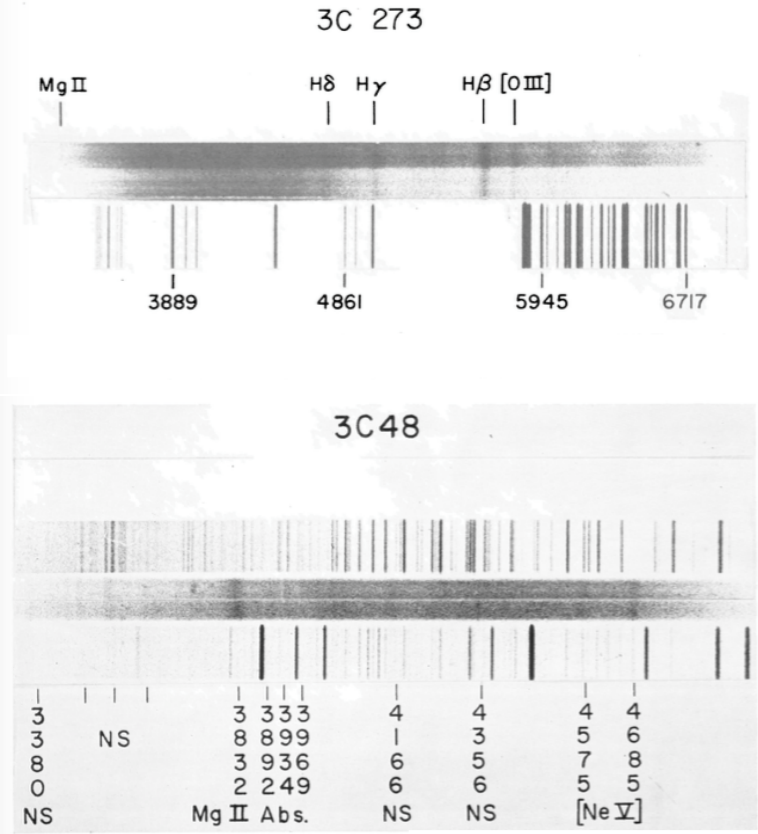

Figure 1.1: Spectra of the QSOs: 3C273 and 3C48. Redshifted emission lines of the Balmer series were identified for the source 3C273 and the redshifted lines on MgII and [NeV] were detected for the source 3C48. Images from Greenstein & Schmidt (1964).

emitters) and later some other studies identified QSOs/Seyfert galaxies/radio galaxies showing only narrow lines or no lines at all.

In 1968 the Steward Observatory (University of Arizona) hosted the first conference on Seyfert galaxies, soon after the discovery of quasars. Here, the researchers started to question whether quasars were truly compact sources (i.e., naked) or whether they were nuclei of currently active galaxies.

Seyfert galaxies and QSOs became very popular and with their popularity increased also the confusion trying to describe them as different (or not) objects. People needed to wait few years later when Orr & Browne (1982) tried to classified them through their radio spectra. Lately, the Unification scheme, with which the diversity of the AGN observed properties are explained as a viewing angle effect and anisotropic nuclear obscuration, became more valid (Antonucci,

1993; Urry & Padovani, 1995).

1.1 The AGN anatomy

Active Galactic Nuclei (AGN) is the name attributed to those sources which show energetic phenomena in their central region. They are believed to be powered by the accretion of matter onto a Super Massive Black Hole (SMBH, Rees, 1984). AGN are complex systems that are present in the center of a minority of galaxies (∼10% of the galaxies are active). These systems are a unique physical laboratory where testing extreme environment conditions and extreme physical processes. As already outlined, Seyfert galaxies and QSOs are just two elements of the same big family, the AGN one, for which their properties and therefore their classification are highly dependent on the orientation of these objects with respect to the observer's line of sight. Before talking about the unification scheme, presented in the section 1.2, I will briefly describe the main constituents of an AGN (Fig. 1.16).

1.1.1 The supermassive black hole

An AGN produces an enormous quantity of energy (its luminosity is L∼ 10^{46} erg/s) in a very small volume (smaller than a cubic parsec). In the current picture, the central engine of the AGN is a system consisting of a hot accretion disk surrounding a SMBH (Rees, 1984). The energy is produced by gravitational infall of material forming the accretion disk onto the SMBH, a very massive object with M_{BH}∼10^7-10^{10} solar masses ($M_\odot$). Its compactness is determined by the Schwarzschild radius R_S= $2GM_{BH}/c^2$ where G is the gravitational constant and c is the value of the speed of light. The Schwarzschild radius defines a surface called "event horizon", within which the escape velocity becomes larger that the speed of light. Therefore, no radiation can escape from the black hole (hence its name). A black hole can also rotate (Kerr BH), thus it has a spin value α_*=$Jc/GM_{BH}{}^2$ (where J is the angular momentum of the BH) that takes values between 0 and 1. Due to the rotation of the black hole, the event horizon becomes narrow reaching a value of $0.5R_S$ for a maximum spinning black hole (α_*=1). The Kerr black hole produces an important phenomenon called dragging of inertial frames (Thirring, 1918), meaning that a rotating black hole drags all the material with an orbital motion following the same black hole rotating direction. The drag effect increases with the vicinity of the material to the event horizon. However, before reaching the event horizon, a particle reaches a *static limit* within which the dragging is very strong and no object can remain in a quiet state. This static limit equals the radius of the event horizon at the polar direction and it could be double the

radius of the event horizon (depending on the BH spin value) on the equatorial plane. The elliptical shape region that is formed is called the ergosphere (see Fig. 1.2). Within it the particles not necessarily disappear in the event horizon, but they can actually gain energy from the rotation and escape with energy larger than the one they had at the entrance of the ergosphere with the result of loss of angular momentum of the black hole (Penrose process, Penrose & Floyd, 1971). This mechanism is important in the context of the jet formation.

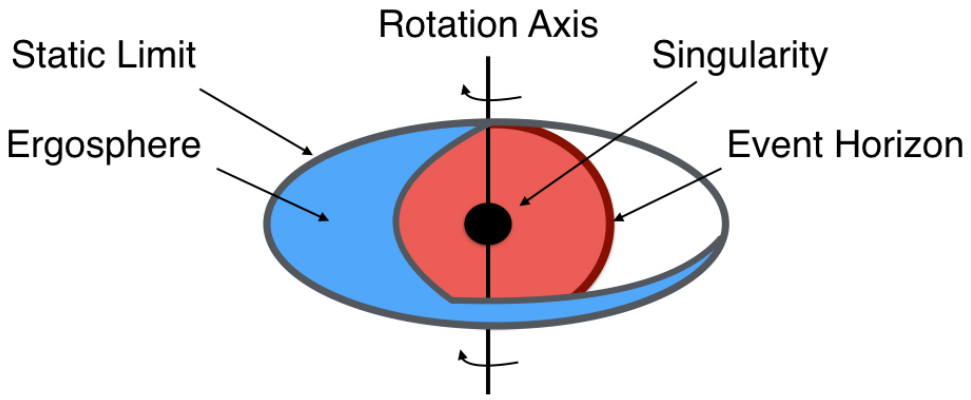

Figure 1.2: The static limit and the ergosphere of a Kerr BH.

However, since the black holes are invisible, how can we be sure about their existence? Astronomers can determine the presence of a black hole by the influence it has on the surrounding ambient or objects. Indeed, dynamical studies, either of the gas or of the stellar populations orbiting a SMBH, is one of the important methods for the determination of the mass of the black hole, e.g. studies of the motion of stars in the galactic center of our Milky Way (Ghez et al., 2000; Eckart et al., 2002; Meyer et al., 2012). Megamaser studies provide compelling evidence that a massive black hole exists at the centre of NGC4258 (Miyoshi et al., 1995). These are special cases due to the vicinity of the systems, however the technique called reverberation mapping (Blandford & McKee, 1982) is a useful method that can be applied to high redshift systems. This method connects the variability of the continuum emission from the accretion disk with the variability of the emission line produced by the surrounding gas clouds. Very recently the Laser Interferometer Gravitational-Wave Observatory (LIGO) for the first time observed ripples of spacetime, the so called gravitational waves, produced from cataclysmic event of a merges of two black holes (Abbott et al., 2016). Although the nature of the two black holes are of stellar type, this new technique will open new frontiers and the SMBH will be also visible through this fascinating general relativity new eyes.

1.1.2 The accretion disk

The accretion disk is the key element for a galaxy to be active. AGN are indeed characterized by significant accretion activity onto the SMBH that is responsible for the high energy produced. Therefore, a huge quantity of gas needs to be accumulated and to fall into the gravitational potential of the central object. The central regions contain a lot of gas that can be moved inward through asymmetries, perturbations, viscosity, hydrodynamic effects, radiation and magnetic field transportation.

The differential rotation of the material in the disk gives rise to the thermal radiation produced by friction. If the luminosity is as high as the gravitational energy, the accretion stops. The luminosity of the objects reaches a limit, called the Eddington luminosity limit:

$$L_{Edd} = 1.26 \cdot 10^{38} \frac{M_{BH}}{M_{\odot}} \qquad [erg/s] \tag{1.1}$$

Thus, also the accretion rate is limited and it is expressed by:

$$\dot{M}_{Edd} = \frac{L_{Edd}}{\eta c^2} = 1.5 \cdot 10^{25} M_{BH,8} \qquad [gr/s] \qquad \approx 0.2 M_{BH,8} \tag{1.2}$$

where $M_{BH,8}$ is a 10^8 $M_{\odot}$ BH and η is an efficiency factor that depends on the physical condition of the disk; it is maximised if the disk is assumed to be optically thick and geometrically thin (Shakura & Sunyaev, 1973).

It can be assumed that the optically thick disk radiates as a black-body, thus the temperature T of the disk depends on the radial distance R from the centre and is proportional to $T(R) \propto (M_{BH}\dot{M}/R^3)^{1/4}$ and typically is in the range of 10^4-10^6. At this high temperature, the radiation emits in the optical-UV, producing the so called *blue bump* in the AGN spectra.

1.1.3 The broad and the narrow line regions

The Broad Line Region (BLR) and the Narrow Line Region (NLR) are clouds of gas surrounding the SMBH.

The BLR is the region where broad emission lines dominate the optical spectra. The spectral lines are Doppler-broadened, therefore the line widths are measured in velocity units. The most intense lines from the BLR, are usually the lines of hydrogen (Lyman alpha) and the Carbon lines CIV and the semi-forbidden CIII]. Typical values of the line widths are $\Delta v_{FWHM} \approx$ 5000 km s^{-1}, but they range from a minimum of $\Delta v_{FWHM} \approx$ 500 km s^{-1} to $\Delta v_{FWHM} \approx 10^4$ km s^{-1}. These values are produced by gas of high density, with $n_e \approx 10^9$ cm^{-3}, at a temperature of 10^4 K (Peterson, 2006). The large Doppler widths of some broad lines and the short time delay between the variability of the continuum,

produced from the central source, and of the lines suggests that the BLR is extremely close to the central engine (less than 1 parsec). Fig. 1.3 shows a composite quasar spectra at different luminosities (vanden Berk et al., 2004).

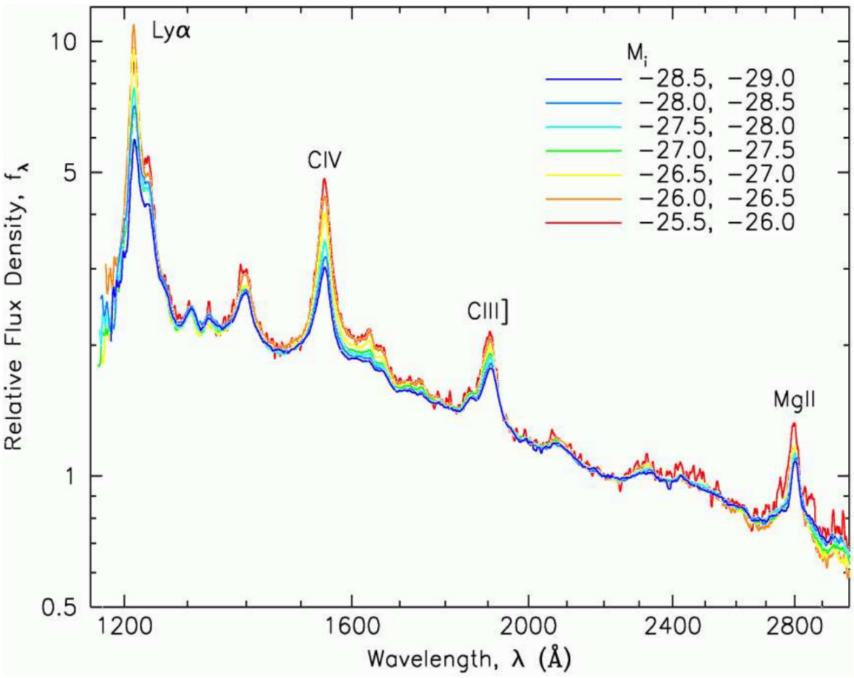

Figure 1.3: Typical broad lines detected in an AGN. Here, a composite quasar spectra at different luminosities (vanden Berk et al., 2004).

However, the BLR is not observed in all AGN. While this absence may be intrinsic in some low luminosity AGN, in most of the cases it is caused by the absorption from a thick torus obscuring the nucleus. The broad lines scattered by this material can be observed in polarized light (Antonucci & Miller, 1984).

The Narrow Line Region (NLR) is the region placed far from the BLR. It is a unique laboratory placed at boundary between the host galaxy and the region dominated by the AGN, it is typically extended from just outside the torus to hundreds and even thousand of parsecs (Netzer, 2015). The NLR is also the only AGN component which is spatially resolved in the optical (Evans et al., 1991; Macchetto et al., 1994). Fig 1.4 shows the high spatial resolution [OIII] λ5007 image of the NLR of NGC 1068 (prototypical Seyfert 2 galaxy) that is resolved in several distinct clouds (Evans et al., 1991) . The full widths at half maximum of the narrow emission lines fall in the range 200 $\lessapprox \Delta v_{FWHM} \lessapprox$ 500 km s^{-1} with most of the values being around 350-400 km s^{-1}. Often it is possible to detect forbidden lines, implying that they arise in low-density gas clouds with $n_e \approx 10^3$ cm^{-3}.

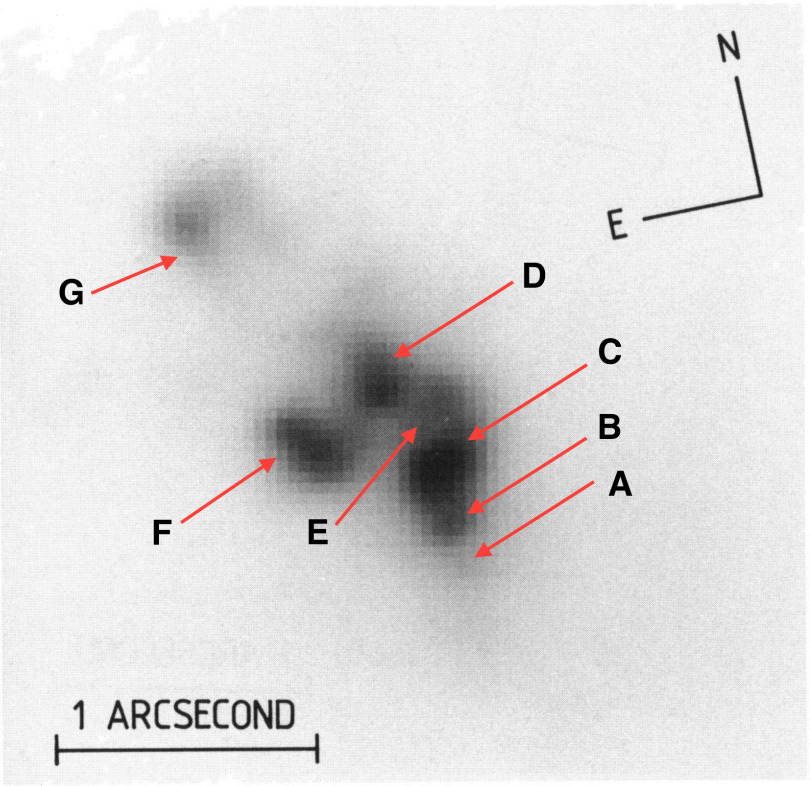

Figure 1.4: Continuum-subtracted [O III] image of the nuclear region of NGC1068; seven clouds are identified (Evans et al., 1991).

1.1.4 The torus

The very inner constituents of an AGN, i.e. the SMBH, the accretion disk and the BLR, can be hidden when the object if viewed edge-on, by the presence of circumnuclear, optically thick material with a toroidal shape. From modelling studies, the torus is supposed to have a radius smaller than 6 pc from the central object (Ramos Almeida et al., 2012). The dust sublimation radius is the radius at which large graphite grains rapidly sublime (at a temperature T≈ 1700 K) and it depends on the AGN bolometric luminosity L (Laor & Draine, 1993):

$$r_{min} \simeq 0.20\sqrt{L_{46}} \qquad [pc] \tag{1.3}$$

Therefore, if one can estimate the AGN bolometric luminosity, it could be possible to know whether the observed clumpy regions are coming from the torus or from regions closer to the central engine.

Observations of strong extinction, suggests the presence of a large quantity of dust, dense enough to be opaque to hard X-ray. Its column density is of the order

of $\sim 10^{24}$ cm$^{-}2$ (Krolik & Begelman, 1988). Near and mid-infrared observations confirm the existence of emission associated both with warm and hot dust, in a range of temperatures between 10^2-10^3 K (Raban et al., 2009).

A direct image of the torus has not been observed yet but more extended dusty regions have been detected. For example, with the Hubble Space Telescope Jaffe et al. (1993) discovered a large disk of cool dust and gas surrounding the bright unresolved nucleus in the active galaxy NGC 4261 (see Fig. 1.5, Jaffe et al., 1993). Moreover, recent ALMA observations on NGC1068 reveals the presence of intense emission of CO, HNC, HCO+, CS in the nuclear regions (see Fig. 1.6, Garcia-Burillo et al., 2014). This suggests the possible presence of a considerable fraction of molecular gas in the torus, which can survive to the extreme environmental conditions thanks to the screening from the dust.

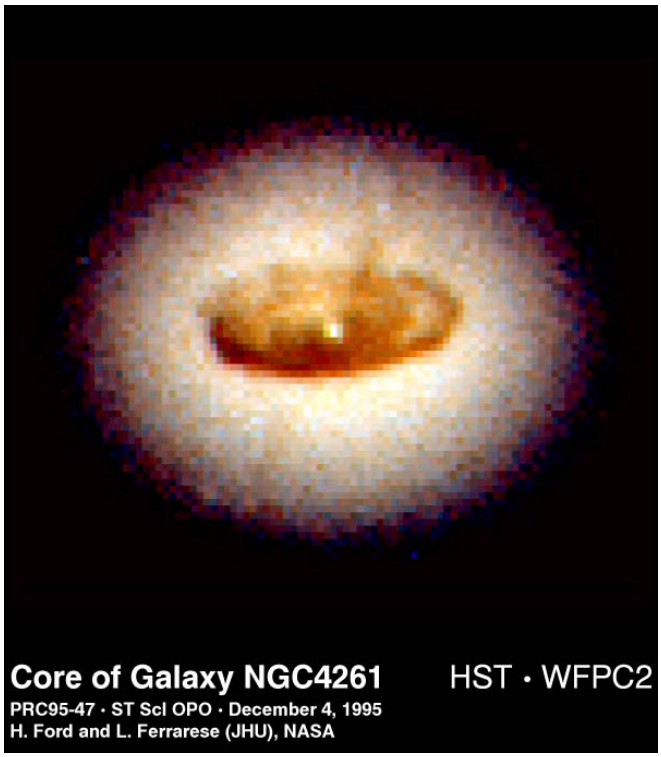

Figure 1.5: HST image of the large dusty region around the central nucleus in NGC 4261(Jaffe et al., 1993).

Polarization observations can also be used to help to reveal the dusty torus. Very recently Gratadour et al. (2015) detects the presence of an extended nuclear torus again at the centre of NGC 1068. In this study, the polarized intensity, that is dominated by scattered light from the central source, reveals a compact elongated region in the inner arc-second around the nucleus (see Fig. 1.7).

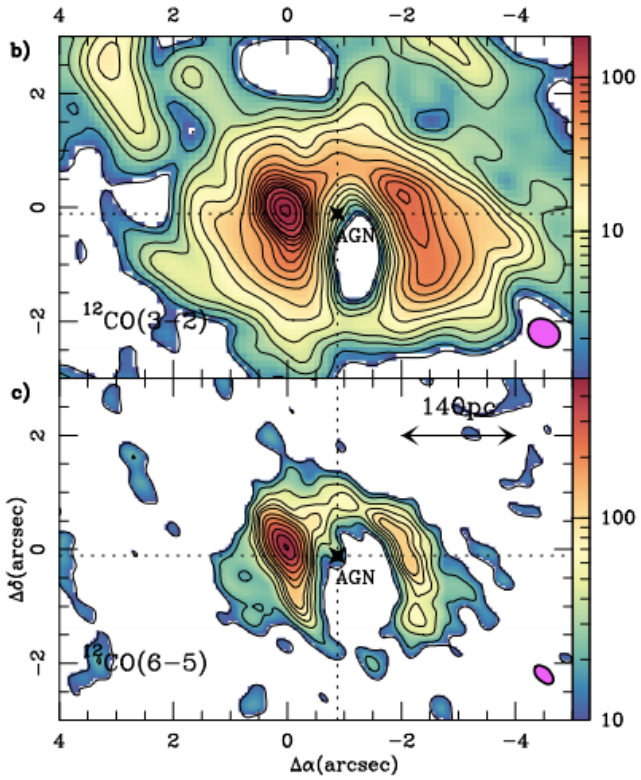

Figure 1.6: ALMA observations of the circumnuclear disk of NGC 1068; *b)*: CO(3–2) integrated intensity map; *c)* Same as *b)* but for the CO(6–5) line (Garcia-Burillo et al., 2014).

Although the dimensions of the objects detected in the above works are bigger than the supposed dimension of the real dusty torus, astronomical instrumentation is almost capable to detect it.

1.1.5 The jet

The study of the astrophysical jets, from the observational and theoretical point of view, is one of the important branches in astronomy both because of their presence in several astrophysical systems, e.g. Young Stellar Objects (YSOs), X-ray binaries, AGN and Gamma-ray bursts, and because its nature is not yet well understood. Jets are collimated outflows of plasma and magnetic field, ejected from the central region of an astronomical object. In AGN, jets are thought to propagate at relativistic speed with a wide range of Lorentz factors up to ∼40, while intrinsically weak jets are only mildly relativistic (Lister et al., 2013). The Lorentz factor is a value needed to transform an object's quantity while that

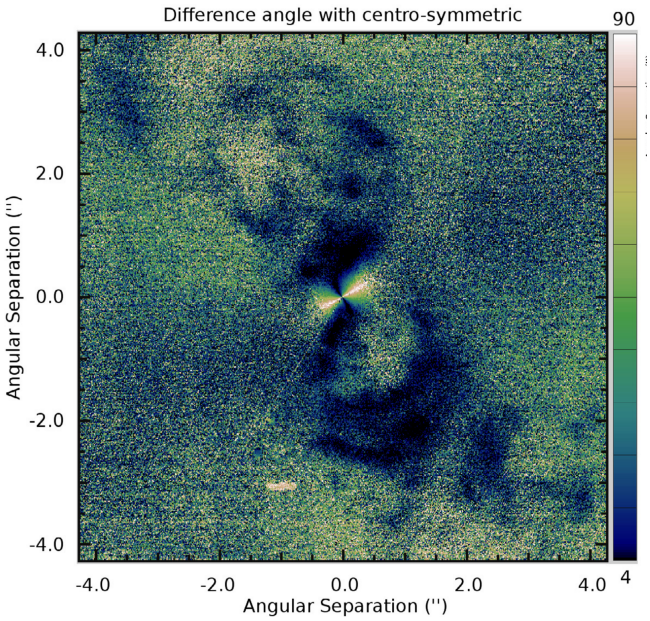

Figure 1.7: Polarization observations of a dusty region in NGC 1058 (Gratadour et al., 2015).

object is moving. It is expressed as:

$$\gamma = \frac{1}{\sqrt{(1 - v^2/c^2)}} = \frac{1}{\sqrt{(1 - \beta^2)}} \tag{1.4}$$

where c is the speed of light and β is the ratio between the velocities v and c. The power of the jets is typically considered to be in the range between 10^{43}–10^{48} erg s^{-1} (Ghisellini et al., 2014) and it can propagate up to some kpc distance from the core and sometime to Mpc scales (Mack et al., 1997). Since they are synchrotron emitters, the jets must contain magnetic field and relativistic electrons. To balance the negative charges, they should also contain some positive charges, i.e. protons, but also there could be positrons (supposed from galactic γ-ray burst observations at 511 keV associated to positrons-electrons annihilation, Leventhal et al., 1978).

The particles within the jet are moving at relativistic speed. However, it is difficult to obtain direct evidence for such high velocities. The most compelling evidence for relativistic speed involves radio observations of material (the knots) ejected from the core at apparent superluminal velocities (see Fig. 1.8). The superluminal motion does not contradict special relativity and can be explained by studying the geometry of the system. Suppose that from the stationary feature, considered to be the radio core, a photon is emitted along the line of sight at the time t_a=0 and at distance d from Earth. At the same time, a blob of

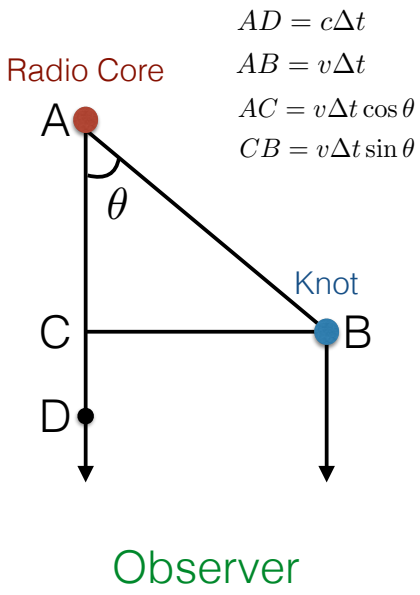

Figure 1.8: Sketch of the superluminal motion

matter is ejected from the radio core with speed v in a direction forming an angle θ with the line of sight of the observer. At time t_b=t_a+Δt the photon emitted from the core is a distant D, while the knot is at the position B and it emits a photon. Therefore, the observer will receive the two signals with a time delay (Δt_{obs}) due to the fact that the photon emitted from the knot has to travel an extra distance CD that depends on the aperture θ:

$$\Delta t_{obs} = \frac{CD}{c} \tag{1.5}$$

$$CD = AD - AC = c\Delta t - v\Delta t \cos\theta \tag{1.6}$$

Moreover, due to projection effects, the knot itself appears to be closer to the radio core of a quantity BC= $v\Delta t \sin\theta$. Therefore, the observed velocity (v_{obs}) of the knot can be expressed as following:

$$v_{obs} = \frac{BC}{\Delta t_{obs}} = \frac{v\Delta t \sin\theta}{(c\Delta t - v\Delta t \cos\theta)/c} \tag{1.7}$$

therefore, substituting β=v/c:

$$\beta_{app} = \frac{\beta \sin\theta}{1 - \beta \cos\theta} \tag{1.8}$$

For small viewing angles and large intrinsic speeds, β_{app} can reach large values (Fig. 1.9). To date, apparent speeds as large as $\approx$ 50c have been measured in extragalactic jets (Lister et al., 2009).

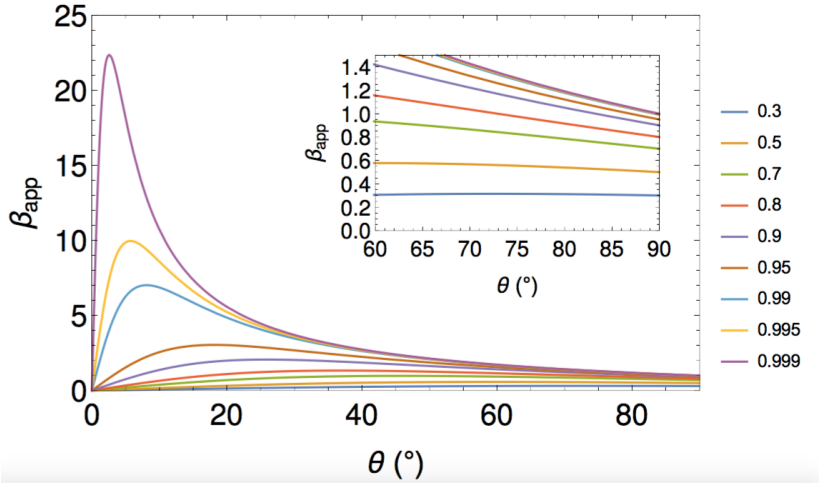

Figure 1.9: Apparent beta versus viewing angle for different values of the intrinsic speed (Karamanavis, 2015).

The physics of the jets is very complex and it is not already full understood. For simplicity one assumes that the jet is in adiabatic equilibrium. However, this is not realistic; indeed, there are dissipative processes that convert the kinetic energy of the jet into thermal energy. Moreover, depending on the orientation of the AGN, the jets can be affected by relativistic effects. The relativistic beaming is maybe the most striking feature of relativistic jets. The observed luminosity is increased, as a result of the superposition of different relativistic effects, by a factor δ^4, where:

$$\delta = \frac{1}{\gamma(1 - \beta \cos\theta)} \tag{1.9}$$

is known as relativistic Doppler "beaming"; γ is the Lorentz factor and β the ratio between the velocities v/c. The beaming is stronger for small viewing angles θ and large β, with δ that diverges to infinity for $\theta = 0$ and $\beta = 1$ (Fig. 1.10).

An important consequence of the beaming is the jet sidedness. It is believed that all jets are intrinsically two-sided, but relativistic effects allow to detect only the jet that is approaching towards the observer. The strong beaming of the approaching jet and de-beaming of the counter-jet results in the ratio R between the two observed flux densities, which is derived to be:

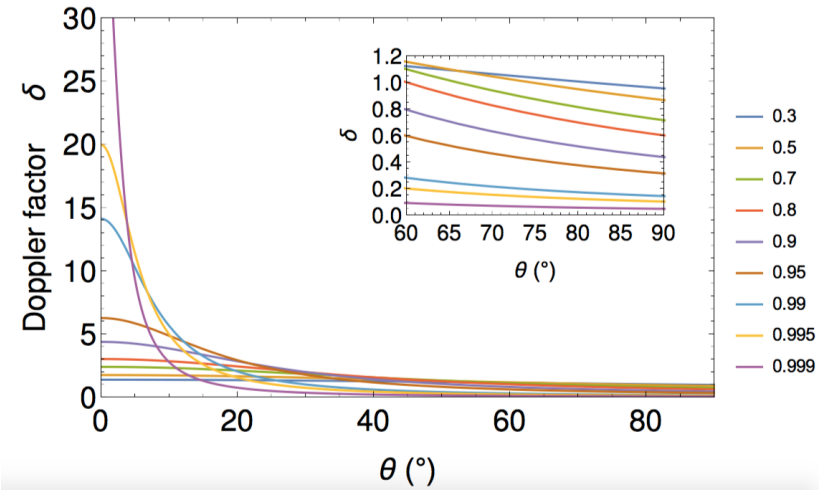

Figure 1.10: Doppler factor δ as a function of viewing angle θ for different values of intrinsic speed β (Karamanavis, 2015).

$$R = \left(\frac{1+\beta\cos\theta}{1-\beta\cos\theta}\right)^{3-\alpha} \tag{1.10}$$

The mechanism of jet launching is one of the hot topics in AGN studies. The principal ingredient for the formation and launch of a jet are the presence of an accretion disk and a magnetic field. A pressure gradient P in the central region of an AGN is needed in order accelerate the plasma. The accretion disk orbits around the SMBH and it produces a magnetosphere. The rotation of this magnetized accretion disk can efficiently power a jet (BP mechanism, Blandford & Payne, 1982). Since the magnetic field lines are frozen in the plasma, a rotation of the central object also implies a rotation of the magnetosphere. The free charges on the surface of the disk will experience a Lorentz force $f = q\mathbf{v}\times\mathbf{B}$, with q being the electric charge, $\mathbf{v}$ the linear rotational velocity and $\mathbf{B}$ the magnetic field. This leads to a separation of the charge on the disk surface. If the magnetic momentum vector is aligned with the spin vector, the current will flow from the poles to the equator. After the plasma is channeled into a jet, the energy content of the flow is mostly dominated by the magnetic field. In order for the jet to reach Lorentz factors of the order of tens, typically observed on parsec scales, this magnetic energy has to be converted into kinetic energy. Moreover, there must be some mechanism which collimates the flow. We refer to specific books for detailed explanations on the jet launching and collimation like George (1991) and Robson (1996).

Moreover, models predicts that all around the relativistic spine, the jet is covered by a much slower wind. Therefore, two different flows exist. One flow

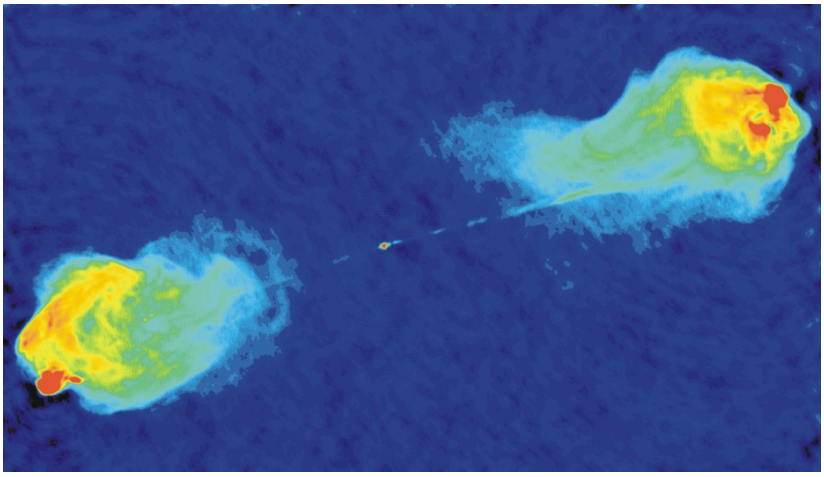

Figure 1.11: Multiconfiguration VLA observations of the radio jet and lobes of the radio galaxy Cygnus A at 1.4 and 5 GHz. Red shows regions with the brightest radio emission, while blue shows regions of fainter emission (Perley et al., 1984).

is the beam of relativistic particles assumed to be extracted from the funnel or the innermost part of the accretion disc and accelerated to a bulk Lorentz factor of order of 10. It is responsible for the the VLBI pc-scale jet and the observed superluminal motion. The second flow consists of a classical or mildly relativistic wind coming out from all parts of the accretion disc. It is related to the large jet observed at kpc scale (Sol et al., 1989). This scenario is essential to model the SEDs of the strong TeV BL Lacs, where the high energy emission can hardly be reconciled with the low Lorentz factors observed from VLBI studies. Therefore, Ghisellini et al. (2005) advanced the hypothesis of a jet being composed by a slow layer and a fast spine. This possible spine-sheath jet structure is supported by recent observational evidence coming from detailed VLBI radio maps, showing, e.g in Mkn 501, a limb brightening morphology, interpreted as evidence of a slower external flow surrounding a faster spine (Giroletti et al., 2004) or from 43 GHz (7mm) observations of the famous radio galaxy Cygnus-A where kinematics and light-curves analysis revealed the existence of an acceleration region in the inner-jet extending up to a de-projected distance of $\sim$0.9 pc (considering the Cyg-A viewing angle of 74.5°) and the outer-jet with a lower speed (Boccardi et al., 2016).

Interferometric techniques is the most suitable method to observe AGN jets. It can provide detailed images of the kilo-parsec scale of the objects (Fig. 1.11, Perley et al., 1984) or it can distinguish the several compact features in the very innermost pc scales (Fig. 1.12, Boccardi et al., 2016). Theoretical and

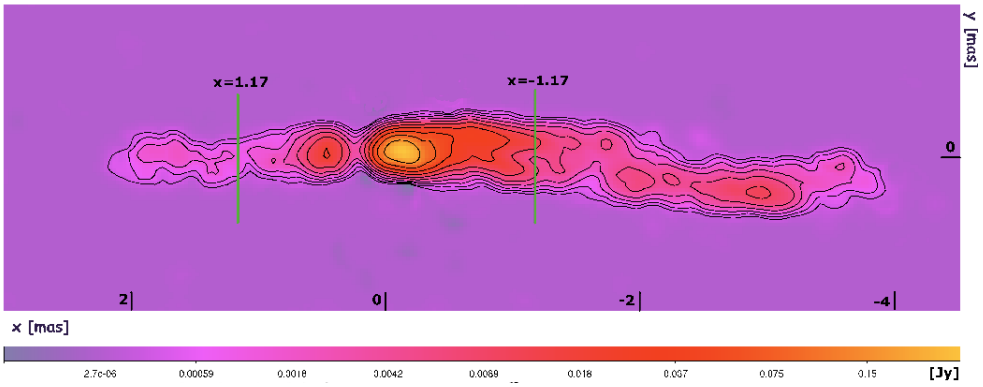

Figure 1.12: Global VLBI image of Cygnus A at 45 GHz (7 mm); ultra-high resolution image reaching scales down to 90 μas (Boccardi et al., 2016).

observational studies of the radio jets are important to study the jet formation (e.g. the new and exciting work done with RadioAstron performing the innermost region of BL Lacertae at the highest resolution of 21 μarcsec, Fig. 1.13, Gómez et al., 2016), to study the geometry of the jet magnetic field (that can be obtained by looking for Faraday rotation gradients across the jet width Laing, 1981; Asada et al., 2002; Gabuzda et al., 2004) and to study the evolution of the powerful FRI jets (through numerical simulation, e.g. Perucho & Martí, 2007) with the generation of standing recollimation shocks, features still debated (Fig. 1.14).

1.2 AGN and the unified scheme

Two large subclasses of AGN are Seyfert galaxies and Quasars and the distinction between them is in the amount of radiation emitted by the compact central region. For the Seyfert galaxies the total energy emitted by the central core at visible wavelengths is comparable to the energy emitted by the stars in the galaxy (i.e. $\sim 10^{11}$ L$\odot$), while the nuclear source of a QSO is a factor of hundreds brighter than the stars. This is justified by the high-z distances of the QSOs with respect to the Seyfert galaxies.

Nowadays, we have reached a global understanding on what an AGN is but still a lot of work has to be done to understand the physical properties of these extreme objects and their classification is sometimes confusing. Indeed, the taxonomy of AGN is rather complicated, but now it is quite accepted that most of the differences of the observational properties of the various AGN depend on the orientation of the systems with respect to the line of sight of the observer (this is indeed considered the orientation-based scheme).

It sounds natural today to talk about a unified scheme for AGN, but it

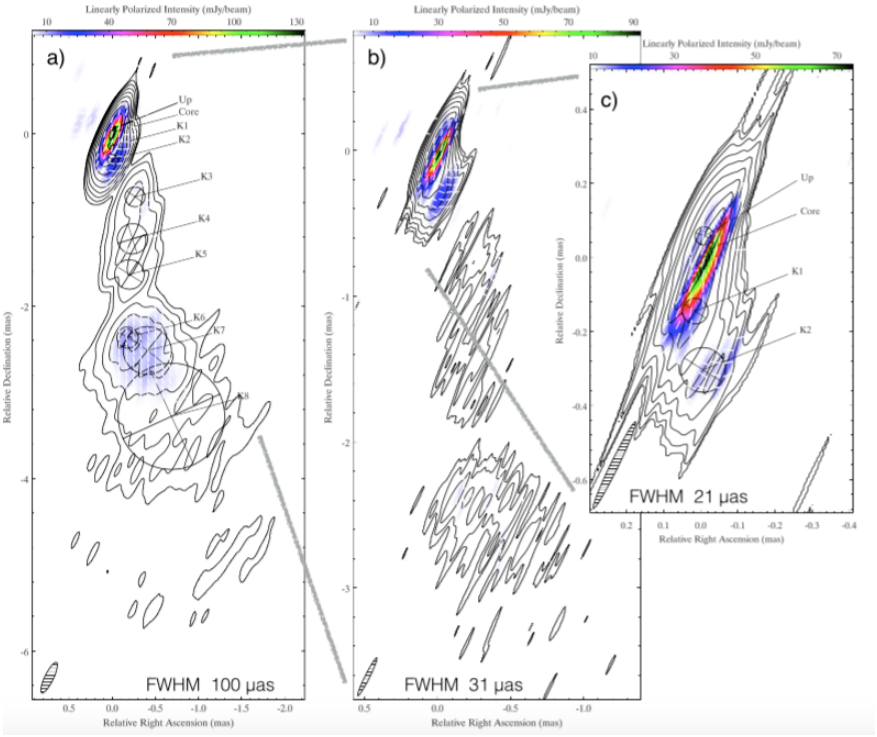

Figure 1.13: RadioAstron polarimetric space VLBI images of BL Lac at 22 GHz. Total intensity is shown in contours. Linearly polarized intensity is shown in colors and white bars indicate the (uncorrected for Faraday rotation) EVPAs (Gómez et al., 2016).

took almost 30 years from the discovery of the first QSOs to collect all different manifestations of these objects (Seyfert galaxies and all the flavor of QSOs) under the umbrella of AGN and its unified model. Indeed, only in the '90s Antonucci (1993) and Urry & Padovani (1995) elaborated a unified scheme for AGN in which the wide variety of AGN phenomena seen is only due to two parameters: the orientation and the luminosity, with the former being the most fundamental. In Fig. 1.15, the basic aspects of a general unification scheme are summarized and in Fig. 1.16 a sketch of the main constituents of an AGN is shown.
Key elements in this scheme are the orientation of the obscuring torus and the presence or absence of the synchrotron-emitting radio jet. Indeed, depending on the orientation of the torus, the AGN can be divided into three types:

- Type 1: the nucleus is face on. Spectral broad lines and narrow lines coming respectively from the BLR and from the NLR are detected and the spectrum is characterized by a strong continuum and strong hard X-rays.

- Type 2: the nucleus is edge on. The torus is obscuring the very central

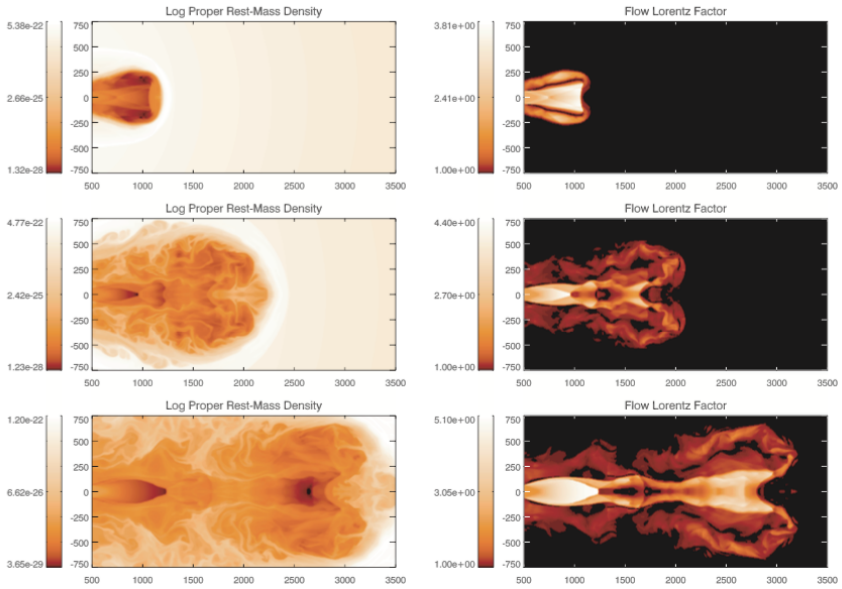

Figure 1.14: logarithm of rest-mass density and Lorentz factor at different times of the first stages of evolution. During the jet evolution (middle and bottom panels), the jet is slowed down in recollimation shocks (Perucho & Martí, 2007).

part, i.e. the SMBH, its accretion disk and the clumpy clouds of the BLR. Therefore only narrow lines, from the NLR are detected in the spectrum. The continuum emission is reduced but instead the dust emission is responsible for a strong infrared emission.

- Type 0: the nucleus is partly obscured. Therefore the observational properties are intermediate between the type 1 and type 2 AGN.

Another important parameter is the AGN brightness in the radio band, called "radio loudness". This property is given considering the ratio of radio flux density at 5 GHz (F_5) with optical flux density measured in the B-band (F_B). The characteristic of the radio loudness itself could be related to the host galaxy type (Smith et al., 1986) or to black hole spin (Blandford et al., 1990; Wilson & Colbert, 1995) which might enable the formation of a relativistic jets. AGN could be considered:

- Radio quiet: with the ratio $F_5/F_B < 10$ (roughly ~ 90 % of the AGN);
- Radio loud: with the ratio $F_5/F_B > 10$ (roughly ~ 10 % of the AGN).

The principal objects that are considered radio-quiet are:

- Seyfert galaxies: low redshift objects for which the host galaxy is clearly detected and it is usually a spiral;

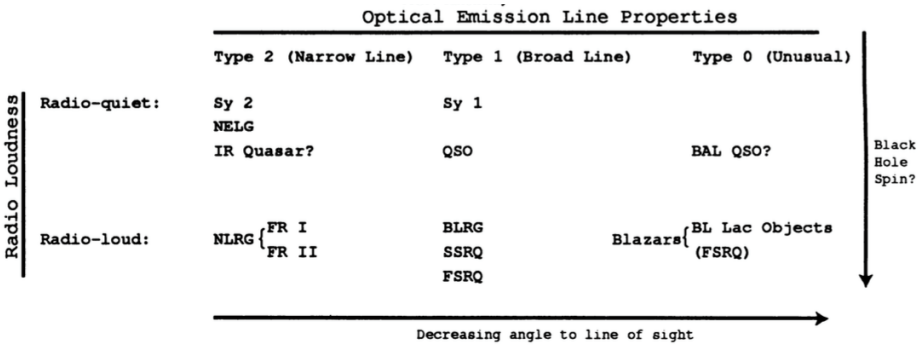

Figure 1.15: AGN taxonomy in a possible unified scheme (Urry & Padovani, 1995)

- Quasi Stellar Objects (QSOs): they maintained the historical name (matter sometime of confusion) and they are high redshift objects, hosted typically by an elliptical galaxy. The emission of these objects is dominated by the accretion process.

However, as mentioned above, AGN can show powerful relativistic jets. In this case AGN are considered radio-loud. The presence of a jet affects, often dramatically, the observed emission (Blandford & Königl, 1979; Barthel, 1989), leading to consider these objects as forming a more complicated class. In this case, not only the orientation of the torus is important but also the orientation of the jet.

The most important objects are:

- Radio galaxies: they are radio-loud AGN with a jet oriented close to the plane of the sky and they have very bright and diffuse radio emission that can extend to mega-parsecs scales. Among these objects, Fanaroff & Riley (1974) separated the radio galaxies into two distinct luminosity classes. Indeed, depending on their luminosity in the radio band at 1.4 GHz, radio galaxies are considered to be:

  - FRI: weaker radio galaxies with a luminosity $L < 10^{41}$ erg/s. They are very bright at the centre and their luminosity decrease towards the edge. Their darkened twin lobes are connected by a not well collimated and often double-sided jets.
  - FRII: more luminous radio sources with a luminosity $L > 10^{41}$ erg/s. They have radio lobes with prominent hot spots and bright outer edges. Jets, when seen, tend to be highly collimated and often they appear one-sided.

- Blazars: radio-loud AGN with a jet oriented close to the line of sight of the observer. Therefore their emission is strongly affected by relativistic effects. An important characteristic is that they are core dominated objects (Kapahi & Saikia, 1982), i.e. the parsec scale radio emission already include most of the total flux density. Moreover, they are characterized by strong variability and high degree of polarization. Based on spectral properties and luminosity, they are further divided in:

  - BLLac objects: low power and low redshift Blazars. They are characterized by weak broad emission lines.
  - Flat Spectrum Radio Quasars (FSRQs): high power and high redshift Blazars showing strong broad emission lines.

This explained above is the AGN zoo in which at the end all the objects are just the same but oriented in a different way. That is the principal aspect that cause the variety of sources that are so unique but at the same time so similar to each other.

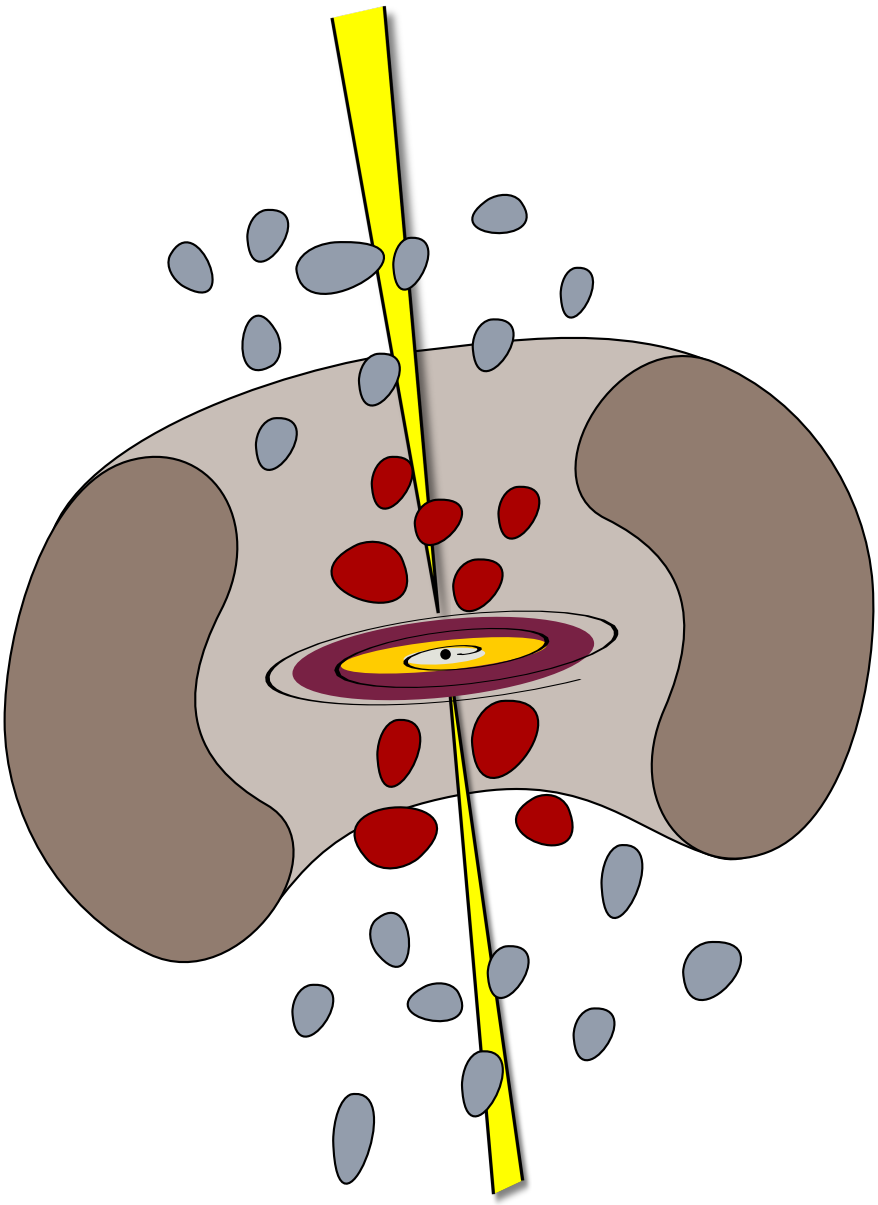

Figure 1.16: Sketch of the main constituents of an AGN (Karamanavis, 2015). The black point at the center is the supermassive black hole, surrounded by the accretion disk (in orange and violet). The broad line region and the narrow line regions are drawn as clouds of gas rotating around the nucleus. They are responsible for broad (red clouds) and narrow (blue clouds) emission lines respectively. A thick dusty torus (gray, donut-like structure) covers the central regions. In some cases, a relativistic jet (yellow) is emitted from the nucleus.

1.3 Synchrotron radiation

Synchrotron radiation is a non-thermal radiation, meaning that the distribution of the emitting particles is not Maxwelian, thus these particles are not in thermal equilibrium. This mechanism is yielded through the motion of highly relativistic charged particles within a magnetic field and it can occur over a large frequency regimes, from radio to X-rays. It is considered a very important phenomenon observed in many classes of astrophysical objects such as:

- jets of radio galaxies
- radio to X-ray emission from BL Lacs
- supernovae remnants
- galaxies and cluster halos

Synchrotron radiation is emitted by charged particles, usually electrons, moving at relativistic speeds in magnetic fields ($\vec{B}$). In a magnetic field a charged particle is forced to circle around the field line in a helical path. An accelerating charged particle emits electromagnetic radiation that is radiated along the direction in which the particle is moving (Fig. 1.17).

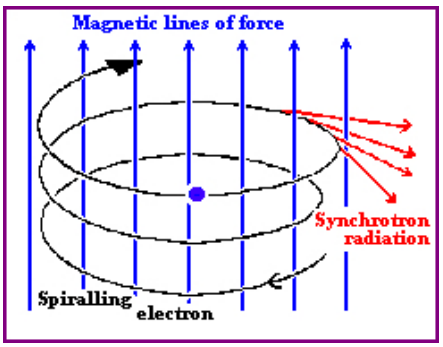

Figure 1.17: Sketch of the helicoidal shape of the synchrotron radiation (credit: NASA, University of Hertfordshire).

When a region is emitting synchrotron radiation, then a population of particles is subject to this mechanism the energy distribution of which is described with as a power law distribution:

$$N(E)dE = kE^{-p}dE \tag{1.11}$$

Thus, the energy radiated at a certain frequency is:

$$S(\nu) \propto \nu^{(1-p)/2} = \nu^{\alpha} \tag{1.12}$$

being p the power law slope of the particle energy distribution and α the spectral index of the synchrotron emission. This result is important because it links an observable parameter, α, to the power law slope of the particle energy distribution. A typical value for the spectral index is α=–0.7 for radio galaxy, corresponding to p=2.5. In Fig. 1.18 the combination of many individual emissions producing a power spectrum is illustrated with the spectral index $\alpha \approx$ –0.7.

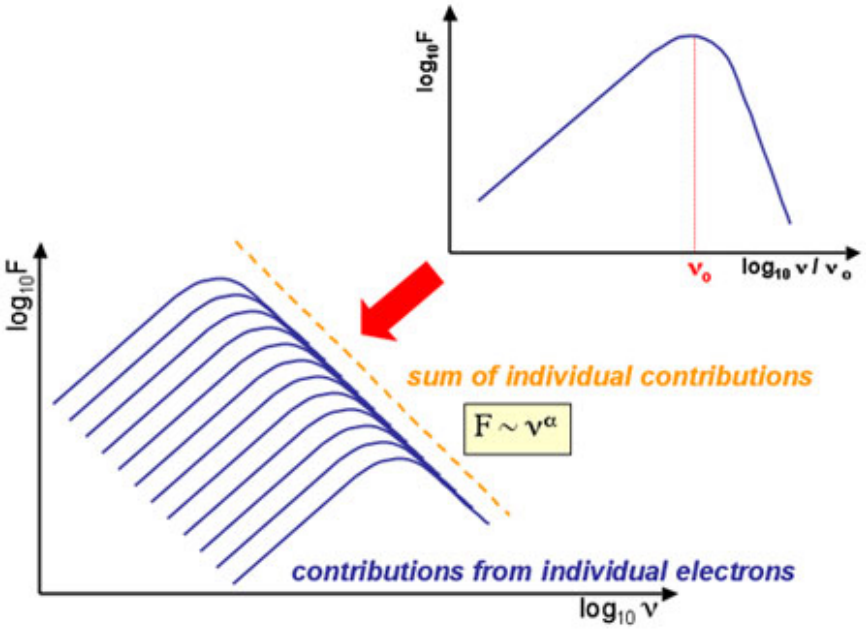

Figure 1.18: Superposition of the single-particle synchrotron spectra following a power-law distribution (credit: The SAO Encyclopedia of Astronomy, Swinburne University).

Deviations from the simple power law exist; they are due to processes that reduce the energy of the relativistic electrons. Therefore, the spectrum can change its slope becoming steeper after a certain frequency and from that change, the "age" of the electrons population could be estimated.

Another characteristic of the synchrotron radiation is that the particles responsible for the emission not only radiate but also can absorb it. This occurs when the brightness temperature (T_B) of a source equals the kinetic temperature (T_k) of the electrons. Therefore the radiation is not transparent anymore to its own emission and the electrons absorb it again with the result of a decreasing of the source luminosity. A detailed calculation, taking into account the radiation transport, shows the following frequency dependence of the resulting radio spectrum: the flux density increases with frequency with a slope of 2.5, it reaches a maximum and it decreases with a slope given by α (usually α=–0.7; see Fig.

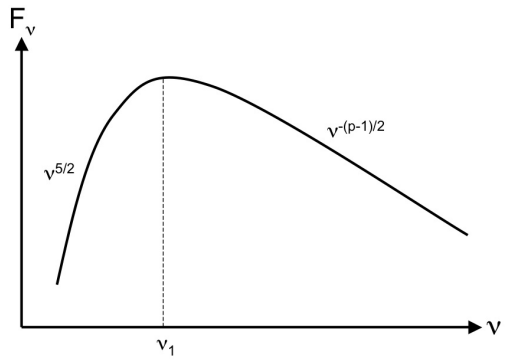

Figure 1.19: Behavior of a Synchrotron Self-Absorption source; before the radiation reaches its maximum, the source is optically thick and it increases with $\nu^{2.5}$, then the radiation follows a power law behavior with $\nu^{-\alpha}$ (credit: Institute of Astronomy, University of Hawaii)

1.19). This kind of spectrum (with a convex shape) is typical in the radio regime and it is characteristic of compact sources, e.g. the nuclei of AGN.
It is possible to verify that the frequency at which the radiation reaches its maximum, ν_{max}, is associated to the angular dimension Θ and the strength of the magnetic field of the radio source. The relation is (Kellermann & Pauliny-Toth, 1981):

$$\nu_{max} = \Theta^{-4/5} S_{max}^{2/5} B^{1/5} (1+z)^{(1/5)} \tag{1.13}$$

where θ is the angular dimension in [mas], S is the flux density expressed in [Jy], B is the magnetic field expressed in [G] and z is the redshift. In general at higher frequency, the synchrotron components are more compact.

1.3.1 The synchrotron radio spectrum of an AGN

Before continuing with the characteristics of the synchrotron radiation, I will briefly describe the typical radio spectra of the extragalactic radio sources. The dimensions of the radio sources vary from few pc to Mpc with QSOs that have small dimensions ($\sim$ 30 kpc) and the radio galaxies that have large dimensions ($\sim$ hundreds of kpc). Although the differences in the linear dimensions, radio sources are all described with a standard structure. They are indeed characterized by:

- the radio lobs;
- the hot spots;
- the jets;
- the nucleus;

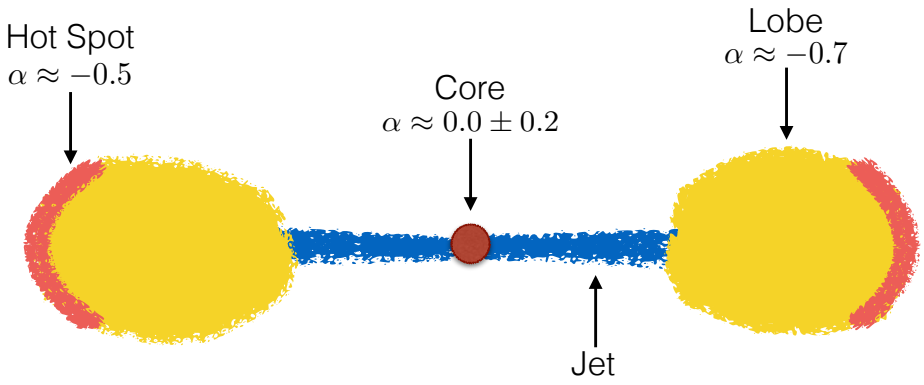

Figure 1.20: Sketch of the main features of a radio galaxy and their main spectral index values.

A prototype of radio galaxy with all these features is Cygnus A (Fig. 1.11). Depending on the dominant synchrotron component or on the orientation of the AGN, the above features show a different radio spectra (see Fig. 1.20).

The radio lobs are extended structures, with ellipsoidal shape, that are symmetric with respect the central object. Their radio spectra is characterized by a power law with typical values of $\alpha \approx -0.7 \div -1.0$.

The hot spots are small regions (few kpc of diameter) at the end of the radio lobes. They trace the shock front of the termination of the jet with the intergalactic medium. They are brighter than the radio lobes and they can contribute to few % of the total luminosity of the radio source. The spectral index is in general flatter than the radio lobes, with $\alpha \approx -0.5$, suggesting the presence of younger electrons.

The jets are the channels, the beam, within which the energy, the magnetic field, the relativistic particles and the thermal plasma are piped from the nucleus towards the external lobs. The jets are visible because of radiative energy losses along their path. However, their long travel time imply that there are also some particle acceleration processes. Therefore, the jets may be experience internal shocks that accelerate the charged particles by magnetically squeezing them, reflecting them back and forth inside the shock. Thus, depending on the involved process, jets can present flattish and steep, like the radio lobes, radio spectra.

The nucleus, or core, is the central and compact ($<$ 1 - 100 pc) object of a radio source. Its contribution to the total emission is, in most of the cases, small with percentages of 0.1% to few %, unless the object is classified as compact radio source or it is oriented towards the observer. The radio spectrum is characterized by a flat or convex shape with a typical spectral index of $\alpha \approx 0.0 \pm 0.2$. The nucleus is the feature of the AGN which most likely is characterized by SSA, therefore it

is opaque to its own radiation.

The ratio between the luminosity of the different components can vary among sources, but this could be an indicator on the type of the source. Indeed, in extreme cases where the core luminosity dominates the other features, the objects are called "core dominated" while radio sources for which the core luminosity is weak, are called "lobe dominated".

1.3.2 The polarization of the synchrotron radiation

An important characteristic of the synchrotron radiation is its polarization and it is a fundamental aspect for the aim of this Thesis. The Stokes parameters (I, Q, U and V), are the values, defined by George Gabriel Stokes in the 1852, that describe the polarization state of electromagnetic radiation and are the observable quantities needed to obtain information on the polarization. The relationship of the Stokes parameters I, Q, U and V to intensity and polarization ellipse parameters is shown in the equations below and in figure 1.21.

$$S_0 = I = S \tag{1.14}$$
$$S_1 = Q = I_p \cos 2\psi \cos 2\chi \tag{1.15}$$
$$S_2 = U = I_p \sin 2\psi \cos 2\chi \tag{1.16}$$
$$S_3 = V = I_p \sin 2\chi \tag{1.17}$$

Here I_p, 2ψ and 2χ are the spherical coordinates in the "Poincaré sphere" of the three-dimensional vector of cartesian coordinates (S_1, S_2, S_3) that define the Stokes parameters (Fig. 1.21); S is the total intensity. The factor of two before ψ represents the fact that any polarization ellipse is indistinguishable from one rotated by 180°, while the factor of two before χ indicates that an ellipse is indistinguishable from one with the semi-axis lengths swapped by a 90° rotation.

In astrophysical cases the AGN Stokes parameter V has a very small value, typically V $< 1\%$ therefore negligible. The Stokes parameters I, Q and U are instead used to determine the following linear polarized quantity. The linear polarized flux density (S_{Pol}) is defined as:

$$S_{Pol} = \sqrt{Q^2 + U^2}, \tag{1.18}$$

The fractional linear polarization is the ratio between the linear polarized flux density (S_{pol}) with the total flux density, expressed with the Stokes parameter I:

$$p = \frac{S_{pol}}{I}. \tag{1.19}$$

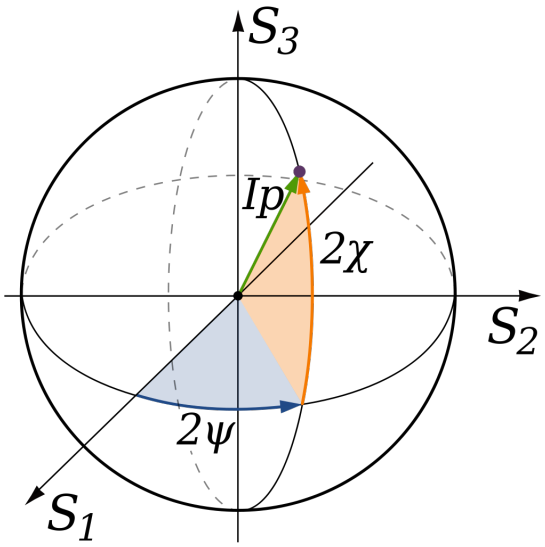

Figure 1.21: Sketch of the Poincaré sphere (credit: Wikipedia, Wikimedia Commons).

The observed Electric Vector Polarization Angle (EVPA) can also be expressed using the observable Stokes parameters Q and U:

$$\chi = \frac{1}{2} \cdot \arctan \frac{U}{Q}. \tag{1.20}$$

From these quantities, it is possible to study two important aspects of the linear polarization and essential for this project: the Faraday rotation and the Faraday depolarization. They can probe the interstellar medium (ISM) and the strength of the magnetic field of the host galaxy. To perform this kind of study, observations in a wide wavelength range are necessary.

The Faraday rotation is the rotation of an electromagnetic wave that occurs when it passes through a magnetised plasma (Fig. 1.22).

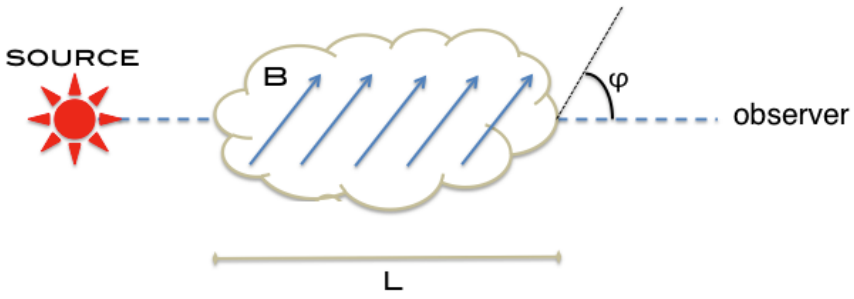

Figure 1.22: Sketch of the Faraday rotation.

When the radiation travels through the magnetized cloud, it could be described as the decomposition of two circular polarized waves: the Right Circular Polarized wave (RCP) and the Left Circular Polarized wave (LCP). These two waves have different velocities within the plasma thus, after a path dl they are summed up and the initial polarization vector changed:

$$\chi(\lambda) = RM\lambda^2 + \chi(0) \qquad [\text{rad}]. \tag{1.21}$$

with RM being the Rotation Measure that, in the simplest case of a homogeneous medium, it is described as:

$$RM = \frac{e^3}{2\pi m_e^2 c^4} \int_d^0 n_e B_{\parallel} dl, \tag{1.22}$$

where n_e is the electron density of the medium (expressed in cm^{-3}), $\text{B}_{\parallel}$ is the component of the magnetic field along the line of sight (expressed in μG), and l is the geometrical depth of the medium along the line of sight (expressed in parsecs). The integral is performed along the line of sight from the source (at distance d) to the observer. Note that the three parameters (n_e,$\text{B}_{\parallel}$ and dl) on which the RM depends, are not determined separately, instead the RM information is an integrated measure of these parameters. However, the determination of RM (from eq. 1.21) suffers from nπ ambiguity. Indeed, from the polarized vector, it is possible to know only its direction and not its orientation; here comes the necessity to apply a number of wraps on the polarized angle in order to obtain a reasonable linear fit of the data (Fig. 1.23).

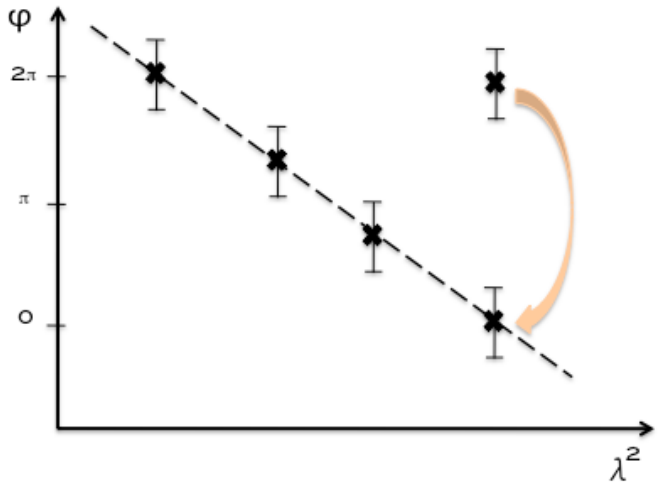

Figure 1.23: Interpolation of the polarization angle; there is one measurement that contains an ambiguity of 2π

If the medium is inhomogeneous or unresolved, the RM can change within the source, and a deviation, more or less strong, from the λ^2 law occurs (Burn, 1966; Vallee, 1980; Saikia & Salter, 1988). This can indicate the presence of multiple RM components, marking the complexity of the source.

In addition to the Faraday rotation, a magnetized plasma might cause a change of the polarization degree of the radiation. When the Faraday rotation causes the reduction of the fractional polarization, the source is subjected to depolarization, a process that describes the changes of the fractional polarization (p) with the observed wavelength. The depolarization can be internal or external; the first occurs when the Faraday rotating component is intermixed to the radio emitting region, and the second when several Faraday screens are somewhere between the radio source and the observer. Several depolarization and repolarization (where the fractional polarization increases at longer wavelengths) models have been developed (Burn, 1966; Tribble, 1991; Homan et al., 2002; Rossetti et al., 2009; Mantovani et al., 2009; Hovatta et al., 2012). We refer to the next section for a description of the models available to explain the depolarization behavior.

The analysis of these two features, the Faraday rotation and the depolarization, can give information about the density distribution of the ISM that surrounds the radio source, its clumpiness, and the strength of the magnetic field.

1.3.3 Depolarization models

In this section we will report a brief description on the models that have been suggested to describe the depolarization behavior. One of the most important work that is still taken as reference is the work done by Burn (1966). From this some other suggestions, improvements and considerations have been proposed to describe this peculiar physical aspect. Here the main models that we decided to follow during the polarization analysis of this Thesis are presented and qualitatively explained. We refer to the individual works for the mathematical details of the models.

All the derivations below start from the following general form of the polarization signal that can be expressed with its complex equation:

$$p = p_0 e^{2i(\chi_0 + \phi\lambda^2)}, \tag{1.23}$$

with

$$\phi = K \int_0^r n_e \vec{B} dl, \tag{1.24}$$

where p_0 and χ_0 are the intrinsic degree of polarization and the intrinsic polarization angle respectively and ϕ is the Faraday depth, that in the simplest

case of Faraday thin objects with a uniform medium and a constant magnetic field it is none other than the RM. The ratio between p/p_0 is the depolarization of the signal. Therefore, in the simplest case where depolarization effects are related only to different Faraday rotations, the degree of polarization generally decreases with wavelength following eq. 1.23. However, depolarization can also occur due to mixing of emitting and rotating media, as well as from the finite spacial resolution of the observed beam (called "beam depolarization"). Three are the main depolarization mechanism (see for more details: Burn, 1966; Tribble, 1991; Sokoloff et al., 1998):

- Differential Faraday rotation (DFR): this occurs when the emitting and the rotating region are intermixed and in a purely regular magnetic field. The polarization signal (or better its plane) passes through this magnetized plasma and it undergoes a different amount of Faraday rotation from the far-side towards the near-side of the slab with respect to the observer. Therefore, following Burn (1966):

$$p = p_0 \frac{\sin \phi\lambda^2}{\phi\lambda^2} e^{2i(\chi_0 + \frac{1}{2}\phi\lambda^2)}, \tag{1.25}$$

  where ϕ is the Faraday depth (or intrinsic Faraday rotation measure) through the region.

- Internal Faraday dispersion (IFD): this occurs when the emitting and rotating regions are intermixed and contain a turbulent magnetic field. In this case the polarized signal suffers from depolarization because of a random walk through the region. It can be described by the formula (Sokoloff et al., 1998):

$$p = p_0 \frac{1 - e^{(-S)}}{S}, \tag{1.26}$$

  where S=$2\lambda^4\sigma_{RM}^2$ -$2i\lambda^2\phi$. Here, σ_{RM} is the internal Faraday dispersion of the random magnetic field within the volume traced by the telescope beam. The RM dispersion σ_{RM} is defined as:

$$\sigma_{RM} = 0.81 < n_e > B_r (Ld)^{1/2} \tag{1.27}$$

  Where $< n_e >$ is the average thermal electron density along the line of sight [cm^{-3}], B_r is the strength of the component of the random magnetic field along the line of sight [μG], L is the total path-length through the ionized gas [pc] and d is the diameter of a turbulent cell [pc] (Fletcher et al., 2011).

- External Faraday dispersion (EFD)/beam depolarization: this occurs when the Faraday screen is just rotating and not-emitting. Therefore, the

magneto-ionic region devoid of relativistic electrons is located between the source of the synchrotron emission and the observer. For a region that is not emitting synchrotron radiation, the only way to cause depolarization is through a turbulent magnetic field and/or systematically varying magnetic field within the beam. Profound treatment on the depolarization in an external screen are found in Burn (1966); Tribble (1991). This effect is described by the equation:

$$p = p_0 e^{-2\sigma_{RM}^2 \lambda^4} e^{2i(\chi_0 + RM\lambda^2)}, \tag{1.28}$$

where σ_{RM} is the dispersion about the mean RM across the source on the sky. There is also a variation of this equation that represent the "partial coverage" of a source. This behavior has been described with the formula (Rossetti et al., 2008):

$$p = p_0 \left[f_c e^{-2\sigma_{RM}^2 \lambda^4} + (1 - f_c) \right], \tag{1.29}$$

if a source is only partially covered by the screen, a fraction (1-f$_c$) of the source radiation is non-depolarized and it maintains a constant level of fractional polarization at long wavelengths.

However, usually the sources behave more complex than these simple models describe. Indeed, there are also cases in which a "repolarization", i.e. an increase in fractional polarization with decreasing frequency, has been detected (Homan et al., 2002; Montenegro-Montes et al., 2008; Mantovani et al., 2009). Such repolarization can be explained as increased ordering of the magnetic field in the component of the source nearest to the observer's line of sight. Moreover, it could happen that the change of the degree of polarization is due to multiple interfering RM components internal and/or external or a combination of the two. To complicate more, the different Faraday rotating screens can be located one next to the other within the beam or one in front of the other. In the former case, multiple components models are simply constructed as p=p$_1$+p$_2$+...+p$_n$ (O'Sullivan et al., 2012), while in the latter case one has to account for the effect of wavelength-dependent depolarization of the regions in front (see 3.3.1). For the analysis of this Thesis we decided to follow the approach done by O'Sullivan et al. (2012) therefore, adding several Faraday rotating screens and considering them located one next to the other on the plane of the sky (see 3.3).

1.4 The environment of an AGN

The idea that the AGN with its radio jets can interact with the surrounding environment is not new. The evolution of the galaxies is strongly correlated

with the evolution of the central black holes (Kormendy & Richstone, 1995; Magorrian et al., 1998; Ferrarese & Merritt, 2000). An interplay of the SMBH and the ambient medium, called feedback mechanism, can regulate the growth of the host galaxy (Bower et al., 2006) and vice versa; the environment can influence the growth and evolution of the radio emission. The study of this connection has implications on the importance of the AGN feedback and to discern the structure of the AGN. Indeed, it is possible to investigate whether the ambient medium is already organized in settled structures, such as circumnuclear disk/torus or whether it is still in a clumpy newly burn phase. Physical conditions of the medium can be obtained from studies of emission line, X-ray emission, IR radiation and Faraday rotation and depolarization of the synchrotron radiation. The latter is the approach followed in this Thesis.

The influence among the radio source and the host can take place in different ways. Depending on the contents, distribution and the density of the gas in the host galaxy, the radio source can die rapidly, expand, or remain confined inside its host. An important class of objects that show the latter characteristic are the young AGN called the High Frequency Peakers (HFP), the GHz Peaked Spectrum (GPS) and the Compact Steep Spectrum (CSS) sources. These objects belong to the same "family", but they are believed to be just in a different evolutionary stage (Fanti et al., 1995; Snellen et al., 2000), being the HFP the younger and the CSS the more evolved. Their radio spectra is characterized by a convex shape with the turnover peak located at different frequencies: HFP around 10 GHz, GPS around 2 GHz, and the CSS around several hundreds of MHz (Fanti et al., 1990, 1995; O'Dea, 1998; Dallacasa et al., 2000; Dallacasa, 2003).

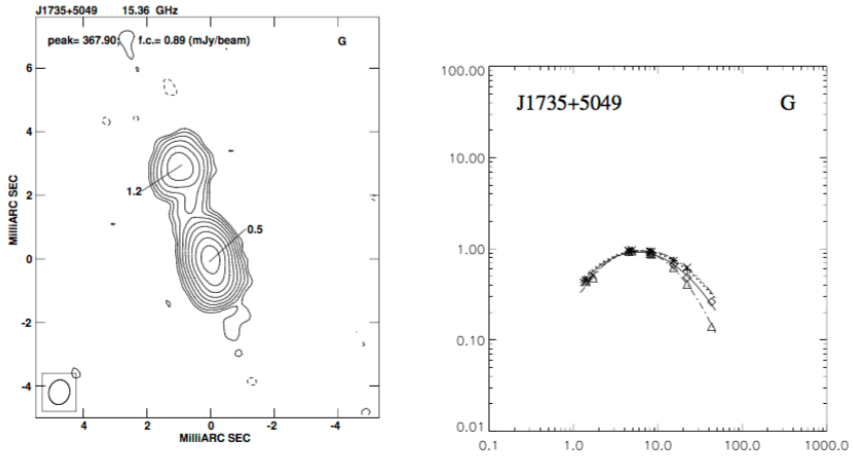

Figure 1.24: Morphology and radio spectrum of a HFP (Dallacasa et al., 2000).

An anti-correlation between the projected linear size and the peak frequency, as a result of the synchrotron self absorption (SSA) mechanism, exists (O'Dea &

Baum, 1997): the higher the peak frequency, the smaller the source. Therefore, these objects are compact radio sources with the HFP radio emission coming from regions of few tens of pc (Dallacasa et al., 2000; Dallacasa, 2003; Orienti, 2009), the GPS emission contained within the narrow line region (< 1 kpc) and the CSS emission contained within the host galaxy (< 15 kpc). Most likely they are candidates to be the progenitors of the large scale FR sources (for CSS and GPS review see O'Dea, 1998). Therefore, in such a scenario these compact objects strongly interact during their evolution with the ambient medium as they propagate through it, from central regions to kpc scales. The discovery of the emission line gas aligned and, probably, co-spatial with CSS, indicates that they strongly interact with the ambient medium through shocks interactions (de Vries et al., 1997, 1999; Axon et al., 2000). The GPS have an expansion velocity higher than the large scale classical double radio sources (Alexander & Leahy, 1987) therefore, considering the evolving scenario, GPS are expected to decelerate when they interact with the ambient medium (De Young, 1993; Carvalho, 1998).

The study of the absorption of the atomic hydrogen, a tracer of a dense medium produced most likely as a result of a merger (Morganti et al., 2004), is also an indicator of interaction of the radio source with the surrounding environment. Studies of HI outflows (Fig. 1.25), but also molecular and ionized gas outflows, in young or restarted radio sources provide an indication of jet-ISM (interstellar medium) interaction and they underline the role of the radio jets in feedback mechanism (Morganti et al., 2013; Mahony et al., 2013).

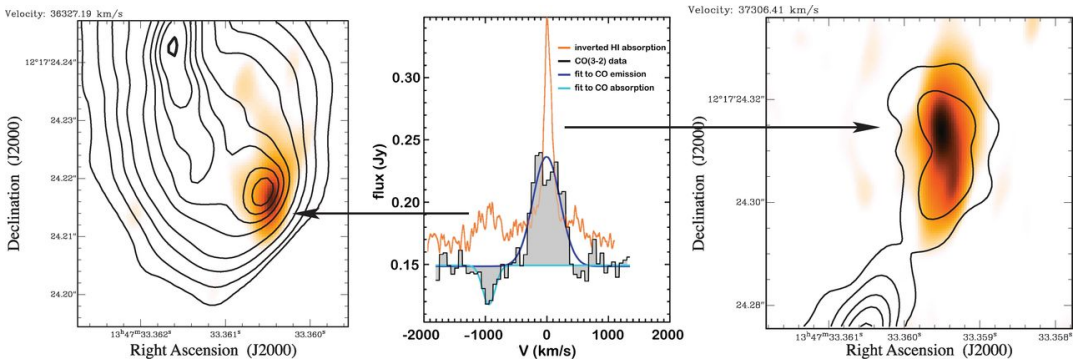

Figure 1.25: The distribution of the HI in two velocity channels showing the location of the two clouds of HI detected in absorption (orange-white) superimposed on the continuum of 4C12.50 (contours) (Morganti et al., 2004).

An empirical anti-correlation between the linear size and the column density N_{HI} have been shown for young radio sources (Pihlström et al., 2003; Gupta et al., 2006), the smaller the sources the larger the column density is. This can be explained with a torus/disk scenario. However, it seems that the HFPs deviate from this trend, highlighting the complexity of the environment for these very

young objects (Orienti et al., 2006).

Jet bending is also an indication of interaction of the radio source with the environment. Generally, this bending is the result of ram pressure from the motion of the source through a dense medium that could also be the intergalactic medium (IGM) (see Fig. 1.26 as example). This is supported by the fact that these features are mostly seen in massive and sometimes, surprisingly, also in low mass systems of clusters (Giovannini et al., 1989; Nielsen & Wilcots, 2015). Studying bent jets, also called narrow-angle tail radio source, in galaxy clusters help to estimate the density of the IGM and sometimes it can reveal that the presence of the IGM could be so strong to significantly remove the ISM of the galaxy (McBride & McCourt, 2014).

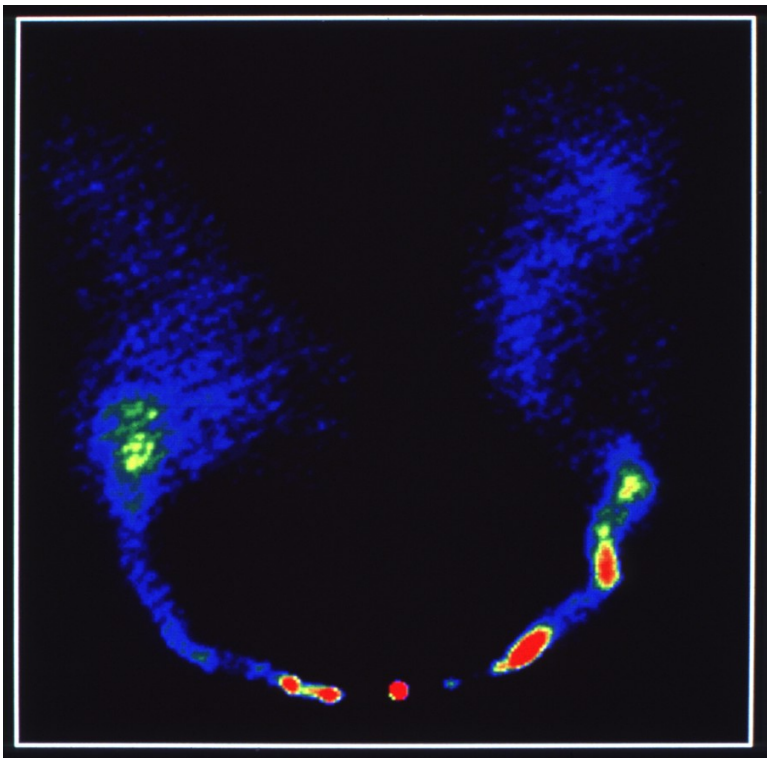

Figure 1.26: Multifrequency VLA observations of the prototypical narrow-angle tail radio source NGC 1265 (O'Dea & Owen, 1986). HeadÐtail sources are usually interpreted as an AGN-driven jet bent back by ram pressure as it moves through the ICM.

Clear evidence of a high resolved bent jet due to interaction with the ambient medium is 3C120, a close AGN (z=0.033, Burbidge, 1967) for which interferometric VLBA observations (total and linear polarization flux density) reveal a region in the relativistic jet where superluminal components flash on and off over time scale of months while the polarization angle rotates. This can be ex-

plained by interactions between the jet and the interstellar cloud located in the very vicinity of the central region of the galaxy (≈8 pc). This cloud represent a link layer between the ultra-dense BLR clouds and the lower density NLR clouds (Gómez et al., 2000, 2008).

In some cases radio jets are not perpendicular to the equatorial plane of the host galaxy. Examples are reported from water maser disk observations (Kondratko et al., 2005; Greene et al., 2013) and from radio observations (Reynolds et al., 2009, 2013). Indeed, significant misalignment of ≈ 30° between the normal to the plane of the dusty torus and the axis of the (sub)parsec scale jet is estimated to occur in 20%-30% of AGN (Fig. 1.27, Reynolds et al., 2013). Therefore, a misaligned torus in some AGN should not be unexpected. This implies the radio jets to differently interact with clumps within the host and also, depending on the inclination of the jet, to interact with the dusty torus.

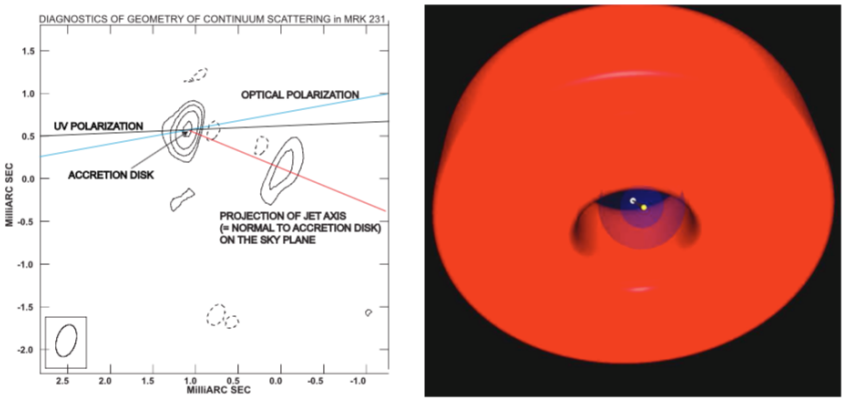

Figure 1.27: Left: observations of Mrk 231 at 43 GHz obtained with VLBA from Reynolds et al. (2009). The optical and UV continuum polarization directions from Smith et al. (1995) are superimposed on the radio image. The right frame depicts a three-dimensional physical representation of the two-dimensional data projected on the sky plane that is presented in the left frame (Reynolds et al., 2013).

Recently, there were studies proposing that the slightly larger regions around the central engine of AGN are not structured in the canonical way with well defined BLR, torus and NLR. Instead, a funnel-shaped thin shell outflow creates all of these features (Elvis, 2000). Therefore, these objects are a mixture of gas and dust that could cause the production of particular observational features.

1.5 The High-RM project

The AGN unification scheme, where their appearance strongly depends on their orientation (Orr & Browne, 1982; Urry & Padovani, 1995), is by now accepted by most of the scientific community, but there are still several open questions, e.g. how the medium of the hosting galaxy in the vicinity of the SMBH is characterized and how strong the magnetic field is. These are important elements needed to understand the jet ejection mechanism which is not yet well understood. It is also important to understand whether AGN are characterized, in the radio band, by some periodic activity phase (Marecki et al., 2006; Saikia & Jamrozy, 2009; Czerny et al., 2009) or some evolutionary stage, from HFP (Dallacasa et al., 2000) to CSS (Saikia, 1988; Fanti et al., 1990) passing through the state of GPS (Gopal-Krishna et al., 1983; Stanghellini et al., 1990; O'Dea et al., 1991). However, whether AGN are really experiencing the above evolution from young quasars to large-scale radio sources (O'Dea, 1998) remains in doubt.

The study and analysis of the polarization information in the radio band, i.e. the Faraday rotation and the depolarization, are powerful tools that can help to clarify some of the above questions. The importance of connecting the polarization properties, such as a very high RM value and the strong changes of the fractional polarization, with the ambient medium, has been evident for years (Burn, 1966; Laing, 1984; Tribble, 1991; Rossetti et al., 2008). Some observational works revealed sources with very high RM with single-dish and interferometric techniques (Kato et al., 1987; Benn et al., 2005; Trippe et al., 2012; Kravchenko et al., 2015) and also with studies with the higher resolution VLBI technique (Zavala & Taylor, 2004; Attridge et al., 2005; Jorstad et al., 2007). However, a deep study of a relationship between the RM and the ambient medium is very difficult since it would require the study of a large sample in a wide range of frequencies and with simultaneous observations.

With this project we want to study whether any connection is present between the AGN-hosting galaxy medium with some evolutionary track and/or some periodic activity phase of the AGN itself. To reach this goal we have made use of polarimetric measurements of a sample of bright point-like AGN that show an essential characteristic: they are unpolarized at 1.4 GHz in the NRAO VLA Sky Survey (NVSS) (Condon et al., 1998). These sources may suffer from strong in-band depolarization, i.e. a large rotation of the polarization angle at this frequency that lead to a final vector pair cancellation of the angles along the path towards the observer and the subsequent depolarization of the signal. This feature is very important since we want to search for high-RM sources and study their ambient medium. Indeed, from what previously said, when a source is strongly depolarized, the polarization degree decreases towards longer wavelengths. Therefore, the unpolarized AGN at 1.4 GHz could be polarized at higher

frequencies. This could be a sign of very dense medium and/or strong magnetic field that result in a strong Faraday rotation (with subsequent high RM value) and strong depolarization. We started with a single dish observational campaign using the 100-m Effelsberg telescope at 10.45 GHz in order to select the possible high-RM candidates. These were studied in more details (again with the 100-m Effelsberg telescope) at different frequencies from 2.6 GHz to 15 GHz. The Effelsberg results, data analysis and discussion are presented in Chapter 2. We then analyzed the sources showing high RM values (with $|RM|$>500 rad/m^2) using the Karl G. Jansky Very Large Array (JVLA) interferometric data at L, C and X bands. Thanks to its wide band spectropolarimeters we could follow the dramatic changes of both the fractional polarization and the polarization angle of the targets. For some of them we could also performed good depolarization modeling. The JVLA results, data analysis and discussion are presented in Chapter 3. A summary and a description of the future works are presented in Chapter 4.

◦

Chapter 2

Effelsberg campaign

2.1 Introduction

In this chapter we present a homogeneous observational study performed with the 100-m Effelsberg telescope of a medium-sized sample of radio sources. The aim is to select the suitable candidate sources to have high-RM, therefore to start a profound analysis, at first using single dish data and then using interferometric data, investigating whether any connection is present between the AGN-hosting galaxy medium and the activity phase of its AGN itself.

We selected sources showing a lack of polarized flux density assuming that this is caused by in-band Faraday depolarization due to high-RM. As mentioned in the previous chapter (1.3.3), in the simplest case, Faraday rotation can produce a reduction of the fractional polarization with a wavelength dependance (the external depolarization/beam depolarization is not an effect wavelength dependence because it is produced by dis-homogeneities of the magnetic field within the observed beam). Therefore, the depolarization effect is less strong at shorter wavelength, because the polarized signal is passing through a thinner layer of the dense magnetized medium. This is a very important aspect for this project; it is indeed the starting point of our large single dish observational campaign. This initial large sample was then observed in a follow-up program at several frequencies in the 2-15 GHz range. We could model and analyze the radio total intensity spectra, we could measure the RM value of each of the sources and, for some of them, we could apply some simple models of depolarization.

A complete description on the sample selection criteria and our possible selection biases are presented in 2.2 and 2.3. The observations are reported in section 2.4 and a description of the comparison sample is reported on section 2.5. The results and discussion of the Effelsberg observational campaign are reported on section 2.6. Finally a summary and conclusion is given in section 2.7.

2.2 Sample selection criteria

Our sample was created by selecting sources from the NRAO VLA Sky Survey (NVSS) (Condon et al., 1998), a survey at 1.4 GHz, which contains a total of

1 773 484 entries. From these, we considered only those sources that match the following criteria:

- Flux density $S_{NVSS} \geq 300$ mJy;
- Unresolved with major axis $\theta^{maj}_{NVSS} \leq 45''$;
- Declination $\delta \geq -10°$;
- Polarization flux density $S^{pol}_{NVSS} \leq 0.87$ mJy, i.e. unpolarized sources.

The minimum flux density of 300 mJy at 1.4 GHz was chosen in order to be able to detect enough total flux density at higher frequencies (roughly S=70 mJy at 10.45 GHz) to perform polarization studies, assuming that the majority of the AGN could be characterized by a steep radio spectrum with α= –0.7. The last point is essential because we are interested in studying sources suffering from a strong depolarization at 1.4 GHz, which is a hint of a possible high RM. The value 0.87 mJy represents the $3\sigma^{pol}_{1.4}$ (where the rms fluctuation level $\sigma^{pol}_{1.4}$ = 0.29 mJy/beam, for the NVSS survey) (Condon et al., 1998). The result of this selection is a list of 2890 point-like sources with no detected polarization flux density (thus ∼20% of the brightest sources in the NVSS do not have polarization detection).

As a second step, we cross-correlated the obtained sample with the Faint Images of the Radio Sky at Twenty-cm (FIRST) catalogue (White et al., 1997). With a better angular resolution, only unresolved sources were selected, i.e. with a angular size $\leq 5''$. The objective of this was to increase the probability of selecting possibly compact and/or high-redshift candidates. The result of the cross correlation is a list of 537 bright, point-like, and unpolarized sources.

Given the strong dependence of the Faraday depolarization effect with the observing frequency (the lower the frequency, the stronger the depolarization becomes), we observed the entire cross-correlated list with the 100-m Effelsberg telescope at 10.45 GHz (see 2.4.1), in order to search for polarized flux density, thus suggesting a strong depolarization at 1.4 GHz. The final sample of high RM candidates is composed of 30 sources ($\sim$ 6% of the initial cross correlated sample). We checked that the targets are isolated sources by extracting images from the FIRST catalogue using an image size of $5'$, which corresponds to the size of the Effelsberg beam at 11cm (2.64 GHz). The final sample was then observed at several frequencies (see 2.4.2) in order to determine their SEDs and their RM (see 2.6.2 and 2.6.4 respectively).

2.3 Possible selection biases

The selection criteria we followed could result in two possible biases present in our sample. The first is the lack of sensitivity of our observations for sources weaker than 150 mJy at 10.45 GHz. This could exclude a fraction of steep spectrum sources for which the polarized flux density drops below the minimum 3 mJy limit detectable in our observations. In fact, starting from the original list (537 unpolarized sources at 1.4 GHz), 30 sources show significant polarization at 10.45 GHz, but the remaining 507 do not. Setting a 3 mJy upper limit (3σ, assuming the Effelsberg rms=1 mJy/beam) on their polarized flux density and assuming that a typical detectable fractional polarization is larger than 2% (Condon et al., 1998), we can only assert that the unpolarized sources are 77 targets with no polarization detection at 10.45 GHz and $S_{10.45} \gtrsim$ 150 mJy. Thus for the remaining 430 targets, we cannot discern whether they are polarized or not, so we cannot include them into our study.

In contrast, our flux density selection criterium ($S_{1.4GHz} \geq$ 300 mJy) should exclude potential sources with synchrotron spectra peaking at higher frequencies from our analysis, thus potential GPS-HFP targets. These sources, peaking in the range between 2 and 10 GHz, are optically thick at 1.4 GHz. Then, at this frequency their emission increases with a spectral index of 2.5. Therefore, while they can be very bright at high frequencies, we are excluding them from our analysis because of their weakness at 1.4 GHz.

2.4 Observations

In the following, we describe the observational campaign carried out for this work with the 100-m Effelsberg single-dish telescope.

2.4.1 10.45 GHz observations

To identify high-RM candidates, we initially selected unpolarized sources at 1.4 GHz in the NVSS catalogue, assuming that the non-polarization in some cases is caused by in-band depolarization due to a very high RM. Therefore the strategy we adopted was to observe at higher frequencies searching for polarized flux density. Using the 100-m Effelsberg telescope, observations at 10.45 GHz on the initial sample of 537 targets were performed during the winter semester 2012-13. The 10.45 GHz receiver has a bandwidth of 300 MHz, a system temperature (Tsys) of ∼50 K on the sky (zenith) and a FWHM of 69″. The system delivers right and left circular polarization (RCP and LCP) and is connected to an IF-polarimetry that provides full polarization information, thus giving the Stokes parameters: I, Q, U and theoretically also V. Since the Stokes V is expected to

be weak in extragalactic sources (Legg & Westfold, 1968; Saikia & Salter, 1988), it has not been taken into consideration for the purpose of our study. All 537 sources are point-like compared to the Effelsberg beam. Therefore they were observed in cross-scan mode, along azimuth and elevation with a scan length of $6'$ and a scanning speed of $\sim 7''$/sec, using a total of twelve subscans (6 scans for each direction). Since the sources are bright enough, focus and pointing were checked by the targets themselves. 3C286, 3C48, and 3C161 have been observed as flux density calibrators, the flux densities of which were based on the scale of Baars et al. (1977) and counter-checked with more recent data coming from the 100-m Effelsberg calibrators monitoring program (Kraus et al., 2003). The polarization information (the fractional polarization p and the polarization angle χ) of the mentioned calibrators were checked using the recent and continuously updated values available in the Effelsberg wiki-page[1]. NGC7027 and 0951+69 have been chosen as unpolarized calibrators to determine the leakage terms, the instrumental polarization, which is of the order of 1%. This first observational session at high frequency led to a list of 30 sources, which became the high RM candidates.

2.4.2 Follow-up program

For the 30 sources with detected polarization at 10.45 GHz, a follow-up program was performed to determine their RM value. These sources have been observed in cross-scan mode at 2.64 GHz (FWHM of $275''$), 4.85 GHz (FWHM of $146''$), 8.35 GHz (FWHM of $80.6''$), 10.45 GHz (FWHM of $69''$), and 14.60 GHz (FWHM of $51''$) (see the Effelsberg wiki-page[2] for more details on the receivers). The scan length and the scan velocity were chosen based on the technical parameters of the different receivers. As previously done with the observations at 10.45 GHz, suitable sources, such as 3C286, 3C48, and 3C161, were observed to calibrate flux density and also to check for the polarization information (m and χ). Again NGC7027 and 0951+69 were observed for determining the instrumental polarization. The total intensity and the polarization information for all the 30 targets were collected and are presented in Sec. 2.6. The sample was observed quasi-simultaneously with time between observations from a few hours to a few days (in few cases in order to repeat some bad observations). Tables *A*.1 in the Effelsberg appendix contain the values of total intensity and the polarization information of the high-RM candidates collected during this follow-up campaign.

[1]https://eff100mwiki.mpifr-bonn.mpg.de/doku.php "Calibrators and their polarization" section in the Effelsberg User Guide

[2]https://eff100mwiki.mpifr-bonn.mpg.de/doku.php; the section "Receiver and calibration" in the Effelsberg User Guide

2.4.3 Time variability

Flux density and polarization variability over the entire electromagnetic spectrum is a common phenomenon in AGN (Peterson, 2001) and could therefore also influence our observations. However, strong variations are usually seen only at frequencies > 10 GHz and mainly in blazar sources (radio-loud AGN seen at small angles to the axis of the jet) with variations of several factors in the total flux density (e.g. by a factor of ∼4 for the sources BL Lac and 3C 273 at 15.0 GHz within 20 years) (Lister et al., 2009).

During the follow-up observations, the high RM candidates were observed nearly simultaneously at the various frequencies; the time between the individual scans was in most cases only a few minutes (except for a few cases where bad observations had to be repeated). From the obtained SEDs (presented in 2.6.2) of our targets, we can assert that the high RM sample is mainly composed of radio loud quasars, and we can most likely exclude contamination from blazar type sources. Besides this, most of our observations were performed at frequencies ≤10 GHz, so that strong variations are rather unlikely. Furthermore, our repeated observations at 10.45 GHz (for the follow-up campaign; 2.4.2) did not reveal any strong variations - at most, small oscillations (of a few %) have been seen on a time scale of a few months.

A considerable time window for this project is given by the NVSS and low-frequency surveys, which, as said, should not give any variability problems. Since our sources do not seem to be strongly variable at the higher observed frequency (10.45 GHz), we can expect that the combination of the new Effelsberg data and the data taken from literature is not strongly affected by a time variability that is significant for the purposes of this work. Therefore, we can safely assume that neither our RM determination nor the SEDs are significantly influenced by source variability.

2.4.4 Data reduction

Data was reduced using the TOOLBOX package for single-dish data (see the Effelsberg wiki-page[3]). For coherency, the same data reduction procedure has been followed for all frequencies, such as the correction for the opacity, determined by a fit between the Tsys versus airmass distribution and the pointing offsets, where the offsets in longitude are applied to the latitude data and vice versa. Moreover, a baseline subtraction, an averaging of all the subscans, and a few other standard adjustments were applied. Flux calibration was done using the [Jy/K] factor calculated from the flux calibrators opportunely observed during

[3]https://eff100mwiki.mpifr-bonn.mpg.de/doku.php section "Using the Toolbox to inspect cross-scans" in the Effelsberg User Guide

the different observational sessions. The leakage terms were adequately obtained through observations of unpolarized point like calibrators. The errors were calculated through error propagation taking uncertainties from the Gaussian fit to the cross-scanned data, pointing correction and various calibration uncertainties into account, e.g. changes in the noise diode or changes in the focus.

2.5 Comparison samples

We compared our results with two comparison samples. We used the 77 bona fide unpolarized sources at 10.45 GHz, listed in Table 2.1, to compare their spectral indices with those of our high-RM candidates. We also compared our RM results with the sample of Farnes et al. (2014). They present a catalogue of multi-wavelength linear polarization and total intensity radio data for polarized sources from the NVSS. The result of this work is a catalogue of 951 sources with the SEDs in both total intensity and fractional polarization.

2.6 Results and discussion

In Table 2.2 we present information about the 30 high-RM candidates: the source coordinates taken from the FIRST catalogue (they are more precise, compared to the NVSS survey, thanks to the better angular resolution of the survey), their total flux density at 1.4 GHz from the NVSS catalogue, their total flux density measured with the Effelsberg telescope at 10.45 GHz (both expressed in mJy), the spectral index between 1.4 GHz and 10.45 GHz ($\alpha_{1.4-10.45}$), the observed RM value (RM_{obs}), the redshifts (when available from the literature), the contribution of the RM of our Galaxy (RM_{mw}), the values of which have been taken from the most recent work by Oppermann et al. (2015), and finally the rest-frame RM corrected by their redshifts ($\mathrm{RM}_{rf}=\mathrm{RM}_{obs}(1+\mathrm{z})^2$). Where the redshift was not available in the literature, we assumed a mean value: $\mathrm{z}_{mean} = 1.5$ in order to have a rough idea of the intrinsic RM value. For the source 0845+0439, we received a redshift value from spectroscopic measurement tests at the Large Binocular Telescope (LBT, Dr. J. Heidt private communication). Almost all the targets are QSO type.

In the following, we discuss the spectral index distribution, their SEDs, and their polarization information with a detailed explanation of the RM determination and the depolarization behavior.

Table 2.1: Table of the 77 bona fide unpolarized sources at 10.45 GHz.

Name	RA [J2000]	DEC [J2000]	$S_{1.4}$ [mJy]	$S_{10.45}$ [mJy]	$P_{10.45}$ [mJy]	$\alpha_{1.4}^{10.45}$
1327+4326	13:27:20.964	43:26:27.90	660 ± 20	340 ± 30	< 30	-0.32 ± 0.10
1333+1649	13:33:35.771	16:49:04.18	390 ± 10	410 ± 10	< 9	0.02 ± 0.04
1339+6328	13:39:23.766	63:28:58.13	480 ± 10	183 ± 3	< 9	-0.47 ± 0.03
1347+1835	13:47:23.484	18:35:37.82	360 ± 10	270 ± 10	< 9	-0.14 ± 0.054
1357+4353	13:57:40.584	43:53:59.73	690 ± 10	290 ± 10	< 9	-0.43 ± 0.04
1358+4737	13:58:40.667	47:37:58.12	690 ± 20	260 ± 10	< 6	-0.48 ± 0.05
1407+2827	14:07:00.394	28:27:14.78	820 ± 20	920 ± 10	< 9	0.05 ± 0.03
1410+3647	14:10:43.043	36:47:21.83	1230 ± 40	220 ± 10	< 9	-0.85 ± 0.06
1413+1509	14:13:41.645	15:09:39.65	470 ± 10	170 ± 10	< 9	-0.50 ± 0.07
1442+4044	14:42:59.305	40:44:28.79	960 ± 30	153 ± 3	< 9	-0.91 ± 0.04
1450+0910	14:50:31.184	09:10:28.03	330 ± 10	390 ± 10	< 6	0.08 ± 0.04
1451+1343	14:51:31.498	13:43:24.07	690 ± 20	181 ± 3	< 9	-0.66 ± 0.03
1458+3542	14:58:43.413	35:42:57.50	710 ± 20	190 ± 3	< 9	-0.65 ± 0.03
1504+3249	15:04:07.545	32:49:21.16	340 ± 10	190 ± 10	< 9	-0.28 ± 0.06
1507+5857	15:07:47.370	58:57:27.71	540 ± 20	180 ± 10	< 30	-0.54 ± 0.07
1509+4726	15:09:19.830	47:26:56.31	1270 ± 40	180 ± 10	< 9	-0.97 ± 0.07
1511+2208	15:11:05.568	22:08:06.70	410 ± 10	173 ± 3	< 9	-0.42 ± 0.03
1528+3738	15:28:27.922	37:38:09.48	780 ± 20	151 ± 4	< 9	-0.81 ± 0.04
1539+6113	15:39:48.117	61:13:56.36	500 ± 20	211 ± 3	< 9	-0.42 ± 0.04
1545+4751	15:45:08.526	47:51:54.69	690 ± 20	220 ± 10	< 6	-0.56 ± 0.06
1606+3124	16:06:08.526	31:24:46.41	660 ± 20	550 ± 10	< 9	-0.09 ± 0.04
1630+2131	16:30:11.240	21:31:34.38	510 ± 20	240 ± 4	< 30	-0.37 ± 0.04
1640+1144	16:40:58.869	11:44:04.18	330 ± 10	220 ± 10	< 9	-0.20 ± 0.06
1644+1305	16:44:41.199	13:05:19.69	1340 ± 50	163 ± 3	< 9	-1.04 ± 0.04
1644+2536	16:44:59.061	25:36:30.98	730 ± 20	271 ± 3	< 9	-0.49 ± 0.03
1645+1113	16:45:54.692	11:13:52.59	460 ± 10	170 ± 3	< 30	-0.49 ± 0.03
1647+1720	16:47:41.833	17:20:11.76	2130 ± 70	490 ± 10	< 9	-0.73 ± 0.04
1711+3019	17:11:19.937	30:19:17.67	1040 ± 30	240 ± 10	< 9	-0.72 ± 0.05
1735+5049	17:35:48.985	50:49:11.68	430 ± 13	920 ± 10	< 9	0.37 ± 0.03
2126–0119	21:26:32.768	–01:19:32.37	340 ± 10	220 ± 10	< 9	-0.21 ± 0.06
2145+0431	21:45:17.756	04:31:32.05	1430 ± 40	234 ± 4	< 9	-0.90 ± 0.03
2151+0552	21:51:37.876	05:52:12.87	680 ± 20	500 ± 10	< 9	-0.15 ± 0.04
2153+1241	21:53:04.651	12:41:05.19	430 ± 10	210 ± 10	< 30	-0.35 ± 0.06
2322+0812	23:22:36.097	08:12:01.66	1180 ± 40	430 ± 20	< 9	-0.50 ± 0.06
2331+0705	23:31:55.513	07:05:42.08	540 ± 20	181 ± 4	< 9	-0.54 ± 0.04
2333–0903	23:33:47.282	–09:03:04.17	1000 ± 30	170 ± 10	< 9	-0.88 ± 0.07
2341+0018	23:41:06.908	00:18:33.56	430 ± 10	190 ± 10	< 9	-0.40 ± 0.06
2354–0019	23:54:09.171	–00:19:47.89	350 ± 10	291 ± 4	< 9	-0.09 ± 0.03

Table 2.1: Table of the 77 bona fide unpolarized sources at 10.45 GHz. Continued.

Name	RA [J2000]	DEC [J2000]	$S_{1.4}$ [mJy]	$S_{10.45}$ [mJy]	$P_{10.45}$ [mJy]	$\alpha_{1.4}^{10.45}$
0132–0804	01:32:41.129	–08:04:04.83	310 ± 10	181 ± 2	< 6	-0.27 ± 0.04
0134+0003	01:34:12.700	00:03:45.29	920 ± 30	263 ± 1	< 6	-0.62 ± 0.04
0249+0619	02:49:18.010	06:19:51.85	500 ± 20	620 ± 10	< 9	0.11 ± 0.05
0323+0534	03:23:20.254	05:34:11.93	2790 ± 80	330 ± 3	< 6	-1.06 ± 0.03
0706+4647	07:06:48.082	46:47:56.39	1590 ± 50	270 ± 10	< 9	-0.88 ± 0.06
0737+6430	07:37:58.988	64:30:43.25	420 ± 10	350 ± 10	< 9	-0.09 ± 0.04
0805+2106	08:05:38.530	21:06:51.92	930 ± 30	430 ± 30	< 12	-0.38 ± 0.09
0808+2646	08:08:36.756	26:46:36.73	450 ± 10	250 ± 10	< 9	-0.29 ± 0.05
0830+2323	08:30:21.693	23:23:25.72	1100 ± 30	173 ± 3	< 6	-0.92 ± 0.03
0902+4310	09:02:30.934	43:10:14.07	340 ± 10	530 ± 20	< 9	0.22 ± 0.05
0923+3849	09:23:14.443	38:49:39.74	380 ± 10	320 ± 4	< 9	-0.08 ± 0.03
0945+4636	09:45:42.096	46:36:50.60	470 ± 10	290 ± 4	< 9	-0.24 ± 0.02
0952+2828	09:52:06.089	28:28:32.37	1360 ± 40	260 ± 4	< 6	-0.82 ± 0.03
0954+2639	09:54:39.795	26:39:24.56	310 ± 10	170 ± 3	< 30	-0.29 ± 0.04
1006+1713	10:06:31.755	17:13:17.15	570 ± 20	230 ± 10	< 12	-0.45 ± 0.06
1028+3844	10:28:44.304	38:44:36.67	660 ± 20	180 ± 4	< 6	-0.64 ± 0.04
1033+3935	10:33:22.051	39:35:51.12	400 ± 10	280 ± 10	< 9	-0.17 ± 0.04
1035+5628	10:35:07.058	56:28:46.81	1800 ± 50	620 ± 10	< 9	-0.53 ± 0.03
1047+1456	10:47:32.403	14:56:46.57	372 ± 10	590 ± 30	< 30	0.22 ± 0.06
1057+0012	10:57:15.781	00:12:03.74	890 ± 30	190 ± 3	< 6	-0.76 ± 0.04
1058–0309	10:58:10.991	–03:09:26.81	450 ± 10	180 ± 4	< 12	-0.45 ± 0.03
1101+3904	11:01:30.074	39:04:32.78	340 ± 10	200 ± 4	< 6	-0.26 ± 0.04
1110+6028	11:10:13.085	60:28:42.29	430 ± 10	210 ± 10	< 9	-0.35 ± 0.06
1124+1919	11:24:43.869	19:19:29.53	880 ± 30	190 ± 10	< 9	-0.76 ± 0.07
1135+4258	11:35:55.999	42:58:44.64	1450 ± 40	170 ± 2	< 9	-1.06 ± 0.03
1143+1834	11:43:26.063	18:34:38.40	310 ± 10	220 ± 4	< 9	-0.17 ± 0.04
1148+0752	11:48:30.779	07:52:07.54	610 ± 20	200 ± 3	< 6	-0.55 ± 0.04
1148+5924	11:48:50.352	59:24:56.68	480 ± 10	450 ± 10	< 9	-0.03 ± 0.03
1155+4555	11:55:10.998	45:55:39.85	610 ± 20	170 ± 4	< 9	-0.63 ± 0.04
1204+5202	12:04:18.615	52:02:17.83	960 ± 30	152 ± 4	< 6	-0.91 ± 0.04
1208+5413	12:08:27.495	54:13:19.74	440 ± 10	200 ± 10	< 9	-0.39 ± 0.06
1215–0628	12:15:14.412	–06:28:03.96	360 ± 10	200 ± 10	< 30	-0.29 ± 0.06
1220+2916	12:20:06.820	29:16:50.70	390 ± 10	173 ± 4	< 9	-0.40 ± 0.03
1234+4753	12:34:13.330	47:53:51.40	360 ± 10	230 ± 10	< 9	-0.22 ± 0.05
1244+4048	12:44:49.200	40:48:06.35	1340 ± 40	370 ± 10	< 6	-0.64 ± 0.04
1254+0859	12:54:58.953	08:59:47.57	670 ± 20	250 ± 3	< 9	-0.49 ± 0.03
1313+5458	13:13:37.869	54:58:23.89	1310 ± 40	264 ± 4	< 9	-0.79 ± 0.03
1324+4048	13:24:12.067	40:48:11.58	350 ± 10	190 ± 10	< 9	-0.30 ± 0.06
1326+5712	13:26:50.572	57:12:06.85	520 ± 20	193 ± 4	< 9	-0.49 ± 0.05

NOTE. - The coordinates were taken from the FIRST survey and the flux density are taken from the NVSS survey. It follows the flux densities at 10.45 GHz, the upper limits on the polarization flux density at 10.45 GHz measured with Effelsberg, and finally the spectral index between the two frequencies.

Table 2.2: Parameters of the high-RM candidates.

Source	RA [J2000]	DEC [J2000]	$S^{NVSS}_{1.4GHz}$ [mJy]	S^{Eff}_{10GHz} [mJy]	$\alpha^{10.45}_{1.4}$	RM_{obs} [rad/m^2]	z	RM_{mw} [rad/m^2]	RM_{rf} [rad/m^2]
0239–0234	02:39:45.480	-02:34:40.98	300 ± 10	723 ± 6	0.44 ± 0.04	–40 ± 10	1.1	–100 ± 100	–190 ± 30
0243–0550	02:43:12.464	-05:50:55.36	560 ± 17	548 ± 2	-0.01 ± 0.04	600 ± 100	1.8	–100 ± 100	4500 ± 400
0742+4900	07:42:02.763	+49:00:15.65	398 ± 12	430 ± 1	0.04 ± 0.04	–200 ± 30	2.3	30 ± 10	–2170 ± 370
0751+2716	07:51:41.492	+27:16:31.65	590 ± 20	82 ± 1	-0.98 ± 0.04	500 ± 100	3.2	–20 ± 10	8800 ± 900
0845+0439	08:45:17.151	+04:39:46.64	380 ± 10	682 ± 6	0.30 ± 0.04	1920 ± 20	0.28	–100 ± 100	3145 ± 32
0925+3159	09:25:32.726	+31:59:52.86	551 ± 17	97 ± 4	-0.86 ± 0.06	–100 ± 100	1.5*	–10 ± 10	–400 ± 300
0958+3224	09:58:20.939	+32:24:02.16	1250 ± 40	660 ± 6	-0.32 ± 0.04	2200 ± 100	0.5	–10 ± 10	5200 ± 200
1015+0318	10:15:34.024	+03:18:50.06	416 ± 13	91 ± 2	-0.76 ± 0.04	200 ± 100	1.5*	–40 ± 10	1600 ± 300
1043+2408	10:43:09.032	+24:08:35.45	320 ± 10	1070 ± 10	0.60 ± 0.04	–60 ± 10	0.6	30 ± 20	–150 ± 20
1044+0655	10:44:55.921	+06:55:37.94	490 ± 20	295 ± 5	-0.25 ± 0.06	–210 ± 20	2.1	20 ± 40	–2030 ± 170
1048+0141	10:48:22.850	+01:41:47.46	380 ± 10	328 ± 3	-0.07 ± 0.03	–2510 ± 30	0.7	–100 ± 100	–7160 ± 90
1146+5356	11:46:44.186	+53:56:43.36	367 ± 11	614 ± 6	0.26 ± 0.04	–450 ± 10	2.2	10 ± 10	–4570 ± 90
1213+1307	12:13:32.146	+13:07:20.43	1340 ± 40	421 ± 3	-0.60 ± 0.04	20 ± 2	1.1	20 ± 20	90 ± 10
1246–0730	12:46:04.231	-07:30:46.63	550 ± 20	1040 ± 10	0.32 ± 0.04	880 ± 10	1.2	10 ± 40	4610 ± 60
1311+1417	13:11:07.835	+14:17:46.69	734 ± 22	207 ± 1	-0.63 ± 0.03	570 ± 10	1.9	10 ± 10	4940 ± 100
1312+5548	13:12:53.193	+55:48:13.21	590 ± 20	140 ± 3	-0.72 ± 0.04	–1000 ± 200	1.5*	20 ± 10	–6000 ± 1000
1351+0830	13:51:16.926	+08:30:39.82	350 ± 10	308 ± 5	-0.06 ± 0.05	70 ± 20	1.4	50 ± 30	410 ± 120
1405+0415	14:05:01.113	+04:15:35.87	930 ± 30	712 ± 10	-0.13 ± 0.04	1153 ± 4	3.2	30 ± 60	20420 ± 80
1435–0414	14:35:39.884	-04:14:55.20	480 ± 10	146 ± 1	-0.60 ± 0.03	1080 ± 30	0.8	100 ± 100	3500 ± 80
1549+5038	15:49:17.447	+50:38:05.87	630 ± 20	813 ± 1	0.135 ± 0.04	100 ± 100	2.2	20 ± 10	1400 ± 500
1616+0459	16:16:37.530	+04:59:31.96	330 ± 10	1035 ± 10	0.57 ± 0.04	2530 ± 40	3.2	150 ± 10	44630 ± 720
1616+2647	16:16:38.340	+26:47:01.39	1480 ± 50	294 ± 5	-0.80 ± 0.06	–140 ± 30	1.5*	10 ± 10	–880 ± 190
1647+3752	16:47:25.735	+37:52:18.32	630 ± 20	152 ± 2	-0.70 ± 0.04	80 ± 10	1.5*	–20 ± 10	490 ± 80
1713+2813	17:13:25.930	+28:13:07.10	1030 ± 40	124 ± 2	-1.05 ± 0.05	84 ± 2	1.5*	3 ± 8	530 ± 20
1723+3417	17:23:20.801	+34:17:57.85	520 ± 20	162 ± 1	-0.58 ± 0.04	83 ± 2	0.2	–30 ± 10	120 ± 10
2050+0407	20:50:06.240	+04:07:49.22	565 ± 17	566 ± 2	0.01 ± 0.06	60 ± 10	1.5*	100 ± 100	380 ± 60
2101+0341	21:01:38.833	+03:41:31.29	630 ± 20	969 ± 1	0.21 ± 0.04	70 ± 10	1.0	200 ± 100	260 ± 40
2147+0929	21:47:10.162	+09:29:46.63	930 ± 30	760 ± 5	-0.10 ± 0.04	1400 ± 20	1.1	–10 ± 40	6260 ± 110
2200+0708	22:00:57.607	+07:08:29.01	896 ± 32	113 ± 1	-1.03 ± 0.04	–15 ± 2	1.5*	–20 ± 100	–90 ± 20
2245+0324	22:45:28.284	+03:24:08.71	480 ± 10	379 ± 7	-0.12 ± 0.04	–800 ± 100	1.3	–40 ± 100	–4400 ± 500

2.6.1 Spectral index distribution

From the first observation run, we were able to determine the spectral index (defined here as S $\propto \nu^{\alpha}$) between 1.4 GHz (from the NVSS catalogue) and 10.45 GHz. This allows us to have a qualitative idea of the source type presented in the sample. As mentioned in 2.5, we compared the 30 high-RM candidates with the 77 unpolarized sources at 10.45 GHz.

In Fig. 2.1 the spectral index distributions for the targets considered to have a high RM (red colors) are shown with the unpolarized targets (black colors) and its cumulative plot distribution. Both the histograms were normalized with the number of the sources. We chose the bin dimension larger than the 3σ of the largest error of the spectral index in our sample (in this case $3\sigma_{\alpha}$= 0.18). From the cumulative plot (Fig. 2.1*b*), the two distributions seem to follow a similar tendency up to a value of $\alpha\sim$–0.6, then they separate. In fact, the spectral index distribution of the unpolarized sources (black histogram Fig. 2.1*a*) peaks at $\alpha_{peak}\simeq$ –0.5, thus we mainly see steep radio spectra sources. On the other hand, the spectral index distribution of the high RM candidates (red histogram Fig. 2.1*a*) shows three different groups of objects. The three distributions indeed peak at different spectral indices, revealing the following classes of spectra:

- steep spectrum radio sources with $\alpha_{peak}\simeq$ –0.8;
- flat spectrum radio sources with $\alpha_{peak}\simeq$ –0.1;
- inverted spectrum radio sources with $\alpha_{peak}\simeq$ +0.2.

The distribution of radio spectral indices can be symptomatic of the orientations of radio sources (Orr & Browne, 1982). The first group could be associated to "lobe-dominated" objects where large-scale structures dominate the radio synchrotron emission and where the steepness of the spectrum is due to the radiative loss of the relativistic electrons. Flat-spectrum radio sources could be associated with objects where the lines of sight are closer to the radio axis. In these objects, we can see a superposition of several features, thus a continuous injection of relativistic electrons that become opaque at widely different frequencies. The latter kinds of objects could be representative of core-dominated objects where the dominant synchrotron component is very compact and where it is possible that the synchrotron self absorption occurs. If a turnover peak is revealed in the spectra of these objects, it is possible to associate them to the GPS source that is supposed to be AGN in an early phase of activity (O'Dea, 1998).

From the comparison of the histograms in Fig. 2.1, we can assert that, although they represent the low number in our sample, the high-RM candidates do not seem to be represented by a particular class of targets. Instead, the three

main types of spectra seem to represent these peculiar objects equally. In contrast, the other sources without detected polarization at high frequency seem to be dominated by very steep spectra. This could be an indication that the objects without high RM could be dominated by very extended and probably old synchrotron components, while high RM values could be found in different objects where the combined contribution of electron density and magnetic field is strong.

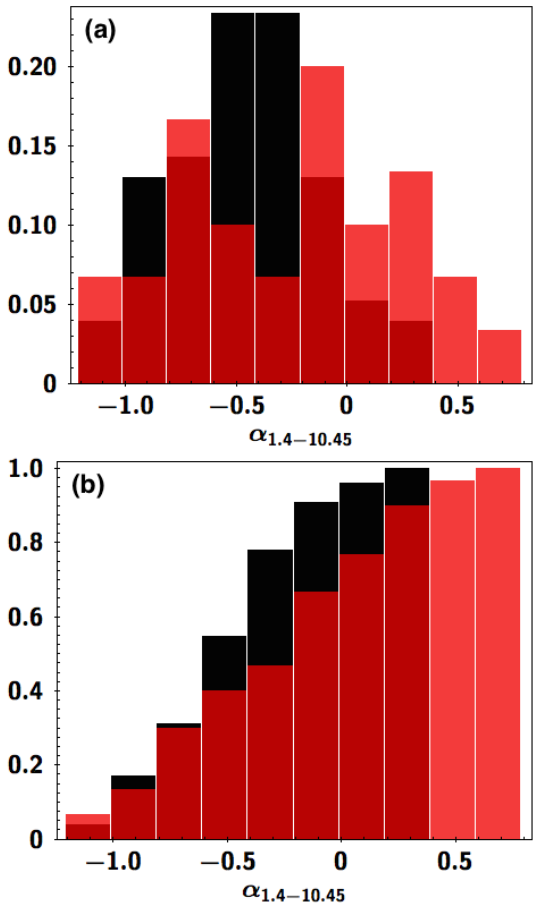

Figure 2.1: Spectral index distributions. (a) Comparison of the spectral index distribution for the high-RM candidates (30 sources; red histogram) and the unpolarized sources (77 sources; black histogram). The distribution of the unpolarized sources peaks at $\alpha_{peak}\sim$ –0.5. The high-RM distribution shows 3 different types of objects: steep ($\alpha_{peak}\sim$ –0.8), flat ($\alpha_{peak}\sim$ –0.1), and inverted ($\alpha_{peak}\sim$ +0.2) spectrum radio sources. (b) The same but cumulative histograms.

2.6.2 The radio spectral energy distribution

The wide frequency coverage obtained with our follow-up observations, plus data from the literature, allows us to study the SED shape of these sources that are all characterized by synchrotron emission. We indeed extended the SEDs to frequencies lower than 1.4 GHz, using the following surveys: VLSS (74 MHz with a resolution of 80″) (Cohen et al., 2007), 7C (151 MHz with a resolution of 70″) (Hales et al., 2007), WENSS (325 MHz with a resolution of 54″× 54″cosecδ) (Rengelink et al., 1997), and TEXAS (365 MHz with a resolution of ∼50″) (Douglas et al., 1996). Their values are listed in Tables *A*.1. As discussed in 2.2, we checked that our targets are isolated up to 5′. Therefore, the different beam sizes of each frequency should not be affected by back- or foreground sources. Moreover, all the sources were selected to be compact in the FIRST survey, therefore effects on the flux density due to extended structures do not affect our analysis either.

For each source in our sample, we fit several models representing its SEDs:

- a power law, representing a purely optically thin synchrotron spectrum with a slope α_{thin}:
$$S_\nu^{pl} \propto \nu^{\alpha_{thin}}; \tag{2.1}$$
- a power law with a break (symptomatic of an aging of the radio source) at frequency ν_b:
$$S_\nu^{plb} = S_\nu^{pl} \left\{ 1 - \exp \left[\left(\frac{\nu}{\nu_b} \right)^{\alpha_{break} - \alpha_{thin}} \right] \right\}, \tag{2.2}$$
where α_{thin} is the spectral index at frequencies lower than ν_b and α_{break} is the spectral index at higher frequencies;
- a single synchrotron self-absorption component:
$$S_\nu^{s} \propto \nu^{2.5} \left\{ 1 - \exp \left[- \left(\frac{\nu}{\nu_0} \right)^{\alpha_{thin} - 2.5} \right] \right\}, \tag{2.3}$$
where ν_0 is the frequency where the emission changes from optically thick, with a spectral index of 2.5, to optically thin with a spectral index α_{thin};
- a single synchrotron component with a break at frequency ν_b:
$$S_\nu^{sb} = S_\nu^{s} \left\{ 1 - \exp \left[\left(\frac{\nu}{\nu_b} \right)^{\alpha_{break} - \alpha_{thin}} \right] \right\}; \tag{2.4}$$
- a combination of several synchrotron components (S_ν^{s+}) with fixed α_{thin}= –0.7;

- a combination of a power law with one or two synchrotron components (S_ν^{pls}) with α_{thin}= free or α_{thin}= –0.7.

For each source, we selected the best model according to the lowest residual value. Table A.7 shows the chosen parameters for the different fitting functions used for the SEDs study. Table 2.3 is a quick look at the values for α_{thick} and α_{thin} that we decided to use for each model.

Based on the fitted SEDs we noticed three main groups. We refer to them from now on with:

- *Older*: sources fitted with a power law (with or without a break) and sources with one synchrotron component with a break (the presence of a frequency break is an indication of an aging of the source);
- *GPS-like*: SEDs with several synchrotron components peaking at frequencies $\geq$ 100 MHz;
- *Mixed*: the combination of the two above, thus a combination of a power law or a synchrotron component peaked at low frequency (with peak frequency $\leq$ 100 MHz) and one or more synchrotron components at higher frequencies (with peak at frequencies $\geq$ 100 MHz).

Table 2.3: Quick look at the spectral indices α_{thick} and α_{thin} used for each model.

Model	α_{thick}	α_{thin}
S_ν^{pl}	–	free
S_ν^{plb}	–	free
S_ν^{s}	2.5	free
S_ν^{sb}	2.5	free
S_ν^{s+}	2.5	–0.7
S_ν^{pls}	2.5	free or –0.7

In Fig. 2.2, we show three examples of the three object types we identified. Together with the radio total intensity SED, information on the polarization flux density, the fractional polarization (here expressed in percentage: m [%]) and the polarization angle (in the plot: PA [deg]) are shown for each of the targets. An explanation and a discussion about the polarization characteristics is presented in subsections 2.6.4 and 2.6.5. Similar plots for all the sources are available in Appendix A.3.

From the analysis of the radio spectra, we find that the sample splits into three (equal sized) parts:

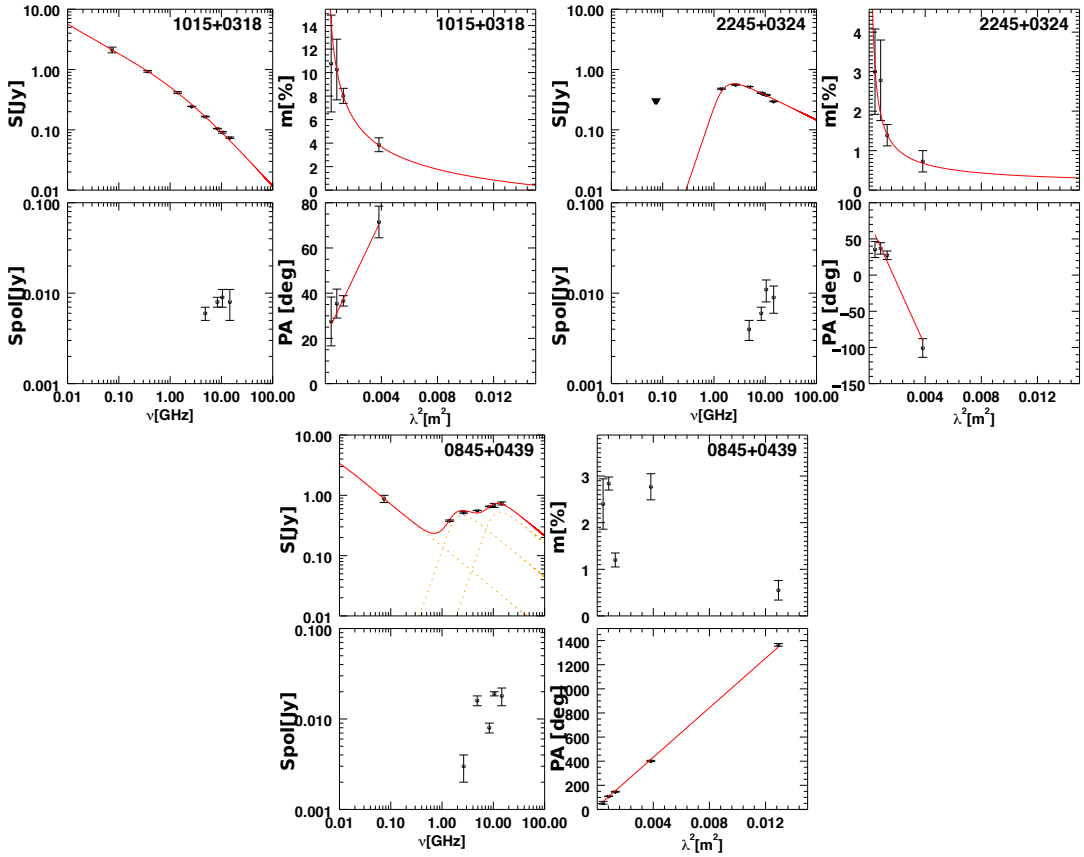

Figure 2.2: SEDs for the sources: 1015+0318 classified as *Older*, 2245+0324 classified as *GPS-like,* and 0845+0439 classified as *Mixed*. Black dot points are the Effelsberg and low-frequency data from the literature; 3-sigma upper limits are drawn as triangles. Where present, various synchrotron components are plotted with an orange dashed line. The fit of the spectra is the red straight line. polarization information is presented with the SEDs.

- 1/3 of the sample can be considered as *Older* sources. Since for these sources the synchrotron peak is not visible or it peaks at very low MHz value, it is possible to assert that these sources have an extended and probably old synchrotron component;

- 1/3 of the sample are characterized by a *GPS-like* SED. These targets could have a more compact and probably early-phase synchrotron components.

- 1/3 of the sample can be considered to have a *Mixed* spectrum, i.e. a combination of *Older* and *GPS-like* features. This behavior could be an indication of sources in which a restart radio emission activity occurs.

These results suggest that the high-RM candidates are mainly (66%) sources with compact high-frequency components, thus probably new growing radio components. We can associate these targets with objects in a particular compact young phase (the *GPS-like*) or in a reactivated activity phase (*Mixed*).

For the *Older* sources, a possible explanation for a high-RM value could be a very dense intervening material surrounding the already extended radio component. From these considerations, in all the cases, the contribution inferred by the medium in which the source is embedded and/or the several Faraday screens that the radiation passes through (see 2.6.4 and 2.6.5 for details) is very important.

2.6.3 Magnetic field estimation

Together with the characterisation of the type of the targets, the magnetic field was considered. Lower limits on the magnetic field were computed from observable quantities. Assuming that the spectral peaks seen on the SEDs are due to SSA, the magnetic field B of a homogeneous synchrotron component can be derived using the following relation (see e.g. Kellermann & Pauliny-Toth, 1981):

$$B \sim \theta^4 \nu_{max}^5 S_{max}^{-2} (1+z)^{-1}, \qquad [\mathrm{G}] \tag{2.5}$$

where θ is the angular dimension [mas], S_{max} and ν_{max} are the peak flux density [Jy] and the peak frequency [GHz] of the synchrotron component, and z is the redshift.

Since all our targets are unresolved for the FIRST beam, we do not have any information on their angular size. We obtained lower limits for the angular sizes by considering the inverse Compton limit for which the brightness temperature (T_B) is assumed to not exceed its maximum value $T_B \leq 10^{12}$ K (Kellermann & Pauliny-Toth, 1981):[4]

$$T_B = 1.22 \cdot 10^{12} \frac{S_{max}}{\theta^2 \cdot \nu_{max}^2} \leq 10^{12} \qquad [\mathrm{K}]; \tag{2.6}$$

therefore,

$$\theta = 1.1 \cdot \frac{\sqrt{S_{max}}}{\nu_{max}} \qquad [\mathrm{mas}]. \tag{2.7}$$

From the lower limits in the angular size, we obtained lower limits for the magnetic field strength [μG] for those targets with synchrotron component/s in their SEDs. For the sources with no information on the redshift z, the mean value

[4] Recent studied pointed out that the value of T_B could be bigger that 10^{12} K (Kovalev et al., 2016) with consequents implications on the non-thermal continuum emission in the vicinity of SMBH and the jet speeds.

of the sample (z_{mean}=1.5) was used in order to have a rough estimation of their magnetic field strength. The lower limit values are listed in Table 2.4 and are, for most of the sources, in the range of 1-100 μG.

2.6.4 Rotation measure

The polarization angle χ for all the targets was calculated and, by combining several frequencies, their RM estimated. To determine the RM value, we fit a straight line (linear regression fit) to the plot of the EVPA versus λ^2. The data at our disposal cover a wide range in λ but with large gaps in the λ^2 coverage, so the resulting RM values suffer from $n\pi$ ambiguity. The strategy we adopted was to trust the observed polarization angle values at the highest frequency, which suffer less from Faraday rotation, and to apply, where necessary, wrapping by some integer multiple of 180 degrees to the lower frequencies data (mostly to the 2.64 GHz and to the 4.85 GHz data). The maximum number of wraps we decided to apply had been fixed to five.

In Table 2.2 the values of the observed RM (RM_{obs}) are listed, together with the rest-frame RM (RM_{rf}), both given in rad/m^2. As is known, our Milky Way introduces a RM contribution that varies with the galactic latitude. The high RM targets are mainly at latitudes $|b| > 30°$, thus above the Galactic plane, but following pioneer works (Kronberg & Simard-Normandin, 1976; Kronberg et al., 1977), the Galactic contribution should be subtracted to the observed RM value. Looking at the most recent foreground galactic RM (RM_{mw}) map by Oppermann et al. (2015), we noticed that the RM_{mw} contributions at the positions of our sources, are very small compared to the observed RM_{obs} of our targets. However, the uncertainties of the RM_{mw} are quite large. Therefore, since the correction for the Galactic contribution in our case would only increase the uncertainty of the measures without a significant correction on the RM value, we decided to not apply it. For the same reason we decided to ignore also the cosmic-web contribution that is only a few rad/m^2, too (Akahori & Ryu, 2011). The source rest frame RM_{rf} was then calculated following the relation:

$$RM_{rf} = RM_{obs} \times (1+z)^2 \qquad [\mathrm{rad/m^2}]. \tag{2.8}$$

For those sources with unknown z, we used the approximate mean value of our sample (z_{mean}=1.5) to have at least an indication of the intrinsic RM of the source. In Appendix A.3 all the plots showing the RM fit for the 30 targets are shown, along with the radio SEDs and other polarization information.

The fitted data points for the RM almost always showed a linear regression with the lowest χ^2 fit, as expected for the goodness of the fit. However, for 10 sources ($\sim$ 33% of the sample; 0239–0234, 0742+4900, 1043+2408, 1213+1307, 1616+2647, 1713+2813, 2050+0407, 2101+0341, 2200+0708, 2245+0324), we

noticed a deviation from the λ^2 law. Among these, six sources ($\sim$ 60%) are *GPS-like*. This suggests that these compact sources are characterized by several Faraday screens intervening in the medium. Indeed, if the radiation passes through different magnetized plasma, the latter could rotate the polarization angle differently, leading to a non-linear behavior by the data. This explains, in general, the low-RM (observed) associated with the majority of these 10 sources ($\sim$ 90%).

In Fig. 2.3 we show the distribution of the fitted RM (RM_{obs}) for our 30 high-RM sources (red histogram) compared with the targets from the Farnes catalogue (Farnes et al., 2014) (blue histogram) and its cumulative plot. Both the histograms have been normalized with the number of the sources of each sample: 30 sources for our sample and 951 for the Farnes sample. For better visibility of the whole distribution, the histograms are shown on logarithmic scale. Farnes et al. (2014) show a RM_{obs} distribution that is centered on zero with a $\sigma\sim$100 rad/m^2. From the two histograms in Fig. 2.3, it is evident that the distribution of the $|RM_{obs}|$ of our sample is different with respect to the sources chosen from the Farnes catalogue. The cumulative plot underlines that 80% of the Farnes targets have a $|RM_{obs}|$ value below 20 rad/m^2, while 80% of our targets have a $|RM_{obs}|$ value of $\gtrsim$ 100 rad/m^2. To check the discrepancy, we also ran the Kolmogorov-Smirnov test to the distributions, and it gives a probability of 3×10^{-6} that the two distributions are comparable; the two distributions are different at a confidence level >95%.

We also compared the RM for the three main object types we found by analyzing the radio SEDs. Their cumulative plot of the $|RM_{obs}|$ and the $|RM_{rf}|$ are shown in Fig. 2.4. In Fig. 2.4*a* it is clear that the three groups are different, and it seems that the *Mixed* targets are those with the highest values of $|RM_{obs}|$. Indeed, after the correction of the observed RM to its value in the rest frame (Fig. 2.4*b*), we can assert that all the *Mixed* targets show $|RM_{rf}|$ higher than 1000 rad/m^2, while for the two others, only 50% are above 500 rad/m^2, still 5σ away from the Farnes distribution. This seems to suggest that sources that show a mixed SED, with an old component at low frequency and compact components at high frequencies, i.e. radio sources that are restarting their activity, are related to high values of the RM.

2.6.5 Fractional polarization, depolarization, and repolarization

The analysis of the fractional polarization, as a function of λ^2 indicates that the majority of the sources have a fractional polarization that decreases with increasing wavelength (Saikia & Salter, 1988). This is indicative of a non-homogeneous medium that is present between the source and the observer.

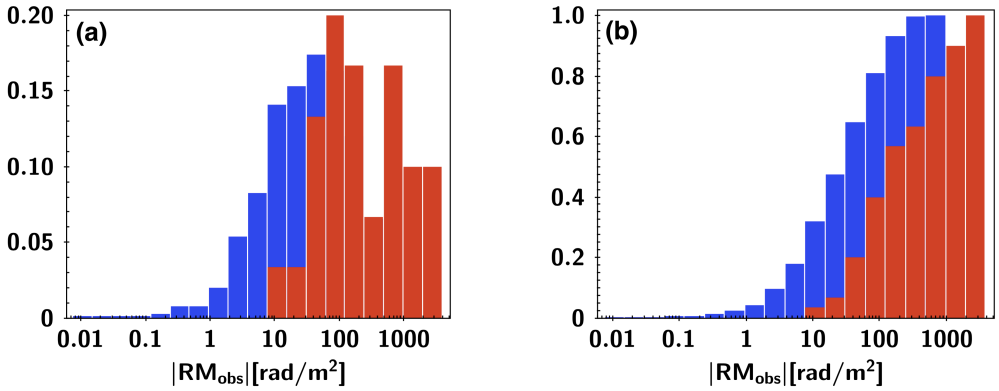

Figure 2.3: a): Histogram showing the distribution of the fitted rotation measure of our targets (red histogram) together with the Farnes catalogue (blue histogram). b): The same but cumulative.

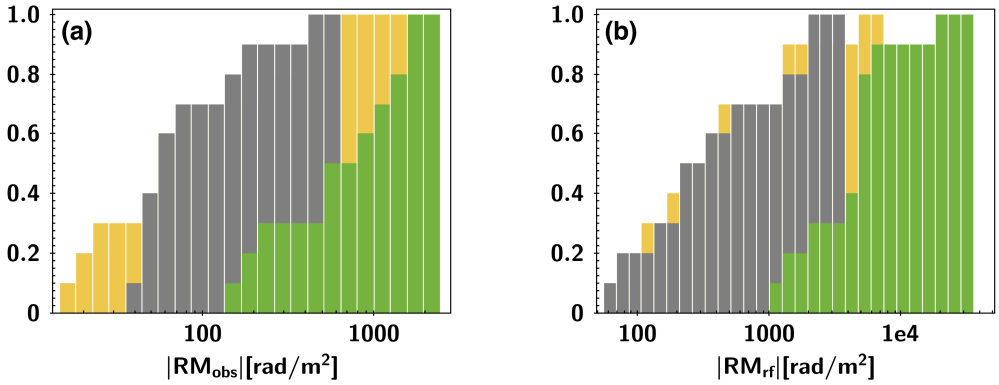

Figure 2.4: (a) Cumulative plot of the RM_{obs} for the three object type. Yellow: *Older* type; grey: *GPS-like* type; green: *Mixed* type. (b) Cumulative plot of the RM_{rf} for the three objects types.

Several depolarization (DP) models have been developed to explain the physical processes behind this behavior. The main models that one needs to consider are the *Slab* model (Burn, 1966), the *Tribble* model (Tribble, 1991), the *Rossetti-Mantovani* model (Rossetti et al., 2008; Mantovani et al., 2009), and the *Repolariser* model (Homan et al., 2002; Mantovani et al., 2009; Hovatta et al., 2012). Most of these models assume an optically thin emitting region, and all of them make the assumption that we detect the same emitting region at each frequency. We saw from our SEDs that the majority of the sources have different synchrotron components that contribute to the shape of the total intensity distribution. Thus, our unresolved sources can have several overlaps of optically thick and optically thin components together. This can, in the end, modify the polarization behavior from the simplified way described from the models.

Since we cannot be sure that the polarized emitting region comes from the same emitting region within the frequency range, and the lack of a complete coverage along the bandwidth led us to decide to follow a similar approach to the one adopted by Farnes et al. (2014), we chose three models that are just a mathematical generalization that can mimic the wavelength dependence of polarization of the various physical models: a Gaussian (DP_{Gauss}), a power law (DP_{PL}), and a Gaussian with a constant term (DP_{Gauss+}):

$$DP_{Gauss} = p_0 \times \exp(-(\lambda - c_1)^2/2c_2^2); \tag{2.9}$$

$$DP_{PL} = p_0 \times \lambda^{c_3} + b; \tag{2.10}$$

$$DP_{Gauss+} = p_0 \times \exp(-(\lambda - c_1)^2/c_2^2) + b, \tag{2.11}$$

where λ is in centimeters, p_0 in %, c_1 and c_2 in centimeters, c_3 is unit-less, and b is a constant. The Gaussian model is representative of the *Slab* model, the power law model represents the *Tribble* or, thanks to its flexibility, the *Repolariser* model, and finally the Gaussian with the constant term can provide the *Rossetti-Mantovani* model.

Owing to the different number of degrees of freedom for the various models, the Gaussian and the power law models have been used whenever three or more data points were available, and the Gaussian with constant model have been adopted when four or more data points were available. Proper fitting constraints were applied during the fitting process to ensure that only values of c_i that correspond to meaningful physical solutions were obtained. Repolarized sources have been identified thanks to the flexibility of the power law model, which provides a polarization spectral index $\mathrm{c}_3 > 0$. The determination of the residuals, together with a visual inspection, provides a measure for the goodness of the fit. See the Appendix A.3 for the plots of the depolarization models.

Some of the sources ($\sim$ 30% of the sample; see 0845+0439 as an example, Fig. 2.2) show complex behavior with rising and decaying of the fractional polarization; for them, none of the three models fit the data properly. The behavior of these sources can be studied better with better frequency-sampled data and/or higher angular resolution observations. Still from this first analysis, it is possible to note that:

- 1/3 of the sample follow a model of a Gaussian, DP_{Gauss}, or a Gaussian with a constant term, DP_{Gauss+};
- 1/3 of the sample follow a power law model, DP_{PL}; and
- 1/3 of the sample cannot be fitted by any of the three models because of their complex shape, thus we can assert the existence of a complex model $\mathrm{DP}_{complex}$ not discussed here, owing to the lack of points for the fitting.

We did not find any correlation between the DP models and the SEDs shapes or the RM values. Thus from this first single-dish analysis of the polarization fraction, it is not possible to indicate a possible trend that these objects are following.

2.7 Summary and conclusions

In this part of the work, we presented the search for sources with a very high RM, as well as some follow-up studies of appropriate candidates. Assuming that a high RM causes strong in-band depolarization, we observed a sample for unpolarized sources from the NVSS with the 100-m Effelsberg telescope at 10.45 GHz. After identifying 30 potential high-RM sources, we performed observations at 2.64, 4.85, 8.35, 10.45, and 14.60 GHz as well, in order to determine the SED and the RM of the sources. In some cases, exceptionally **high intrinsic RM were found, as in 1616+0459 where its $\mathbf{RM}_{obs}$ of $\sim$ 2550 rad/m^2 corresponds to a $\mathbf{RM}_{rf}$ of $\sim$ 44300 rad/m^2**. Our main conclusions can be summarized as follows.

- From our statistical study it turned out that the **high-RM candidates are not characterized by a specific object type**. Indeed, the spectral index distribution of the 30 high RM candidates shows three peaks representing all the possible object type (steep, flat, and inverted spectrum radio sources).
- **SEDs were characterized and three groups** (*Older*, *GPS-like*, *Mixed*) identified. The high-RM candidates are mainly (66%) sources with compact high-frequency components, probably new growing radio components,

thus objects in a particular compact young phase (the *GPS-like*) or in a reactivated activity phase (*Mixed*). The *Older* sources showing high RM could be surrounded by a very dense intervening material.

- Due to the lack of angular resolution, **lower limits for the magnetic field strength were calculated** for those sources with well-defined synchrotron component/s in their SEDs.

- The behavior of the **fractional polarization with λ^2 were fitted** using simple mathematical representations of the main physical depolarization models: the *Slab* model, the *Tribble* model, the *Repolariser*, and the *Rossetti-Mantovani* model. Three groups were detected: sources following a Gaussian or a Gaussian with a constant term model, sources following a power-law model, and sources having a complex behavior for which we cannot fit any of the models because of their complex shape. No correlation between the SED type and the fractional polarization behavior has been found.

- The **RM was determined** for the all the sources in the sample, and among these, **11 sources show a deviation from simple linear behavior**. This feature could indicate that **several Faraday screens within the medium** are affecting the polarization angle distribution differently. Owing to the lack of well sample data, we could not reconstruct their real behavior.

- **A strong correlation between the *mixed* SEDs and a high value of the RM was found**. Indeed, the *mixed* sources have a RM_{rf} larger than 1000 rad/m^2. This could be an indication that these particular sources, showing a restarting phase at high frequency, are characterized by a really dense and/or a magnetized medium that rotates the polarization angle strongly.

Extreme cases, i.e. all the sources with $|\mathrm{RM}_{obs}|\geq$500 rad/m^2, have been studied by us with the interferometric technique, using the JVLA, VLBA, and EVN interferometers. The results in the next chapter.

Table 2.4: Estimation of the magnetic field for those targets with one or more synchrotron components in their SEDs.

Name	z	SEDfit	θ [mas]	B [μG]				
2050+0407	1.5*	S_ν^s	0.8	20.0				
2245+0324	1.3	S_ν^s	0.3	47.9				
Name	z	SEDfit	θ [mas]	B [μG]				
0751+2716	3.2	S_ν^{sb}	7.0	2.2				
1311+1417	1.9	S_ν^{sb}	0.8	17.8				
1435-0414	0.8	S_ν^{sb}	16.3	1.7				
Name	z	SEDfit	θ_1 [mas]	B_1 [μG]	θ_2 [mas]	B_2 [μG]		
1351+0830	1.4	S_ν^{s+}	0.5	26.4	0.1	173.3		
1549+5038	2.2	S_ν^{s+}	1.4	10.2	0.1	106.1		
1616+2647	1.5*	S_ν^{s+}	12.2	1.9	2.2	11.2		
2101+0341	1.0	S_ν^{s+}	0.5	19.4	0.1	220.8		
Name	z	SEDfit	θ_1 [mas]	B_1 [μG]	θ_2[mas]	B_2 [μG]	θ_3[mas]	B_3 [μG]
0239-0234	1.1	S_ν^{s+}	1.2	11.0	0.2	82.0	0.1	247.6
0742+4900	2.3	S_ν^{s+}	0.9	7.7	0.3	36.1	0.04	186.5
1043+2408	0.6	S_ν^{s+}	1.7	12.0	0.2	121.8	0.1	437.4
1044+0655	2.1	S_ν^{s+}	13.0	1.5	0.2	45.4	0.03	183.4
1048+0141	0.7	S_ν^{s+}	12.5	2.5	0.2	71.5	0.03	261.8
1146+5356	2.2	S_ν^{s+}	2.9	3.4	0.3	40.3	0.1	137.1
1246-0730	1.3	S_ν^{s+}	12.5	2.3	0.2	84.7	0.1	292.6
2147+0929	1.1	S_ν^{s+}	18.0	2.0	0.3	56.0	0.1	227.0
Name	z	SEDfit	θ[mas]	B [μG]				
1312+5548	1.5*	S_ν^{pls}	1.4	12.0				
Name	z	SEDfit	θ_1[mas]	B_1 [μG]	θ_2[mas]	B_2 [μG]		
0243-0550	1.8	S_ν^{pls}	0.6	19.0	0.1	105.3		
0845+0439	0.28	S_ν^{pls}	0.3	87.0	0.1	475.0		
1405+0415	3.2	S_ν^{pls}	1.0	10.1	0.1	87.6		
1616+0459	3.2	S_ν^{pls}	0.3	35.0	0.1	85.3		

NOTE.- We give lower limits of the magnetic field B[μG] considering their lower limit in angular size [mas] (calculated from the inverse Compton relation). These estimations are corrected for the redshifts. Where the redshift was not available from the literature, we used the mean value of z from the sample: z_{mean}=1.5, marked in the table with an asterisk.

Chapter 3

JVLA campaign

3.1 Introduction

The Effelsberg single dish observations presented in the previous Chapter allowed us to define a subsample having a very high observed RM ($|RM|>\simeq 500$ rad/m^2; half of the initial sample). However, while we assigned a single RM value for each of the sources, one of the main result from the Effelsberg observations was the evidence of a deviation from a linear fit for most of the sources. Therefore, this suggests that the RM in these sources is not constant within the 1 to 15 GHz frequency range. Moreover, where enough polarized data were available, we also noticed a complex behavior of the fractional polarization, deviating also from the predictions of simple depolarization models. However, the lack of well frequency-sampled polarization data did not allow us to perform a proper modeling of the data in order to explain their behavior.

We decided to obtain new observations of the high RM sample using the Karl G. Jansky Very Large Array (JVLA) in order to further investigate about their nature. We selected 14 sources (0239–0234, 0243–0550, 0751+2716, 0845+0439, 0958+3224, 1048+0141, 1146+5356, 1246-0730, 1311+1417, 1312+5548, 1405+0415, 1549+5038, 1616+0459, 2245+0324) to be observed at L, C and X bands. Most of these sources show the highest observed RMs with the single dish data ($|RM|>\simeq 500$ rad/m^2). We also observed two sources showing a low RM value but with a clear deviation from the linear fit (0239-0234, 1549+5038) for which we wanted to test whether their lower observed RM is "intrinsic" or whether it is due to strong in-band depolarization within the observed frequency range.

The JVLA is the most suitable instrument for this kind of study thanks to its wide band spectropolarimeter (2 GHz at L band and 4 GHz at C and X bands) allowing us to perform high sensitive multifrequency wide band observations. We decided to use this frequency coverage because it follows that of the previous single dish observations. Moreover, from our previous SEDs determination, we noticed that most of our targets show several synchrotron components at high frequencies (peaking around 4-10 GHz). Therefore, we wanted to collect polarization information of these higher frequency components which most probably are tracing emitting material very near the central engine. Moreover, having a

Table 3.1: Information: frequencies and resolutions of the projects

Project	Band	λ (cm)	ν-Range (GHz)	nspw	chan per spw
13B-236	L	20 cm	1.0 – 2.0	16	64
13B-236	C	6 cm	4.0 – 6.0	16	64
13B-236	X	3 cm	8.0 – 10.0	16	64
14B-184	L	20 cm	1.0 – 2.0	16	64
14B-184	C	6 cm	4.0 – 8.0	32	64
14B-184	X	3 cm	8.0 – 12.0	32	64

better polarization data coverage, we are able to perform modeling of the Stokes parameters Q and U and of the polarization angle. In this way, we try to give an explanation of the complex depolarization behavior and an overview of the status of the ambient medium.

In this chapter, we present the results obtained from this JVLA observational campaign. The observations and data reduction are showed in section 3.2, the depolarization modeling are described in section 3.3, the results with a discussion are shown in section 3.4 and 3.5, and finally the conclusions is given in section 3.6.

3.2 Observations and data reduction

We observed in full polarization mode a sample of 14 sources by using the Karl. G. Jansky Very Large Array (JVLA) of the National Radioastronomy Observatory (NRAO)[1]. Observational details are summarized in Tables 3.1 and 3.2.

Observations were made in different epochs during semesters 2013B, 2014B and 2015A, and used different configurations of the JVLA (see Table 3.1). Two of the sources were observed in project 13B-236 at L, C, and X bands, while the other 12 sources were observed in project 14B-184 only at L, C, and X bands (see Tables 3.1, 3.2). Different observational setups were used for C and X bands at the different projects (2 GHz bandwidth in 13B-236, and 4 GHz bandwidth in 14B-184; see Table 3.1). For L band, bandwidths of 1 GHz was used.

Due to their high brightness, phase calibration of the sources were achieved by self-calibrating assuming they are point-like sources at the resolution of the JVLA (highest JVLA resolution reached is 0.6″ at B configuration). On-source times has been set around 1 minute per source/band. This integration time was

[1]The NRAO is a facility of the National Science Foundation operated under cooperative agreement by Associated Universities, Inc.

Table 3.2: Log file of the projects.

Sources	Date	Conf	Bands	Flux/Pol.Ang. cal.	Leakage cal.
Project Code 13B-236					
0243–0550	19th-Nov-13	B	L C X	3C48	J0319+4130
0239–0234	19th-Nov-13	B	L C X	3C48	J0319+4130
Project Code 14B-184					
0751+2716	28th-Nov-14	C	C X	3C138	J0713+4349
0751+2716	16th-Jan-15	CnB	L	3C286	J1407+2827
0845+0439	28th-Nov-14	C	C X	3C138	J0713+4349
0845+0439	16th-Jan-15	CnB	L	3C286	J1407+2827
0958+3224	8th-Nov-14	C	C X	3C138	J0713+4349
0958+3224	16th-Jan-15	CnB	L	3C286	J1407+2827
1048+0141	9th-Jan-15	CnB	C X	3C286	J1407+2827
1048+0141	16th-Jan-15	CnB	L	3C286	J1407+2827
1146+5356	8th-Jan-15	CnB	C X	3C286	J1407+2827
1246–0730	9th-Jan-15	CnB	C X	3C286	J1407+2827
1246–0730	16th-Jan-15	CnB	L	3C286	J1407+2827
1311+1417	9th-Jan-15	CnB	C X	3C286	J1407+2827
1311+1417	16th-Jan-15	CnB	L	3C286	J1407+2827
1312+5548	8th-Jan-15	CnB	C X	3C286	J1407+2827
1312+5548	16th-Jan-15	CnB	L	3C286	J1407+2827
1405+0415	8th-Jan-15	CnB	C X	3C286	J1407+2827
1405+0415	16th-Jan-15	CnB	L	3C286	J1407+2827
1549+5038	17th-Apr-15	B	L C X	3C286	J1407+2827
1616+0459	17th-Apr-15	B	L C X	3C286	J1407+2827
2245+0324	10th-Oct-14	C	L C X	3C48	J2355+4950

considered enough to have a good signal to noise for both the total intensity and polarization detection. In each session, we included observations of a standard flux/polarization angle calibrator, as well as a leakage calibrator (see Table 3.2).

Data editing and calibration were made by using the data reduction package CASA (Common Astronomy Software Applications[2]; version 4.4.0) following standard VLA procedures. We wrote scripts in order to perform calibration in a quasi-automatic way. Our calibration scripts use prior known corrections of the data provided by the NRAO (antenna positions, antenna gain curves, atmosphere opacity corrections, and requantizer gains). Then, it performs bandpass and delays calibrations (using the flux calibrator of each run), and complex gain calibration (by self-calibrating each source) and polarization calibration. The

[2]https://science.nrao.edu/facilities/vla/data-processing

procedure checks the calibrated data, makes additional flags when necessary after a visual inspection, and re-run the calibration scripts. This is repeated until the calibration of all the sources is satisfactory.

For the flux calibration of the Stokes I, we used resolved models of the flux calibrators provided by the CASA package. Total flux density at each frequency is set by using their known spectrum (Perley & Butler, 2013a). However, for the calibration of the stokes parameters Q and U, similar models are not available. Therefore, in order to calibrate in linear polarization our wide band observations, we used the known values of the fractional polarization and polarization angle at different frequencies reported by Perley & Butler (2013b). Then, we fitted polynomial functions to these data trying to fit the full Q and U spectrum in the 1 to 45 GHz frequency range. The result of these fittings are shown in Figures 3.1. We also constrained the solutions to short baselines in order to avoid effects because of possible extended structures emission.

Once the data have been calibrated, wide band images of Stokes I, Q and U have been made for all the targets. We run the task CLEAN using the parameter nterms=2 (that takes into account the spectral index of the source) and different weight values of the robust parameter (Briggs, 1995). All the sources appear unresolved at the highest angular resolution reached of 0.6″.

Images of Stokes parameters I, Q and U were also made for each 128 MHz spectral windows and for each band (using nterms=1 in the task CLEAN). On the individual spectral windows images we perform a Gaussian fit to the source, considering a circular region with a diameter 2 times the deconvolved beam size of the image. In this way, information on the Stokes I, Q and U for each 128 MHz subband have been collected. These high spectral resolution information allow us to well sample the SEDs and the polarization information, i.e. the polarization flux density, the fractional polarization and the polarization angle, for each target.

3.3 Depolarization models

Total intensity observations of these sources have revealed complex radio spectra, which in most cases could be fitted with multiple synchrotron components. Therefore, the change of the degree of polarization could be due to multiple interfering RM components, either along the line of sight or on the plane of the sky on scales smaller than our spatial resolution. To distinguish between the two scenarios and to discern how they affect the RM, we fitted the broad band Stokes Q and U spectra following the procedure proposed by O'Sullivan et al. (2012). As explained in section 1.3.3, the mixing of Faraday rotating and synchrotron emitting media yield to wavelength dependent depolarization and can

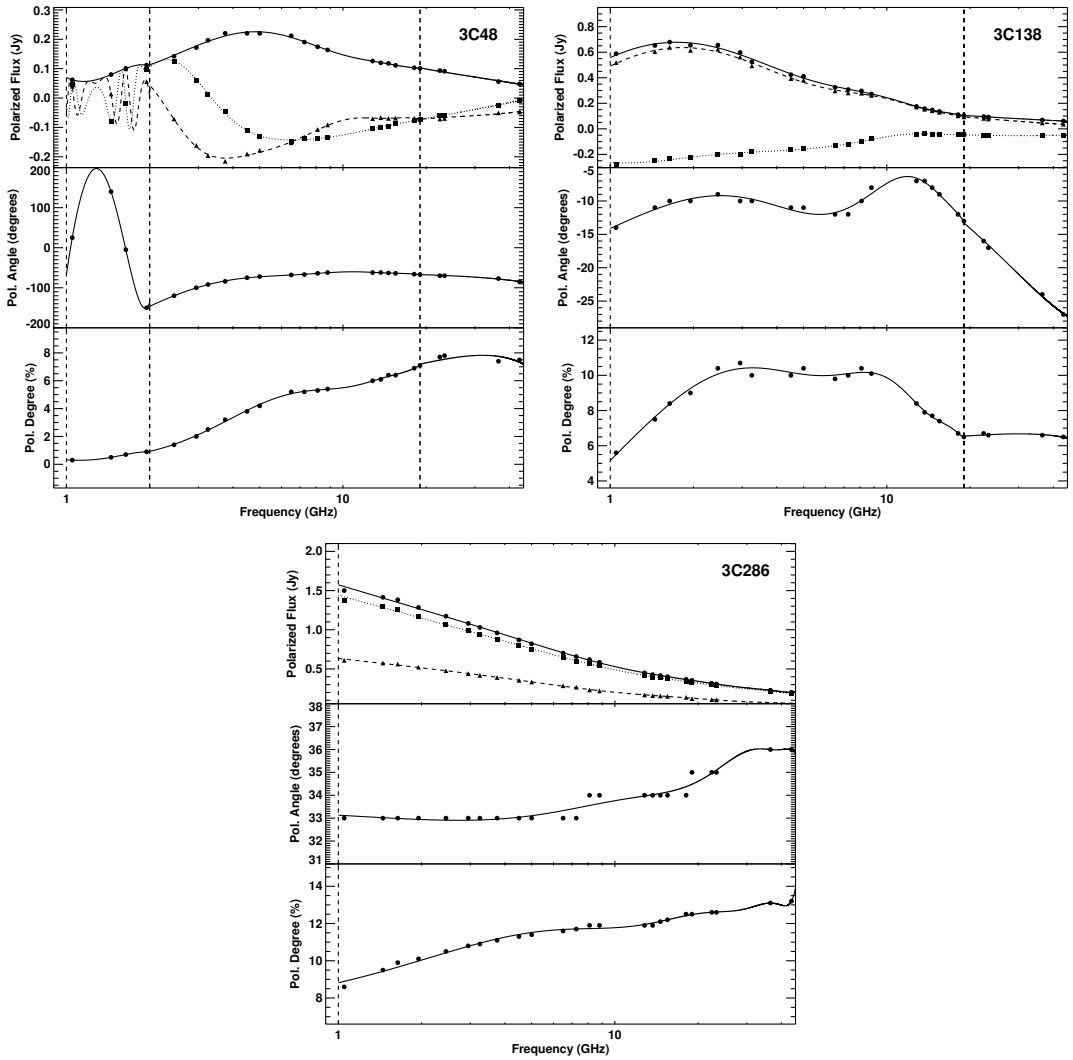

Figure 3.1: Modelling of the polarization parameters for the calibrators: 3C48, 3C138 and 3C286. Frequency coverage: from 1 GHz to 45 GHz.

be described by: (1) differential Faraday rotation (DFR), (2) internal Faraday dispersion (IFD) and (3) External Faraday dispersion (EDF) (see Burn, 1966; Sokoloff et al., 1998; O'Sullivan et al., 2012).

We adopt the same notation as O'Sullivan et al. (2012) and define the complex linear polarization (P) as,

$$P = Q + iU = p_0 I e^{2i\phi}. \tag{3.1}$$

Just as a reminder, I, Q and U are the Stokes parameters and ϕ is the observed angle of polarization given by $\phi = 0.5 \arctan(U/Q)$. The degree of

polarization is $p = P/I$ and it is given by $\sqrt{q^2 + u^2}$, where $q = Q/I$ and $u = U/I$.

For a volume of plasma which is synchrotron emitting and rotating in the presence of a uniform magnetic field, i.e. the DFR, the complex degree of polarization is given by,

$$p = p_0 \frac{\sin R\lambda^2}{R\lambda^2} e^{2i\left(\phi_0 + \frac{1}{2}R\lambda^2\right)}, \tag{3.2}$$

where, p_0 and ϕ_0 are the intrinsic degree of polarization[3] and polarization angle, respectively, and R is the Faraday depth through the region. Note that R corresponds to the RM in the simplest case of an homogeneous medium.

If the emitting plasma also contains a turbulent magnetic field together with a uniform magnetic field, i.e., the IFD, the degree of polarization is then given by,

$$p = p_0 e^{2i\phi_0} \left(\frac{1 - e^{-S}}{S}\right), \tag{3.3}$$

where $S = 2\sigma_{\rm RM}^2\lambda^4 - 2iR\lambda^2$ and $\sigma_{\rm RM}$ is the internal Faraday dispersion of the random field within the volume traced by the telescope beam. It represents the distribution of the parallel component of the turbulent magnetic field cells of the Faraday component within the telescope beam.

External Faraday dispersion arises for the case when the magneto-ionic medium contains turbulent magnetic field but does not emit synchrotron radiation. In this case,

$$p = p_0 e^{-2\sigma_{\rm RM}^2\lambda^4} e^{2i(\phi_0 + RM\lambda^2)}. \tag{3.4}$$

When multiple emitting and/or rotating components exist and they are unresolved within the telescope beam, the complex polarization can be simply described as, $p = p_1 + p_2 + ... + p_N$ (O'Sullivan et al., 2012). This is the approach we adopted for the modeling of the sources. We just considered for simplicity only the sum of the same model type, i.e. multiple of DFR or multiple of IFD or multiple of EFD. We tried also one case in which we combined one IFD and one EFD. The equations that describe the models we try to fit are the following (the subscript "0" expresses the intrinsic value of the written quantity):

- **Single** represents a single Faraday rotating component:

$$p = p_0 e^{2i(\phi_0 + RM\lambda^2)} \tag{3.5}$$

[3]For synchrotron emission arising in the presence of uniform magnetic field within the telescope beam, the intrinsic degree of polarization (p_0) depends on the synchrotron spectral index (α) as, $p_0 = (1 + \alpha)(5/3 + \alpha) \approx 0.75$ for a typical $\alpha = 1$.

- **Double** where the subscripts 1 and 2 are related to the first and the second Faraday rotating components:

$$p = p_1 e^{2i(\phi_{0,1}+RM_1\lambda^2)} + p_2 e^{2i(\phi_{0,2}+RM_2\lambda^2)} \tag{3.6}$$

- **Triple** where the subscripts 1, 2 and 3 are related to the first, the second and the third Faraday rotating components:

$$p = p_1 e^{2i(\phi_{0,1}+RM_1\lambda^2)} + p_2 e^{2i(\phi_{0,2}+RM_2\lambda^2)} + p_3 e^{2i(\phi_{0,3}+RM_3\lambda^2)} \tag{3.7}$$

- **Single Burn** is the classical equation proposed by Burn (1966), also called the DFR, that considers a simultaneously emitting and rotating Faraday medium:

$$p = p_0 \frac{\sin(R\lambda^2)}{R\lambda^2} e^{2i(\phi_0+\frac{1}{2}R\lambda^2)} \tag{3.8}$$

- **Double Burn** is a combination of two internal Faraday emitting and rotating media, identified by the subscripts 1 and 2:

$$p = p_1 \frac{\sin(R_1\lambda^2)}{R_1\lambda^2} e^{2i(\phi_{0,1}+\frac{1}{2}R_1\lambda^2)} + p_2 \frac{\sin(R_2\lambda^2)}{R_2\lambda^2} e^{2i(\phi_{0,2}+\frac{1}{2}R_2\lambda^2)} \tag{3.9}$$

- **Internal Dispersion** is Sokoloff et al. (1998) IFD equation that takes into account the contribution of the turbulent magnetic field coexisting with an ordered magnetic field within the emitting and rotating Faraday region:

$$p = p_0 e^{2i\phi_0} \left(\frac{1 - e^{2iR\lambda^2 - 2\sigma_{\rm RM}^2\lambda^4}}{2\sigma_{\rm RM}^2\lambda^4 - 2iR\lambda^2} \right) \tag{3.10}$$

- **Double Internal Dispersion** is the IFD but considering two Faraday regions with turbulent magnetic fields that emit and rotate.

$$p = p_1 e^{2i\phi_1} \left(\frac{1 - e^{2iR_1\lambda^2 - 2\sigma_{\rm RM_1}^2\lambda^4}}{2\sigma_{\rm RM_1}^2\lambda^4 - 2iR_1\lambda^2} \right) + p_2 e^{2i\phi_2} \left(\frac{1 - e^{2iR_2\lambda^2 - 2\sigma_{\rm RM_2}^2\lambda^4}}{2\sigma_{\rm RM_2}^2\lambda^4 - 2iR_2\lambda^2} \right) \tag{3.11}$$

- **Single External Dispersion** is equivalent to the EFD for one single external Faraday rotating screen:

$$p = p_0 e^{-2\sigma_{\rm RM}^2\lambda^4} e^{2i(\phi_0+RM\lambda^2)} \tag{3.12}$$

- **Double External Dispersion** is the EFD considering two external Faraday rotating screens:

$$p = p_1 e^{-2\sigma_{\rm RM_1}^2\lambda^4} e^{2i(\phi_{0,1}+RM_1\lambda^2)} + p_2 e^{-2\sigma_{\rm RM_2}^2\lambda^4} e^{2i(\phi_{0,2}+RM_2\lambda^2)} \tag{3.13}$$

- **Internal External Dispersion** is the combination between the one internal and one external Faraday dispersion, both with turbulent magnetic field.

$$p = p_1 e^{-2\sigma^2_{\mathrm{RM}_1}\lambda^4} e^{2i(\phi_{0,1}+RM_1\lambda^2)} + p_2 e^{2i\phi_2}\left(\frac{1-e^{2iR_2\lambda^2-2\sigma^2_{\mathrm{RM}_2}\lambda^4}}{2\sigma^2_{\mathrm{RM}_2}\lambda^4-2iR_2\lambda^2}\right) \tag{3.14}$$

These models have a strong interdependence of the different parameters and are highly non linear equations. To evaluate the goodness of the fit we performed the chi-squared-test to the data using the python *LMfit* function that provides a non-linear optimization curve fitting for these kind of equations. In some cases these statistic values were good enough to consider the model suitable for those targets. Indeed, we could find good models for roughly half of the sample. For the remaining targets this modeling procedure gave us just an indication about the trend followed by the depolarization behavior. However, we consider this as a good starting point for a further more complex modeling. In section 3.3.1, we discuss possible alternatives to improve the modeling. The results of the modeling are shown in section 3.4, Fig.s 3.14–3.23 and Tab. 3.3.

3.3.1 Depolarization models: possible improvements

Here we present a possible alternative to improve the modeling of the complex depolarization effects that broadband polarization observations are revealing more often. An improvement we are testing is to combine different type of models together (e.g. a Single Burn model plus an External Faraday Dispersion etc..). This could indeed trace a more complex disposition of the Faraday screens within the beam. Indeed, in some cases we noticed that the longer wavelength data points are not well fitted by the above combination of models and it seems that a combination of internal and external Faraday depolarization models could be more suitable. A clear example of this behavior is seen for the source 1312+5548 (Fig. 3.20). The *Double Burn* model follows quite well the longer wavelength data but not the shorter wavelength data, while the *Double External Dispersion* model seems to represent better the shorter wavelength data points than the longer data points. A combination both models may describe better the depolarization trend.

Another possible way to study the depolarization behavior is considering a superposition of Faraday components along the line of sight. If the polarized components lie behind each other along the line of sight, then one has to account for the effect of wavelength-dependent depolarization of the regions in front. In Figure 3.2 we show the possible configurations of different emitting and rotating

regions along a line of sight. The screens in layer A, B and C have intrinsic degree of polarization $p_{0,A}$, $p_{0,B}$ and $p_{0,C}$, respectively and the angle of polarization $\phi_{0,A}$, $\phi_{0,B}$ and $\phi_{0,C}$, respectively.

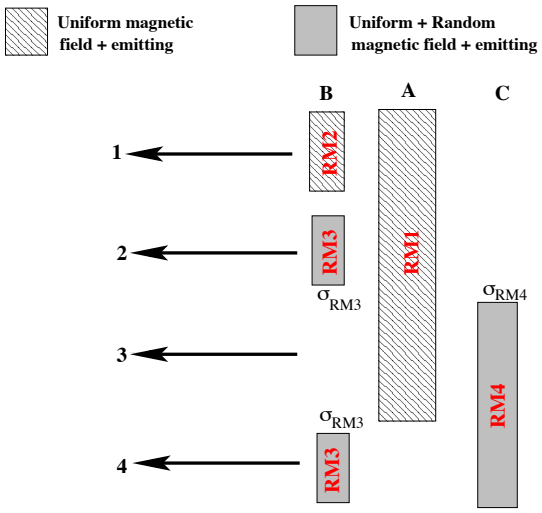

Figure 3.2: The figure shows the line-of-sight through different possible Faraday rotating media. The hatched regions represents volume that has uniform magnetic field along the line-of-sight and is emitting synchrotron radiation (described as DFR in O'Sullivan et al. (2012)). The gray regions represents volume that contains uniform magnetic field as well as random magnetic field and is also emitting synchrotron radiation (described as IFD in O'Sullivan et al. (2012)).

We describe the possible scenarios below:

- *Line-of-sight 1.* Along this line of sight, there are two DFR screens. For each of the screens A and B, the polarized emission is given by Equation 3.2. However, screen B acts as a simple Faraday rotating screen for screen A. Thus, screen A in the background undergoes an extra rotation given by $e^{2i(1/2RM_2\lambda^2)}$. Thus, the observed degree of polarization is given by,

$$p = p_{0,B}\frac{\sin RM_2\lambda^2}{RM_2\lambda^2}e^{2i(\phi_{0,B}+\frac{1}{2}RM_2\lambda^2)} + p_{0,A}\frac{\sin RM_1\lambda^2}{RM_1\lambda^2}e^{2i\left[\phi_{0,A}+\left(\frac{1}{2}RM_1+RM_2\right)\lambda^2\right]} \tag{3.15}$$

In the general case with N such regions along the line-of-sight, this can be written as,

$$p = \sum_{i=1}^{N} p_{0,i}\frac{\sin RM_i\lambda^2}{RM_i\lambda^2}e^{2i\left(\phi_{0,i}+\left(\frac{1}{2}RM_i+\sum_{j=i+1}^{N}RM_j\right)\lambda^2\right)} \tag{3.16}$$

- *Line-of-sight 2.* For observations along a line-of-sight that contains an IFD region in front of an DFR region, the degree of polarization is given by Equations 3.3 and 3.2, respectively. But, note in this case, the IFD region acts as an external Faraday dispersion screen for the DFR screen. Hence, the observed degree of polarization is given as,

$$p = p_{0,B} e^{2i\phi_{0,B}} \left(\frac{1 - e^{-S_B}}{S_B} \right) + p_{0,A} \frac{\sin RM_1\lambda^2}{RM_1\lambda^2} e^{-2\sigma^2_{\mathrm{RM}_3}\lambda^4} e^{2i\left[\phi_{0,A} + \left(\frac{1}{2}RM_1 + RM_3\right)\lambda^2\right]} \tag{3.17}$$

  Here, $S_B = 2\sigma^2_{\mathrm{RM}_3}\lambda^4 - 2iRM_3\lambda^2$.

- *Line-of-sight 3.* In this line of sight the IFD and DFR regions are interchanged w.r.t the previous case. In this case, the DFR region acts as a simple Faraday rotating screen for the IFR region. The degree of polarization in this case is given as,

$$p = p_{0,A} \frac{\sin RM_1\lambda^2}{RM_1\lambda^2} e^{2i(\phi_{0,A} + \frac{1}{2}RM_1\lambda^2)} + p_{0,C} e^{2i(\phi_{0,C} + RM_1\lambda^2)} \left(\frac{1 - e^{-S_C}}{S_C} \right) \tag{3.18}$$

  Here, $S_C = 2\sigma^2_{\mathrm{RM}_4}\lambda^4 - 2iRM_4\lambda^2$.

- *Line-of-sight 4.* This line of sight contains two IFD screens behind each other. In this case, the screen B acts as an external Faraday dispersion screen similar to the case discussed above. The observed degree of polarization in this case is given by,

$$p = p_{0,B} e^{2i\phi_{0,B}} \left(\frac{1 - e^{-S_B}}{S_B} \right) + p_{0,C} e^{2i(\phi_{0,C} + RM_3\lambda^2)} e^{-2\sigma^2_{\mathrm{RM}_3}\lambda^4} \left(\frac{1 - e^{-S_C}}{S_C} \right). \tag{3.19}$$

For both the possible improvement, the main problem is the strong interdependence of the different parameters and the highly non linear characteristic of all these equations. This makes difficult to these models to converge properly. A possible solution would be constrain some of the parameters with additional information.

3.4 Results

We present all the observational results in Figures 3.3–3.13. The SEDs (Fig. 3.3 and Fig. 3.4) were made by using our JVLA data at L, C and X bands, as

well as data at lower frequencies reported in several surveys, the same used to perform the single dish radio SEDs (i.e. the VLSS at 74 MHz, the 7C at 151 MHz, the WENSS at 325 MHz and the TEXAS at 365 surveys). We fitted the total intensity data with several synchrotron components following a similar approach performed for the single dish fitting (previous single dish chapter, 2.6.2). The results of these new radio SED fitting are consistent with previous single dish results.

In Fig.s 3.5–3.11 we show the polarization properties (the Stokes Q and U together with the polarized flux density S_{pol}, the fractional polarization p and the polarization angle χ) for each source at each of the frequencies within the C and X bands. Our JVLA observations confirmed the previous results from the Effelsberg campaign, i.e. for most of the sources, the behavior of the polarization angle deviates significantly from a simple linear trend (see Fig.s 3.5–3.11). This implies that we cannot assign a single RM for these sources in the 4-12 GHz range, but the RM adopts different values at different frequencies. Therefore, in Fig.s 3.12 and 3.13 we show the value of the RM with frequency. The objective is to understand how the polarized angle behaves with frequency, whether it increases with frequency or not as suggested by Jorstad et al. (2006); O'Sullivan & Gabuzda (2009). We calculated the RM at each frequency ν_0 by performing a local linear fit to the data points in a $\pm$512 MHz range around ν_0. The estimated error at each frequency is obtained from the error of the fit based on the residuals. We then plotted the derivative of the polarization angle, calculated in this way, as a function of frequency. The orange stripe in the figures represent the 1σ error of the derivative.

Figure 3.3: Radio spectra using L, C and X bands and literature. Total flux density is expressed in [mJy] and the frequency in [GHz]. Blue points are the JVLA and literature data and green points are upper limits.

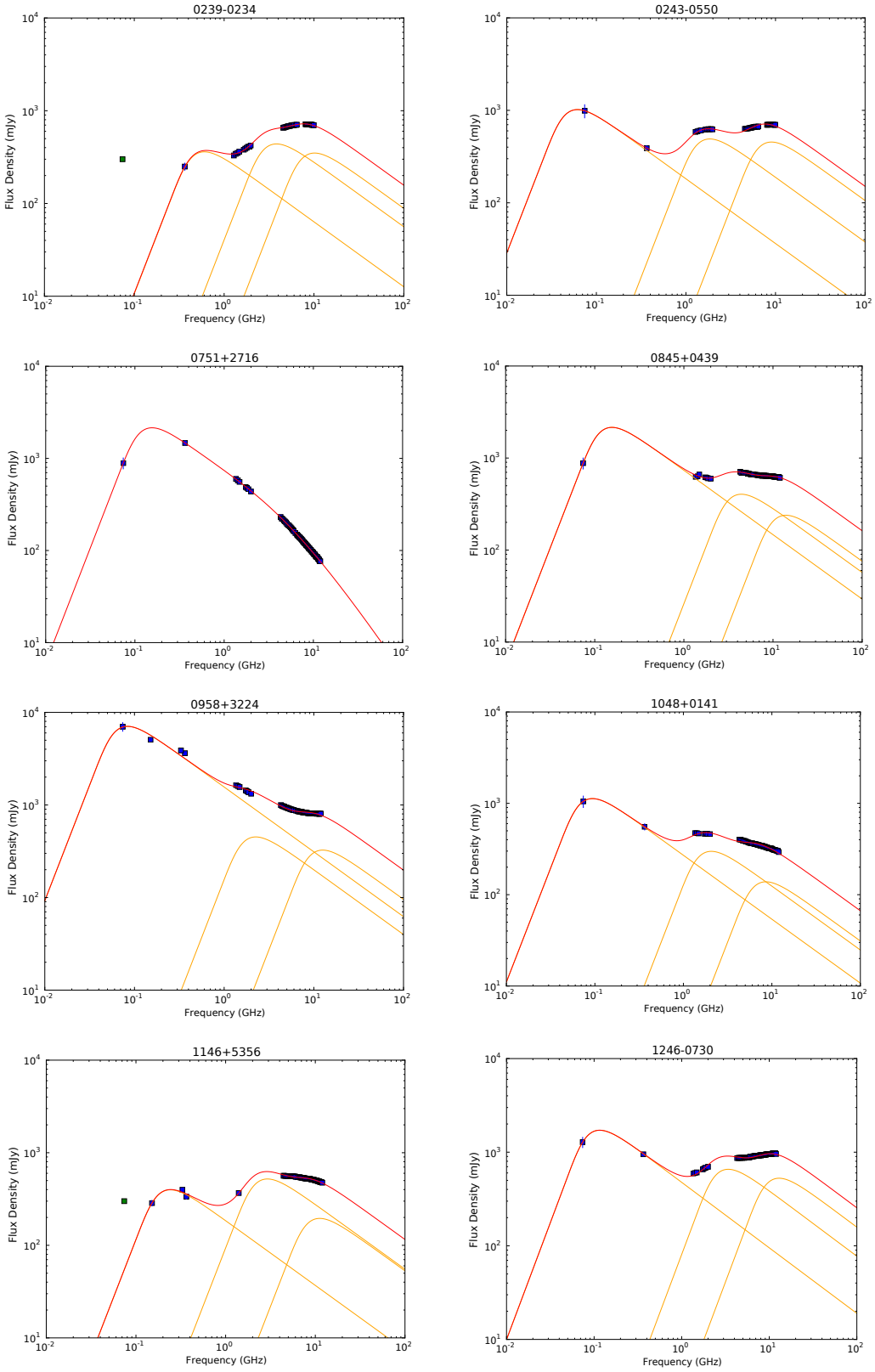

Figure 3.4: Radio spectra using L, C and X bands and literature. Continued.

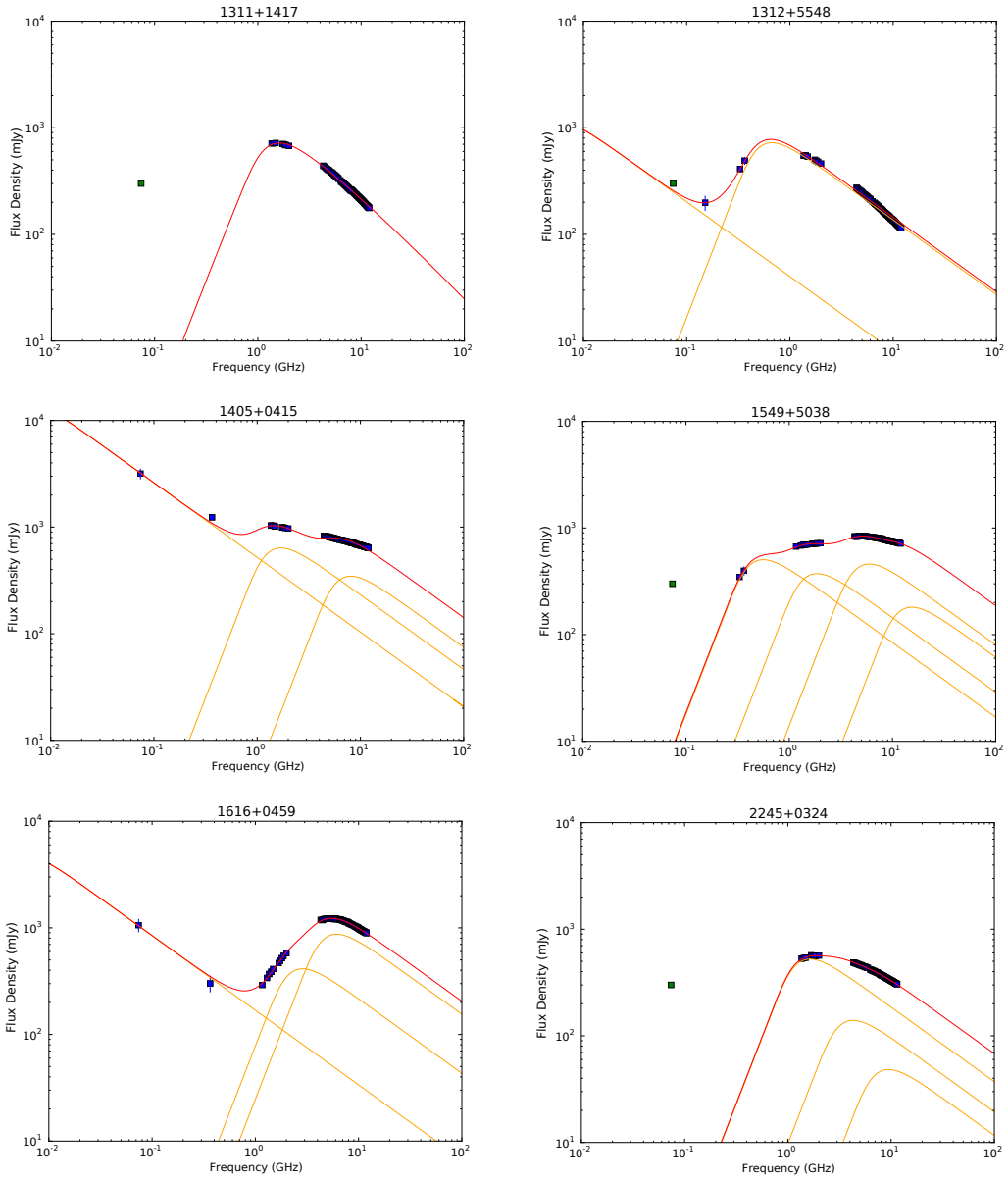

Figure 3.5: Polarization information of the sources at C and X bands. In the plots: S_{pol}: Polarized flux density [mJy]; SQ and SU: Stokes parameters Q and U [mJy]; fp: fractional polarization; χ: polarization angle [deg]

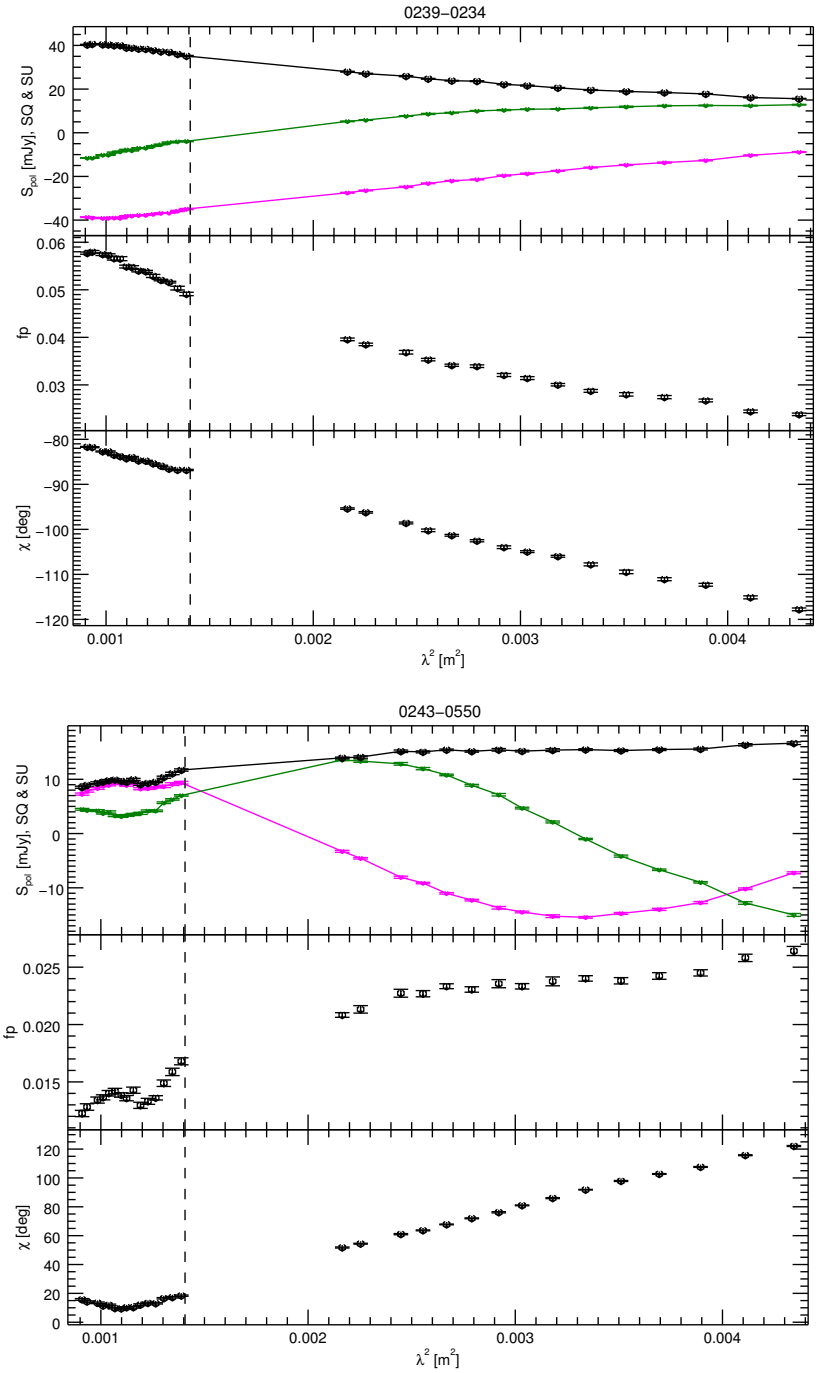

Figure 3.6: Polarization information of the sources at C and X bands. Continued.

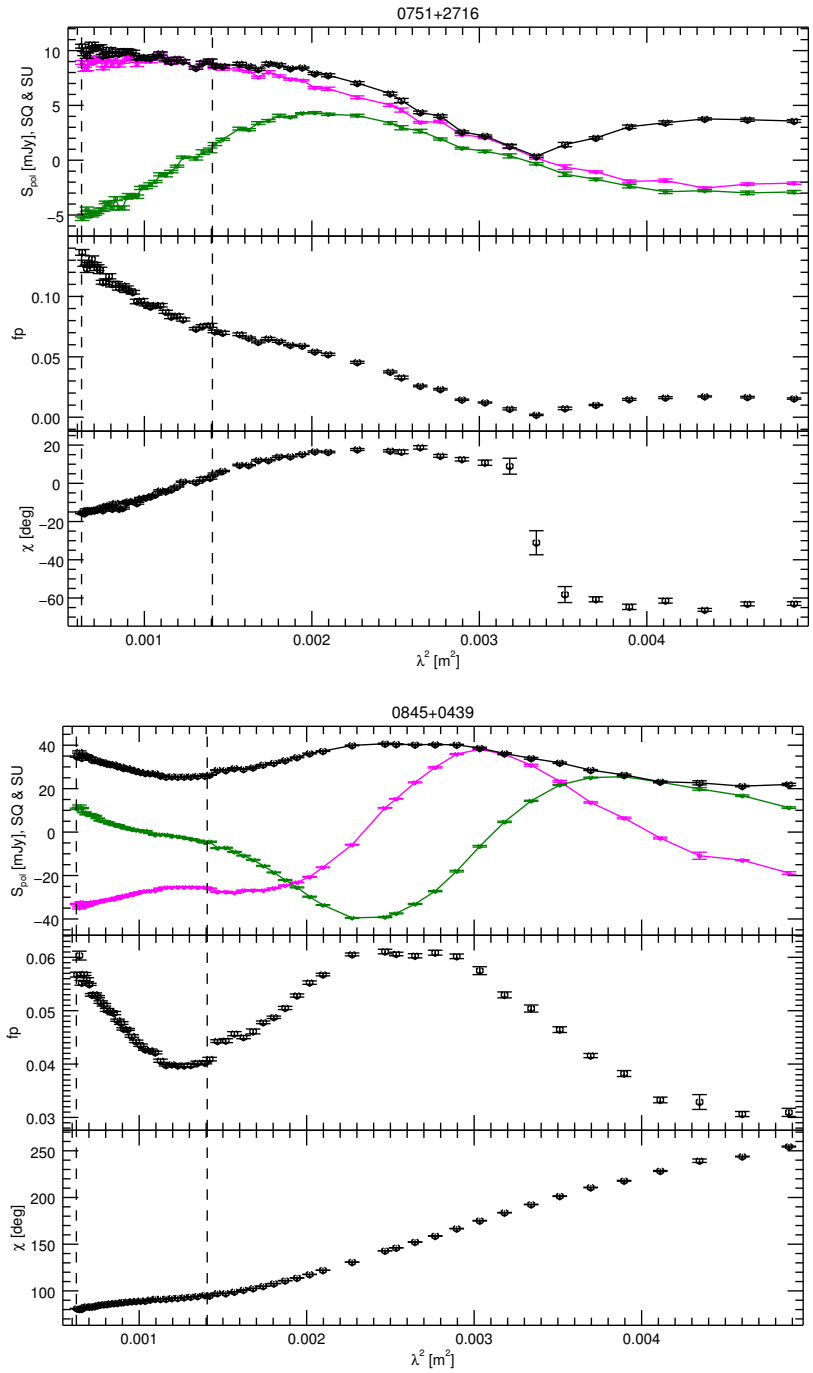

Figure 3.7: Polarization information of the sources at C and X bands. Continued.

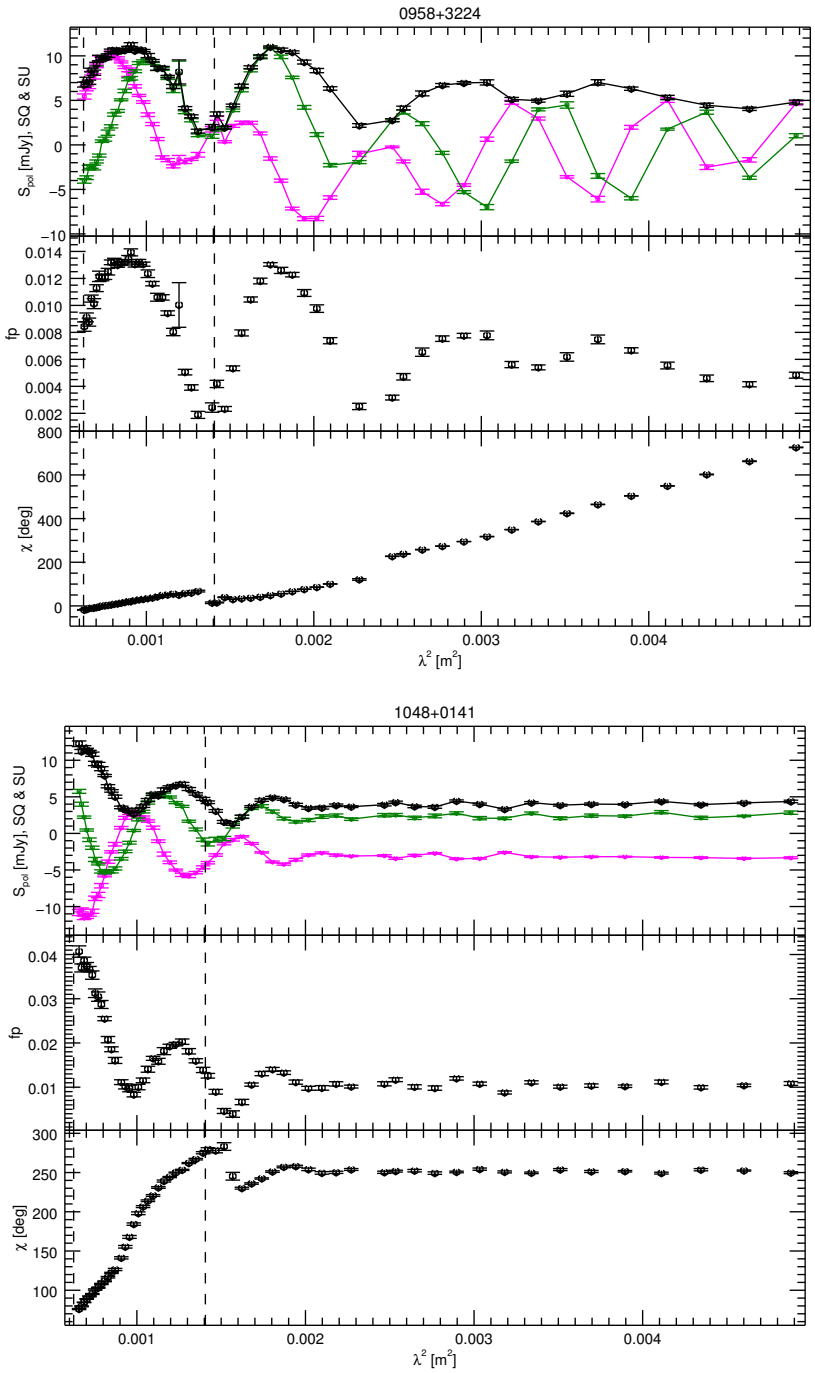

Figure 3.8: Polarization information of the sources at C and X bands. Continued.

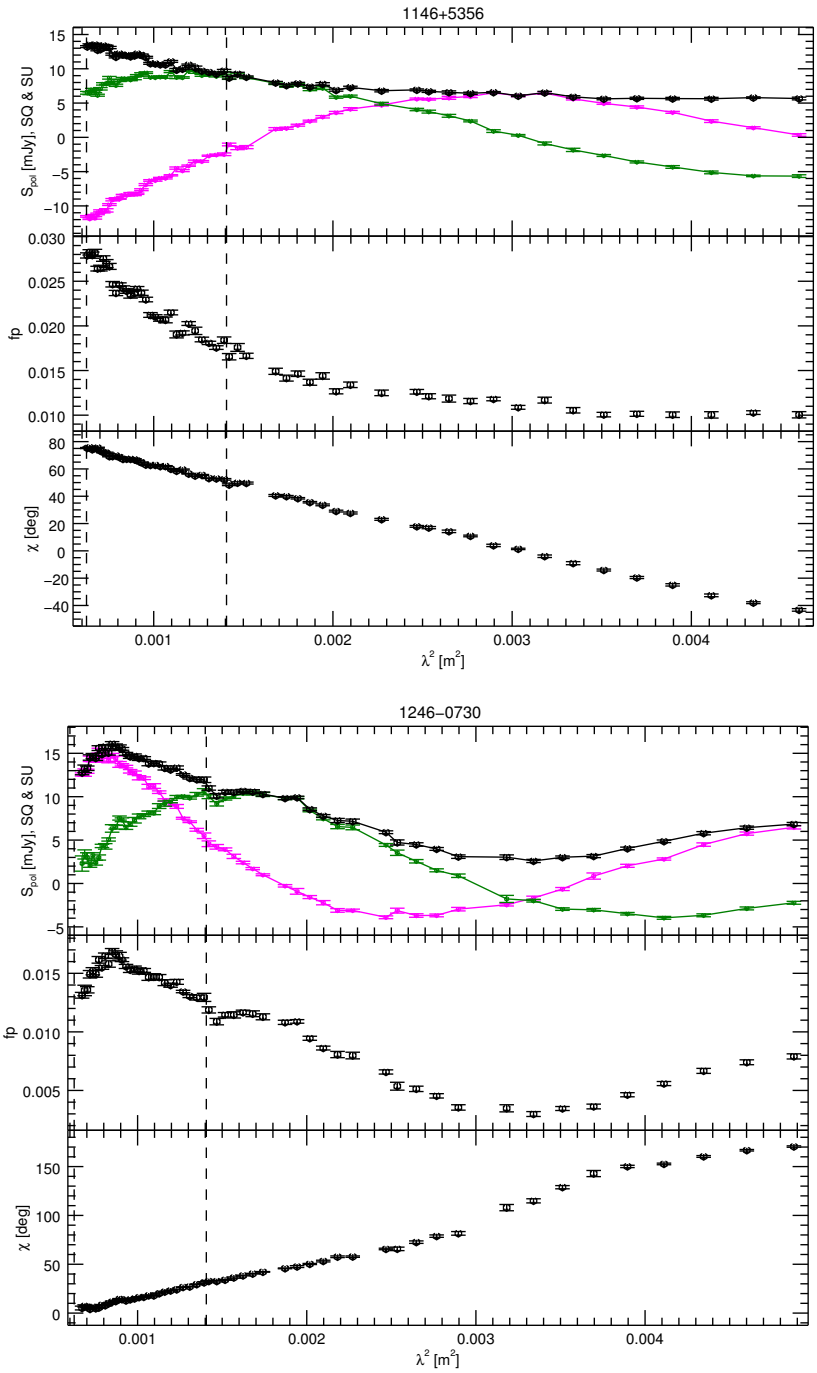

Figure 3.9: Polarization information of the sources at C and X bands. Continued.

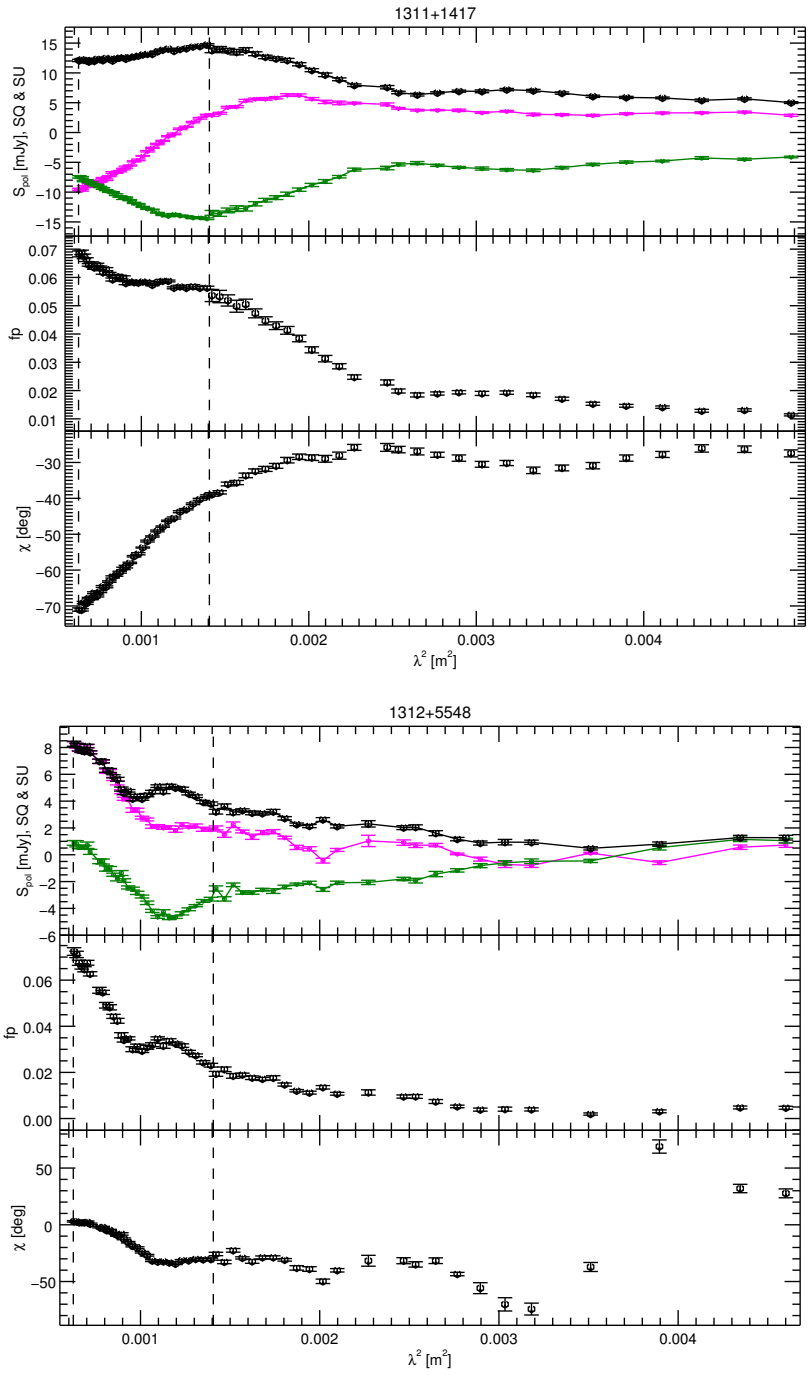

Figure 3.10: Polarization information of the sources at C and X bands. Continued.

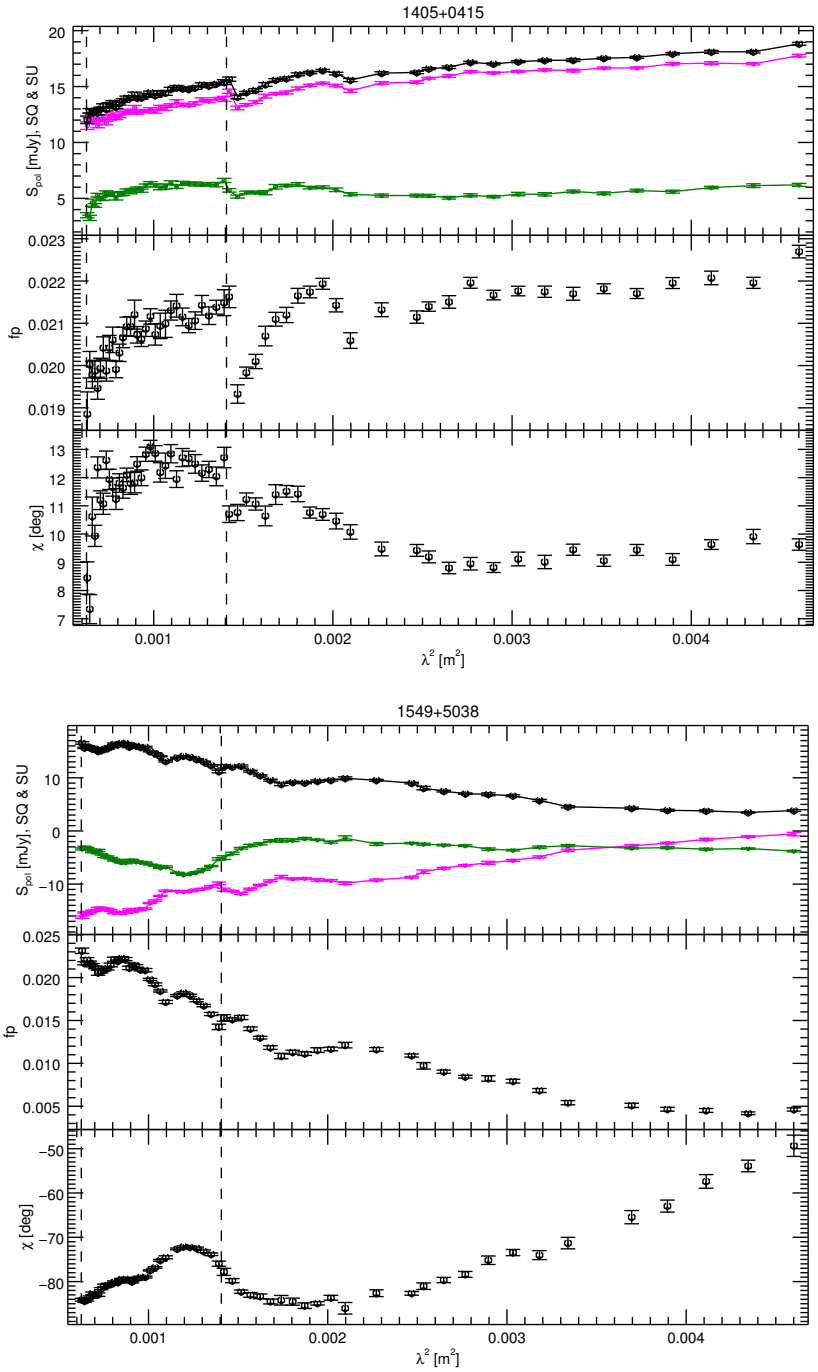

Figure 3.11: Polarization information of the sources at C and X bands. Continued.

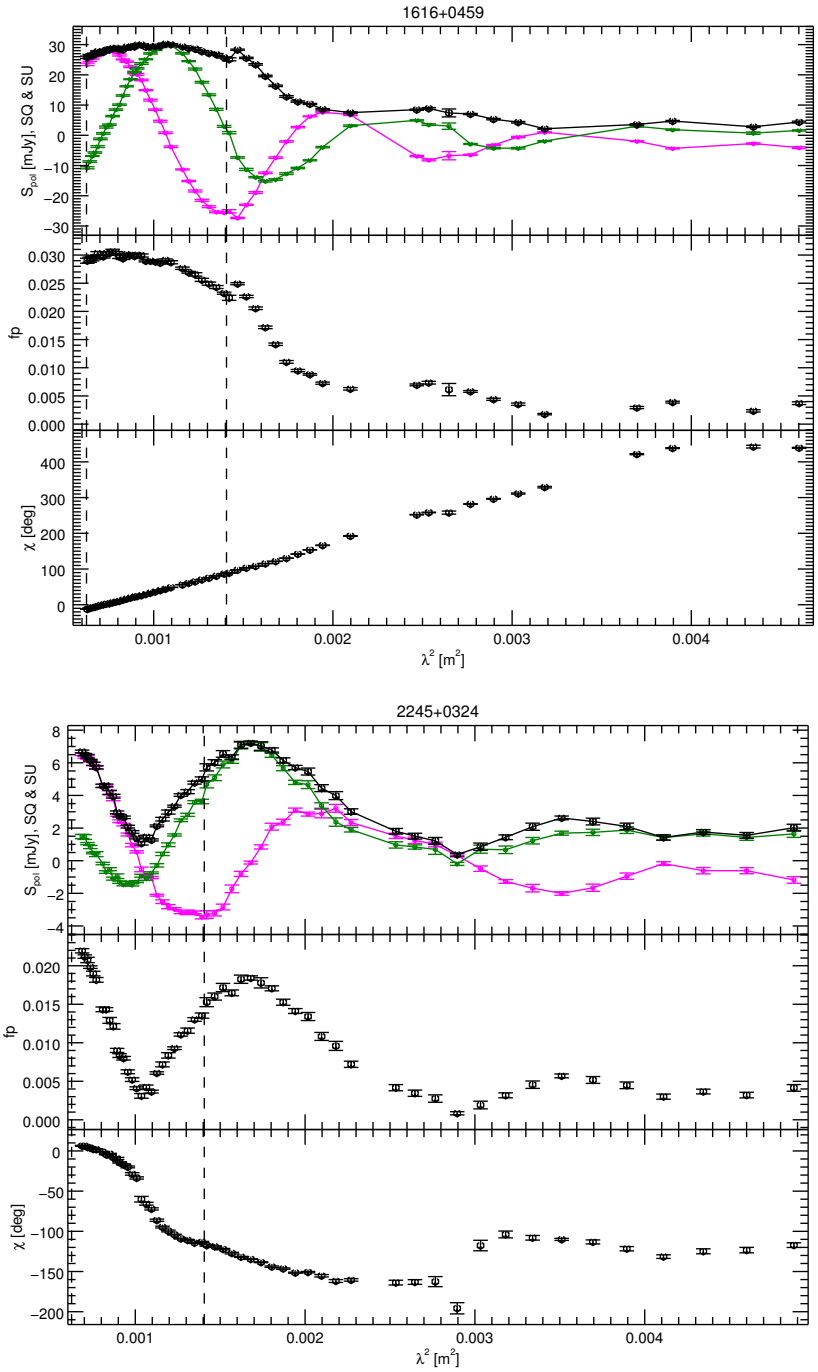

Figure 3.12: RM with frequency behaviour at C and X bands.

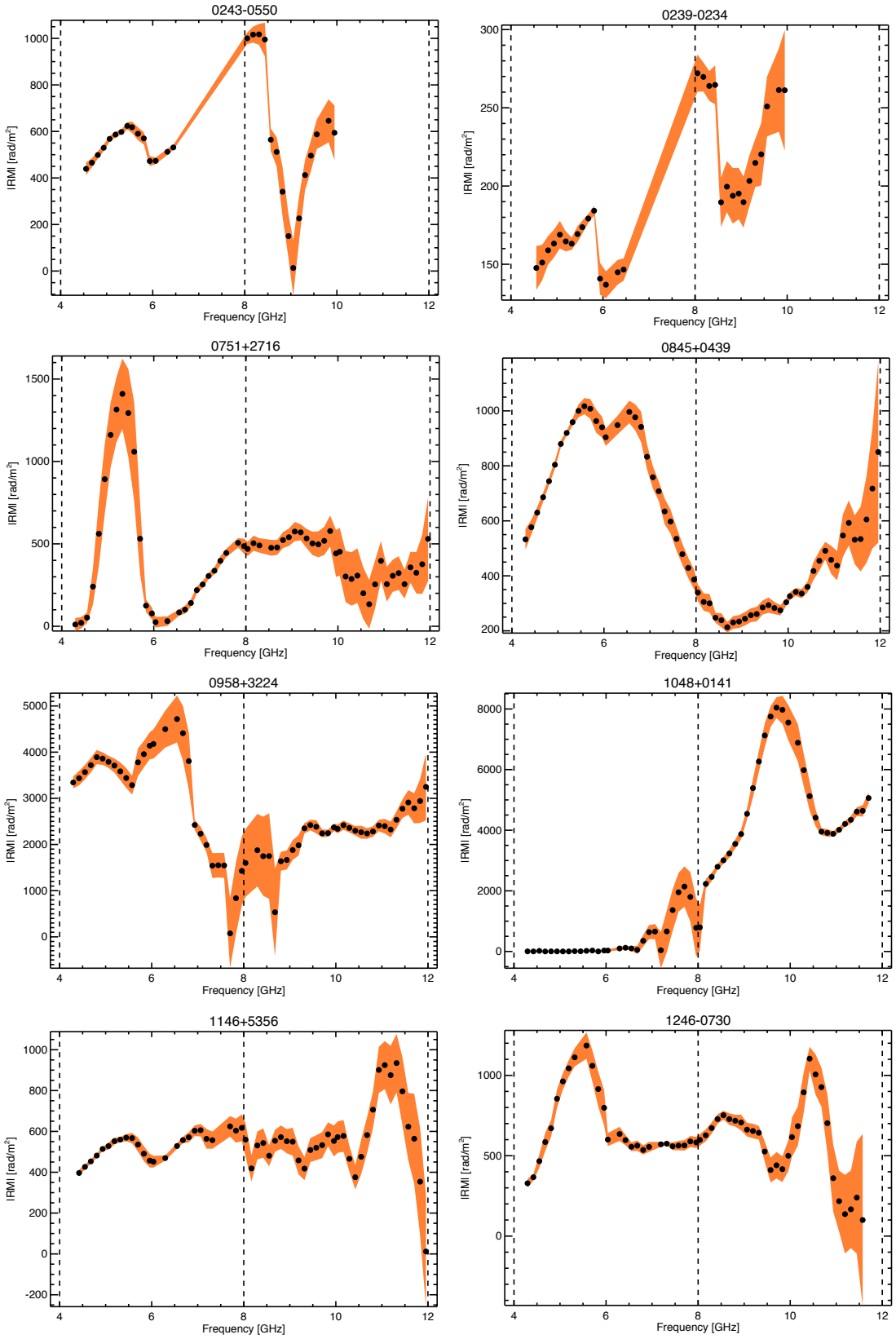

Figure 3.13: RM with frequency behaviour at C and X bands. Continued.

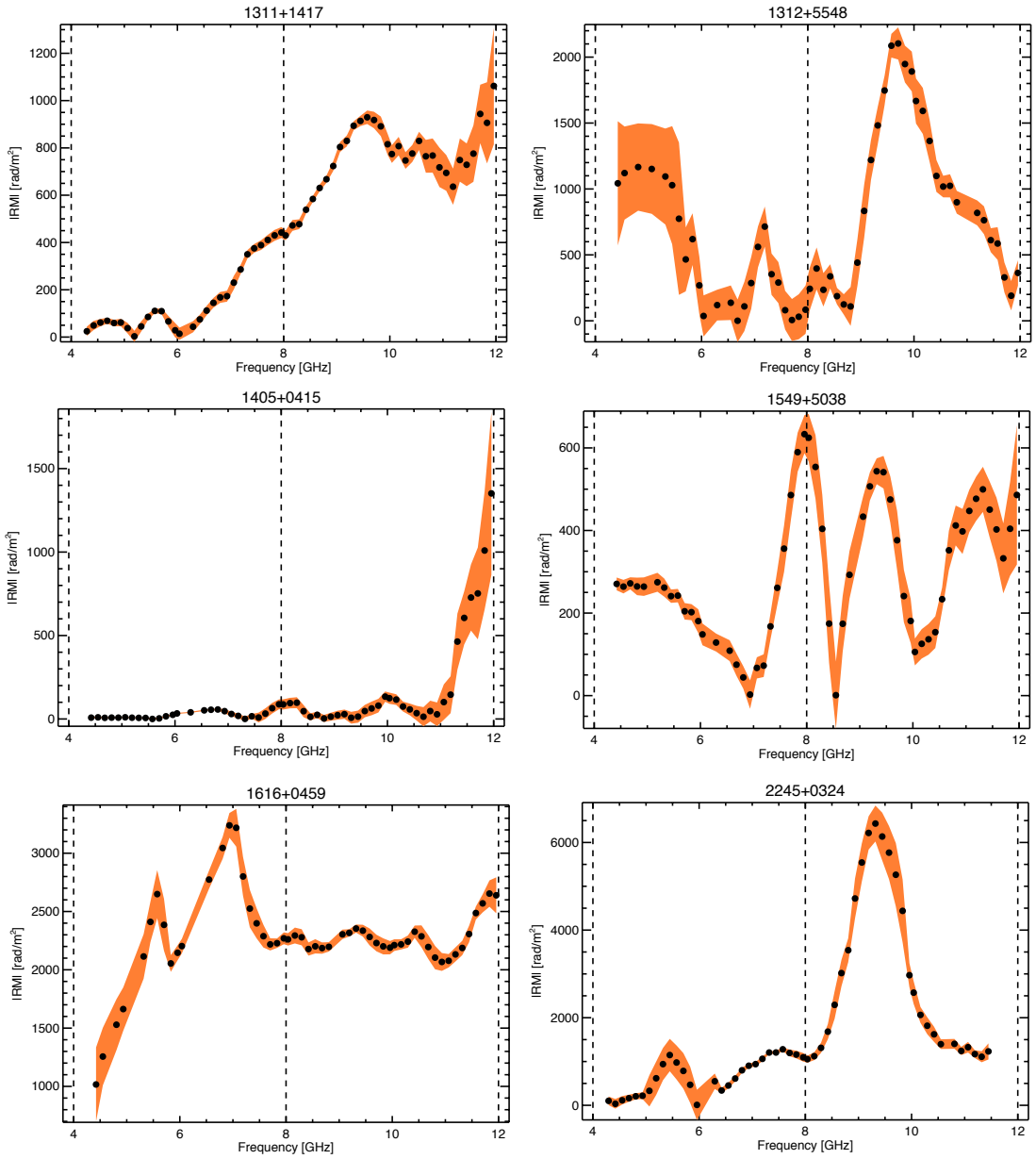

Table 3.3: Parameters of the model-fit of the sources.

SourceName	Model	fp_1 [%]	$\chi_{0,1}$ [deg]	fp_2 [%]	$\chi_{0,2}$ [deg]	fp_3 [%]	$\chi_{0,3}$ [deg]	RM_1 [rad/m^2]	RM_2 [rad/m^2]	RM_3 [rad/m^2]	σ_{RM1} [rad/m^2]	σ_{RM2} [rad/m^2]	χ^2
0239–0234	DB	100 ± 4*10^4	100 ± 640	100 ± 4*10^4	-11.0 ± 700	–	–	-360 ± 2*10^3	-305 ± 22*10^3	–	–	–	0.8
0243–0550	DED	2.3 ± 0.1	-22 ± 2	1.7 ± 0.3	5 ± 10	–	–	600 ± 10	1650 ± 110	–	0.01 ± 45*10^4	460 ± 50	2.0
0751+2716	DB	8.4 ± 0.1	-18.7 ± 1.4	3.0 ± 0.2	167 ± 5	–	–	710 ± 20	-320 ± 50	–	–	–	16
0845+0439	DED	6.5 ± 0.1	39 ± 1	2.7 ± 0.1	-110.8 ± 1.2	–	–	780 ± 10	1660 ± 12	–	130 ± 5	200 ± 10	1.5
0958+3224	T	0.5 ± 0.02	-174 ± 2	0.4 ± 0.1	-30 ± 10	0.3 ± 0.1	-30 ± 10	3900 ± 14	740 ± 50	1110 ± 50	–	–	10
1048+0141	DED	0.98 ± 0.02	76 ± 1	3.6 ± 0.1	-112.5 ± 1.3	–	–	-23 ± 10	5100 ± 24	–	0.04 ± 104*10^4	590 ± 10	1.9
1146+5356	DED	1.36 ± 0.05	90 ± 1	1.9 ± 0.1	-84.1 ± 1.8	–	–	-513 ± 10	-500 ± 50	–	100 ± 10	620 ± 30	0.7
1246-0730	DED	0.6 ± 0.4	110 ± 50	2.2 ± 0.6	170 ± 10	–	–	300 ± 140	500 ± 50	–	0.04 ± 92*10^3	230 ± 60	3.9
	DB	0.7 ± 0.1	96 ± 5	2.3 ± 0.1	-7.7 ± 1.4	–	–	380 ± 60	840 ± 20	–	–	–	5.3
1311+1417	ID	7.4 ± 0.3	105 ± 1	– ± –	– ± –	–	–	1720 ± 50	– ± –	–	200 ± 60	–	15
	DB	4.4 ± 0.3	108 ± 2	6.0 ± 1.0	-7.0 ± 7.5	–	–	720 ± 20	-2760 ± 80	–	–	–	23
1312+5548	DB	2.0 ± 0.2	180 ± 2	3.4 ± 0.4	51.5 ± 2.8	–	–	-774 ± 32	-2030 ± 40	–	–	–	14
	DED	1.3 ± 0.3	-20 ± 10	8.4 ± 2.0	50 ± 10	–	–	-120 ± 60	-1100 ± 200	–	200 ± 30	800 ± 70	12
1405+0415	S	2.09 ± 0.02	11.7 ± 0.3	– ± –	– ± –	–	–	-9 ± 2	– ± –	–	–	–	1.2
	D	1.4 ± 2.0	-160 ± 20	1 ± 2	-5.8 ± 34.4	–	–	-50 ± 60	40 ± 160	–	–	–	1.1
1549+5038	DED	1.7 ± 0.1	76 ± 4	1.6 ± 0.3	-104.4 ± 6.0	–	–	175 ± 21	960 ± 110	–	200 ± 10	480 ± 50	3.6
	IED	0.6 ± 0.1	180 ± 40	3.8 ± 0.1	-99.6 ± 1.4	–	–	602 ± 56	2070 ± 150	–	160 ± 20	560 ± 30	3.7
1616+0459	DED	1.4 ± 0.4	170 ± 70	5.2 ± 1.1	-97.6 ± 15.6	–	–	2060 ± 290	2200 ± 30	–	160 ± 1*10^{-7}	380 ± 70	39
2245+0324	DID	5.3 ± 0.4	134 ± 2	11.0 ± 0.4	51.4 ± 1.3	–	–	-2780 ± 30	-4034 ± 112	–	180 ± 10	560 ± 20	4.2

NOTE:
S: Single model; D: Double model; T: Triple model; DB: Double Burn model; DED: Double External Dispersion model; ID: Internal Dispersion model; DID: Double Internal Dispersion; IED: Internal External Dispersion.
The sources with a good reduced χ^2 value are marked in bold face.

In Figs. 3.14–3.23 and in Tab. 3.3 we report the results of the modeling of the polarization parameters as explained in Sec. 3.3. Our modeling approach only could obtain a reasonable fit for roughly half of the sample. The RM values obtained with the depolarization modeling are reported also in Tab. 3.4 with their correction to the rest frame. The source 1616+0459 shows the highest RM values in the rest frame (RF) with $RM_{1RF} \approx 36000$ rad/m^2 and $RM_{2RF} \approx 38000$ rad/m^2. In the following we describe the depolarization modeling results for each source.

- Source 0239–0234 (Fig. 3.14): for this source we could obtain reasonable fit considering a *Double Burn* model. However this model does not follow the fractional polarization data points at short wavelength. Probably to combine a *single* model, therefore adding an exponential dependence, could help to better follow the data.

Figure 3.14: Depolarization model for the source 0239–0234: Double Burn model

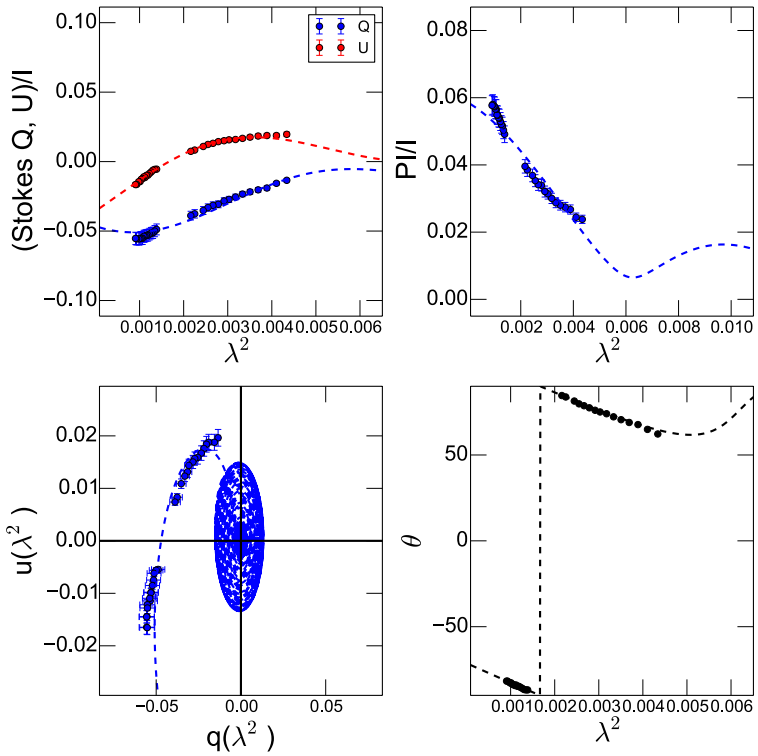

- Source 0243–0550 (Fig. 3.15): for this source a *Double External Dispersion* model is the best fit to the data. A repolarization trend is visible in fractional polarization and is probably due to ordering of magnetic field within the source. However, this model cannot well describe the data at very long wavelength where the polarized signal seems to increase more. Probably an

addition of a third external Faraday screen (for the very long wavelength data) could help describing the polarization information.

Figure 3.15: Depolarization model for the source 0243–0550: Double External Dispersion model

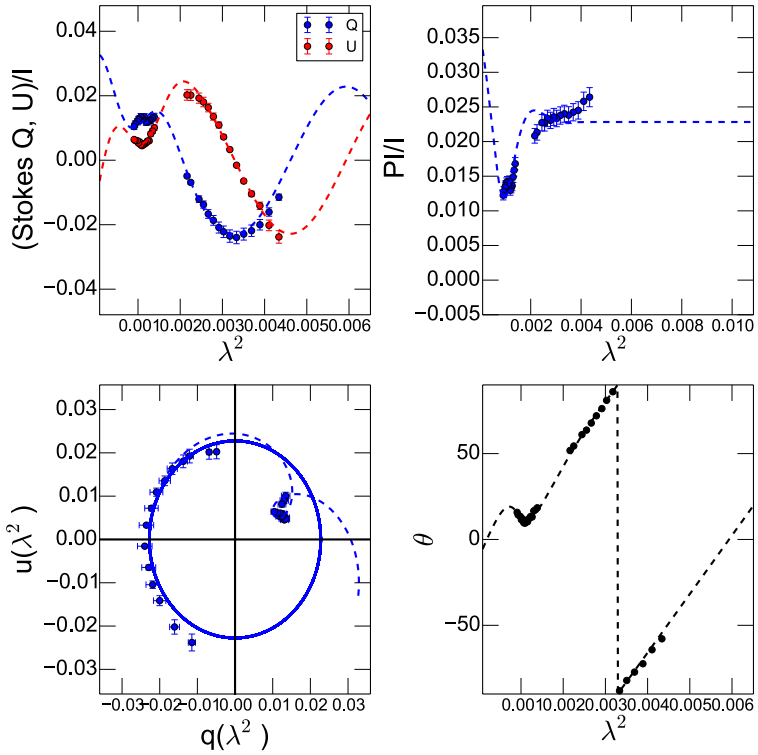

- Source 0751+2716 (Fig. 3.16): for this source a *Double Burn* model gives only an indication on the trend of the data. Indeed, the model does not follow the short wavelength data points. It seems to trace quite well the trend of the fractional polarization but is not tracing at all the polarized angle at longer wavelength.

- Source 0845+0439 (Fig. 3.17a): this source is very well fitted by a *Double External Dispersion* model, just few fractional polarization data points at long wavelength are not well represented by the fit.

- Source 0958+3224 (Fig. 3.17b): for this source we found a *triple* model to be the best model to fit the data. Note in Fig. 3.17*b* the large rotation of the Stokes parameters Q and U.

- Source 1048+0141 (Fig. 3.18a): a *Double External Dispersion* fit quite well the data. At long wavelength the Stokes parameters Q and U are

Figure 3.16: Depolarization model for the source 0751+2716: Double Burn model

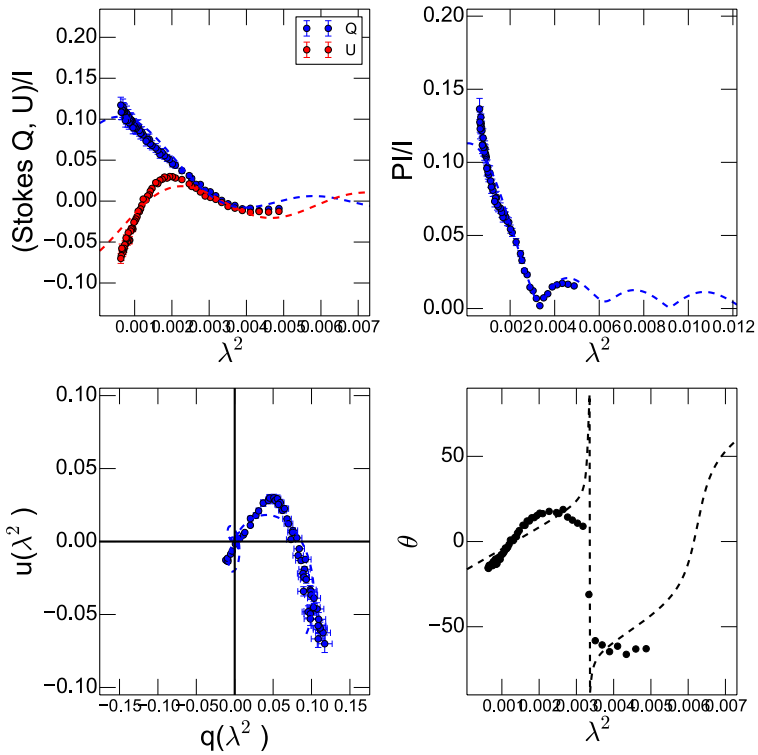

not crossing each other with the result of a constant fractional polarization and polarization angle, while at short wavelength the parameters cross very frequently. Moreover, the blue and the red dashed lines of the modeling are showing that at higher frequencies the Stokes parameters Q and U continue crossing each other, with the result of a possible increase of the RM value towards higher frequency, as indicated in Fig. 3.12 (for the 1048+0141 source).

- Source 1146+5356 (Fig. 3.18b): this source is well represented by a *Double External Dispersion* model, with a good description of both the shorter and longer data points. The only comment is that probably the model decreases too rapidly at long wavelength.

- Source 1246-0730 (Fig. 3.19): the trend of the polarization values are not well defined by a single model. Two models, a *Double Burn* and a *Double External Dispersion* models are trying to represent the data with no good success for the fractional polarization, while the trend of the polarization angle is quite good for both the models. The very first and last data points of the fractional polarization at short and long wavelength are not represented by these models. These points at both the extremities are

experiencing a rude change of values which are difficult to be followed. We tried the combination of internal and external Faraday dispersion model, but it does not fit well the data.

- Source 1311+1417 (Fig. 3.21a): this is a complex target. An *Internal Dispersion* model give some good indications on the depolarization trend that the source is experiencing. However, at short wavelength the fractional polarization seems to have another feature that is not described by this model. Moreover, the Stokes parameters Q and U are not crossing each other anymore with a flattening of the polarization angle that is difficult to represent by the model. However, as for the case of the source 1048+0141, the Stokes Q and U are going to cross at least twice at higher frequency with the result of an increase of the RM, as suggested in Fig. 3.13 (for this source).

- Source 1312+5548 (Fig. 3.20): this is a very complex target. A *Double Burn* and a *Double External Dispersion* models give some indications on the depolarization trend. However, the *Double Burn* seems to fit better the polarization angle but it does not fit the fractional polarization at short wavelength, the *Double External Dispersion* does instead. The combination of these models do not improve the quality of the fit.

- Source 1405+0415 (Fig. 3.21b): this source could be the case for which the application of nπ ambiguity to the data brings to a misleading high RM detection or the source could be variable. From single dish observations we determined a very high RM value (thousands of rad/m^2) by adding nπ ambiguity to the polarized angle (Section 2.6.4). From our JVLA wide band polarimetric observations it turns out that this source seems to have mainly a low RM value, although from the RM vs frequency plot (Fig. 3.13), an increase of the RM towards high frequency, i.e. closer to the radio core, seems to be present. Here, indeed, a *Double* model, seems to be the best model to follow the data and that can also detect the high frequency-high RM value ($\sim$400 rad/^{2}) component.

- Source 1549+5038 (Fig. 3.22): this is a complex target for which a *Double External Dispersion* and the *Internal External Dispersion* models give us indications on the depolarization trend, with a preferentially tendency towards the combination of internal and external Faraday dispersion models. Indeed, the latter follows better the polarization angle behavior.

- Source 1616+0459 (Fig. 3.23a): this source is quite well represented by a *Double External Dispersion* model, although longer wavelength do not follow the simple decrease of the model. The contribution from an internal

Faraday dispersion might be helpful, although the combination of a single internal and External Faraday dispersion model does not seem to help. A more complicated model is needed to represent the long wavelength data points.

- Source 2245+0324 (Fig. 3.23b): this source seems to be quite well fitted by a *Double Internal Dispersion* model, although few data points at long wavelength are not well fitted.

Table 3.4: RM of the modeling corrected in the rest frame (subscript RF).

Source	Model	z	RM_{1RF} [rad/m^2]	RM_{2RF} [rad/m^2]	RM_{3RF} [rad/m^2]
0239–0234	DB	1.1	-1570 ± 10*10^3	-1530 ± 11*10^3	–
0243–0550	DED	1.8	4680 ± 80	12900 ± 870	–
0751+2716	DB	3.2	12500 ± 290	-5570 ± 890	–
0845+0439	DED	0.3	1270 ± 10	2720 ± 20	–
0958+3224	T	0.5	8770 ± 30	1670 ± 110	2500 ± 120
1048+0141	DED	0.7	-70 ± 20	14740 ± 70	–
1146+5356	DED	2.2	-5250 ± 60	-5130 ± 500	–
1246-0730	DED	1.2	1420 ± 660	2410 ± 250	–
	DB		1850 ± 270	4070 ± 90	–
1311+1417	ID	1.9	14470 ± 380	–	–
	DB		6080 ± 190	-23250 ± 650	–
1312+5548	DB	1.5	-4840 ± 200	-12690 ± 204	–
	DED		-770 ± 380	-6690 ± 1180	–
1405+0415	S	3.2	-170 ± 40	–	–
	D		-840 ± 1110	770 ± 2900	–
1549+5038	DED	2.2	1790 ± 210	9860 ± 1110	–
	IED		6170 ± 580	21210 ± 1520	–
1616+0459	DED	3.2	36420 ± 5060	38750 ± 560	–
2245+0324	DID	1.3	-14730 ± 140	-21340 ± 590	–

NOTE: S: Single model; D: Double model; T: Triple model; DB: Double Burn model; DED: Double External Dispersion model; ID: Internal Dispersion model. For the source 1312+5548 we do not have information on the redshift; therefore, we considered the mean value of redshift of the sample.

Figure 3.17: Depolarization models for the sources 0845+0439 and 0958+3224

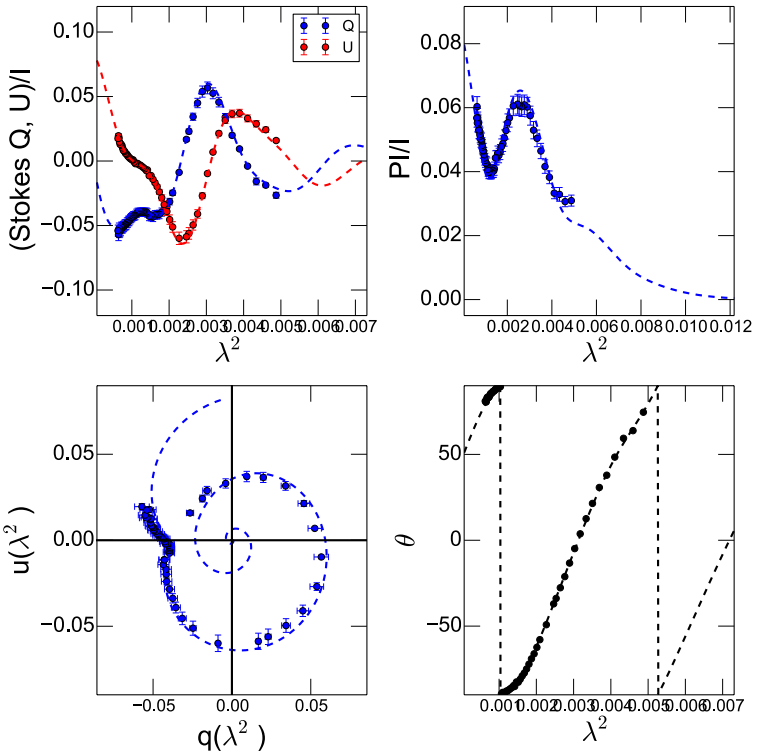

(a) 0845+0439 Double External Dispersion model

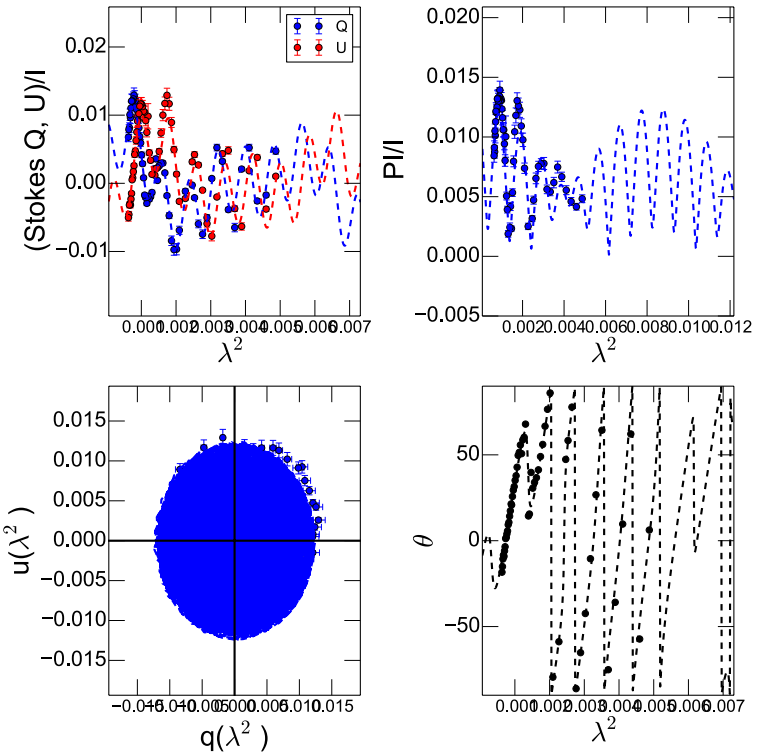

(b) 0958+3224 Triple model

Figure 3.18: Depolarization models for the sources 1048+0141 and 1146+5356.

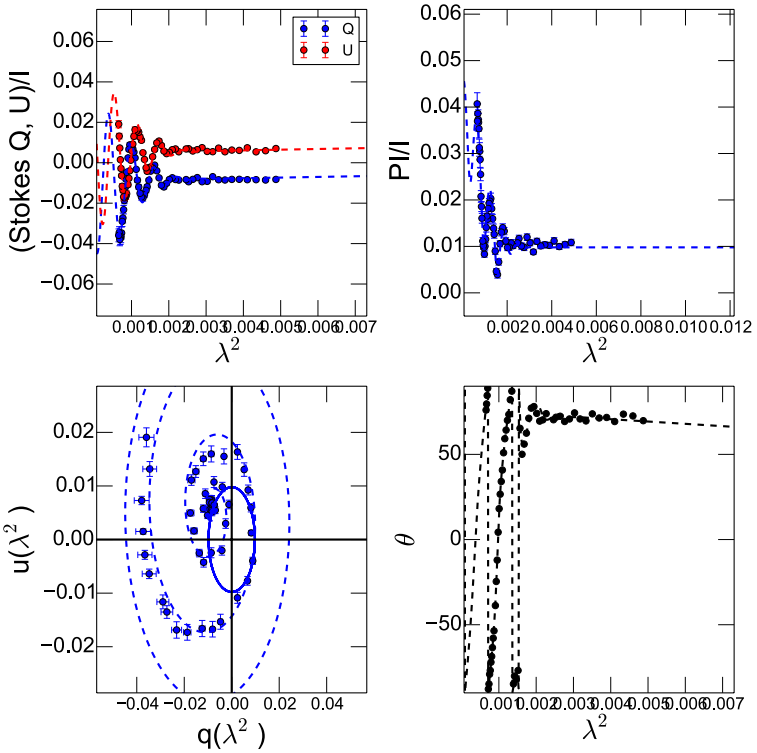

(a) 1048+0141 Double External Dispersion model

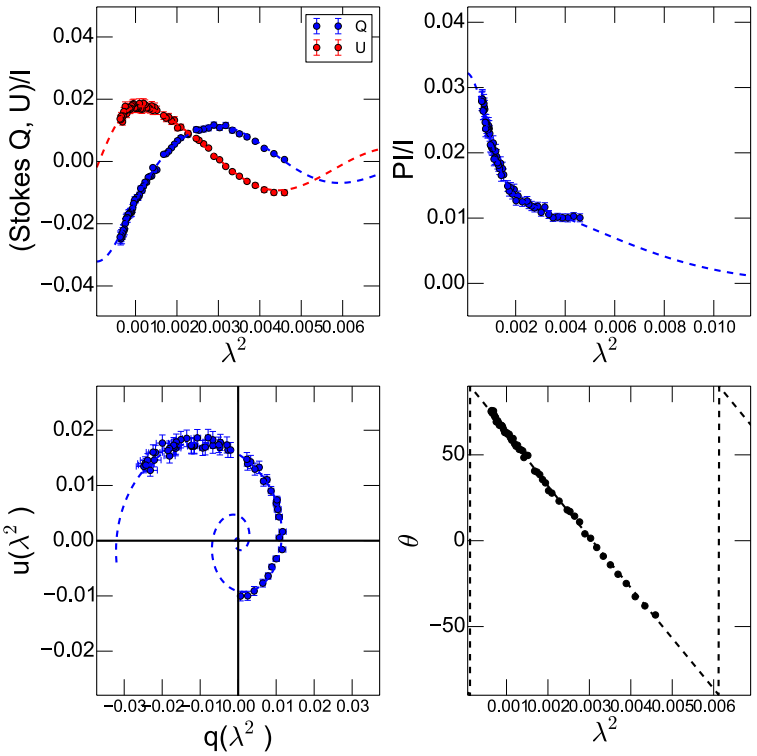

(b) 1146+5356 Double External Dispersion model

Figure 3.19: Depolarization models for the source 1246–0730

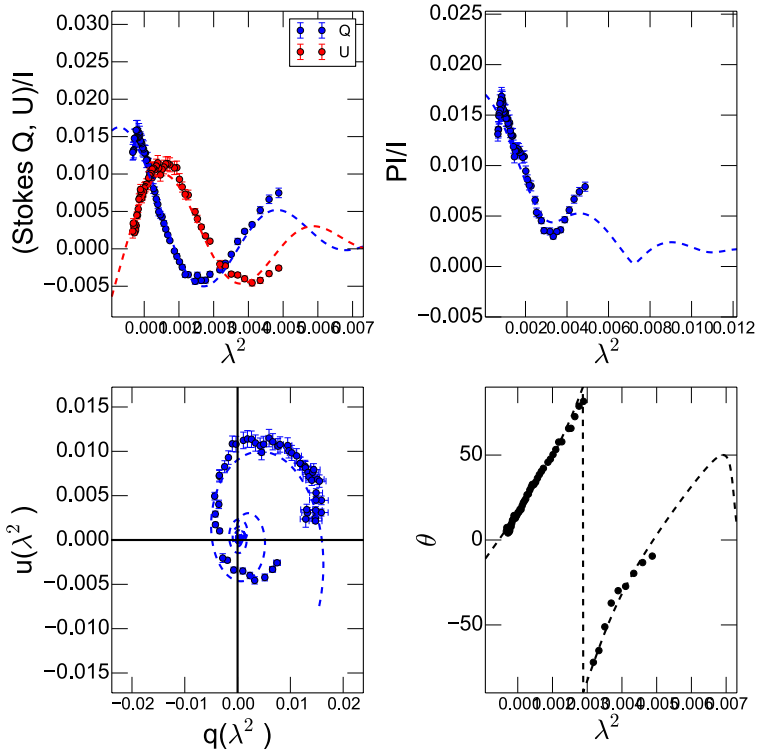

(a) 1246-0730 Double Burn model

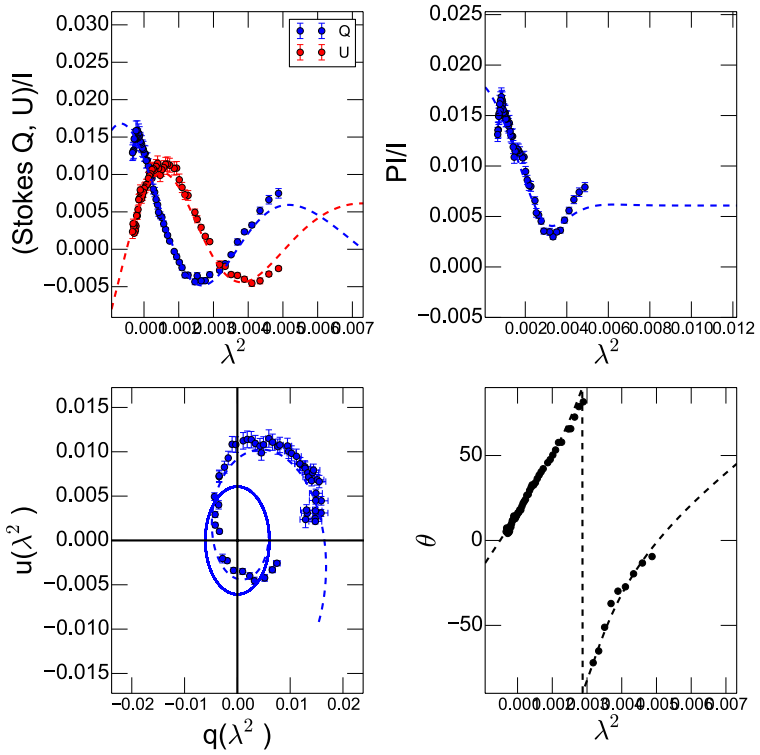

(b) 1246-0730 Double External Dispersion model

Figure 3.20: Depolarization models for the source 1312+5548

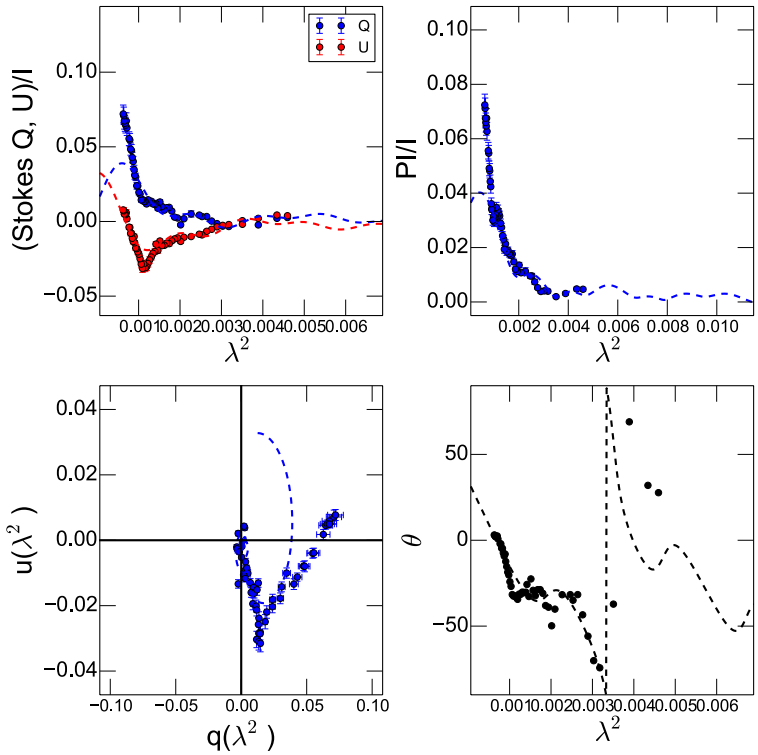

(a) 1312+5548 Double Burn model

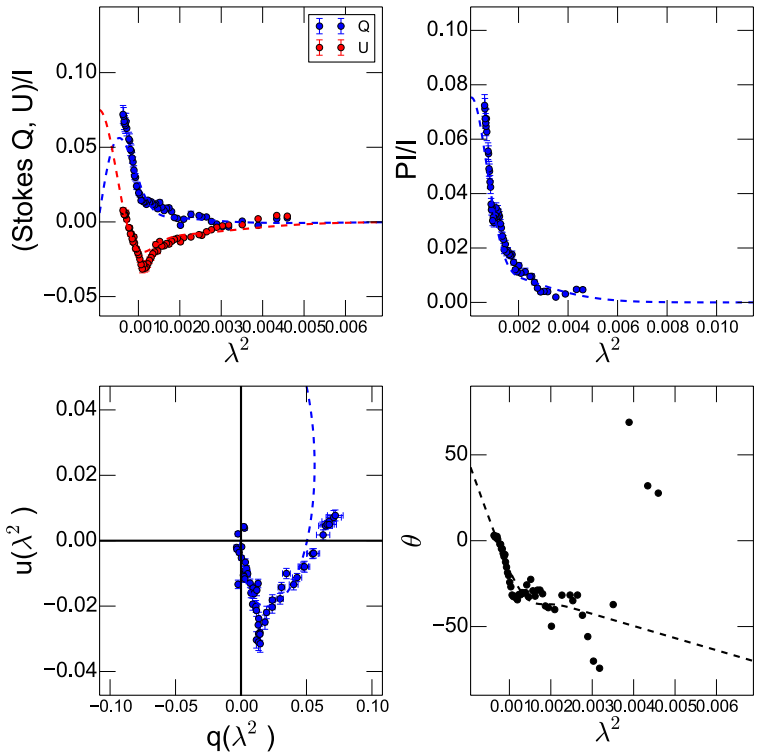

(b) 1312+5548 Double External Dispersion model

Figure 3.21: Depolarization models for the sources 1311+1417 and 1405+0415

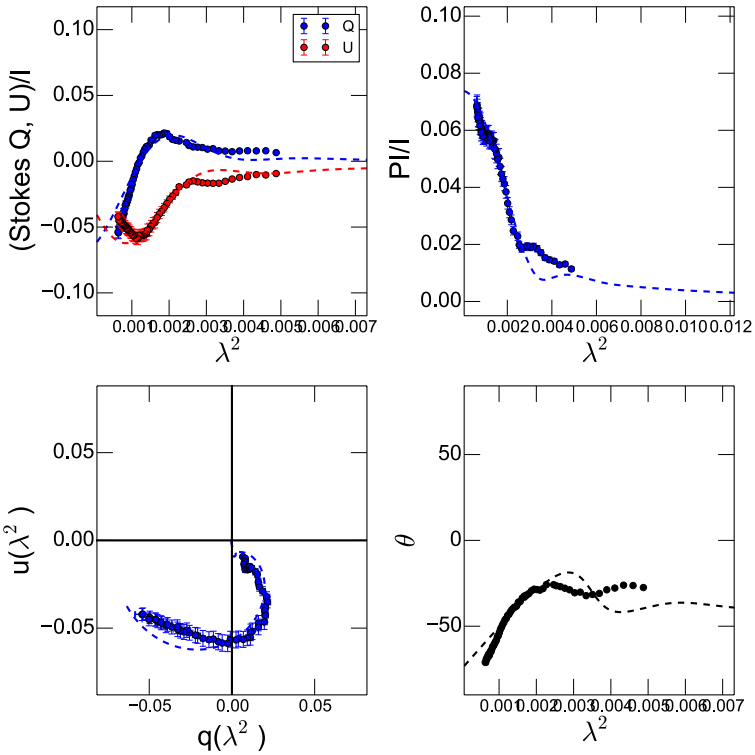

(a) Source 1311+1417 Internal Dispersion model

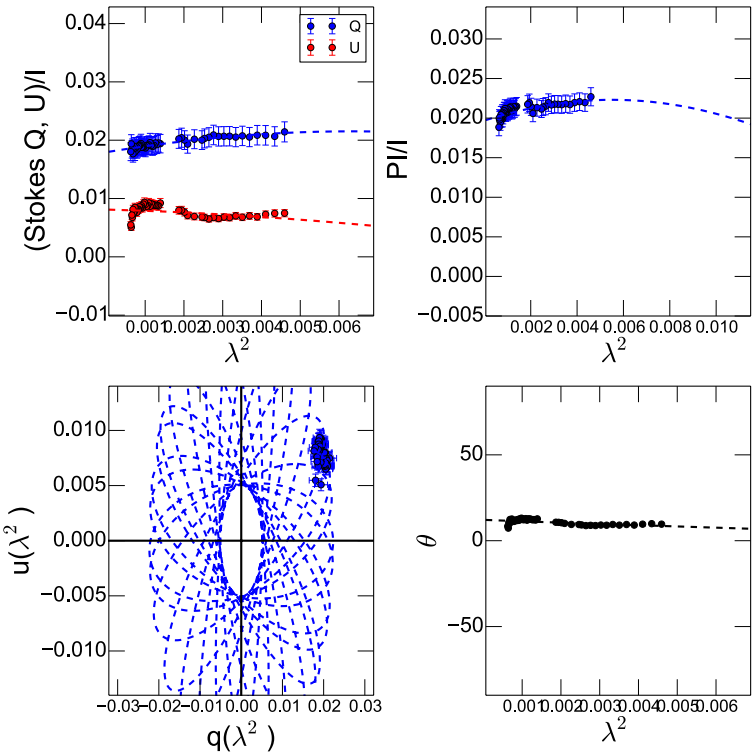

(b) Source 1405+0415 Double model

Figure 3.22: Depolarization models for the sources 1549+5038

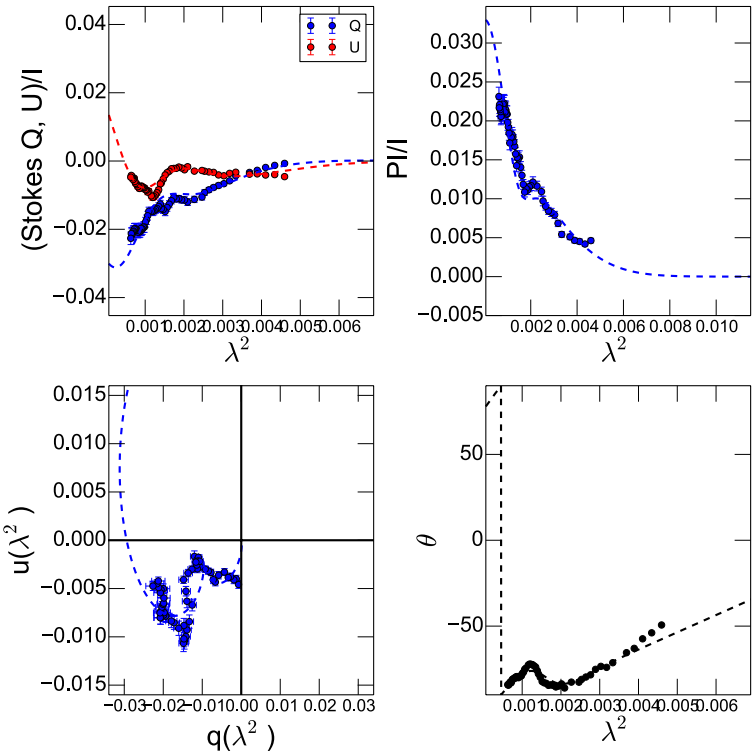

(a) 1549+5038 Double External Dispersion model

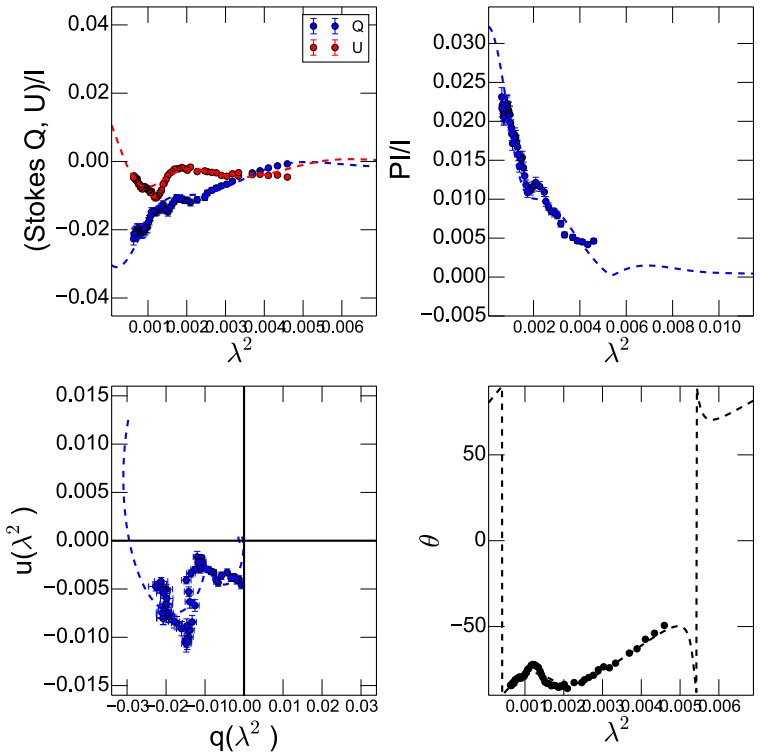

(b) 1549+5038 Double External Dispersion model

Figure 3.23: Depolarization model for the sources 1616+0459 and 2245+0324

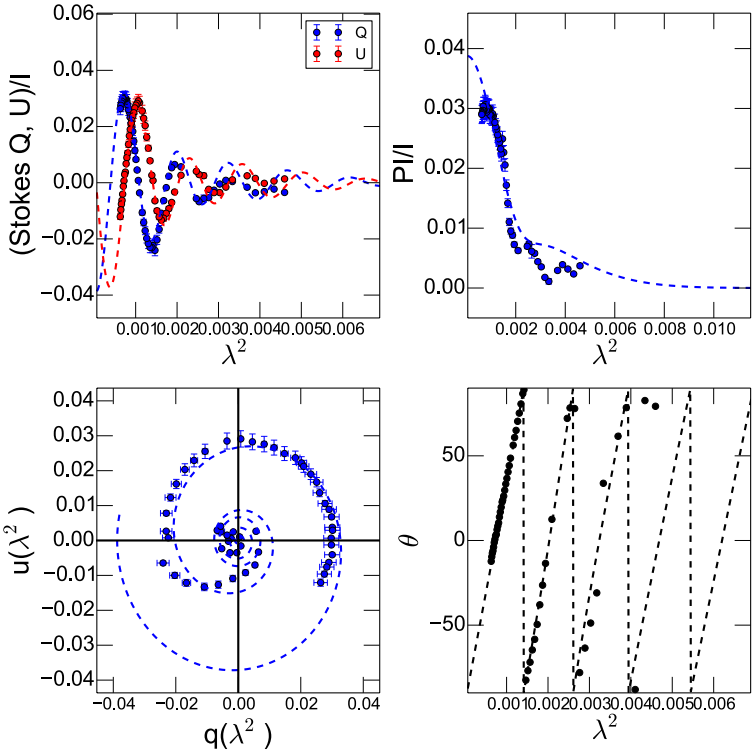

(a) 1616+0459 Double External Dispersion model

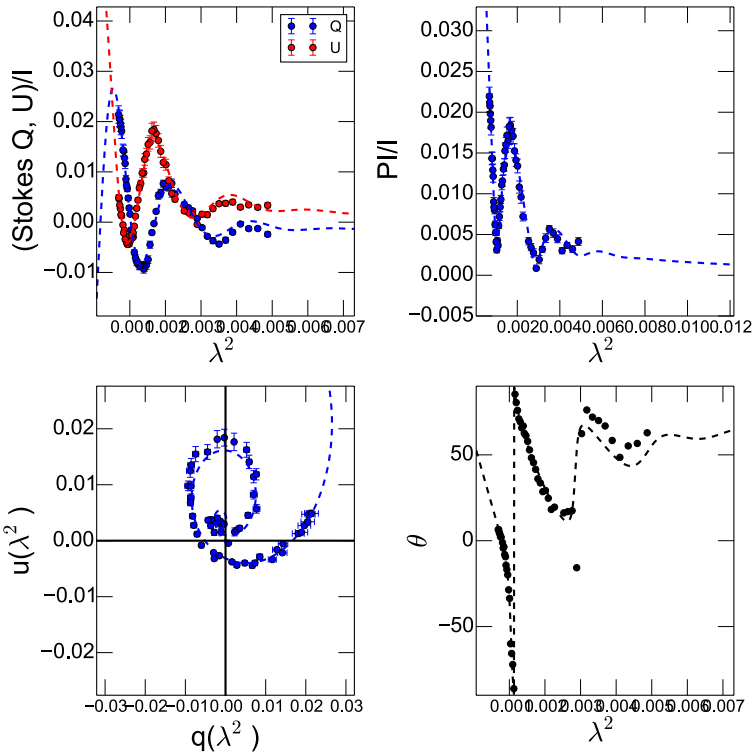

(b) 2245+0324 Double Internal model

3.5 Discussion

3.5.1 Comments on the individual sources

Here, we give first interpretations of all our observational and modeling results in the context of the AGN environment. We consider and combine all the wide-band observational results (the radio spectrum, the polarization information and the depolarization modeling results) together with higher resolution VLBI images. These VLBI images (showed in the JVLA Appendix B), are mainly VLBA (Very Long Baseline Array) images downloaded from the NRAO calibrator search tool webpage[4]. These images are not suitable for a profound analysis; they are not always recent images, but they provide a first and rough indication about the targets' morphology on pc scale. Moreover, to help in the study of the radio spectral properties of the sources we estimated the core dominance (CD) for each of the targets, by considering the ratio between the flux density at the VLBI pc scale and the flux density at the JLVA kpc scale, both at 8.6 GHz. The core dominance values together with the radio spectra shape of the sources, give us a hint to determine the objects' type. The values are reported in Tab. 3.5.

- Source 0239-0234 -
This AGN shows a radio spectrum rising at low frequencies and flat at high frequencies. We can fit this spectrum with three synchrotron components (see Fig. 3.3). Its polarization percentage decreases from 6% at X band to 3% at C band and it shows small deviation from the linear fit in the determination of the RM value (Fig. 3.5). The depolarization model that better fit the polarization behavior is a *Double Burn* (Fig. 3.14), which consists on two components that are synchrotron emitting and Faraday rotating at the same time in the presence of a regular magnetic field.

Higher angular resolution VLBA images at S and X bands show a compact bright source with a weak extended emission (see images in Appendix B.1). VLBA images at K band (22 GHz, HPBW $<$ 1mas) and Q band (43 GHz, HPBW $<$ 1mas), still show a strong and compact radio source (Charlot et al. (2010)). The core dominance of this source (Tab. 3.5) and the decrease in flux density between short and long VLBA baselines (see Appendix B.1) suggest that a possible radio emission from an extended component is lost as we observe smaller scales.

All these results suggest the presence of two emission components: one weak and slightly extended component, probably low density plasma, and a more compact and bright component, probably high density plasma nearer to the central engine. It is reasonable to associate each emission component with each

[4]http://www.vlba.nrao.edu/astro/calib/

Table 3.5: Core Dominance (CD) values at 8.6 GHz. S_{JVLA}: is the JVLA total flux density at 8.6 GHz; S_{VLBA}: is the peak flux density in the 8.6 GHz VLBA map; CD: it the core dominance value, the ratio between the JVLA flux density and the VLBA flux density at 8.6 GHz

Source	S_{JVLA}	S_{VLBA}	CD
0239–0234	713	458	0.6
0243–0550	698	396	0.6
0751+2716	111	–	–
0845+0439	640	103	0.2
0958+3224	817	500	0.6
1048+0141	331	125	0.4
1146+5356	523	198	0.4
1246–0730	935	747	0.8
1311+1417	246	83	0.3
1312+5548	155	–	–
1405+0415	707	507	0.7
1549+5038	774	523	0.7
1616+0459	1077	482	0.4
2245+0324	359	417	1.1

Faraday component obtained from the modeling. Thus, the component showing a $RM_1 \approx 400$ rad/m^2 is most likely associated with the low density component and that with $RM_2 \approx 850$ rad/m^2 is most likely associated with the high density compact component.

- Source 0243-0550 -

The SED of this source could be fitted with three synchrotron components: one peaking at a low frequency (∼74 MHz) and the other two peaking at higher frequencies (∼1.5 GHz and ∼10 GHz; see Fig. 3.3). On the overall, the radio spectrum at high frequency is a flat-spectrum. Its fractional polarization is increasing at longer wavelength (Fig. 3.5), suggesting a repolarization at lower frequencies. Repolarization process can be explained with the increasing of the ordering of the magnetic field with the increasing of wavelength (Sokoloff et al. (1998)), with partly coverage of the target by a rotating and depolarizing layer (Mantovani et al. (2009)) or through an helical and randomly tangled magnetic fields (Homan et al. (2002)).

We were able to fit this global trend of the fractional polarization with a *Double External Dispersion* model (Fig. 3.15). Our modeling suggests one com-

ponent with $RM_1 \simeq 570$ rad/m^2 and with a regular magnetic field ($\sigma_{RM1} \simeq 0.0001$ rad/m^2), and a second component with $RM_2 \simeq 1020$ rad/m^2 with a more disordered magnetic field ($\sigma_{RM1} \simeq 400$ rad/m^2; see Tab. 3.3). Moreover, in Fig 3.12 we note that at low frequencies the RM is indeed around 500 rad/m^2, a value near that of the external screen with an ordered magnetic field. This seems to suggest that there could be indeed an ordering of the magnetic field towards low frequency that seems to be consistent with the observed repolarization (Fig. 3.5). We also can see in the polarization information plot (Fig. 3.5) and in the depolarization modeling plot (Fig. 3.15) that the data points at short wavelength exhibit a sharp turnover: from negative at higher frequencies, to positive at lower frequencies. Another Faraday component closer to the central region than those already fitted by the model, could be responsible for this behavior.

VLBA images reveal a compact core-jet source (see image in Appendix B.2). Its core dominance value is $\sim$0.6 (Tab. 3.5) therefore, part of the flux density is lost as we observe at smaller scale. Moreover, the VLBA data also suggest extended emission which has been resolved at the highest resolution.

A possible interpretation of these results is that the source has an intermediate viewing angle towards the observer. In this case the radio emission would be coming from the relativistic jet and the external depolarization would be produced by the slower wind that contains both thermal and non-thermal electrons. Moreover, the wind could be experiencing some kind of ordering of the magnetic field from the closest to the most distant part of the radio emission.

- Source 0751+2716 -

This source has been fitted with a synchrotron component with a break (see Fig. 3.3). Its fractional polarization drops down from 15% to few % from X band to C band (Fig. 3.6). Its RM tendency at X band is quite high ($\simeq$500 rad/m^2), and at C band it seems to have no rotation of the polarization angle, except for a narrow frequency range, in which a dramatic change of the polarization angle occurs and the fractional polarization reaches a minimum (see Fig. 3.6). Indeed, in Fig. 3.12 it can be seen a RM $\approx$ 1500 rad/m^2 takes place at $\sim$ 5 GHz.

We fitted the source with a *Double Burn* model (Fig. 3.16), suggesting that there are two different emitting and rotating components with regular magnetic field within the beam. However, the polarization angle data points could not be very well fitted. Improvement on the modeling have to be done. Nevertheless, the RM values determined from our modeling ($RM_1 \simeq$ –1700 rad/m^2 and $RM_2 \simeq$780 rad/m^2, Tab. 3.3) are in agreement with the values seen in the RM vs frequency plot (Fig. 3.12). That could be at least a proof of the possible presence of two Faraday components that behaves differently at the different bands.

There are no VLBI images available. That could either mean, there were no observations, or that the source is not compact. In the latter case, the source

could be very extended, most likely a misaligned radio source, consistent with its radio spectrum. In this case, the viewing angle would be large and therefore, the relativistic effects are less strong. The jet, containing non thermal electrons, and the wind, containing thermal and non-thermal electrons, are emitting as a whole structure.

Therefore, since the best model suggests an Internal Faraday depolarization and the source could be misaligned, it could be possible that the synchrotron emission is coming from the jet and its wind and the the latter, that is still a synchrotron emitter, is producing a strong depolarization due to high thermal electron density.

- Source 0845+0439 -

The radio SED of this source could be fitted with an old component at low frequency ($\sim$ 100 MHz) and two synchrotron components at higher frequencies ($\sim$ 3 GHz and $\sim$ 10 GHz respectively; see Fig. 3.3). However, the spectrum is also consistent with a flat spectrum with the whole frequency range. The fractional polarization follows a sinusoidal-like behavior and its polarization angle clearly does not follow a linear trend (see Fig. 3.6), with RM changing between 500 and 1000 rad/m^2 at C band (see Fig. 3.12).

The polarization properties behavior can be very well explained with a *Double External Dispersion* model (Fig. 3.17a). We obtained two high dispersive σ_{RM} ($\sigma_{RM1} \simeq$130 and $\sigma_{RM2} \simeq$ 200) components with high values of RM (RM$_1 \simeq$ 780 rad/m^2 and RM$_2 \simeq$ 1660 rad/m^2; see Tab.3.3). The magnetic field could be characterized by a high presence of random cells of magnetic field.

Higher resolution VLBA images at S band and X band show a compact source with a possible weak extended feature to the east (see Appendix B.3). Its core dominance value does not indicate a core dominated source (Tab. 3.5). Its vale is 0.2, meaning that an important contribution of flux density emission is been lost between VLA and VLBA scale. This could imply the presence of a structure of the scale of the VLA which is not detected by the VLBA.

A possible scenario could be that the radio jet is passing through or two magnetized media, or one large medium with a gradient in its properties. Most probably, due to the smooth changes in the polarization angle, the Double Faraday Dispersion is due to a single magnetized layer surrounding the AGN/jet structure with a gradient in the Faraday depth. This layer is not emitting synchrotron radiation but it is responsible for the external Faraday depolarization behavior with the result of high RM values. Therefore this medium should be characterized by a high value of thermal electron density. This would be consistent with the dramatic loss of flux density between the VLA (sensitive to thermal and non-thermal emission) and the VLBA (only sensitive to non-thermal emission).

Another possibility is that, considering the flattish radio spectrum and the compact feature at pc scale, the source, has a quite small viewing angle with respect to the observer. The doppler busted radio emission from the relativistic jet would dominates over the wind synchrotron emission. Therefore, the total intensity emission would come from the fast jet but the depolarization would come from the dense and slower wind that in this case contribute only as an external Faraday layer.

- Source 0958+3224 -

The spectrum of this source could be fitted with an old component at low frequency ($\sim$ 100 MHz) and two synchrotron components at higher frequencies ($\sim$ 2 GHz and $\sim$ 10 GHz respectively; see Fig. 3.3). Its fractional polarization is following a sinusoidal-like behavior (see Fig. 3.7). The RM seems to vary within the C and X bands with values $\gtrsim$ 1000 rad/m^2 (see Fig. 3.7 and Fig. 3.12).

The polarization properties are quite well represented by a *Triple* model (Fig. 3.17b), for which the depolarization comes from the presence of three external Faraday layers with regular magnetic field. Therefore, in this case one can visualize it with the presence of at least three clumpy regions producing a different RM each. The values of the resulting RMs are very high (RM$_1\simeq$ 3900 rad/m^2 RM$_2\simeq$ 740 rad/m^2 and RM$_3\simeq$ 1110 rad/m^2, Tab. 3.3), suggesting a very dense magnetized media.

Higher resolution VLBA images at S band and X band seems to show an extended feature towards the south (see Appendix B.4), but as we go to higher frequency the emission seems to be dominated by the compact component. Véron-Cetty & Véron (2006) classify this object as Seyfert 1.8 (Sy 1.8) therefore, the torus is obscuring the very central part of this galaxy. The kpc scale observations, from low to high frequency (data from literature and L, C and X bands JVLA data), are tracing different dominant emission regions. Low frequency data from literature and from our new broad band, L band JVLA data, are most likely dominated by the powerful extended emission of the galaxy, i.e. the radio emission from the lobes. High frequency JVLA data, still unresolved at our kpc scale, are dominated by the central core. This explain the steep radio spectral shape at low frequency and its flattening at high frequency. Moreover, the above description could explain the compactness observed at pc VLBA scale. Therefore, the source has a large viewing angle with respect the observer and shows different radio emission contribution at different scales.

Altogether these information suggest that the radio emission at high frequency comes from the central region of the galaxy and it goes through at least three external Faraday screens that depolarize at C and X bands. These Faraday screens can be identified as clumpy regions of the obscuring torus surrounding the AGN and/or the non relativistic wind that covers the relativistic jet.

- Source 1048+0141 -
The radio spectrum of this object could be fitted with an old component at low frequency ($\sim$ 100 MHz) and two components at higher frequencies ($\sim$ 2 GHz and $\sim$ 10 GHz respectively; see Fig. 3.3). Its fractional polarization decreases following a sinc-like trend and reaching a constant values of 1% for almost the entire C band. The polarization angle increases at X band and it reaches a constant value at C band (see Fig. 3.7). In Fig. 3.12 the RM covers a range of very high values between 4000 and 10000 rad/m^2 within the X band while it decreases towards low value at C band.

The polarization properties are quite well fitted by a *Double External Dispersion* model (Fig. 3.18a) with a low RM$_1$ ($\simeq$–20 rad/m^2) and a very high RM$_2$ ($\simeq$ 5100 rad/m^2). Note in Tab. 3.3 that the σRM$_1$ has a large error; this means that the first external Faraday component with random magnetic field is in principle not necessary. However, it is quite certain that at C band the source does not show high RM, suggesting a less dense magnetized medium at this frequency (Fig. 3.12).

Higher resolution VLBA images do not help much understanding the morphology of the source. They show an unresolved compact source even at X band (see Appendix B.5). The compactness of the source and its radio spectrum at high frequency could suggest a QSO with a small or moderate viewing angle with respect to the line of sight. However, its core dominance value is quite small (Tab. 3.5), which is consistent with two options: we are losing a moderately extended component (few hundred of pc) or a low brightness component detected only by the VLA.

We could interpret these results with a QSO that emits synchrotron radiation from the relativistic jet moderately close to the observer's line of sight, and passing through the slower wind that depolarized the radio emission. At C band, the emission seems to trace a less extreme medium. Therefore the wind could be less dense at low frequency.

- Source 1146+5356 -
This source could be fitted with three components: one at $\sim$ 200 MHz and the other two at higher frequencies ($\sim$ 2 GHz and $\sim$ 10 GHz respectively; see Fig. 3.3). Overall the radio spectrum could also be considered flat, consistent with a small viewing angle source. The polarized properties seem to follow a simple behavior with the fractional polarization decreasing exponentially with wavelength and the polarization angle follows a linear trend (see Fig. 3.8) with a high RM value $\sim$ 550 rad/m^2 (see Fig. 3.12).

A *Double External Dispersion* model fit very well the source (Fig. 3.18b), with the results of two external Faraday screens components both with RMs

around -500 rad/m^2, but with two different values of the RM dispersion (σ_{RM1} of 100 and σ_{RM2} of 620; see Tab.3.3). This suggests that the magnetic field is more ordered within the first Faraday screen than the second Faraday screen.

High angular resolution VLBA images at L, S, C and X bands are collected (see Appendix B.6). From these images, we identify a bright compact core and a possibly large structure thus, a core-jet object. The low core dominance value (0.4, Tab. 3.5) suggest that an emission component detected by the VLA is lost when observe at the scale of the VLBA. This is consistent with a loss of intermediate scale structure or a loss of a thermal component.

The interpretation of all these results is difficult. Several scenario are possible: the radio synchrotron emission coming from the radio jet could be passing either a complex ambient medium surrounding the source or a slower wind located around the jet.

- Source 1246-0730 -

This source could be fitted with an old component at low frequency ($\sim$ 100 MHz) and two components at higher frequencies ($\sim$ 3 GHz and $\sim$ 10 GHz respectively; see Fig. 3.3). The spectrum looks flat at higher frequency. The fractional polarization decreases until roughly 6 GHz and then it increases with the result of a repolarization (Fig. 3.8). In a similar way, the polarization angle seems to follow a linear trend with a corresponding RM value $\sim$ 500 rad/m^2 at high frequency (from 6 until 12 GHz), while below 6 GHz it deviates, reaching a higher RM value around 1000 rad/m^2 (Fig. 3.12).

The polarization properties are not well fitted by a single model. However we can extract some indication about the trend of the polarized data fitting a *Double Burn* model and a *Double External Dispersion* model(Fig. 3.19 and Tab. 3.3). The longer and shorter wavelength data points are not well fitted by this kind of simple combination of models.

High angular resolution VLBA images at S and X band show a compact source with a possible extended feature towards the west direction (see Appendix B.7). The core dominance vale is large (0.8, Tab. 3.5), consistent with a small viewing angle source. Indeed, the source is monitored in the MOJAVE program and show a very high apparent velocity with β_{app}= 22c. The MOJAVE polarization image shows that the polarized flux density is located within the central region and the value of the RM measured is in agreement with the previous single dish measurement with RM $\approx$ 700$\pm$150 rad/m^2 (Hovatta et al., 2012). However, the new modeling of the wide band JVLA observations reveals the presence of at least two Faraday components. Moreover, the source is variable with the polarization angle that changed from 173 deg in 2006 to 23 deg in 2010 (see Tab. B.1 in appendix B.7). This is a sign that the detected radiation is coming from the central region.

The synchrotron radiation is emitted from the relativistic jet of this source however, since the modeling allows two different depolarization scenarios, it is not very clear from where the depolarization comes from. Therefore, the depolarization is due to the presence of an intermixed medium of thermal and non-thermal electrons in the jet or is due by the non relativistic wind around the jet.

- Source 1311+1417 -

This source could be fitted with one synchrotron component peaking at L band around 1 GHz (see Fig. 3.4). Its spectrum is characteristic of a GPS source. The fractional polarization decreases from $\sim 7\%$ to $\sim 2\%$ at roughly 7 GHz. At lower frequencies the fractional polarization decreases much more slowly, from $\sim 2\%$ to $\sim 1\%$. In a similar way the polarization angle increases rapidly until 7 GHz and it reaches a constant value (see Fig. 3.9). This behavior is also reflected in the RM vs frequency figure (see Fig. 3.13), in which we identify a RM around 800 rad/m^2 at the highest frequency ($\sim$ 9-12 GHz) and then it decreases linearly with frequency to $\sim$ 0 rad/m^2 at $\sim$ 7 GHz. Note that the behavior of the polarization angle resembles that of 1048+0141. The fractional polarization, although it does not decrease monotonically, has not a clear sinc-like trend.

An indication of the trend of the polarized properties are given by fitting an *Internal Dispersion* model (Fig. 3.21a and Tab. 3.3). It returns a very high RM values, with RM of ≈ 1720 rad/m^2 suggesting a very dense magnetized medium.

High resolution VLBA shows a core-jet object (B.9) and its core dominance value is small (Tab. 3.5). Together with the GPS nature suggested from the radio spectrum, this source is most likely embedded in a dense environment.

We can conclude that the source could be a very compact and most likely young GPS radio galaxy with the radio emission coming from the newly growing jet and the depolarization is coming from regions that emits and rotates at the same time. Therefore, the jet could have a high mixture of thermal and non-thermal electrons.

- Source 1312+5548 -

This source could be fitted with an old component at very low frequency (< 100 MHz) and one component at higher frequencies ($\sim$ 1 GHz; see Fig. 3.4). The fractional polarization decreases from 7 % to $\sim 0\%$ in an exponential way. The polarization angle has large variation within the C and X bands (see Fig. 3.9). The RM, although it has large dispersion, has a value around 500 rad/m^2 at frequencies below 9 GHz. Thereafter, it increases to a value of RM around 2500 rad/m^2 at 10 GHz and it decreases to $\sim$1000 rad/m^2 at the highest frequency (see Fig. 3.13).

Two depolarization models, a *Double Burn* and a *Double External Dispersion*

models, try to give hints on the trend of the polarized emission (Fig. 3.20 and Tab. 3.3). The reduced χ^2 test does not help to discern which model is the most appropriate. The source is very complicated to be fitted with these simple depolarization models, however, the *Double Burn* seems to follow better the variations of the polarization angle than the *Double External Dispersion* model. On the other hand the fractional polarization seems to be better fitted by the latter model than the first one.

High angular resolution VLBI image at 5 GHz (see Appendix B.10) shows a source with a complex morphology, a two sided radio source with a strong bend jet. It appears to be a misaligned radio source.

This complex morphology could yield to the complex polarization behavior. Indeed, the internal depolarization, described by the *Double Burn* model could be due to the emission and rotation of the jet-wind that contains thermal and non-thermal electrons. On the other hand, the *Double External Dispersion* model could be due to a clumpy and dense environment surrounding the source that cause the radio jet to be bent. Most likely a combination of several internal and external Faraday layers could be the right case.

- Source 1405+0415 -

This QSO is fitted with an old component peaking at very low frequency ($<$ 100 MHz) and two synchrotron components at high frequency ($\sim$ 1 GHz and $\sim$ 10 GHz respectively; see Fig. 3.4). The fractional polarization is quite constant within the whole observed band with a value around 2%.The polarization angle from 4 GHz to 7 GHZ remains constant around 9deg, then it increases up to 12deg at 10 GHz. At high frequency it decreases with a high RM value of $\sim$ 1500 rad/m^2 (see Fig. 3.10 and 3.13).

A *Double* model (Fig. 3.21b, Tab. 3.3) trace a good fit to the data. It returns a small values of the RM_1 (–17 rad/m^2). This could be the case in which we add "false" nπ ambiguities to the single dish data with the result of a high RM value (Tab. 2.2). However, from the depolarization modeling and from the RM vs frequency plot, it seems that the source has a higher RM value at high frequency ($RM_2 \approx$ 400 rad/m^2). Therefore, we might have two options: or the source has really no high RM but shows a high RM value at high frequency, or the source is variable.

High angular resolution VLBA at S, X and U bands show a compact source with pc scale flux densities comparable with the kpc scale flux densities. Therefore, the source most likely is a core-dominated source (see Appendix B.11 and Tab. 3.5). Moreover, it is monitored in the MOJAVE program, showing variability in its total flux density. Its polarized flux density could be affected by variability. The variability is a characteristics of emission dominated by the central region of a source. Moreover, the apparent velocity is small, with β_{app}= 7.6c

despite its very high redshift and possibly small viewing angle (just supposed from its compactness at pc scale and from the flat radio spectrum at high JVLA frequencies). The source could be so strongly boosted to produce a decrease of its apparent velocity.

Combining the information altogether we can draw the following scenario: the source is a high redshift blazar pointing the variable radio emission towards the observer. However, the opening angle of the relativistic jet, responsible for the total intensity radio emission, is likely smaller than the observer's viewing angle. Therefore, the synchrotron radiation goes through one or two external layers of the wind that produce the depolarization effects. Moreover, because of its variability, it is possible that the source is also experiencing polarization variability thus, changes with time of the RM values.

- Source 1549+5038 -

This source could be fitted with four synchrotron components (peaking at $\sim$ 300 MHz, $\sim$ 2 GHz, $\sim$ 5 GHz and $\sim$ 15 GHz; see Fig. 3.4). Overall the radio spectrum looks flat. The fractional polarization decreases from 2.5 % to 0.5%. The polarization angle and the fractional polarization show a complex behavior within the whole observed band (see Fig. 3.10). The RM shows several values within the band: $\sim$ 400 rad/m^2 at lowest and the highest frequencies, but it reaches local maximum of $\sim$1000 rad/m^2 at $\sim$8 GHz and $\sim$600 rad/m^2 at $\sim$9 Ghz (see Fig. 3.13).

The source shows complex behavior of the Stokes parameters Q and U difficult to be fitted. However, the *Double External Dispersion* model and the *Internal and External Dispersion* model give some good indications describing the trend of the polarized signal (Fig. 3.22b and Tab. 3.3). Both the reduced χ^2 values are similar and both returns quite high values of RMs and high dispersion σRMs suggesting a dense clumpy and turbulent medium.

High angular resolution VLBI images at L, S, C and X bands show a complex morphology, with several components (see Appendix B.12) that could probably be associated with the several components seen in the radio SED.

Therefore, a possible scenario could be that the radio emission comes from the relativistic jet, while the depolarization could be due: (1) to the external wind around the fast jet or (2) a combination of the non thermal wind and clumpy regions surrounding the AGN that is intercepted by the synchrotron radiation.

- Source 1616+0459 -

This source could be fitted with an old component peaking at very low frequency ($<$ 100 MHz) and two components at higher frequencies ($\sim$ 2 GHz and $\sim$ 6 GHz respectively; see Fig. 3.4). This source forms part of a group of galaxies

at redshift 3.2 (Djorgovski et al., 1987). The fractional polarization decreases with the wavelength from 3% to 0.5%. The polarization angle increases with wavelength following a nearly linear trend (see Fig. 3.11). The RM vs frequency plot of this source suggests that the RM increases rapidly from low value at the lowest frequency towards 2200 rad/m^2 from 6 GHz to 12 GHz (see Fig. 3.13).

The depolarization behavior has been fitted with a *Double External Dispersion* model (Fig. 3.23a and Tab. 3.3). The two external Faraday screens have similar high RM values (around 2100 rad/m^2) and high value of the dispersion of the RM σ_{RM} ($\approx$ 200 rad/m^2 and $\approx$ 400 rad/m^2 for the first and second RM dispersion respectively). Improvements on the depolarization modeling have to be done in order to better follow the changes of the polarization properties at longer wavelength.

The high resolution VLBA images at S and X band show a compact source (see Appendix B.13) although its core dominance value does not suggest a core dominated source (with a core dominance value of 0.4, Tab. 3.5). These images do not help very much to understand the morphology of the source.

Note that, when corrected by the redshift, the RM values of the two components are $\sim 4\times10^4$ rad/m^2, the highest RM value in our sample. Since the source is part of a group of galaxies, the possible scenarios could be: (1) the radiation, coming from the radio jet, is passing through dense regions of the group or (2) the radio emission intercepts the wind flow around the jet.

- Source 2245+0324 -
This source could be fitted with three synchrotron components (peaking at $\sim$ 1 GHz, $\sim$ 3 GHz and $\sim$ 9 GHz; see Fig. 3.4). However, this is also consistent with a convex shape spectrum indicating a possible GPS nature of the source. The fractional polarization seems to follow a sinc-like trend. At C band the polarization angle remains almost constant, with very low RM value. Then, it increases at higher frequencies reaching a maximum of $\sim$ 7000 rad/m^2 at $\sim$ 9 GHz and it decreases again down to RM of $\sim$ 1000 rad/m^2 at the highest frequencies (see Fig. 3.11 and see Fig. 3.13).

High angular resolution VLBA images show a two sided jet; the object has two components at X band image(see Appendix B.14). The core dominance value is large (1.1, Tab. 3.5). This could be consistent with a GPS nature; this kind of sources are very compact and likely dominated by the central region.

We could fit this source with a *Double Internal Dispersion* model (Fig. 3.23 and Tab. 3.3) with both components showing a large RM values ($\approx$ –2800 rad/m^2 and $\approx$ –4030 rad/m^2), suggesting a very dense magnetized emitting region.

3.5.2 Depolarization scenarios

The aim of this work is to study the interaction of the AGN with its medium. The depolarization effect is one of the principle feature that could help to understand the complexity of the AGN environment. From the above described results, it is clear that the depolarization could be due to the AGN jet itself or due to some clumpy regions around the central engine. Therefore, by studying the polarization properties of the sources we can indeed extract important information about the ambient medium and/or the jet structure. In the following, we discuss several possible scenarios that could account for the polarization behaviors observed in our sample.

A possible jet depolarization scenario could be described considering two extreme cases: (1) with the jet viewing angle $\theta\sim$ 0deg (Fig. 3.24) and (2) with the jet viewing angle $\theta\sim$ 90deg (Fig. 3.25). From the physics of the radio jet, we recall that the doppler factor δ is inversely dependent to the jet viewing angle θ: the smaller the viewing angle θ, the larger is the doppler factor δ (see equation 1.9). The luminosity depends linearly on the doppler factor to the third ($L_{obs} \propto L_{intr} * \delta^3$). Moreover, it is important to remember that the relativistic jet contains non-thermal electrons and is all wrapped up by a slower wind, that contains thermal and non-thermal electrons (see section 1.1.5).

In the case of a small viewing angle where $\theta\sim$0deg, the relativistic jet is pointing towards the observer and most likely its opening angle is smaller than the viewing angle of the observer (Fig. 3.24). Therefore, the doppler factor δ of the jet is very large; in extreme cases, when θ is very small, the doppler factor starts to decrease reaching value of 0 (Fig. 1.10).The luminosity of the jet is doppler-boosted by a factor of δ^3 therefore, the radio emission is dominated by the relativistic jet. The surrounding wind is non relativistic with its doppler factor δ and therefore, its luminosity small.

Therefore, in this scenario general external Faraday depolarization (without specifying any model) could be explained as following:

- the synchrotron radiation is coming from the relativistic spine jet,
- the depolarization is due to the thermal electrons that are present in the low luminous wind.

A general internal Faraday depolarization (without specifying any model) is harder to be explained. We can just speculate that:

- there could be an intermix of wind and jet; the emission and the rotation comes from the same region

In the case of large viewing angle $\theta\sim$90deg (Fig. 3.25) the jet doppler factor δ is small with a small apparent velocity β_{app} (see Fig. 1.9). Therefore, the

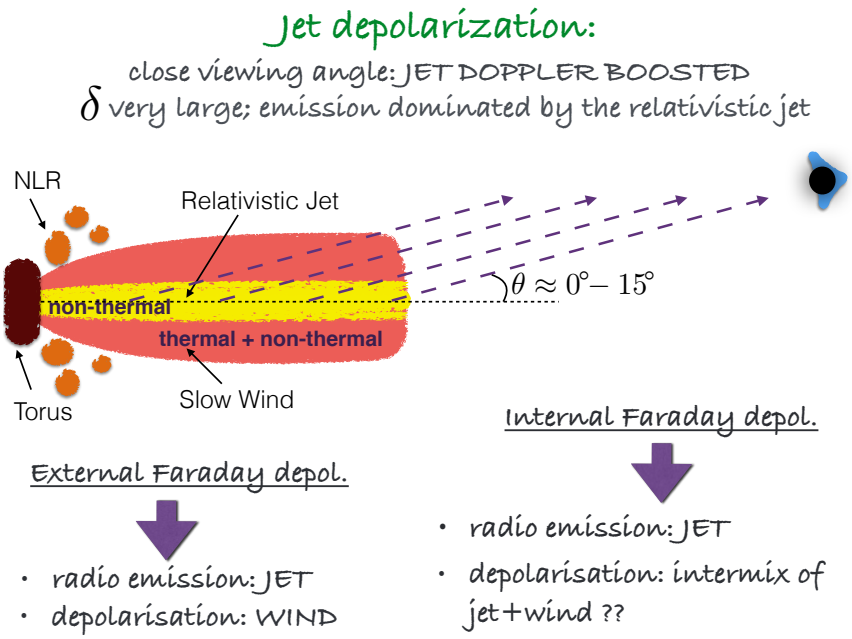

Figure 3.24: Depolarization due to jet with a small viewing angle.

luminosity of the jet is not strongly doppler-boosted and the doppler factor of the wind is ~ 1 or it can be larger than the δ of the jet. In this case, the emission of the wind could dominate over the jet emission. The wind luminosity contributes or dominates the radio emission.

In this scenario, a general external Faraday depolarization (without specifying any model) we have:

- the radio emission coming from the jet; the jet emission in this case dominates over the wind emission
- the depolarization is due to the thermal electrons of the wind.

On the other hand, we justify a general internal Faraday depolarization (without specifying any model) when:

- the radio emission is coming from the jet+wind,
- the depolarization is only due to the thermal electrons of the wind.

It is clear that the synchrotron radiation is produced by non-thermal electrons within a magnetic field. In the radio band the jets are the important feature that emits synchrotron radiation. In order to have depolarization due to the surrounding environment, a possible case is when the radio source is misaligned,

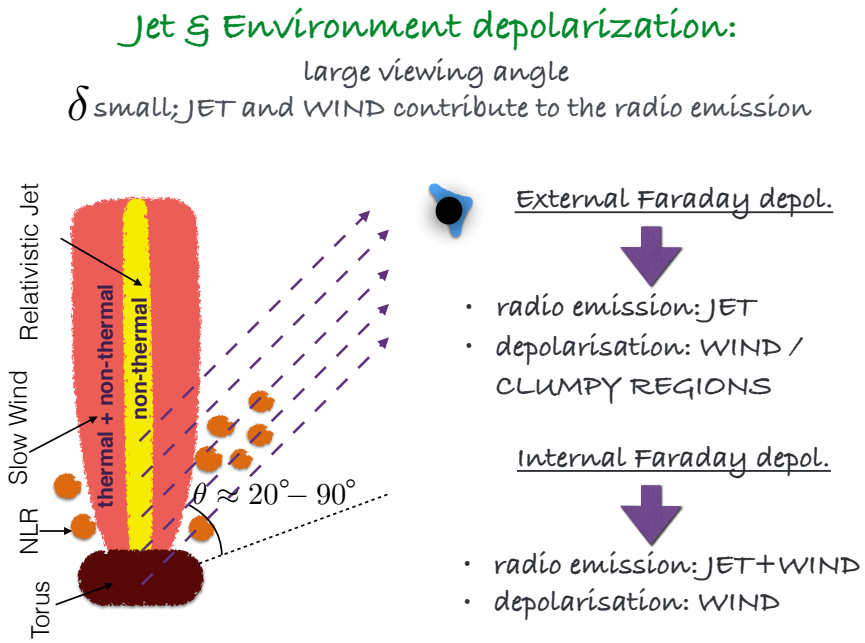

Figure 3.25: Depolarization due to jet and media surrounding the AGN. The viewing angle is large.

with a large viewing angle with respect the observer (Fig. 3.25). A misaligned radio source, could be depolarized by external clumpy regions when the emission from the relativistic jet goes through dense regions e.g. of the torus or the NLR (Fig. 3.25). Moreover, if the radio source is a newly growing object, i.e. a GPS source, the depolarization could also be considered internal because of its not well defined regions. Therefore, the newly born radio jet is intermixed with the whole clumpy and dense environment with a mixture of thermal and non-thermal electrons (Fig. 3.26).

3.5.3 The projected linear size and the synchrotron emission

The Compact Steep Spectrum (CSS) and the GHz Peaked Spectrum (GPS) sources are compact and very dense radio sources the former of which are contained within the the host galaxy ($\lesssim$ 20 kpc, Saikia, 1988; Fanti et al., 1990; Dallacasa et al., 1993), and the latter within the NLR ($\lesssim$ 1kpc, O'Dea et al., 1991). O'Dea & Baum (1997) while studying a sample of CSS and GPS sources, found a simple relation between the turnover frequency (ν_m) and the projected linear size (LS, in kpc), that is: $\nu_m \propto \mathrm{LS}^{-0.65}$. Therefore, as the radio source expands (from GPS to CSS) the turnover moves to lower frequencies (from $\sim$ 2

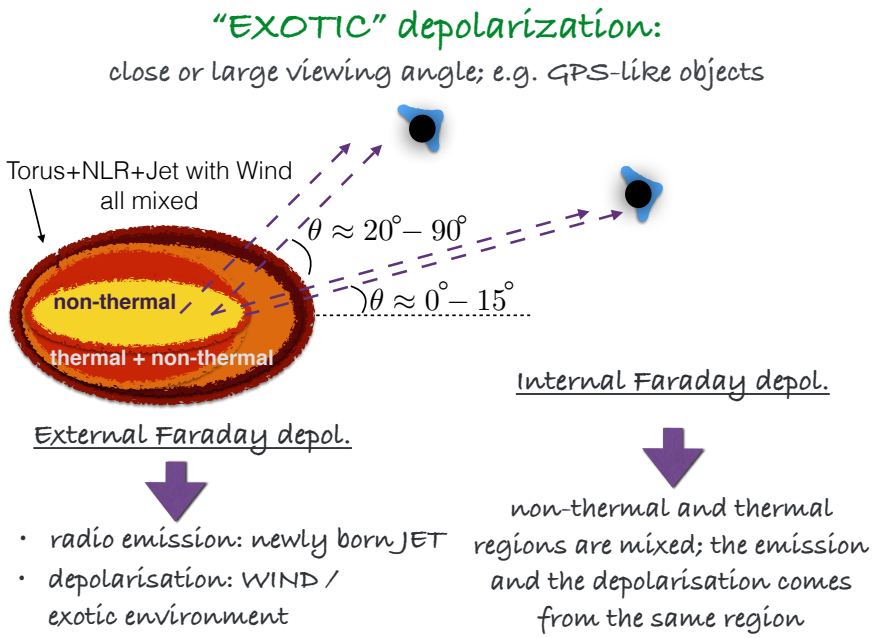

Figure 3.26: "Exotic" depolarization, e.g. GPS-like sources.

GHz to $\sim$ 100 MHz) as the result of a decreased energy density within the radio emitting region. It is possible to argue the existence of objects with turnover frequencies at higher frequency ($\sim$ 10 GHz). In this way Dallacasa et al. (2000); Dallacasa (2003) constructed a sample of High Frequency Peakers (HFP): smaller (contained within few tens of pc) and therefore, likely, younger radio sources. This turnover frequency vs projected linear size correlation is the same for the galaxies and quasars (O'Dea, 1998).

Assuming that our several synchrotron components used to fit the SEDs follow the above linear relation, we can estimate the projected linear size of the higher frequency synchrotron components, thus, to have a rough idea on the compactness of the regions from where the radio emission is arising. We consider the CSS/GPS-like (with a convex radio spectrum: 0751+2716, 1311+1417 and 2243+0324) together with the other sources for which a third synchrotron component is present peaking in the C and X bands where most of the interesting changes of the polarization properties, i.e. the high RM values, occur (the remaining 11 sources). After the correction of their turnover frequency in the rest frame, ν_{mRF}=ν_m(1+z), we extrapolate a range of projected linear sizes between $\approx$ 4 and 70 pc with one more extended synchrotron components of few hundred of pc ($\approx$ 140) and two kpc scale synchrotron emitters with projected linear sizes of $\approx$ 0.7 and 2.8 kpc, still in the GPS scale (Tab. 3.6).

Therefore, we can assert that the radio emission is arising mainly from scales

Table 3.6: Projected Linear Size (LS) of the highest frequency synchrotron components. The turnover frequency ν_m is the observed one (therefore it has to be corrected for the redshift z).

Source Name	z	ν_m [GHz]	LS [pc]
0239–0234	1.1	∼6.1	∼24
0243–0550	1.8	∼7.1	∼11
0751+2716	3.2	∼0.1	∼2800
0845+0439	0.3	∼6.3	∼40
0958+3224	0.5	∼17.3	∼8
1048+0141	0.7	∼5.5	∼30
1146+5356	2.2	∼8.8	∼7
1246–0730	1.2	∼10.0	∼10
1311+1417	1.9	∼1.3	∼140
1312+5548	1.5*	∼0.5	∼700
1405+0415	3.2	∼1.4	∼70
1549+5038	2.2	∼12.0	∼4
1616+0459	3.2	∼5.0	∼10
2245+0324	1.3	∼6.3	∼20

NOTE: The projected LS is here expressed in pc for convenience. The $*$ symbol means that the source has no information on the redshift in literature therefore, we choose to apply the mean value of the redshifts of the sample.

of tens of parsecs, thus in close proximity of the central engine. Being emitted from these close distances to the central region, it is likely that the emission in the 4-12 GHz range is passing through the dense and clumpy regions of the NLR and probably from the external part of the halo of the torus but also, for those sources for which the viewing angle could be close to the line of sight, the radiation may pass through material that covers the relativistic radio jet. Moreover, considering the very high RM values, the ambient medium should have a considerable quantity of thermal electrons, thus a dense medium that can act as a Faraday screen. Therefore, the complex behavior of the polarization properties are most likely due to the passage of the non-thermal radiation through a clumpy surrounding regions and/or it is tracing layers covering the AGN relativistic jet.

3.5.4 RM vs frequency dependence

Recent polarimetric studies (Jorstad et al., 2007; O'Sullivan & Gabuzda, 2009; Kravchenko et al., 2015) put some efforts to understand whether and how the RM increases with frequency. This characteristic could help to understand the physical condition of the AGN jet magnetic field. This tendency is given by the power-law relation $|RM| \sim \nu^a$. Theoretical estimation gives a=2, assuming an outflowing sheath around a conically expanding jet with a helical magnetic field Jorstad et al. (2007). This is explained because higher frequencies probe regions closer to the central engine with a denser medium and a stronger magnetic field.

In our study we can not see this tendency because we observed only up to a frequency of 15 GHz. All the sources in our sample do not show a simple RM trend with the frequency and for each of the targets, this RM behavior is different from each other. Instead, the RM vs frequency relation described above has been determined using a wide frequency range and less sampled. Therefore, the trend that (Jorstad et al., 2007; O'Sullivan & Gabuzda, 2009; Kravchenko et al., 2015) are seeing, is the increasing of the RM in its totality. Nevertheless, we can assert that, for all our targets, the complexity of the RM increases towards high frequencies (see Fig.s 3.12 and 3.13). We interpret this as an increasing of the complexity of the medium with the presence of several dense Faraday components close to the relativistic jet base and/or the central engine.

3.5.5 Magnetic field order

The ordering of the magnetic field is an information that can be estimated considering the RM and its σ values therefore, considering those depolarization cases for which the polarized properties are fitted by an e.g. external Faraday depolarization model (i.e. EFD or DED models) or internal Faraday dispersion (i.e. ID model). The measured quantities, RM and its σ_{RM}, contains information of the parallel component of the order magnetic field (B_{reg}) and the distribution of the turbulent magnetic cells within the beam (B_{turb}) respectively. Thus, assuming the electron density is comparable between the ordered and the random cells, we can give an estimation on the grade of order of the magnetic field in each of the Faraday components involved in the modeling, by calculating the ratio between the two quantities.

From our result (Tab. 3.7) we can assert that all the Faraday components have an order and random magnetic field equally distributed (or better its parallel component projected on the plane of the sky). Only in one case, for the source 0243-0550, the ratio $RM_1/\sigma RM_1$ suggests a really ordered magnetic field (see Tab. 3.3 and 3.7) as a consequence of possible repolarization of the source towards low frequency.

Table 3.7: Ordering of the magnetic field. DED: Double External Dispersion model; DID: Double internal Dispersion model; ID: Internal Dispersion model; IED: Internal External Dispersion model.

Source	Model	$RM_1/\sigma RM_1$	$RM_2/\sigma RM_2$
0243–0550	DED	$\simeq 58*10^3$	$\simeq 4$
0845+0439	DED	$\simeq 6$	$\simeq 10$
1048+0141	DED	$\simeq 550$	$\simeq 10$
1146+5356	DED	$\simeq 5$	$\simeq 1$
1246-0730	DED	$\simeq 8*10^3$	$\simeq 2$
1311+1417	ID	$\simeq 10$	–
1312+5548	DED	$\simeq 1$	$\simeq 1$
1549+5038	DED	$\simeq 1$	$\simeq 2$
	IED	$\simeq 4$	$\simeq 3$
1616+0459	DED	$\simeq 13$	$\simeq 5$
2245+0324	DID	$\simeq 15$	$\simeq 7$

3.5.6 Implications of this JVLA study

With this JVLA study we could spectrally resolve multiple polarized components of unresolved AGN. We can exclude polarization contribution from Galactic regions and from cluster radio halo because we do not have the short *uv* spacing to detect that extended emission. Moreover, we observed at quite high radio frequency for which the emission of these giant structures is not dominant. For the majority of the sources we detected multiple RM components. This could be due: (1) because the radiation travels through different magneto-ionic regions and therefore, the polarized emission experiences different amount of Faraday rotation (e.g. in the case of a morphological complex radio sources, or GPS-like sources) or (2) the polarized components may travel through regions all around the relativistic jet therefore, illuminating different part of the inhomogeneous Faraday screen very close to the AGN (e.g. in the case of flat-spectrum/blazar-like AGN). It could also be possible that the synchrotron emission is subject to time variability. As a consequence, also the polarization properties, therefore the different RM components, can be affected by time variability. The polarized and RM structure of VLBI jets has been observed to vary on time-scales as short as months (e.g. Zavala & Taylor, 2001; Gómez et al., 2011) so could also be possible that the polarized flux of some of our targets may also vary on similar time-scales. The polarized components could be moving along the jet and illuminating different regions close to the AGN. Summarizing, this new wide-band

spectropolarimetry approach, can be adopted as a new way to trace in the radio band some clumpy and dense region surrounding the AGN but also study the evolution in time of the jet through an inhomogeneous medium.

3.6 Conclusions

We have performed wide-band multifrequency linear polarization observations on a subsample of point-like AGN using the JVLA at L, C and X bands. We obtained the following results:

- The SEDs have been fitted with several synchrotron components following the same approach adopted for the single dish data (previous chapter §2). The new SEDs fitting are consistent with previous single dish results.

- The polarization properties show a complex behavior with the polarization angle that deviates from a linear trend with wavelength and the fractional polarization that does not follow the canonical exponential decreasing, both behaviors predicted for a single uniform Faraday screen. Indeed, the relation between the RM with frequency (Fig.s 3.12 and 3.13) shows that the RM is not constant and it changes dramatically within the wide frequency range.

- Depolarization have been studied through modeling the behavior of the Stokes parameters Q and U together with the fractional polarization, following the same approach done by O'Sullivan et al. (2012). As a first step, we considered sum of only internal or external Faraday depolarization models always considering the several Faraday components lying one near the other within the beam. For roughly half of them we obtain quite a good fit. The rest of the sources seems to follow a more complicated behavior that require a more complex modeling, that we propose to be a different combinations of the depolarization model (e.g. between internal and external Faraday depolarization models) and considering the Faraday components laying one behind the other. This implies an extra rotation and depolarization contribution to be implemented for the last Faraday screen (the one nearer to the observer).

- From our depolarization results, together with the SEDs study and VLBI images available from literature, we discuss on the possibility that the internal and external depolarization, for some of the sources, could be due to the jet itself. Indeed, the relativistic spine jet is the responsible for the radio synchrotron emission while the slower wind, containing thermal and

non-thermal electrons, could be the responsible for the internal or external depolarization (depending on the orientation of the source).

- From our modeling results, the value characteristics of the random contribution of the magnetic field (σRM) are quite high. Therefore, we can assert that the magnetic field is almost equally tidily and randomly distributed. This is another sign of the complexity of the ambient medium surrounding the relativistic jet and/or the central regions of the AGN. This complexity of the medium is also supported by the presence, for all the modeled source, of at least two Faraday components (internal or external to the emitting region), and all of them with very high RM values. This suggests a really dense magneto-ionic medium in the immediate environment of the sources.

- We commented on the connection between the morphology and the polarization properties of all the sources. The majority of the sources appear to be compact at higher resolution or they might have a complex morphology. Altogether the polarization and the modeling information allow us to suggest that the sources are really compact with a projected linear size of the most compact synchrotron component (at $\sim$ 10 GHz for most of them) of $\sim$4-70 pc and they are embedded in a complex and extreme ambient medium, in which the magnetic field seems to have turbulent cells within the smaller beam and/or a very density medium.

Higher angular resolution VLBA and EVN at C, X, Q and K bands have recently been observed for the very extreme cases (with $|RM_{obs}| \gtrsim 1000\mathrm{rad/m^2}$). These data will give us more details regarding the morphology and polarization characteristics of these really peculiar objects.

Chapter 4

Summary and future work

Summary of the PhD Thesis

In this Thesis we have presented an observational study of a sample of radio AGN sources. We have studied their radio polarization properties in a wide frequency range by observing with the 100-m Effelsberg telescope and the Karl G. Jansky Very Large Array (VLA) interferometer. Our aim was 1) to define a sample of AGN candidates to contain an extreme environment around the SMBH and, 2) to explore the possibility of studying the AGN environment and/or structure by modeling of the polarization properties within a wide frequency range.

We selected an initial sample of 537 sources from the entire northern sky. These sources do not show detectable polarized flux at 1.4 GHz in the NVSS radio survey catalogue. This characteristic indicates a strong depolarization at low frequency which is suggestive of an extreme (high dense and magnetized) medium, that can be identified by a high value of Rotation Measure (RM). We performed single dish observations at 10.45 GHz using the 100-m Effelsberg telescope on the initial sample. At this high frequency, we detected polarized flux density on 30 sources, which became our high-RM candidates. We then characterized their radio spectra and we determined their RMs through a single dish follow up campaign in the 2 to 15 GHz frequency range.

The Effelsberg campaign allow us to characterize the type of sources by modeling their radio spectra using different combinations of synchrotron components. We found that the targets are equally distributed in three groups that we called:

- *Older*: sources with a very extended synchrotron component. Most probably, AGN that suffered a strong activity in the past for which now the extended radio lobes dominate.

- *GPS-like*: sources with a more compact synchrotron component and that are suffering at present strong activity.

- *Mixed*: sources showing a combination of old synchrotron component at low frequency and compact component/s at high frequencies. These objects could be associated with AGN showing a restarting activity.

We estimated the single dish RM as a linear regression fit of the polarization angle versus λ^2. We found that, for 11 sources in our sample, **the polarization angle behavior deviates significantly from the λ^2 law**. This is a clear sign of complex medium, suggesting that **several Faraday screens are present in the intervening medium**. We also noticed that the ***Mixed* objects are those showing the largest values of RM, higher than 1000 rad/m^2**. This result lead to the conclusion that the **high-RM sources are mainly objects with compact high frequency components, probably new growing radio components. Therefore, they could be sources in a particular young activity phase as the GPS sources or in a reactivated activity phase**.

As pointed out from the single dish study, AGN may be characterized by complex Faraday behaviors, probably related to a complex environment. For this reason, we studied the most interesting cases (14 sources) through wide-band high sensitive observations. We performed radio interferometric observations at L (1 GHz BW), C (4 GHz BW), and X (4 GHz BW) bands using the broad-band JVLA spectropolarimeter. Thanks to the high spectral resolution in frequency, we were able to follow the behavior of the fractional polarization and the polarization angle in a well-sampled wide frequency range. This allows us to properly model the polarization properties and thus to obtain important information of the ambient medium characteristics. Our JVLA polarization results confirmed the previous Effelsberg results that the RM of the sources deviates (in some cases strongly) from the linear fit. This change of the polarization angle could be an indication of several Faraday screens that differently rotate the polarization angle, therefore a proof of the complexity of the medium surrounding the AGN. To emphasize this characteristic we also plot the derivative of the polarization angle (the derivative of the polarization angle with wavelength squared) vs frequency. All the sources in our JVLA sample do not show a simple RM trend with the frequency. Indeed, the **complexity of the RM increases towards high frequencies**. As we observe at high radio frequencies, we are preferentially observing emission from the innermost regions of the AGN. Therefore, we interpret this as an increasing of the complexity of the medium with the presence of several dense Faraday components close to the relativistic jet base and/or the central engine. In order to understand this extreme scenario, we modeled the Stokes parameters Q and U together with the fractional polarization and the polarization angle with λ^2. We constructed a set of models which are combination of simple internal and the external Faraday screens. Our modeling approach could obtain a good model fit for half of the sample. This new approach of polarization study allows to spectrally resolve multiple polarized components of unresolved AGN with the result to trace some clumpy and dense region surrounding them. We gave first interpretation of the environment of the AGN taking into account the JVLA wide-band results (their radio spectra, the polarization information and

the depolarization modeling results) together with higher resolution VLBI images from literature and other information when available. The interferometric results lead to some important consideration:

- **most of the Faraday components of all the modeled sources have a magnetic field equally tidily and randomly distributed, suggesting a complex medium;**
- **for the majority of our sources the depolarization (internal or external) could be due by the jet itself. Indeed, the depolarization could be due to the thermal electrons that are present in the low luminous wind that covers the relativistic jet.**

Our study demonstrates that this new spectropolarimetry approach can be adopted **as a new way to trace in the radio band the ambient medium surrounding the AGN/jet and also study the evolution in time of the jet through an inhomogeneous medium.**

The parsec-scale structure with VLBI observations: the future work

At the end of the PhD work we obtained observations for those sources which show the highest RM values with the EVN, at C and X bands, and the VLBA, at U and K bands. These observations will be useful to perform several studies of the physical environment at smaller scales, allowing us to disentangle the properties closer to the AGN, where their effects might be more dramatic. We will be able to:

- produce spectral index maps, in order to discern the nature of the different components;
- estimate of the maximum linear sizes and morphological study;
- estimate of the magnetic field strength through equipartition assumption;

Moreover, thanks to the availability of full Stokes parameters, the detected polarization information will allow us:

- to produce detailed polarization maps of the targets;
- to understand how their polarization angles are distributed;
- to understand which are the components contributing to the already detected high RMs;

- reconstruction of the magnetic field 3-dimensional configuration through the study of the RMs.

Polarization VLBI data are intrinsically related to fundamental questions such as: the formation, launching and collimation of the jets.

Referred publications from the PhD project

The results from the PhD project have been reported in two referred and already published articles and another which is in preparation:

- *A study of a sample of high rotation measure AGN through multifrequencies single dish observations*, **Pasetto A.**, Kraus A., Mack K.-H., Bruni G., Carrasco-González C., Astronomy & Astrophysics, 586-117, 2016
- *A possible link between high rotation measure and CSS-GPS sources*, **Pasetto A.**, Kraus A., Mack K.-H., Bruni G., Carrasco-González C., Astronomische Nachrichten, 2016, DOI: 10.1002/asna.201512271
- *Probing the environment of high rotation measure AGN through interferometric JVLA observations*, **Pasetto A.**, Carrasco-González C., Basu A., Bruni G., O'Sullivan S., Kraus A., Mack K.-H., Astronomy & Astrophysics, in preparation (2016)

Appendix A

Effelsberg Appendix

A.1 Single dish information

Tab. A.1 are the single dish information. For the source 0243-0550, we could only provide flux densities at 10.45 GHz and at 4.85 GHz. For the latter we split the bandwidth (500 MHz) into 3 sub-bands, each of them ∼160 MHz wide. The Effelsberg data are those in the 2.64 to 14.60 GHz range. Values at 1.4 GHz are taken from the NVSS survey, values at 360 MHz cm are taken from the TEXAS survey, values at 320 MHz are taken from the WENSS survey, values at 150 MHz are taken from the 7C survey, and values at 74 MHz are taken from the VLSS survey. Upper limits are indicated with the < symbol and the unavailable data with the – symbol.

Table A.1: Table of values.

Name	ν [GHz]	S [mJy]	S_{Pol} [mJy]	m [%]	χ [deg]
	14.60	650 ± 10	55 ± 4	8.4 ± 0.6	93.9 ± 2.0
	10.45	723 ± 6	51 ± 1	7.0 ± 0.1	88.9 ± 0.4
	8.35	740 ± 6	44 ± 1	6.0 ± 0.2	88.9 ± 0.6
	4.85	666 ± 4	20 ± 1	3.0 ± 0.2	79.5 ± 2.4
0239–0234	2.64	548 ± 7	20 ± 3	3.6 ± 0.6	62.8 ± 4.4
	1.40	300 ± 10	–	–	–
	0.36	250 ± 22	–	–	–
	0.32	–	–	–	–
	0.15	–	–	–	–
	0.07	<300	–	–	–
	10.45	548 ± 2	9 ± 2	1.6 ± 0.4	1.0 ± 9.9
	5.00	673 ± 14	13 ± 4	1.9 ± 0.6	102.1 ± 10.4
	4.80	691 ± 15	13 ± 4	1.9 ± 0.6	109.3 ± 9.5
	4.60	647 ± 3	12 ± 1	1.8 ± 0.1	117.5 ± 2.8
0243–0550	1.40	560 ± 20	–	–	–
	0.36	390 ± 25	–	–	–
	0.32	–	–	–	–
	0.15	–	–	–	–
	0.07	990 ± 160	–	–	–
	14.60	422 ± 3	15 ± 4	3.6 ± 0.8	-17.2 ± 6.8
	10.45	430 ± 1	16 ± 1	3.8 ± 0.2	-14.2 ± 0.9
	8.35	432 ± 2	12 ± 1	2.8 ± 0.2	-16.7 ± 1.8
	4.85	416 ± 2	6 ± 2	1.4 ± 0.4	-53.8 ± 6.3
0742+4900	2.64	489 ± 4	–	–	–
	1.40	398 ± 12	–	–	–
	0.36	–	–	–	–
	0.32	127 ± 4	–	–	–
	0.15	<78	–	–	–
	0.07	<300	–	–	–
	14.60	57 ± 6	14 ± 4	23.8 ± 7.8	-22.2 ± 8.9
	10.45	82 ± 2	11 ± 3	13.3 ± 3.2	-21.9 ± 6.9
	8.35	106 ± 1	9 ± 1	8.2 ± 0.7	-1.5 ± 2.5
	4.85	193 ± 2	5 ± 1	2.5 ± 0.6	58.2 ± 7.0
0751+2716	2.64	325 ± 3	–	–	–
	1.40	590 ± 20	–	–	–
	0.36	1470 ± 80	–	–	–
	0.32	–	–	–	–
	0.15	–	–	–	–
	0.07	890 ± 120	–	–	–
	14.60	735 ± 43	18 ± 4	2.4 ± 0.5	55.2 ± 11.7
	10.45	682 ± 52	19 ± 1	2.8 ± 0.1	109.1 ± 1.6
	8.35	654 ± 5	8 ± 1	1.2 ± 0.1	146.4 ± 3.5
	4.85	560 ± 3	16 ± 2	2.7 ± 0.2	401.5 ± 5.2
0845+0439	2.64	519 ± 13	3 ± 1	0.5 ± 0.2	1364.5 ± 10.9
	1.40	380 ± 10	–	–	–
	0.36	–	–	–	–
	0.32	–	–	–	–
	0.15	–	–	–	–
	0.07	880 ± 120	–	–	–

Table A.2: Table of values A.1. Continued.

Name	ν [GHz]	S [mJy]	S_{Pol} [mJy]	m [%]	χ [deg]
	14.60	63 ± 2	–	–	–
	10.45	97 ± 4	6 ± 2	6.6 ± 2.4	41.1 ± 8.0
	8.35	121 ± 1	6 ± 1	5.0 ± 0.6	38.1 ± 3.6
	4.85	181 ± 2	7 ± 1	3.6 ± 0.6	31.1 ± 6.1
0925+3159	2.64	316 ± 4	–	–	–
	1.40	551 ± 17	–	–	–
	0.36	1800 ± 30	–	–	–
	0.32	1970 ± 4	–	–	–
	0.15	3315 ± 50	–	–	–
	0.07	6160 ± 650	–	–	–
	14.60	584 ± 15	–	–	–
	10.45	660 ± 6	9 ± 3	1.2 ± 0.4	47.7 ± 122.8
	8.35	616 ± 6	17 ± 5	2.8 ± 0.7	106.0 ± 6.9
	4.85	830 ± 3	22 ± 2	2.6 ± 0.2	396.7 ± 5.1
0958+3224	2.64	1100 ± 13	–	–	–
	1.40	1250 ± 40	–	–	–
	0.36	3630 ± 70	–	–	–
	0.32	3880 ± 10	–	–	–
	0.15	5060 ± 700	–	–	–
	0.07	7000 ± 740	–	–	–
	14.60	74 ± 2	8 ± 2	10.7 ± 4.1	27.5 ± 10.8
	10.45	91 ± 3	9 ± 2	10.2 ± 2.5	35.4 ± 6.4
	8.35	105 ± 1	8 ± 1	8.0 ± 0.6	36.6 ± 2.3
	4.85	166 ± 2	6 ± 1	3.8 ± 0.6	71.5 ± 7.0
1015+0318	2.64	244 ± 2	–	–	–
	1.40	416 ± 13	–	–	–
	0.36	933 ± 30	–	–	–
	0.32	–	–	–	–
	0.15	–	–	–	–
	0.07	2120 ± 230	–	–	–
	14.60	1170 ± 10	60 ± 4	5.2 ± 0.3	92.9 ± 1.8
	10.45	1070 ± 10	67 ± 2	6.4 ± 0.2	93.7 ± 1.4
	8.35	1050 ± 10	42 ± 1	4.0 ± 0.1	82.1 ± 0.5
	4.85	903 ± 4	32 ± 1	3.5 ± 0.2	69.9 ± 1.4
1043+2408	2.64	675 ± 3	8 ± 2	1.1 ± 0.3	85.7 ± 6.7
	1.40	320 ± 10	–	–	–
	0.36	460 ± 76	–	–	–
	0.32	–	–	–	–
	0.15	–	–	–	–
	0.07	<300	–	–	–
	14.60	279 ± 3	24 ± 4	8.5 ± 1.3	139.4 ± 4.5
	10.45	295 ± 1	27 ± 1	9.3 ± 0.3	130.9 ± 1.3
	8.35	314 ± 2	26 ± 1	8.4 ± 0.2	126.3 ± 0.8
	4.85	347 ± 2	20 ± 1	5.6 ± 0.3	97.1 ± 5.2
1044+0655	2.64	387 ± 5	6 ± 2	1.4 ± 0.6	-9.2 ± 12.8
	1.40	490 ± 20	–	–	–
	0.36	845 ± 27	–	–	–
	0.32	–	–	–	–
	0.15	–	–	–	–
	0.07	1310 ±160	–	–	–

Table A.3: Table of values *A.1*. Continued.

Name	ν [GHz]	S [mJy]	S_{Pol} [mJy]	m [%]	χ [deg]
	14.60	273 ± 4	8 ± 1	2.7 ± 0.3	182.6 ± 2.1
	10.45	328 ± 4	11 ± 2	3.2 ± 0.7	105.6 ± 6.9
	8.35	342 ± 3	7 ± 1	1.9 ± 0.3	71.4 ± 4.5
	4.85	408 ± 2	12 ± 1	2.8 ± 0.2	-282.4 ± 5.7
1048+0141	2.64	465 ± 6	–	–	–
	1.40	380 ± 10	–	–	–
	0.36	554 ± 43	–	–	–
	0.32	–	–	–	–
	0.15	–	–	–	–
	0.07	1050±150	–	–	–
	14.60	552 ± 4	11 ± 4	2.1 ± 0.7	61.3 ± 8.9
	10.45	614 ± 13	15 ± 1	2.4 ± 0.1	45.3 ± 1.0
	8.35	631 ± 3	15 ± 1	2.4 ± 0.1	34.7 ± 1.5
	4.85	630 ± 2	18 ± 1	3.0 ± 0.2	-17.5 ± 5.2
1146+5356	2.64	578 ± 7	12 ± 2	2.1 ± 0.4	-244.5 ± 5.2
	1.40	367 ± 11	–	–	–
	0.36	340 ± 20	–	–	–
	0.32	398 ± 4	–	–	–
	0.15	286 ± 20	–	–	–
	0.07	<300	–	–	–
	14.60	332 ± 3	13 ± 3	4.0 ± 1.0	51.0 ± 7.4
	10.45	421 ± 2	15 ± 1	3.5 ± 0.3	53.5 ± 1.9
	8.35	487 ± 2	18 ± 1	3.7 ± 0.1	55.7 ± 1.0
	4.85	693 ± 3	23 ± 2	3.3 ± 0.2	58.8 ± 1.5
1213+1307	2.64	976 ± 3	26 ± 1	2.7 ± 0.0	67.2 ± 0.8
	1.40	1340 ± 40	–	–	–
	0.36	2520 ± 70	–	–	–
	0.32	–	–	–	–
	0.15	–	–	–	–
	0.07	4890 ± 510	–	–	–
	14.60	1030 ± 08	13 ± 1	1.2 ± 0.1	-4.7 ± 6.7
	10.45	1040 ± 23	12 ± 1	1.1 ± 0.1	9.1 ± 4.6
	8.35	965 ± 8	8 ± 1	0.8 ± 0.1	29.1 ± 3.6
	4.85	917 ± 4	9 ± 1	1.0 ± 0.2	180.3 ± 6.4
1246–0730	2.64	686 ± 9	13 ± 3	1.8 ± 0.4	576.8 ± 6.2
	1.40	550 ± 20	–	–	–
	0.36	948 ± 37	–	–	–
	0.32	–	–	–	–
	0.15	–	–	–	–
	0.07	1280 ± 160	–	–	–
	14.60	150 ± 3	10 ± 2	6.8 ± 1.0	99.8 ± 3.8
	10.45	207 ± 1	11 ± 1	5.1 ± 0.4	115.9 ± 3.4
	8.35	252 ± 2	14 ± 1	5.4 ± 0.3	136.0 ± 2.0
	4.85	414 ± 3	7 ± 2	1.6 ± 0.4	154.4 ± 6.6
1311+1417	2.64	614 ± 8	4 ± 1	0.6 ± 0.1	494.5 ± 7.2
	1.40	734 ± 22	–	–	–
	0.36	291 ± 25	–	–	–
	0.32	–	–	–	–
	0.15	–	–	–	–
	0.07	<300	–	–	–

Table A.4: Table of values A.1. Continued.

Name	ν [GHz]	S [mJy]	S_{Pol} [mJy]	m [%]	χ [deg]
	14.60	106 ± 3	5 ± 1	4.5 ± 2.3	1.1 ± 15.1
	10.45	140 ± 4	6 ± 1	4.0 ± 0.7	-8.1 ± 0.1
	8.35	164 ± 1	4 ± 1	2.6 ± 0.4	-35.4 ± 4.5
	4.85	253 ± 2	–	–	–
1312+5548	2.64	390 ± 5	–	–	–
	1.40	590 ± 20	–	–	–
	0.36	491 ± 36	–	–	–
	0.32	410 ± 4	–	–	–
	0.15	198 ± 30	–	–	–
	0.07	<300	–	–	–
	14.60	283 ± 4	5 ± 1	1.8 ± 0.5	93.0 ± 8.3
	10.45	308 ± 5	9 ± 2	2.8 ± 0.7	92.1 ± 10.7
	8.35	317 ± 2	8 ± 1	2.3 ± 0.3	94.4 ± 3.6
	4.85	297 ± 2	8 ± 1	2.6 ± 0.4	99.1 ± 6.5
1351+0830	2.64	290 ± 4	6 ± 2	2.0 ± 0.8	140.5 ± 12.0
	1.40	350 ± 10	–	–	–
	0.36	–	–	–	–
	0.32	–	–	–	–
	0.15	–	–	–	–
	0.07	<300	–	–	–
	14.60	723 ± 5	–	–	–
	10.45	712 ± 10	16 ± 5	2.3 ± 0.6	2.2 ± 7.3
	8.35	772 ± 3	13 ± 1	1.7 ± 0.1	9.3 ± 1.6
	4.85	803 ± 3	23 ± 1	2.8 ± 0.1	185.6 ± 2.1
1405+0415	2.64	893 ± 11	33 ± 3	3.6 ± 0.2	728.3 ± 2.0
	1.40	930 ± 30	–	–	–
	0.36	1240 ± 30	–	–	–
	0.32	–	–	–	–
	0.15	–	–	–	–
	0.07	3170 ± 330	–	–	–
	14.60	112 ± 2	13 ± 4	11.8 ± 3.3	121.6 ± 8.1
	10.45	146 ± 1	11 ± 1	7.3 ± 0.3	126.2 ± 0.1
	8.35	175 ± 1	9 ± 1	5.2 ± 0.4	129.8 ± 2.4
	4.85	259 ± 2	8 ± 2	3.1 ± 0.6	134.3 ± 4.4
1435–0414	2.64	375 ± 6	–	–	–
	1.40	480 ± 10	–	–	–
	0.36	753 ± 36	–	–	–
	0.32	–	–	–	–
	0.15	–	–	–	–
	0.07	1070 ± 160	–	–	–
	14.60	733 ± 6	11 ± 4	1.5 ± 0.5	90.2 ± 8.9
	10.45	813 ± 1	14 ± 1	1.7 ± 0.1	99.5 ± 2.1
	8.35	844 ± 4	12 ± 1	1.3 ± 0.1	106.1 ± 1.9
	4.85	812 ± 3	5 ± 1	0.6 ± 0.2	117.1 ± 8.6
1549+5038	2.64	648 ± 8	–	–	–
	1.40	630 ± 20	–	–	–
	0.36	397 ± 35	–	–	–
	0.32	348 ± 4	–	–	–
	0.15	<69	–	–	–
	0.07	<300	–	–	–

Table A.5: Table of values *A.1*. Continued.

Name	ν [GHz]	S [mJy]	S_{Pol} [mJy]	m [%]	χ [deg]
	14.60	885 ± 3	23 ± 1	2.6 ± 0.1	-55.0 ± 1.6
	10.45	1035 ± 10	16 ± 1	1.5 ± 0.1	-1.0 ± 1.4
	8.35	1160 ± 9	19 ± 1	1.6 ± 0.1	70.6 ± 1.5
	4.85	1140 ± 5	–	–	–
1616+0459	2.64	777 ± 9	–	–	–
	1.40	330 ± 10	–	–	–
	0.36	301 ± 50	–	–	–
	0.32	–	–	–	–
	0.15	–	–	–	–
	0.07	1060 ± 140	–	–	–
	14.60	216 ± 1	15 ± 1	6.7 ± 0.4	97.0 ± 3.3
	10.45	294 ± 5	19 ± 1	6.4 ± 0.1	96.0 ± 0.7
	8.35	375 ± 3	20 ± 1	5.3 ± 0.2	93.4 ± 1.1
	4.85	618 ± 3	6 ± 2	1.0 ± 0.2	65.7 ± 6.7
1616+2647	2.64	959 ± 12	–	–	–
	1.40	1480 ± 50	–	–	–
	0.36	1710 ± 36	–	–	–
	0.32	–	–	–	–
	0.15	–	–	–	–
	0.07	1140 ± 130	–	–	–
	14.60	117 ± 1	13 ± 1	10.8 ± 1.1	89.0 ± 2.6
	10.45	152 ± 2	17 ± 1	11.4 ± 0.3	90.1 ± 3.8
	8.35	181 ± 1	19 ± 1	10.4 ± 0.3	92.7 ± 1.0
	4.85	276 ± 2	17 ± 1	6.1 ± 0.4	100.6 ± 2.6
1647+3752	2.64	431 ± 7	7 ± 2	1.5 ± 0.4	147 ± 9.1
	1.40	630 ± 20	–	–	–
	0.36	–	–	–	–
	0.32	1480 ± 5	–	–	–
	0.15	1920 ± 50	–	–	–
	0.07	2730 ± 290	–	–	–
	14.60	080 ± 2	10 ± 3	12.5 ± 4.2	73.2 ± 9.7
	10.45	124 ± 2	15 ± 1	11.7 ± 0.1	78.8 ± 1.6
	8.35	159 ± 1	18 ± 1	11.5 ± 0.4	77.0 ± 1.0
	4.85	301 ± 2	25 ± 1	8.2 ± 0.4	86.4 ± 1.7
1713+2813	2.64	566 ± 2	24 ± 1	4.3 ± 0.1	130.6 ± 1.2
	1.40	1030 ± 10	–	–	–
	0.36	2530 ± 50	–	–	–
	0.32	–	–	–	–
	0.15	–	–	–	–
	0.07	4980 ± 530	–	–	–
	14.60	139 ± 4	7 ± 2	4.8 ± 1.5	82.6 ± 3.7
	10.45	162 ± 1	8 ± 1	5.1 ± 0.6	86.3 ± 0.3
	8.35	176 ± 1	7 ± 1	4.0 ± 0.4	86.3 ± 2.7
	4.85	329 ± 2	8 ± 1	2.3 ± 0.3	98.8 ± 5.4
1723+3417	2.64	716 ± 2	24 ± 2	3.3 ± 0.2	140.5 ± 1.4
	1.40	520 ± 20	–	–	–
	0.36	–	–	–	–
	0.32	4105 ± 3	–	–	–
	0.15	<75	–	–	–
	0.07	<300	–	–	–

Table A.6: Table of values A.1. Continued.

Name	ν [GHz]	S [mJy]	S_{Pol} [mJy]	m [%]	χ [deg]
	14.60	524 ± 6	17 ± 3	3.0 ± 0.5	-49.0 ± 11.1
	10.45	566 ± 2	29 ± 1	5.1 ± 0.1	-38.1 ± 0.2
	8.35	598 ± 5	26 ± 1	4.2 ± 0.1	-37.8 ± 1.1
	4.85	623 ± 3	23 ± 2	3.7 ± 0.3	-28.1 ± 2.0
2050+0407	2.64	607 ± 7	9 ± 3	1.3 ± 0.4	2.6 ± 8.1
	1.40	565 ± 17	–	–	–
	0.36	410 ± 26	–	–	–
	0.32	–	–	–	–
	0.15	–	–	–	–
	0.07	<300	–	–	–
	14.60	918 ± 9	32 ± 4	3.4 ± 0.4	116.3 ± 3.4
	10.45	969 ± 1	42 ± 3	4.3 ± 0.3	116.5 ± 2.1
	8.35	878 ± 7	39 ± 1	4.4 ± 0.1	120.9 ± 0.8
	4.85	853 ± 4	22 ± 2	2.5 ± 0.2	125.7 ± 1.7
2101+0341	2.64	684 ± 5	9 ± 2	1.3 ± 0.3	170.6 ± 6.9
	1.40	630 ± 20	–	–	–
	0.36	–	–	–	–
	0.32	–	–	–	–
	0.15	–	–	–	–
	0.07	<300	–	–	–
	14.60	719 ± 7	15 ± 4	2.1 ± 0.5	-9.2 ± 6.5
	10.45	760 ± 5	16 ± 1	2.1 ± 0.1	15.2 ± 0.2
	8.35	748 ± 6	17 ± 1	2.2 ± 0.1	35.7 ± 1.8
	4.85	700 ± 4	12 ± 1	1.7 ± 0.2	250.9 ± 3.7
2147+0929	2.64	646 ± 5	–	–	–
	1.40	930 ± 30	–	–	–
	0.36	1120 ± 30	–	–	–
	0.32	–	–	–	–
	0.15	–	–	–	–
	0.07	2160 ± 230	–	–	–
	14.60	073 ± 3	–	–	–
	10.45	113 ± 1	7 ± 1	6.4 ± 0.2	69.3 ± 1.6
	8.35	149 ± 1	7 ± 1	5.0 ± 0.6	71.3 ± 3.1
	4.85	282 ± 2	11 ± 1	3.9 ± 0.4	73.6 ± 3.8
2200+0708	2.64	515 ± 1	12 ± 1	2.4 ± 0.1	60.3 ± 1.3
	1.40	896 ± 32	–	–	–
	0.36	2560 ± 76	–	–	–
	0.32	–	–	–	–
	0.15	–	–	–	–
	0.07	5750 ± 600	–	–	–
	14.60	296 ± 4	9 ± 3	3.0 ± 1.1	35.4 ± 11.1
	10.45	379 ± 7	11 ± 3	2.7 ± 1.0	36.9 ± 7.9
	8.35	409 ± 10	6 ± 1	1.3 ± 0.3	27.4 ± 5.9
	4.85	521 ± 3	4 ± 1	0.7 ± 0.3	-100.8 ± 12.9
2245+0324	2.64	559 ± 11	–	–	–
	1.40	480 ± 10	–	–	–
	0.36	–	–	–	–
	0.32	–	–	–	–
	0.15	–	–	–	–
	0.07	<300	–	–	–

A.2 Parameters used for the SEDs fit

Table A.7: Values of the SEDs best fit. Columns: name of the source, the best fit model, α_{thin} (for the steep spectrum and also for the various syncrotron components), peak flux density (S_{max}), the peak frequency (ν_{max}), and the χ^2. The flux density S is in Jy and the frequency ν is in GHz. Explanation on the abbreviation I use in the best-fit column: S_ν^{pl} is linear fit; S_ν^{plb} is linear fit with a break; S_ν^{s} is one synchrotron component; S_ν^{sb} is one synchrotron component with a break; S_ν^{s+} is two or more synchrotron components; S_ν^{pls} is linear fit at low frequency plus one or two synchrotron components at higher frequency.

Name	*type*	α_{thin}	χ^2					
0925+3159	S_ν^{pl}	–0.9	8.0					
0958+3224	S_ν^{pl}	–0.5	1170.0					
Name	*type*	α_{thin}	α_{break}	ν_{break}	S_{break}	χ^2		
1015+0318	S_ν^{plb}	–0.5	–1.0	4.2	0.290	1.4		
1213+1307	S_ν^{plb}	–0.4	–0.9	12.8	0.580	0.1		
1647+3752	S_ν^{plb}	–0.4	–1.0	4.5	0.466	3.0		
1713+2813	S_ν^{plb}	–0.4	–1.3	1.7	1.370	0.02		
2200+0708	S_ν^{plb}	–0.0	–1.0	0.2	6.263	29.0		
Name	*type*	α_{thin}	ν	S_ν	χ^2			
1723+3417	S_ν^{s}	–0.9	2.0	0.550	0.6			
2050+0407	S_ν^{s}	–0.1	1.1	0.700	5.0			
2245+0324	S_ν^{s}	–0.4	2.5	0.580	0.5			
Name	*type*	α_{thin}	α_{break}	ν	S_{nu}	ν_{break}	χ^2	
0751+2716	S_ν^{sb}	–0.0	–1.1	0.2	1.650	0.6	0.2	
1311+1417	S_ν^{sb}	–0.1	–1.2	1.2	0.773	4.0	0.02	
1435–0414	S_ν^{sb}	–0.3	–1.0	0.1	1.071	6.2	0.003	
Name	*type*	$\nu 1$	S_1	$\nu 2$	S_2	χ^2		
1351+0830	S_ν^{s+}	1.4	0.340	9.3	0.210	0.2		
1549+5038	S_ν^{s+}	0.7	0.908	7.6	0.700	8.1		
1616+2647	S_ν^{s+}	0.1	1.320	0.6	1.620	5.1		
2101+0341	S_ν^{s+}	1.9	0.720	9.9	0.700	5.0		
Name	*type*	$\nu 1$	S_1	$\nu 2$	S_2	$\nu 3$	S_3	χ^2
0239–0234	S_ν^{s+}	0.5	0.300	3.9	0.500	11.6	0.380	0.01
0742+4900	S_ν^{s+}	0.6	0.200	2.7	0.400	13.8	0.241	0.2
1043+2408	S_ν^{s+}	0.4	0.470	4.4	0.710	15.7	0.730	0.6
1044+0655	S_ν^{s+}	0.1	1.600	3.2	0.190	12.7	0.130	1.2
1048+0141	S_ν^{s+}	0.1	1.130	2.7	0.320	10.0	0.110	0.1
1146+5356	S_ν^{s+}	0.2	0.400	2.9	0.470	10.0	0.350	1.2
1246–0730	S_ν^{s+}	0.1	1.740	4.4	0.660	15.0	0.600	63.0
2147+0929	S_ν^{s+}	0.1	2.310	2.6	0.360	10.7	0.500	2.3
Name	*type*	α_{thin}	$\nu 2$	S_2	χ^2			
1312+5548	S_ν^{pls}	–0.7	0.7	0.750	0.3			
Name	*type*	$\nu 2$	S_2	$\nu 3$	S_3	χ^2		
0243–0550	S_ν^{pls}	1.2	0.480	6.6	0.450	0.1		
0845+0439	S_ν^{pls}	2.5	0.470	13.6	0.520	2.2		
1405+0415	S_ν^{pls}	1.0	0.770	8.2	0.500	25.0		
1616+0459	S_ν^{pls}	3.3	0.610	8.0	0.720	0.2		

A.3 Plots single dish data

Figure A.1: Sources 0239-0234, 0243-0550, 0742+4900, 0751+2716, 0845+0439, 0925+3159.. For each source we present their SED S[Jy], the polarisation flux density S_{pol}[Jy], the fractional polarisation m[%], and the polarisation angle PA[rad].

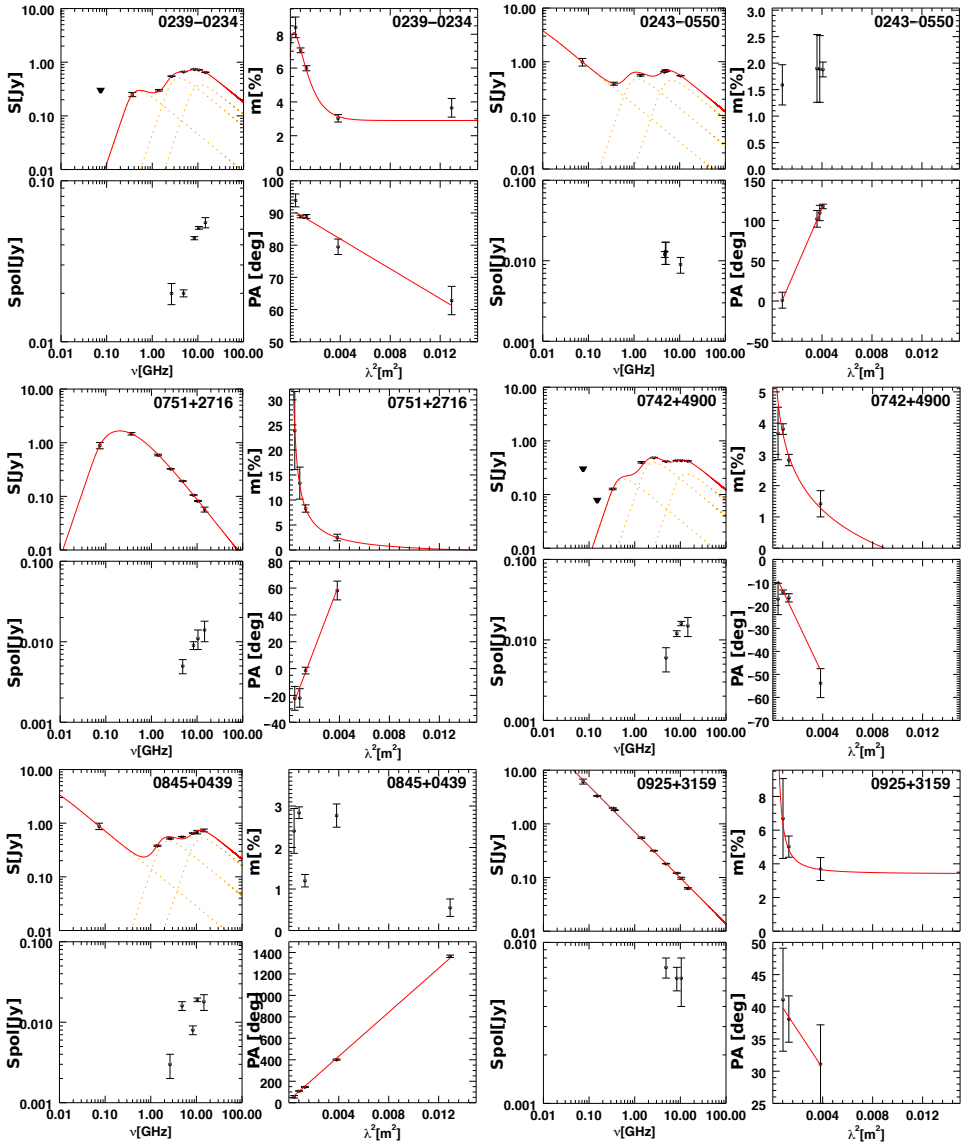

Figure A.2: Sources 0958+3224, 1015+0318, 1043+2408, 1044+0655, 1048+0141, 1146+5356. For each source we present their SED S[Jy], the polarisation flux density S_{pol}[Jy], the fractional polarisation m[%], and the polarisation angle PA[rad].

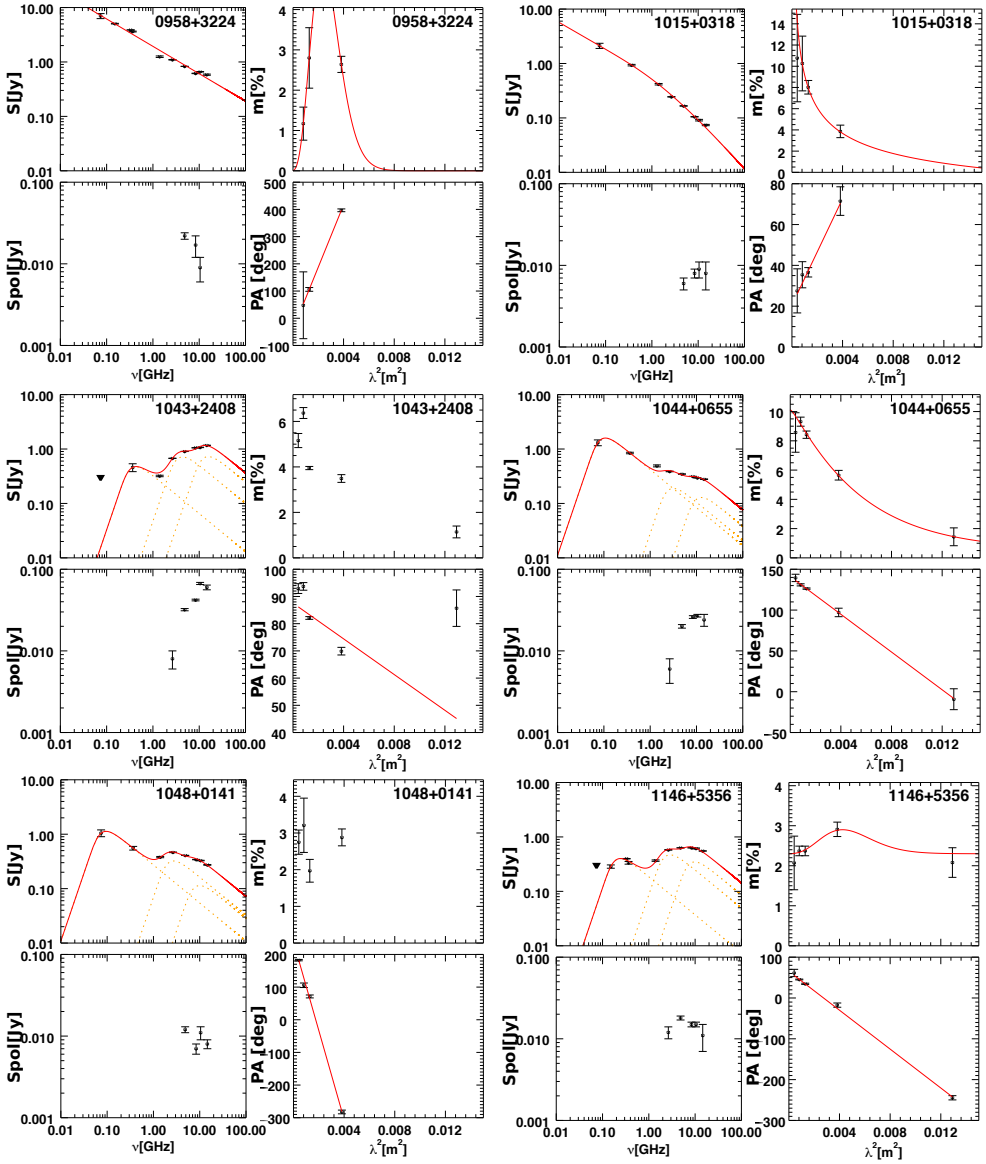

Figure A.3: Sources 1213+1307, 1246-0730, 1311+1417, 1312+5548, 1351+0830, 1405+0415. For each source we present their SED S[Jy], the polarisation flux density S_{pol}[Jy], the fractional polarisation m[%], and the polarisation angle PA[rad].

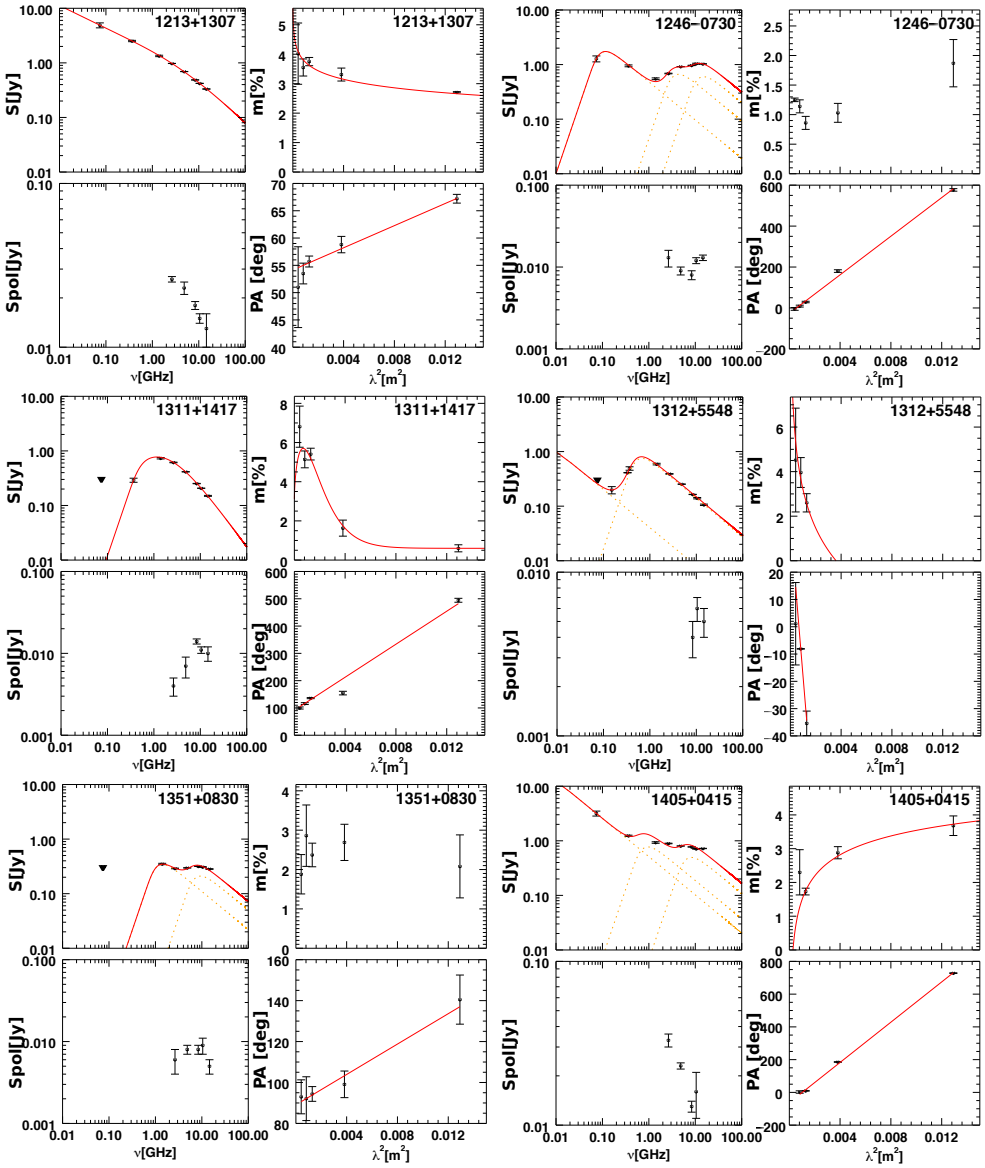

Figure A.4: Sources 1435-0414, 1549+5038, 1616+0459, 1616+2647, 1647+3752, and 1713+2813. For each source we present their SED S[Jy], the polarisation flux density S_{pol}[Jy], the fractional polarisation m[%], and the polarisation angle PA[rad].

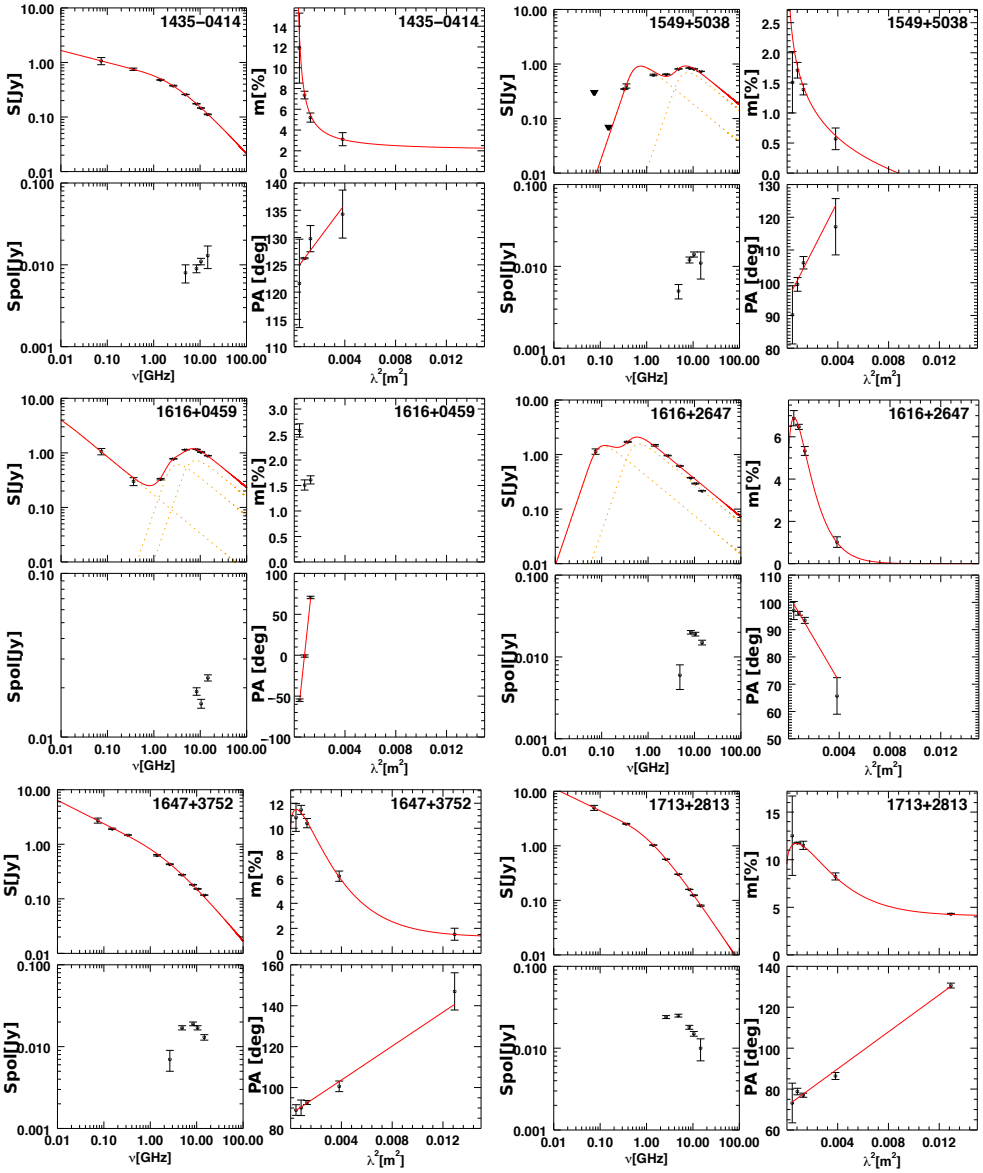

Figure A.5: Sources 1723+3417, 2050+0407, and 2101+0341, 2147+0929, 2200+0708 and 2245+0324. For each source we present their SED S[Jy], the polrization flux density S_{pol}[Jy], the fractional polarization m[%] and the polarization angle PA[rad].

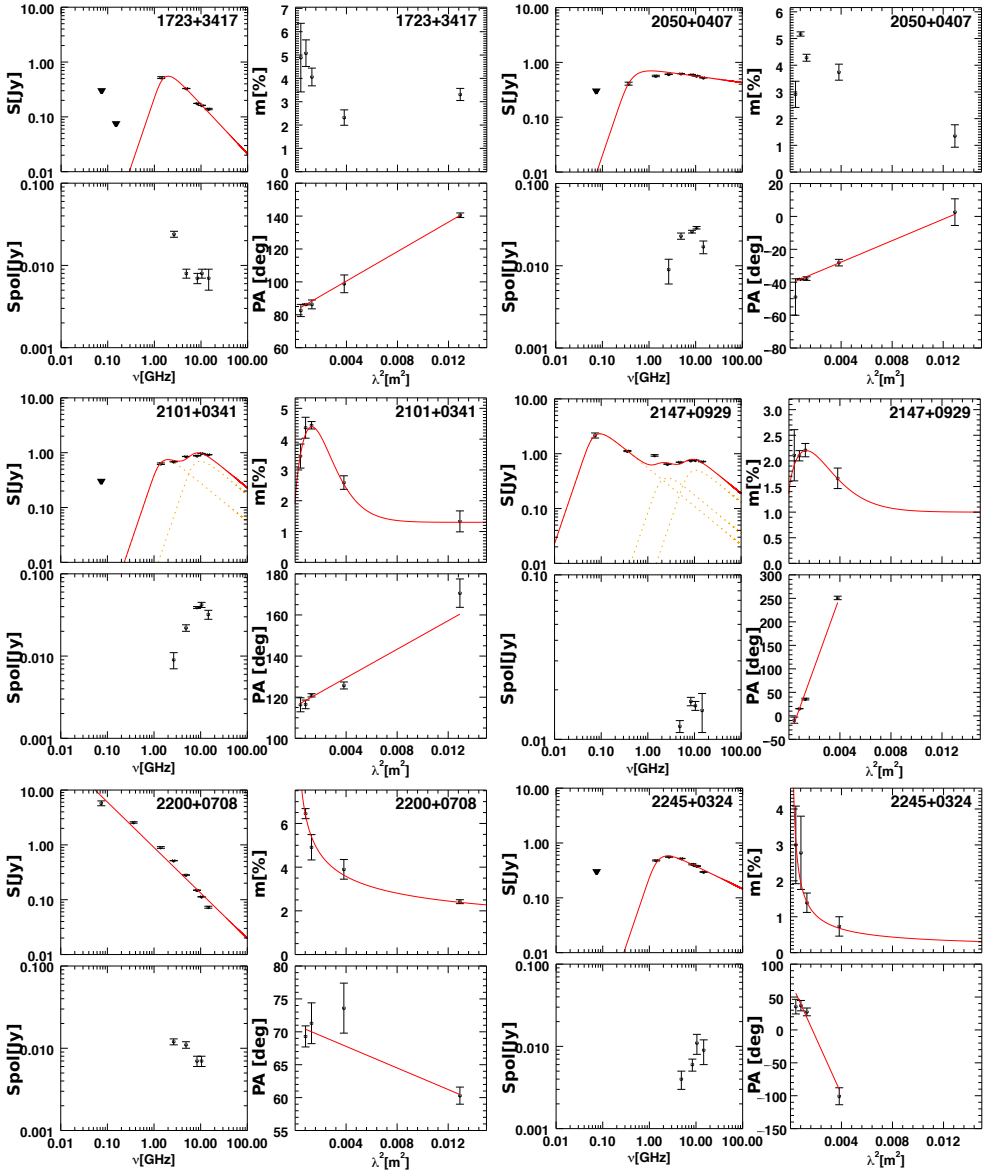

Appendix B

JVLA Appendix

Below we collected all the higher resolution images available mainly from the NRAO calibrator search tool webpage[1]. The other VLBI images have been downloaded from the NED (NASA/IPAC Extragalactic Database) webpage[2] and all of them have their own reference. Where VLBA images are reported, the flux density followed by the acronym "SB" is the flux density at short baseline while that followed by "LB" is the one determined at long baseline. The SDSS (Sloan Digital Sky Survey) spectrum, where available, is referred to the SDSS data release 12 (Alam et al., 2015). Two sources (1246–0730 and 1405+0415) are monitored in the MOJAVE programme (Lister et al., 2009). Their relative information (images and tables) have been downloaded from the MOJAVE web site[3]
In the captions, "ICRF2" catalogue refers to the International Celestial Reference Frame catalogue: see Gemini webpage[4].

–Source 0239-0234–

- VLBA image at S band: 0.30 Jy/beam (SB) and 0.30 Jy/beam (LB)
- VLBA image at X band: 0.48 Jy/beam (SB) and 0.39 Jy/beam(LB)
- VLBI astrometry data at K band (no image available, Lanyi et al., 2010): 0.6 Jy/beam
- VLBI astrometry data at Q band (no image available, Lanyi et al., 2010): 0.4 Jy/beam
- No SDSS spectrum

–Source 0243-0550–

- VLBA image at S band: 0.86 Jy/beam (SB) and 0.44 Jy/beam (LB)
- VLBA image at X band: 0.65 Jy/beam (SB) and 0.44 Jy/beam (LB)
- No SDSS spectrum

Figure B.1: Source 0239-0234: VLBA images at S band and X band (credit: NRAO VLBA calibrator search webpage[1], ICRF2 catalogue[4])

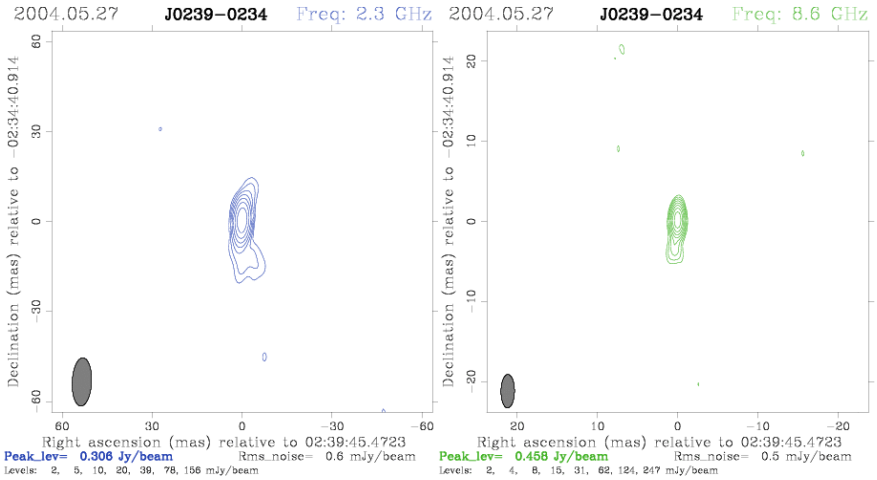

Figure B.2: Source 0243-0550: VLBA images at S band and X band (credit: NRAO VLBA calibrator search webpage[1], ICRF2 catalogue[4])

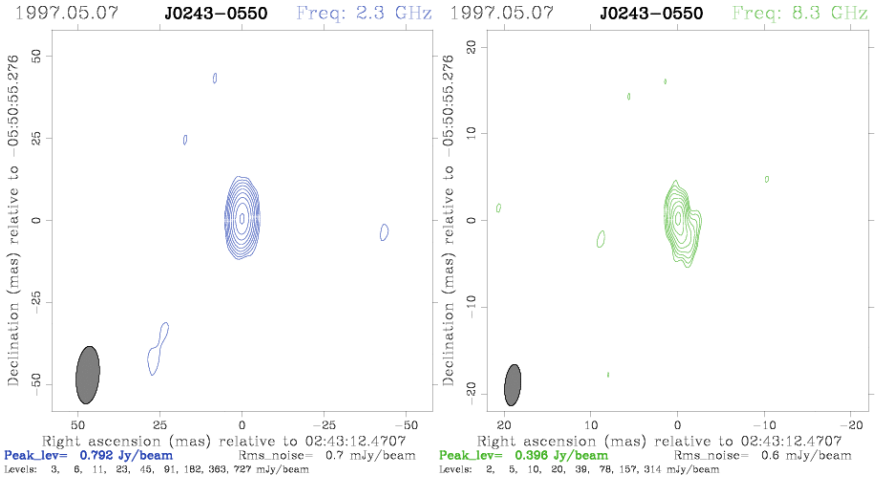

–Source 0845+0439–

- VLBA image at S band: 0.29 Jy/beam (SB) and 0.13 Jy/beam (LB)
- VLBA image at X band: 0.19 Jy/beam (SB) and 0.08 Jy/ beam (LB)
- No SDSS spectrum

[1]http://www.vlba.nrao.edu/astro/calib/
[2]https://ned.ipac.caltech.edu/
[3]http://www.physics.purdue.edu/astro/MOJAVE/index.html
[4]http://gemini.gsfc.nasa.gov/solutions/2010a/2010a.html

Figure B.3: Source 0845+0439: VLBA images at S band and X band (credit: NRAO VLBA calibrator search webpage[1], ICRF2 catalogue[4])

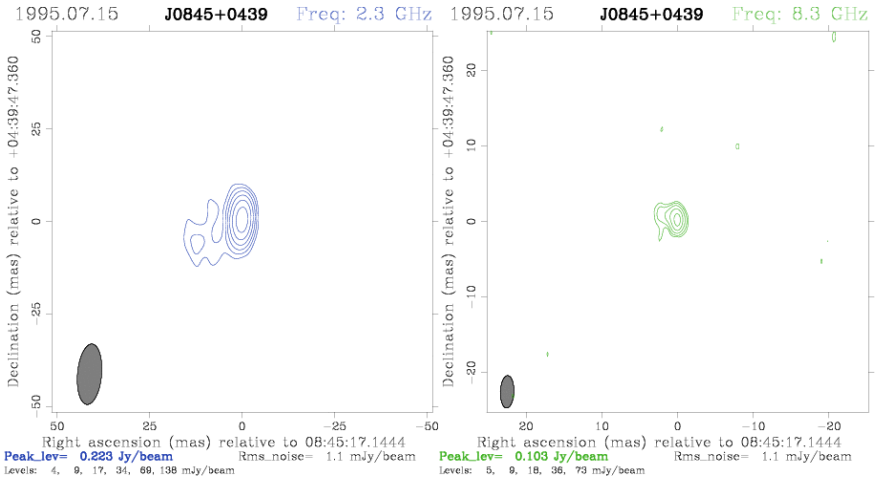

–Source 0958+3224–

- VLBA image at S band: 0.75 Jy/beam (SB) and 0.42 Jy/beam (LB)
- VLBA image at X band: 0.94 Jy/beam (SB) and 0.33 Jy/beam (LB)
- Yes SDSS spectrum (Alam et al., 2015)

Figure B.4: Source 0958+3224: VLBA images at S band and X band (credit: NRAO VLBA calibrator search webpage[1], ICRF2 catalogue[4]); SDSS spectrum (Alam et al., 2015)

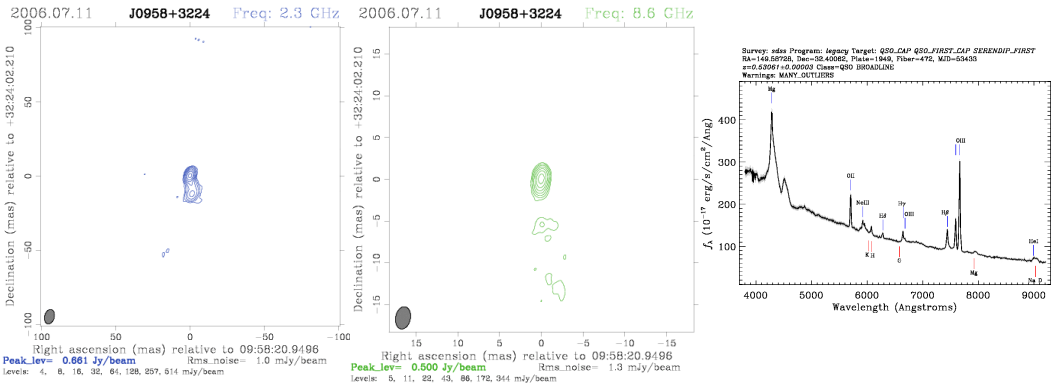

–Source 1048+0141–

- VLBA image at S band: 0.25 Jy/beam (SB) and 0.15 Jy/beam (LB)

- VLBA image at X band: 0.08 Jy/beam (SB) the flux density at larger baseline is not available
- No SDSS spectrum

Figure B.5: Source 1048+0141: VLBA images at S band and X band (credit: NRAO VLBA calibrator search webpage[1], ICRF2 catalogue[4])

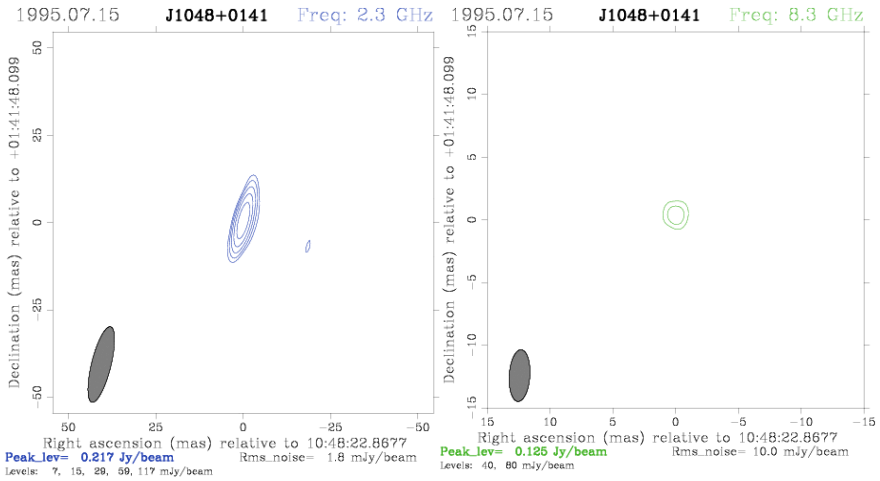

–Source 1146+5356–

- VLBA image at S band: 0.44 Jy/beam (SB) and 0.19 Jy/beam (LB)
- VLBA image at X band: 0.32 Jy/beam (SB) and 0.17Jy/beam (LB)
- VLBI image at L and C band available
- Yes SDSS spectrum (Alam et al., 2015)

–Source 1246–0730–

- VLBA image at S band: 0.67 Jy/beam (SB) and 0.36 Jy/beam (LB)
- VLBA image at X band: 0.93 Jy/beam (SB) and 0.73 Jy/beam (LB)
- It is monitored by the MOJAVE programme (Lister et al., 2009)
- No SDSS spectrum

–Source 1311+1417–

- VLBA image at S band: 0.81 Jy/beam (SB) and 0.26 Jy/beam (LB)
- VLBA image at X band: 0.24 Jy/beam (SB) and 0.08 Jy/beam (LB)

Table B.1: Source 1246–0730: MOJAVE information

epoch	VLBA code	I [mJy]	P [mJy]	VLBA P[%]	VLBA EVPA [deg]
2010-09-27	BL149CQ	1208	11	0.9	23
2010-01-16	BL149CG	1125	11	1.0	58
2009-05-02	BL149BK	1231	24	1.9	10
2008-11-26	BL149BF	1050	23	2.2	19
2008-05-30	BL149AI	1072	10	0.9	21
2007-08-24	BL149AM	1032	14	1.4	142
2007-04-18	BL137Q	899	12	1.3	157
2007-01-06	BL137R	776	17	2.2	155
2006-04-05	BL137C	539	15	2.8	173

- Yes SDSS spectrum (Alam et al., 2015)

–Source 1312+5548–

- No VLBA images available
- VLBI image at 5 GHz (Helmboldt et al., 2007)
- Yes SDSS spectrum (Alam et al., 2015)

–Source 1405+0415–

- NO high RM
- VLBA image at S band: 1.06 Jy/beam (SB) and 0.81 Jy/beam (LB)
- VLBA image at X band: 1.02 Jy/beam (SB) and 0.88 Jy/beam (LB)
- It is a MOJAVE monitored target (Lister et al., 2009)
- Yes SDSS spectrum (Alam et al., 2015)

–Source 1549+5038–

- VLBA image at S band: 0.75 Jy/beam (SB) and 0.24 Jy/beam (LB)
- VLBA image at X band: 1.01 Jy/beam (SB) and 0.51 Jy/beam (LB)
- VLBI images at 1.4 GHZ and 5 GHz available (Xu et al., 1995)
- Yes SDSS spectrum (Alam et al., 2015)

Table B.2: Source 1405+0415: MOJAVE information

Epoch	VLBA code	I [mJy]	P [mJy]	VLBA P[%]	VLBA EVPA [deg]
2015-10-02	BL193AX	653	11	1.7	164
2015-05-08	BL193AR	582	2	0.3	–
2014-05-12	BL193AI	609	9	1.5	17
2014-02-27	BL193AG	625	9	1.4	11
2013-12-15	BL193AA	656	8	1.2	9
1998-12-05	BG077C	629	–	–	–
1998-09-29	BG077B	548	–	–	–
1998-06-05	BG077	555	–	–	–

–Source 1616+0459–

- VLBA image at S band: 0.53 Jy/beam (SB) and 0.40 Jy/beam (LB)
- VLBA image at X band: 0.54 Jy/beam (SB) and 0.29 Jy/beam (LB)
- No SDSS spectrum

–Source 2245+0324–

- VLBA image at S band: 0.68 Jy/beam (SB) and 0.55 Jy/beam (LB)
- VLBA image at X band: 0.59 Jy/beam (SB) and 0.34 Jy/beam (LB)
- No SDSS spectrum

Figure B.6: Source 1146+5356: VLBA images at S band and X band (credit: NRAO VLBA calibrator search webpage[1], ICRF2 catalogue[4]); VLBI images L band and C band (Xu et al., 1995); SDSS spectrum (Alam et al., 2015)

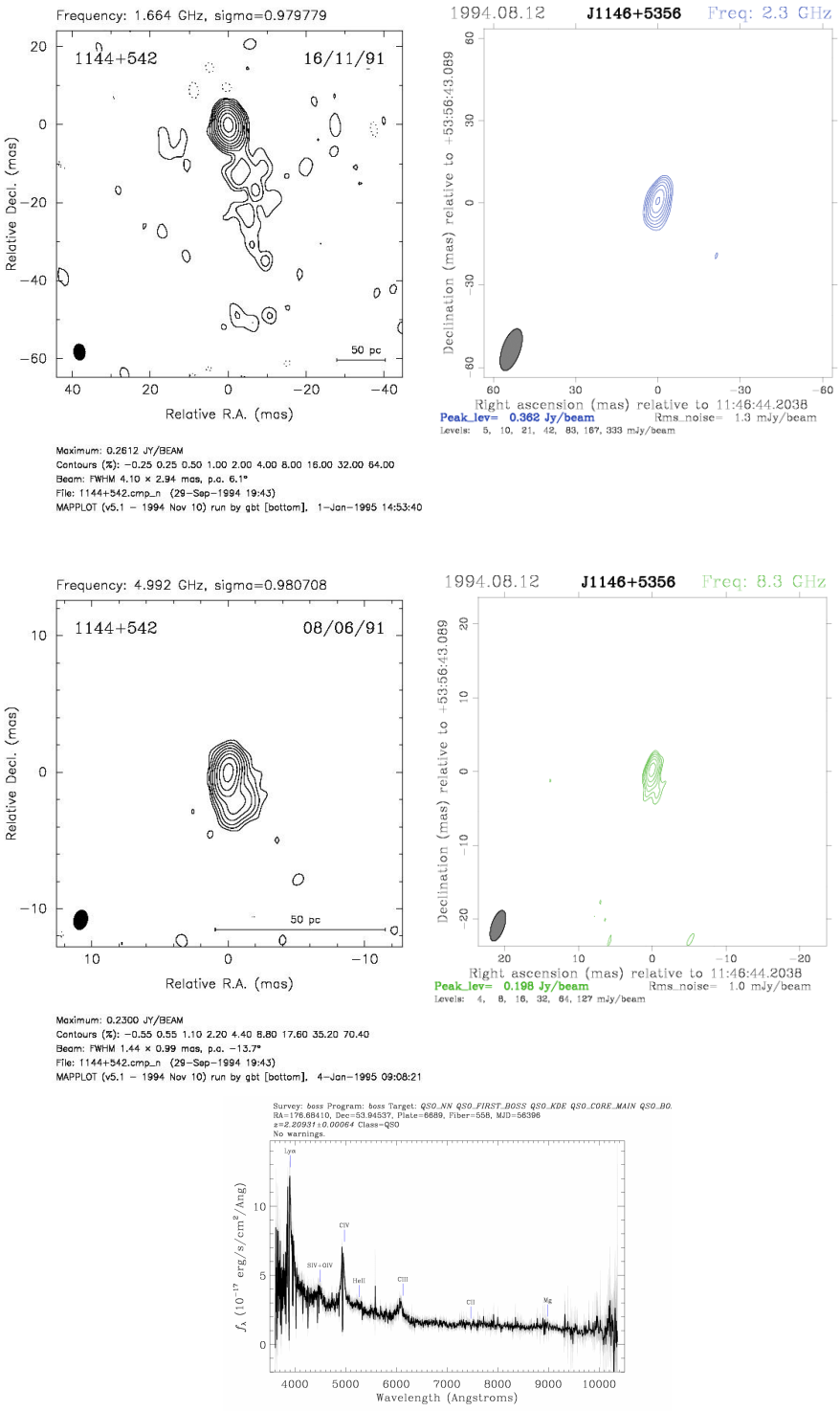

Figure B.7: Source 1246-0730: VLBA images at S band and X band (credit: NRAO VLBA calibrator search webpage[1], ICRF2 catalogue[4]) and MOJAVE image (Lister et al., 2009)

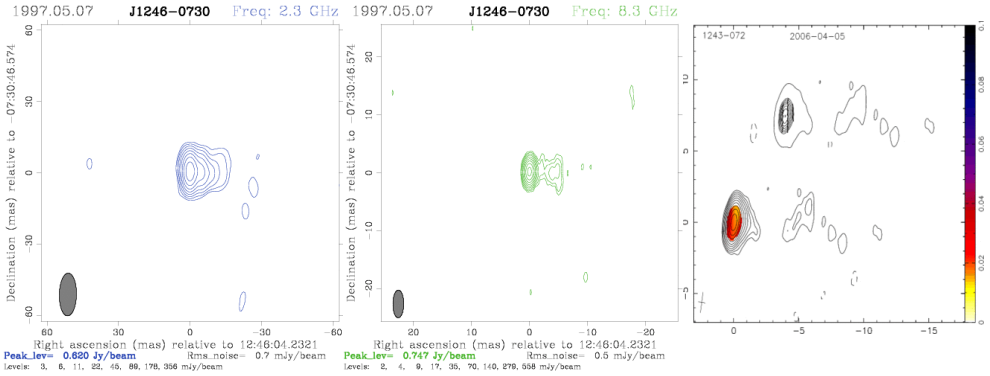

Figure B.8: Source 1246-0730: RM map from MOJAVE data (Hovatta et al., 2012).

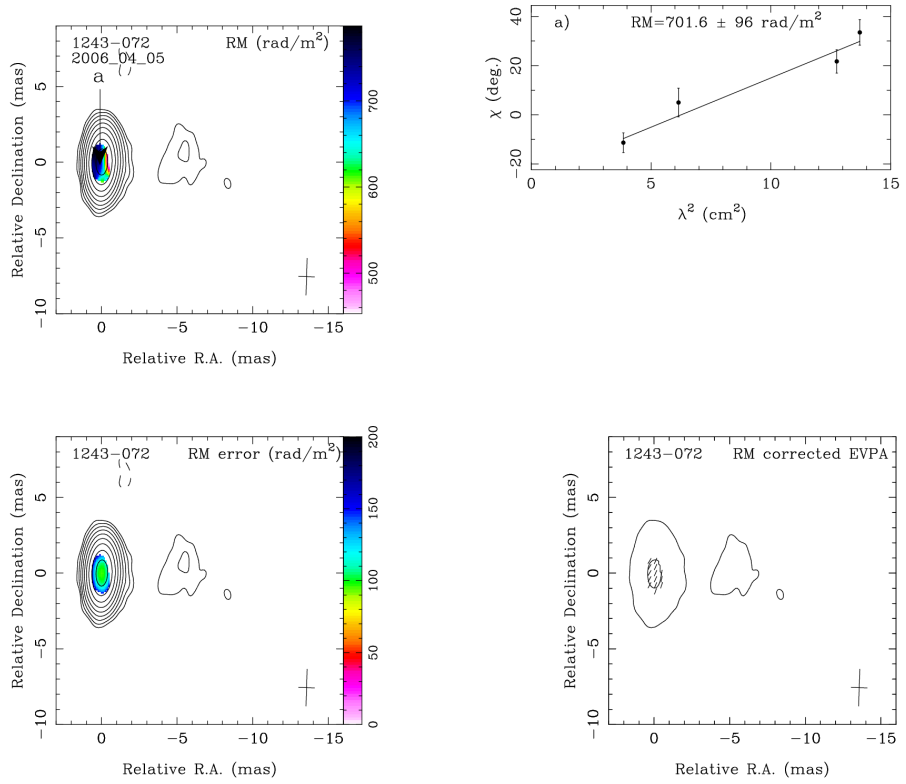

Figure B.9: Source 1311+1417: VLBA images at S band and X band (credit: NRAO VLBA calibrator search webpage[1], ICRF2 catalogue[4]); SDSS spectrum (Alam et al., 2015)

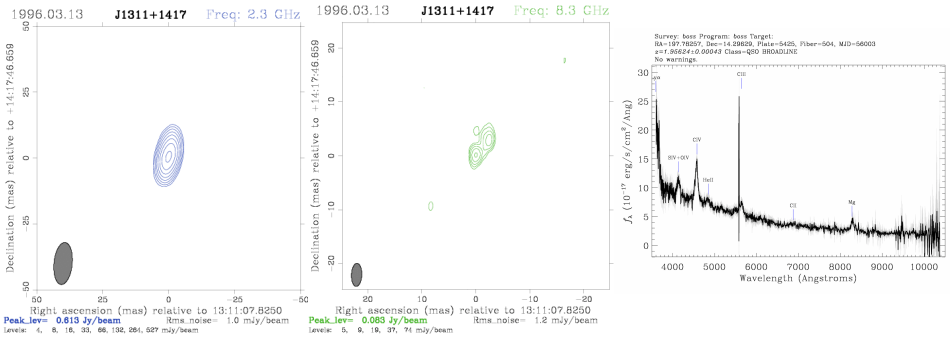

Figure B.10: Source 1312+5548: VLBI image at 5 GHz (Helmboldt et al., 2007) and SDSS spectrum (Alam et al., 2015).

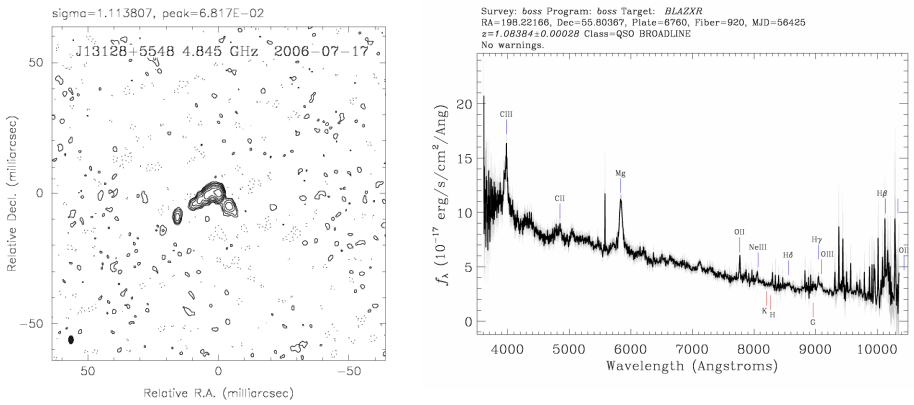

Figure B.11: Source 1405+0415: VLBA images at S band and X band (credit: NRAO VLBA calibrator search webpage[1], ICRF2 catalogue[4]); MOJAVE total intensity and polarization image (Lister et al., 2009) and SDSS spectrum (Alam et al., 2015)

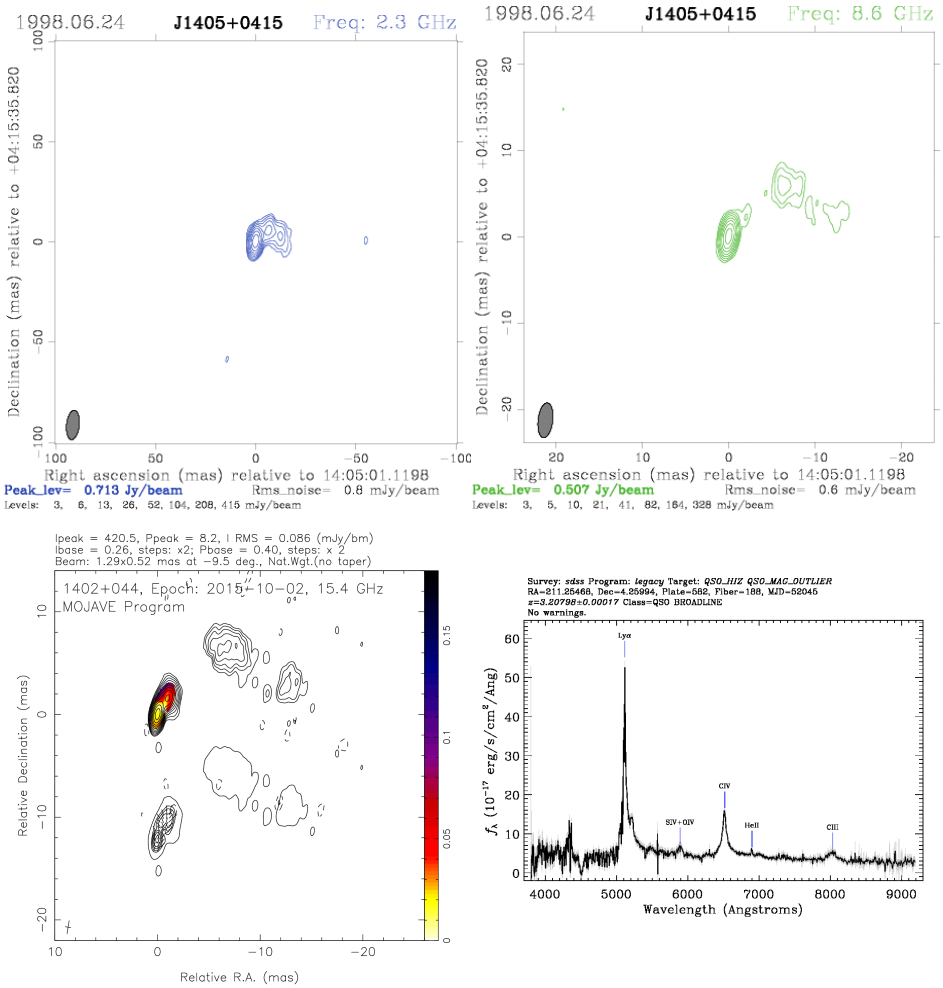

Figure B.12: Source 1549+5038: VLBA images at S band and X band (credit: NRAO VLBA calibrator search webpage[1], ICRF2 catalogue[4]); VLBI images at 1.4 GHz and 5 GHz (Xu et al., 1995) ; SDSS spectrum (Alam et al., 2015).

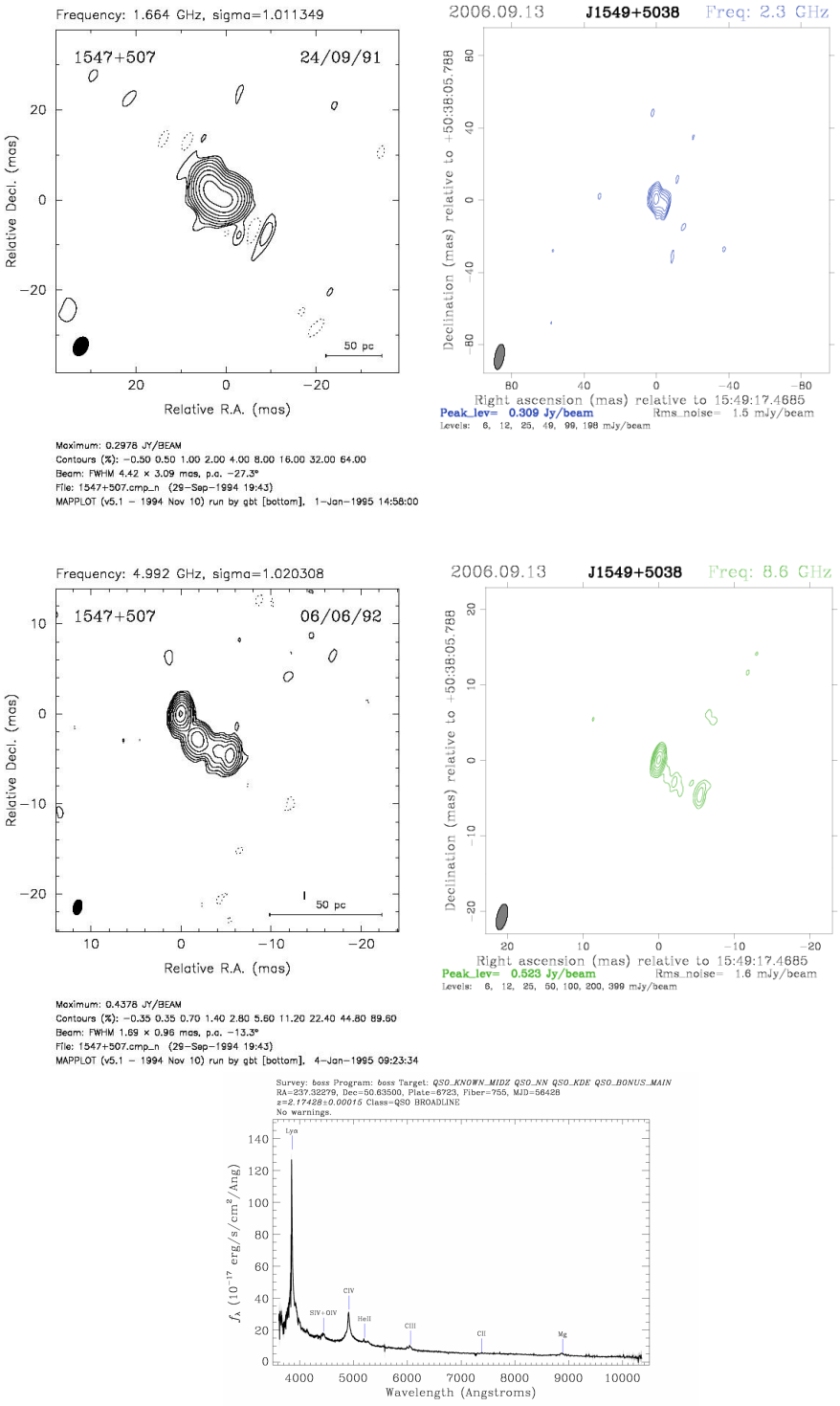

Figure B.13: Source 1616+0459: VLBA images at S band and X band (credit: NRAO VLBA calibrator search webpage[1], ICRF2 catalogue[4])

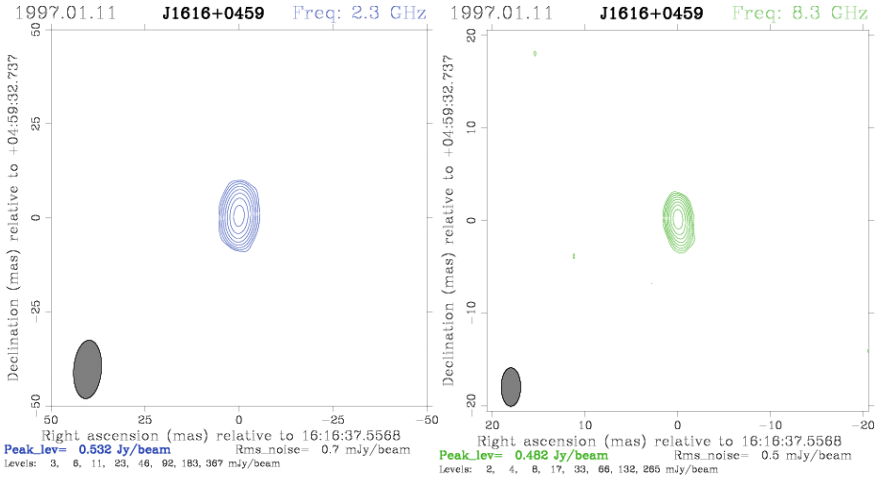

Figure B.14: Source 2245+0324: VLBA images at S band and X band (credit: NRAO VLBA calibrator search webpage[1], ICRF2 catalogue[4])

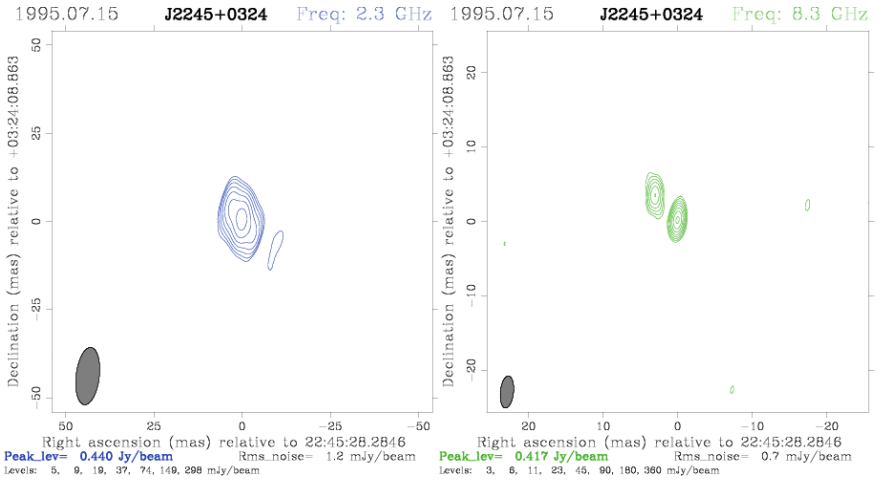

Bibliography

Abbott B. P., Abbott R., Abbott T. D., Abernathy M. R., Acernese F., Ackley K., Adams C., Adams T., Addesso P., Adhikari R. X., et al. 2016, Physical Review Letters, 116, 061102

Akahori T., Ryu D., 2011, ApJ, 738, 134

Alam S., Albareti F. D., Allende Prieto C., Anders F., Anderson S. F., Anderton T., Andrews B. H., Armengaud E., Aubourg É., Bailey S., et al. 2015, ApJS, 219, 12

Alexander P., Leahy J. P., 1987, MNRAS, 225, 1

Antonucci R., 1993, ARA&A, 31, 473

Antonucci R. R. J., Miller J. S., 1984, in Bulletin of the American Astronomical Society Vol. 16 of BAAS, The Seyfert 1 Inside NGC 1068. p. 957

Arp H. C., Bolton J. G., Kinman T. D., 1967, ApJ, 147, 840

Asada K., Inoue M., Uchida Y., Kameno S., Fujisawa K., Iguchi S., Mutoh M., 2002, PASJ, 54, L39

Attridge J. M., Wardle J. F. C., Homan D. C., Phillips R. B., 2005, in Romney J., Reid M., eds, Future Directions in High Resolution Astronomy Vol. 340 of Astronomical Society of the Pacific Conference Series, Concurrent 43 and 86 GHz VLBA Polarimetry Observations of the Quasars 3C 273 and 3C 279. p. 171

Axon D. J., Capetti A., Fanti R., Morganti R., Robinson A., Spencer R., 2000, AJ, 120, 2284

Baade W., Minkowski R., 1954, ApJ, 119, 206

Baars J. W. M., Genzel R., Pauliny-Toth I. I. K., Witzel A., 1977, A&A, 61, 99

Barthel P. D., 1989, ApJ, 336, 606

Benn C. R., Carballo R., Holt J., Vigotti M., González-Serrano J. I., Mack K.-H., Perley R. A., 2005, MNRAS, 360, 1455

Blandford R. D., Königl A., 1979, ApJ, 232, 34

Blandford R. D., McKee C. F., 1982, ApJ, 255, 419

Blandford R. D., Netzer H., Woltjer L., Courvoisier T. J.-L., Mayor M., eds, 1990, Active Galactic Nuclei

Blandford R. D., Payne D. G., 1982, MNRAS, 199, 883

Boccardi B., Krichbaum T. P., Bach U., Mertens F., Ros E., Alef W., Zensus J. A., 2016, A&A, 585, A33

Bower R. G., Benson A. J., Malbon R., Helly J. C., Frenk C. S., Baugh C. M., Cole S., Lacey C. G., 2006, MNRAS, 370, 645

Briggs E. L., 1995, PhD thesis, NORTH CAROLINA STATE UNIVERSITY.

Burbidge E. M., 1967, ApJ, 149, L51

Burn B. J., 1966, MNRAS, 133, 67

Carvalho J. C., 1998, A&A, 329, 845

Charlot P., Boboltz D. A., Fey A. L., Fomalont E. B., Geldzahler B. J., Gordon D., Jacobs C. S., Lanyi G. E., Ma C., Naudet C. J., Romney J. D., Sovers O. J., Zhang L. D., 2010, AJ, 139, 1713

Cohen A. S., Lane W. M., Cotton W. D., Kassim N. E., Lazio T. J. W., Perley R. A., Condon J. J., Erickson W. C., 2007, AJ, 134, 1245

Condon J. J., Cotton W. D., Greisen E. W., Yin Q. F., Perley R. A., Taylor G. B., Broderick J. J., 1998, AJ, 115, 1693

Czerny B., Siemiginowska A., Janiuk A., Nikiel-Wroczyński B., Stawarz Ł., 2009, ApJ, 698, 840

Dallacasa D., 2003, PASA, 20, 79

Dallacasa D., Fanti C., Fanti R., 1993, in Röser H.-J., Meisenheimer K., eds, Jets in Extragalactic Radio Sources Vol. 421 of Lecture Notes in Physics, Berlin Springer Verlag, Compact Steep-Spectrum Radio Sources: A Progress Report. p. 27

Dallacasa D., Stanghellini C., Centonza M., Fanti R., 2000, A&A, 363, 887

de Vries W. H., O'Dea C. P., Baum S. A., Barthel P. D., 1999, ApJ, 526, 27

de Vries W. H., O'Dea C. P., Baum S. A., Sparks W. B., Biretta J., de Koff S., Golombek D., Lehnert M. D., Macchetto F., McCarthy P., Miley G. K., 1997, ApJS, 110, 191

De Young D. S., 1993, ApJ, 402, 95

Djorgovski S., Strauss M. A., Spinrad H., McCarthy P., Perley R. A., 1987, AJ, 93, 1318

Douglas J. N., Bash F. N., Bozyan F. A., Torrence G. W., Wolfe C., 1996, AJ, 111, 1945

Eckart A., Genzel R., Ott T., Schödel R., 2002, MNRAS, 331, 917

Elvis M., 2000, ApJ, 545, 63

Evans I. N., Ford H. C., Kinney A. L., Antonucci R. R. J., Armus L., Caganoff S., 1991, ApJ, 369, L27

Fanaroff B. L., Riley J. M., 1974, MNRAS, 167, 31P

Fanti C., Fanti R., Dallacasa D., Schilizzi R. T., Spencer R. E., Stanghellini C., 1995, A&A, 302, 317

Fanti R., Fanti C., Schilizzi R. T., Spencer R. E., Nan Rendong Parma P., van Breugel W. J. M., Venturi T., 1990, A&A, 231, 333

Farnes J. S., Gaensler B. M., Carretti E., 2014, ApJS, 212, 15

Ferrarese L., Merritt D., 2000, ApJ, 539, L9

Fletcher A., Beck R., Shukurov A., Berkhuijsen E. M., Horellou C., 2011, MNRAS, 412, 2396

Gabuzda D. C., Murray É., Cronin P., 2004, MNRAS, 351, L89

Garcia-Burillo S., Combes F., Usero e. a., 2014, A&A, 567, A125

George I. M., 1991, The Observatory, 111, 256

Ghez A. M., Morris M., Becklin E. E., Tanner A., Kremenek T., 2000, Nature, 407, 349

Ghisellini G., Tavecchio F., Chiaberge M., 2005, A&A, 432, 401

Ghisellini G., Tavecchio F., Maraschi L., Celotti A., Sbarrato T., 2014, Nature, 515, 376

Giovannini G., Dallacasa D., Feretti L., Venturi T., 1989, in Meurs E. J. A., Fosbury R. A. E., eds, European Southern Observatory Conference and Workshop Proceedings Vol. 32 of European Southern Observatory Conference and Workshop Proceedings, Bent Jets in Coma Cluster Radio Galaxies. p. 157

Giroletti M., Giovannini G., Feretti L., Cotton W. D., Edwards P. G., Lara L., Marscher A. P., Mattox J. R., Piner B. G., Venturi T., 2004, ApJ, 600, 127

Gómez J. L., Agudo I., Marscher A. P., Jorstad S. G., Roca-Sogorb M., 2008, MEMSAI, 79, 1157

Gómez J. L., Lobanov A. P., Bruni G., Kovalev Y. Y., Marscher A. P., Jorstad S. G., Mizuno Y., Bach U., Sokolovsky K. V., Anderson J. M., Galindo P., Kardashev N. S., Lisakov M. M., 2016, ApJ, 817, 96

Gómez J.-L., Marscher A. P., Alberdi A., Jorstad S. G., García-Miró C., 2000, Science, 289, 2317

Gómez J. L., Roca-Sogorb M., Agudo I., Marscher A. P., Jorstad S. G., 2011, ApJ, 733, 11

Gopal-Krishna Patnaik A. R., Steppe H., 1983, A&A, 123, 107

Gratadour D., Rouan D., Grosset L., Boccaletti A., Clénet Y., 2015, A&A, 581, L8

Greene J. E., Seth A., den Brok M., Braatz J. A., Henkel C., Sun A.-L., Peng C. Y., Kuo C.-Y., Impellizzeri C. M. V., Lo K. Y., 2013, ApJ, 771, 121

Greenstein J. L., Matthews T. A., 1963, AJ, 68, 279

Greenstein J. L., Schmidt M., 1964, ApJ, 140, 1

Gupta N., Salter C. J., Saikia D. J., Ghosh T., Jeyakumar S., 2006, MNRAS, 373, 972

Hales S. E. G., Riley J. M., Waldram E. M., Warner P. J., Baldwin J. E., 2007, MNRAS, 382, 1639

Helmboldt J. F., Taylor G. B., Tremblay S., Fassnacht C. D., Walker R. C., Myers S. T., Sjouwerman L. O., Pearson T. J., Readhead A. C. S., Weintraub L., Gehrels N., Romani R. W., Healey S., Michelson P. F., Blandford R. D., Cotter G., 2007, ApJ, 658, 203

Homan D. C., Ojha R., Wardle J. F. C., Roberts D. H., Aller M. F., Aller H. D., Hughes P. A., 2002, ApJ, 568, 99

Hovatta T., Lister M. L., Aller M. F., Aller H. D., Homan D. C., Kovalev Y. Y., Pushkarev A. B., Savolainen T., 2012, AJ, 144, 105

Jaffe W., Ford H. C., Ferrarese L., van den Bosch F., O'Connell R. W., 1993, Nature, 364, 213

Jorstad S., Marscher A., Stevens J., Smith P., Forster J., Lister M., Stirling A., Gómez J., Cawthorne T., Gear W., Robson I., 2006, Chinese Journal of Astronomy and Astrophysics Supplement, 6, 247

Jorstad S. G., Marscher A. P., Stevens J. A., Smith P. S., Forster J. R., Gear W. K., Cawthorne T. V., Lister M. L., Stirling A. M., Gómez J. L., Greaves J. S., Robson E. I., 2007, AJ, 134, 799

Kapahi V. K., Saikia D. J., 1982, Journal of Astrophysics and Astronomy, 3, 465

Karamanavis V., 2015, PhD thesis, Max-Planck-Institut für Radioastronomie <EMAIL>vkaramanavis@mpifr.de</EMAIL>

Kato T., Tabara H., Inoue M., Aizu K., 1987, Nature, 329, 223

Kellermann K. I., Pauliny-Toth I. I. K., 1981, ARA&A, 19, 373

Kondratko P. T., Greenhill L. J., Moran J. M., 2005, ApJ, 618, 618

Kormendy J., Richstone D., 1995, ARA&A, 33, 581

Kovalev Y. Y., Kardashev N. S., Kellermann e. a., 2016, AstroPh

Kraus A., Krichbaum T. P., Wegner R., Witzel A., Cimò G., Quirrenbach A., Britzen S., Fuhrmann L., Lobanov A. P., Naundorf C. E., Otterbein K., Peng B., Risse M., Ros E., Zensus J. A., 2003, A&A, 401, 161

Kravchenko E. V., Cotton W. D., Kovalev Y. Y., 2015, in Massaro F., Cheung C. C., Lopez E., Siemiginowska A., eds, IAU Symposium Vol. 313 of IAU Symposium, Rotation measures in AGN jets seen by VLA at 21 cm to 6 mm. pp 128–132

Krolik J. H., Begelman M. C., 1988, ApJ, 329, 702

Kronberg P. P., Reinhardt M., Simard-Normandin M., 1977, A&A, 61, 771

Kronberg P. P., Simard-Normandin M., 1976, Nature, 263, 653

Laing R. A., 1981, ApJ, 248, 87

Laing R. A., 1984, in Bridle A. H., ed., Physics of Energy Transport in Extragalactic Radio Sources Interpretation of Radio Polarization Data. p. 90

Lanyi G. E., Boboltz D. A., Charlot P., Fey A. L., Fomalont E. B., Geldzahler B. J., Gordon D., Jacobs C. S., Ma C., Naudet C. J., Romney J. D., Sovers O. J., Zhang L. D., 2010, AJ, 139, 1695

Laor A., Draine B. T., 1993, ApJ, 402, 441

Legg M. P. C., Westfold K. C., 1968, ApJ, 154, 499

Leventhal M., MacCallum C. J., Stang P. D., 1978, ApJ, 225, L11

Lister M. L., Aller M. F., Aller H. D., Homan D. C., Kellermann K. I., Kovalev Y. Y., Pushkarev A. B., Richards J. L., Ros E., Savolainen T., 2013, AJ, 146, 120

Lister M. L., Cohen M. H., Homan D. C., Kadler M., Kellermann K. I., Kovalev Y. Y., Ros E., Savolainen T., Zensus J. A., 2009, AJ, 138, 1874

Macchetto F., Capetti A., Sparks W. B., Axon D. J., Boksenberg A., 1994, ApJ, 435, L15

Mack K.-H., Klein U., O'Dea C. P., Willis A. G., 1997, A&AS, 123

Magorrian J., Tremaine S., Richstone D., Bender R., Bower G., Dressler A., Faber S. M., Gebhardt K., Green R., Grillmair C., Kormendy J., Lauer T., 1998, AJ, 115, 2285

Mahony E. K., Morganti R., Emonts B. H. C., Oosterloo T. A., Tadhunter C., 2013, MNRAS, 435, L58

Mantovani F., Mack K.-H., Montenegro-Montes F. M., Rossetti A., Kraus A., 2009, A&A, 502, 61

Marecki A., Thomasson P., Mack K.-H., Kunert-Bajraszewska M., 2006, A&A, 448, 479

McBride J., McCourt M., 2014, MNRAS, 442, 838

Meyer L., Ghez A. M., Schödel R., Yelda S., Boehle A., Lu J. R., Do T., Morris M. R., Becklin E. E., Matthews K., 2012, Science, 338, 84

Minkowski R., Greenstein J. L., 1954, ApJ, 119, 238

Miyoshi M., Moran J., Herrnstein J., Greenhill L., Nakai N., Diamond P., Inoue M., 1995, Nature, 373, 127

Montenegro-Montes F. M., Mack K.-H., Vigotti M., Benn C. R., Carballo R., González-Serrano J. I., Holt J., Jiménez-Luján F., 2008, MNRAS, 388, 1853

Morganti R., Fogasy J., Paragi Z., Oosterloo T., Orienti M., 2013, Science, 341, 1082

Morganti R., Greenhill L. J., Peck A. B., Jones D. L., Henkel C., 2004, New A Rev., 48, 1195

Netzer H., 2015, ARA&A, 53, 365

Nielsen D. M., Wilcots E. M., 2015, in Massaro F., Cheung C. C., Lopez E., Siemiginowska A., eds, Extragalactic Jets from Every Angle Vol. 313 of IAU Symposium, The implications of bent jets in galaxy groups. pp 303–304

O'Dea C. P., 1998, PASP, 110, 493

O'Dea C. P., Baum S. A., 1997, AJ, 113, 148

O'Dea C. P., Baum S. A., Stanghellini C., 1991, ApJ, 380, 66

O'Dea C. P., Owen F. N., 1986, ApJ, 301, 841

Oppermann N., Junklewitz H., Greiner M., Enßlin T. A., Akahori T., Carretti E., Gaensler B. M., Goobar A., Harvey-Smith L., Johnston-Hollitt M., Pratley L., Schnitzeler D. H. F. M., Stil J. M., Vacca V., 2015, A&A, 575, A118

Orienti M., 2009, Astronomische Nachrichten, 330, 167

Orienti M., Morganti R., Dallacasa D., 2006, A&A, 457, 531

Orr M. J. L., Browne I. W. A., 1982, MNRAS, 200, 1067

O'Sullivan S. P., Brown S., Robishaw T., Schnitzeler D. H. F. M., McClure-Griffiths N. M., Feain I. J., Taylor A. R., Gaensler B. M., Landecker T. L., Harvey-Smith L., Carretti E., 2012, MNRAS, 421, 3300

O'Sullivan S. P., Gabuzda D. C., 2009, MNRAS, 393, 429

Penrose R., Floyd R. M., 1971, Nature Physical Science, 229, 177

Perley R. A., Butler B. J., 2013a, ApJS, 204, 19

Perley R. A., Butler B. J., 2013b, ApJS, 206, 16

Perley R. A., Dreher J. W., Cowan J. J., 1984, ApJ, 285, L35

Perucho M., Martí J. M., 2007, MNRAS, 382, 526

Peterson B. M., 2001, in Aretxaga I., Kunth D., Mújica R., eds, Advanced Lectures on the Starburst-AGN Variability of Active Galactic Nuclei. p. 3

Peterson B. M., 2006, in Alloin D., ed., Physics of Active Galactic Nuclei at all Scales Vol. 693 of Lecture Notes in Physics, Berlin Springer Verlag, The Broad-Line Region in Active Galactic Nuclei. p. 77

Pihlström Y. M., Conway J. E., Vermeulen R. C., 2003, A&A, 404, 871

Raban D., Jaffe W., Röttgering H., Meisenheimer K., Tristram K. R. W., 2009, MNRAS, 394, 1325

Ramos Almeida C., Levenson N. A., Alonso-Herrero A., Asensio Ramos A., Rodríguez Espinosa J. M., Pérez García A. M., Packham C., Mason R., Radomski J. T., Díaz-Santos T., 2012, Journal of Physics Conference Series, 372, 012004

Rees M. J., 1984, ARA&A, 22, 471

Rengelink R. B., Tang Y., de Bruyn A. G., Miley G. K., Bremer M. N., Roettgering H. J. A., Bremer M. A. R., 1997, A&AS, 124, 259

Reynolds C., Punsly B., Kharb P., O'Dea C. P., Wrobel J., 2009, ApJ, 706, 851

Reynolds C., Punsly B., O'Dea C. P., 2013, ApJ, 773, L10

Robson I., 1996, Journal of the British Astronomical Association, 106, 164

Rossetti A., Dallacasa D., Fanti C., Fanti R., Mack K.-H., 2008, A&A, 487, 865

Rossetti A., Mantovani F., Dallacasa D., Junor W., Salter C. J., Saikia D. J., 2009, A&A, 504, 741

Saikia D. J., 1988, in Miller H. R., Wiita P. J., eds, Active Galactic Nuclei Vol. 307 of Lecture Notes in Physics, Berlin Springer Verlag, Compact Steep Spectrum Radio Sources. p. 317

Saikia D. J., Jamrozy M., 2009, Bulletin of the Astronomical Society of India, 37, 63

Saikia D. J., Salter C. J., 1988, ARA&A, 26, 93

Sandage A., 1965, ApJ, 141, 1560

Scheuer P. A. G., 1974, MNRAS, 166, 513

Schmidt M., 1963, Nature, 197, 1040

Seyfert C. K., 1943, ApJ, 97, 28

Shakura N. I., Sunyaev R. A., 1973, A&A, 24, 337

Shklovskii I. S., 1969, Soviet Ast., 12, 730

Smith E. P., Heckman T. M., Bothun G. D., Romanishin W., Balick B., 1986, ApJ, 306, 64

Smith P. S., Schmidt G. D., Allen R. G., Angel J. R. P., 1995, ApJ, 444, 146

Snellen I. A. G., Schilizzi R. T., Miley G. K., de Bruyn A. G., Bremer M. N., Röttgering H. J. A., 2000, MNRAS, 319, 445

Sokoloff D. D., Bykov A. A., Shukurov A., Berkhuijsen E. M., Beck R., Poezd A. D., 1998, MNRAS, 299, 189

Sol H., Pelletier G., Asseo E., 1989, MNRAS, 237, 411

Stanghellini C., Baum S. A., O'Dea C. P., Morris G. B., 1990, A&A, 233, 379

Thirring H., 1918, Physikalische Zeitschrift, 19, 33

Tribble P. C., 1991, MNRAS, 250, 726

Trippe S., Bremer M., Krichbaum T. P., Krips M., Neri R., Piétu V., Winters J. M., 2012, MNRAS, 425, 1192

Urry C. M., Padovani P., 1995, PASP, 107, 803

Vallee J. P., 1980, A&A, 86, 251

vanden Berk D., Yip C., Connolly A., Jester S., Stoughton C., 2004, in Richards G. T., Hall P. B., eds, AGN Physics with the Sloan Digital Sky Survey Vol. 311 of Astronomical Society of the Pacific Conference Series, Luminosity and Redshift Dependence of Quasar Spectral Properties. p. 21

Véron-Cetty M.-P., Véron P., 2006, A&A, 455, 773

White R. L., Becker R. H., Helfand D. J., Gregg M. D., 1997, ApJ, 475, 479

Wilson A. S., Colbert E. J. M., 1995, ApJ, 438, 62

Xu W., Readhead A. C. S., Pearson T. J., Polatidis A. G., Wilkinson P. N., 1995, ApJS, 99, 297

Zavala R. T., Taylor G. B., 2001, ApJ, 550, L147

Zavala R. T., Taylor G. B., 2004, ApJ, 612, 749

Erklärung

Ich versichere, dass ich die von mir vorgelegte Dissertation selbständig angefertigt, die benutzten Quellen und Hilfsmittel vollständig angegeben und die Stellen der Arbeiteinschlielich Tabellen, Karten und Abbildungen –, die anderen Werken im Wortlaut oder dem Sinn nach entnommen sind, in jedem Einzelfall als Entlehnung kenntlich gemacht habe; dass diese Dissertation noch keiner anderen Fakultät oder Universität zur Prfung vorgelegen hat; dass sie noch nicht verffentlicht worden ist sowie, da ich eine solche Veröffentlichung vor Abschluss des Promotionsverfahrens nicht vornehmen werde. Die Bestimmungen dieser Promotionsordnung sind mir bekannt. Die von mir vorgelegte Dissertation ist von Prof. Dr. Michael Kramer betreut worden.

Unterschift:

_____-

Datum:

_____-